2011

Photonic Non-destructive Measurement Methods for Investigating the Evolution of Polar Firn and Ice

Daniel James Breton

PHOTONIC NON-DESTRUCTIVE MEASUREMENT METHODS FOR INVESTIGATING THE EVOLUTION OF POLAR FIRN AND ICE

By

Daniel James Breton

B.S. Rensselaer Polytechnic Institute, 1997

M.Eng. University of Maine, 2002

A DISSERTATION

Submitted in Partial Fulfillment of the

Requirements for the Degree of

Doctor of Philosophy

(in Physics)

The Graduate School

The University of Maine

May 2011

Advisory Committee:

Gordon S. Hamilton, Associate Professor of Earth Sciences, Advisor

C.T. Hess, Professor of Physics

James Fastook, Professor of Computer Science

Richard Morrow, Professor Emeritus of Physics

Paul Camp, Professor Emeritus of Physics

Gordon Oswald, Research Professor of Earth Sciences

DISSERTATION

ACCEPTANCE STATEMENT

On behalf of the Graduate Committee for Daniel James Breton, I affirm that this manuscript is the final and accepted dissertation. Signatures of all committee members are on file with the Graduate School at the University of Maine, 42 Stodder Hall, Orono, Maine.

Gordon S. Hamilton, Associate Professor of Earth Sciences (Date)

LIBRARY RIGHTS STATEMENT

In presenting this dissertation in partial fulfillment of the requirements for an advanced degree at The University of Maine, I agree that the Library shall make it freely available for inspection. I further agree that permission for "fair use" copying of this thesis for scholarly purposes may be granted by the Librarian. It is understood that any copying or publication of this dissertation for financial gain shall not be allowed without my written permission.

Daniel James Breton (Date)

PHOTONIC NON-DESTRUCTIVE MEASUREMENT METHODS FOR INVESTIGATING THE EVOLUTION OF POLAR FIRN AND ICE

By Daniel James Breton

Dissertation Advisor: Dr. Gordon Hamilton

An Abstract of the Dissertation Presented
in Partial Fulfillment of the Requirements for the
Degree of Doctor of Philosophy
(in Physics)
May 2011

When snow falls on glaciers or ice sheets, it persists for many tens, hundreds and sometimes thousands of years before becoming ice. The granular material in between fresh snow and glacial ice is known as firn and is generally 50 to 100 m thick over polar ice sheets. The compaction mechanism of firn into ice (called densification) has important glaciological ramifications in determination of ice sheet stability and related sea level rise effects via remote sensing altimetry. Firn densification is also important for correctly interpreting ice core paleoclimate records, especially those analyzing gases trapped in air bubbles within the glacial ice.

Densification is thought to depend strongly on microstructure: the sizes, shapes, orientations and inter-particle bonds of the ice grains that make up polar firn. Microstructure-dependent densification is poorly understood and occurs in the region where two-thirds of the overall densification takes place. This work focuses on developing non-destructive methods for simultaneously evaluating changes in both

the bulk density and microstructure of polar firn to better understand structure-dependent densification processes.

The first method is an automated density gauge which uses gamma-ray transmission methods to non-destructively produce high resolution (3.3 mm) and high precision (± 4 kg m^{-3}) density profiles of firn and ice cores. This instrument was used to collect a density profile for the first 160 m of the West Antarctic Ice Sheet Divide WDC06A deep ice core.

The second method involves optical scattering measurements on firn and ice cores to determine the important microstructural parameters of ice grain and air bubble size and air-ice interface surface area. These measurements are modeled using both Monte Carlo radiative transfer and ray-tracing geometric optics methods, and are then tested against experiment using digital photography of the WDC06A core.

Combining the results of both bulk density and optical scattering measurements for the same core reveals that microstructure-dependent densification did occur at this site and is readily detectable by purely photonic methods. This work lays the theoretical and experimental foundations for a novel, non-destructive and field deployable instrument for further study of structure-dependent firn densification.

DEDICATION

For Erika

ACKNOWLEDGEMENTS

I am indebted to many, many people over many years for their help in the completion of this dissertation.

My advisor Dr. Gordon Hamilton provided substantial funding, advice, encouragement and most of all, intellectual freedom to pursue various studies at the intersection of physics, glaciology and paleoclimatology. I think this freedom has borne important fruit in this dissertation, and I wish to sincerely thank him for his wisdom and patience.

Dr. C.T. Hess also deserves thanks for his steadfast support and assistance through the early days of designing, building and testing the firn and ice density gauging instrument described in Chapter 2. Moreover, his enthusiasm and interest in all of my projects (ranging from science to submarining) helped spark my desire to pursue a doctorate in the first place, and for this I am very grateful.

I would also like to thank Dr. James Fastook for not only being a constant source of support and encouragement, but also for explaining to me that "It's okay to be 'just a dirty modeler'." The work in Chapter 3 required a fair amount of numerical simulation and his guidance helped me steer clear of many time-wasting pitfalls.

Dr. Paul Camp deserves thanks for bringing his years of ice experience to bear on some of the problems described in this dissertation. His insightful questions have always pulled me out of the weeds and pointed me in the right direction.

I would like to thank Dr. Richard Morrow for his careful analysis of the scattering models described in Chapter 3. His suggestions helped me better understand my own results and led to consistent explanation for the observed variability in emergent intensity from the WDC06A core.

Thanks go to Dr. Gordon Oswald for his thoughtful use of his expertise in both nuclear and glaciological science in commenting on this dissertation and discussing various instrumental approaches.

I am also grateful for the efforts of Dr. Steven Arcone, whose comments and direction throughout my doctoral education have been invaluable, educational, and often hilarious. His thoughtful appraisal of both this dissertation and the paper that preceded it have improved my work (both intellectual and written) greatly.

Both Dr. Karl Kreutz and Bess Koffman deserve thanks for allowing me access to the WDC06A core to perform the density profiling described in Chapter 4. The additional risks for disaster and/or contamination posed by the density profiling were real, and I greatly appreciate their sharing of this precious resource. Their friendship and encouragement through this process has been refreshing, even in the face of some unforgiving deadlines.

Without the selfless help of the following photon modelers, the results of Chapter 3 and the conclusions drawn in Chapter 4 would have been impossible. I would like thank Dr. Ghislain Picard for not only providing a copy of his SNOWRAT geometric optics modeling software, but also for reviewing and critiquing my modifications to it to ensure they were correct. T.J. Fudge and Benjamin Smith also deserve my sincere thanks for sharing their radiative transfer code and their own documentation for that code. Discussions with all of these researchers were invaluable in writing this dissertation.

I would like to thank Dr. Robert Hawley and Dr. Elizabeth Morris who, through their papers and long discussions at numerous meetings, encouraged me pursue the study of firn optics and microstructure-dependent densification. Without them, this dissertation might consist only of a long chapter on MADGE and a *lot* of Appendices.

Thanks are also given for the help of Patricia Byard, Rebecca Addessi and Betty Lee in navigating the complicated administrative world here at the University. Tom

Tripp also deserves thanks for his assistance in machining many of the parts required to assemble the instrument described in Chapter 2.

Finally, I would like to thank my shipmates on the 2006 and 2007 U.S. International Trans-Antarctic Scientific Expedition. It is impossible to really know what the Ice is really like until you get there, and I am glad to have gotten there with all of you.

TABLE OF CONTENTS

LIST OF TABLES

LIST OF FIGURES

LIST OF SYMBOLS

ℓ	Total photon packet pathlength in sample [m]
ω	Single-scattering albedo
ρ	Density of firn or bubbly ice [kg m^{-3}]
ρ_{ice}	Density of solid ice [kg m^{-3}]
μ_a	Optical absorption coefficient [cm^{-1}]
μ_s	Optical scattering coefficient [cm^{-1}]
μ_t	Optical extinction coefficient [cm^{-1}]
a	Scatterer radius [mm]
g	Asymmetry parameter
j	Coordination number
n_{air}	Index of refraction for air
n_{ice}	Index of refraction for solid ice
A	Albedo [arbitrary units]
E	Emergence [arbitrary units]
E_{act}	Activation energy [kJ mol^{-1}]
L	Photon packet radiance [W m^{-2} sr^{-1}]
L_0	Initial photon packet radiance [W m^{-2} sr^{-1}]
L_{abs}	Mean free path for optical photon absorption [m]
L_{scat}	Mean free path for optical photon scattering [m]
N_{scat}	Number of in-sample scattering events
SSA_m	Specific surface area, unit mass basis [m^{-1}]
SSA_v	Specific surface area, unit volume basis [m^2 kg^{-1}]
T	Transmittance [arbitrary units]

LIST OF ABBREVIATIONS

BI	Air bubbles in ice
BOS	Borehole Optical Stratigraphy
CR	Count rate
CGF	Coarse-grained firn
ECM	Electrical Conductivity Meter
FGF	Fine-grained firn
FWHM	Full width at half maximum
GA	Ice grains in air
GO	Geometric optics
MADGE	Maine Automated Density Gauge Experiment
MDD	Microstructure-dependent densification
NICL	National Ice Core Laboratory
OIS	Optical Imaging System
PMT	Photomultiplier tube
RT	Radiative transfer
SCA	Single Channel Analyzer
WAIS	West Antarctic Ice Sheet
VS	Visual stratigraphy
XCT	X-ray computed tomography

CHAPTER 1
OVERVIEW OF FIRN DENSIFICATION

"Furious activity is no substitute for understanding."

– H. H. Williams

1.1 Introduction

This dissertation is about developing and testing new techniques and instrumentation to measure and understand the physical properties of firn and the evolution of these properties as a function of time and depth. Firn is the material that exists on a glacier or ice sheet between freshly fallen snow and glacial ice (Cuffey and Paterson, 2010). Firn can be over 100 m thick in high, cold polar regions and its macroscopic physical properties (density, air permeability, specific surface area, thermal conductivity) are largely determined by firn *microstructure* (Domine and others, 2008). We will use the term microstructure to describe the physical arrangement of ice grains and the distribution of grain and pore sizes, typically on mm to cm scales. The same term will be used to describe similar properties (arrangement and sizes) of air bubbles in bubbly ice. Fig. 1.1 shows some firn microstructure in detail.

Polar firn microstructures are influenced by local temperature, wind speeds, accumulation rate of new snow (typically expressed in cm a^{-1} water equivalent), solar energy input and, of course, the nature of the snow forming the firn (Albert and others, 2004; Alley, 1988; Braithwaite and others, 1994; Craven and Allison, 1998; Salamatin and others, 2009). This microstructure plays an important role in controlling the compaction or *densification* of firn. The densification rate of firn and its dependence on microstructural and climatic variables is one of the central challenges facing both glaciologists (interested ice sheet mass balance and sea level

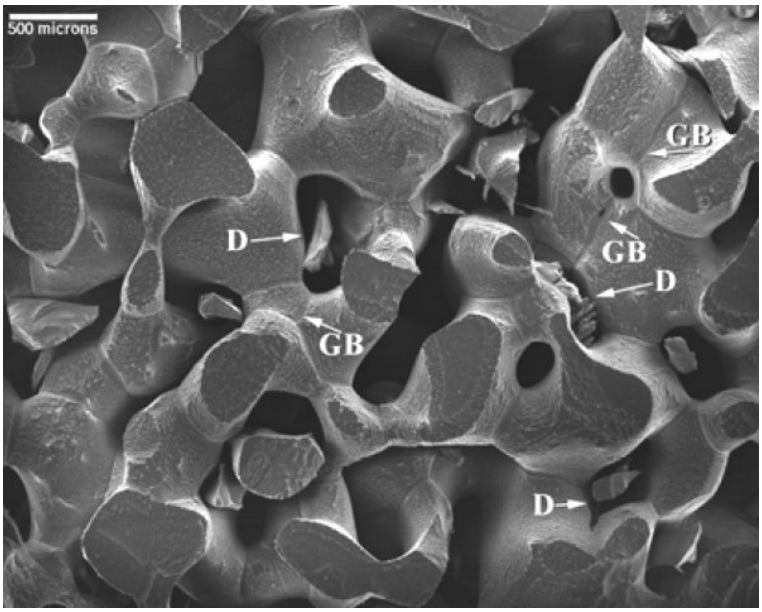

Figure 1.1. SEM image of firn microstructure. Image of South Pole firn from 9.7 m depth. GB = grain boundary, D = debris from sample preparation. From Baker and others (2007).

rise) and ice-core paleoclimate researchers (interested in chemical fluxes, ice and trapped gas age as a function of depth).

1.1.1 Ice Sheet Elevation

Glaciologists often use remote sensing altimeter data to observe temporal changes in ice sheet elevation. These changes, when corrected for isostatic adjustments and integrated over the area of the ice sheet, provide an estimate of the net ice volume change of the ice sheet (Wingham and others, 1998; Thomas and others, 2008). These data are of direct relevance to studies of sea level change since volume lost by an ice sheet will soon be gained by the world's oceans (Peltier and Tushingham, 1989). The use of aircraft- or satellite-based remote sensing data is often the only practical way to rapidly and repeatedly survey ice sheet elevations.

Significant variations in ice sheet elevation can be caused by changes in accumulation rate (Giovinetto and Zwally, 2000; Vaughan and others, 1999) and firn

densification processes (Braithwaite and others, 1994; McConnell and others, 2000). Knowledge of firn densification rates and mechanisms are therefore crucial for the correct translation of elevation change into ice volume change: over a large ice sheet, 10 cm of firn compaction at the top has zero effect on sea levels, while 10 cm of ice loss from the bottom has a profound effect.

1.1.2 Paleoclimate Studies

The development of accurate depth-age timescales is very important for ice-core paleoclimate reconstructions, especially those focused on the study of abrupt climate change (Alley, 2000) where the temporal difference between cause and effect is necessarily small. The age of firn at a given depth below the surface is determined by competition between the compaction velocity (speed with which a point in the firn moves towards the bedrock due to the compaction of firn and ice below) and the accumulation rate (rate at which new material is added to the top of the firn column) (Cuffey and Paterson, 2010).

Average accumulation rates at a given coring site can often be determined by detecting well known radioactive or volcanic layers within the core itself (Legrand and Mayewski, 1997). The water equivalent accumulation rate can then be deduced using the known layer ages and a depth-density profile of the core (Kaspari and others, 2004). Less is known about how to assess the compaction velocity of a given point since it depends on the characteristics of the firn that preceded it and the climate conditions in which densification is occurring (Cuffey and Paterson, 2010). Point measurements of this parameter have been made using the "coffee-can" method of Hamilton and others (1998) and Hamilton and Whillans (2000) where markers are embedded tens of meters deep in the firn column and connected to the surface with a steel cable.

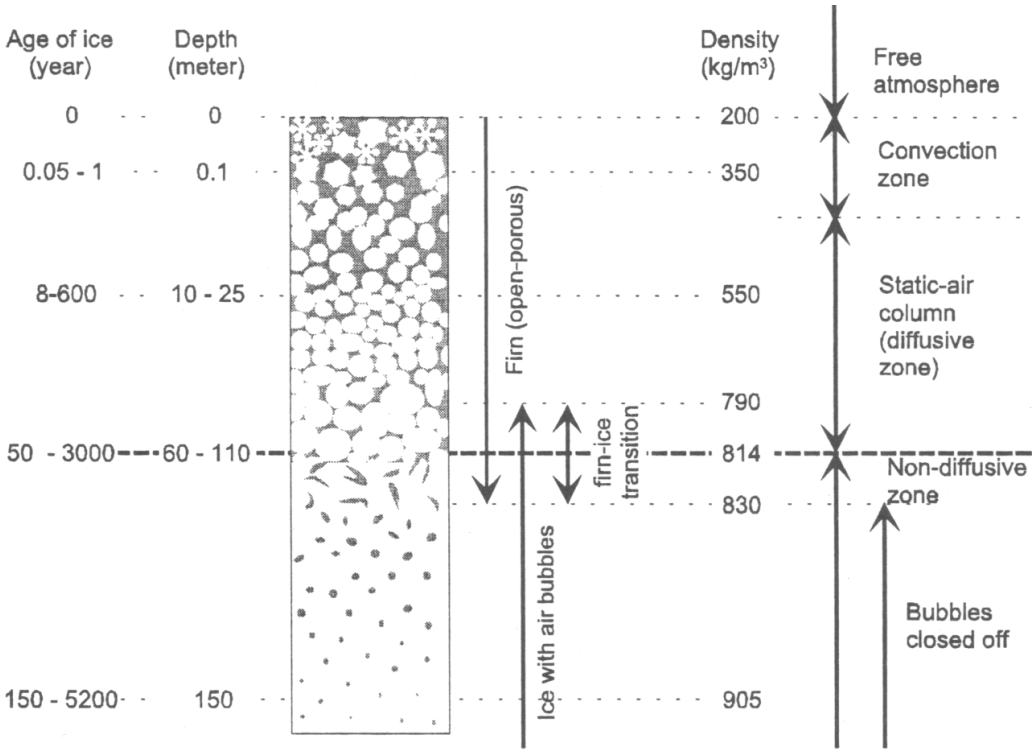

Figure 1.2. Sketch of an idealized polar firn column. From Blunier and Schwander (2000).

Many different modeling approaches have been undertaken to understand firn densification, and these are discussed in Chapter 4. However, few studies have been made which combine measurements of firn strain (related to compaction velocity), density and microstructure as a function of depth. The work of Hawley and others (2004) and Hawley and Morris (2006) comes closest and is discussed in detail in Section 1.2.1 and Chapter 4.

1.2 Firn Densification

Firn surface densities are generally in the 300-400 kg m^{-3} range, while cold glacial ice is 920 kg m^{-3}, a tripling of density. In brief, dry firn compaction is believed to proceed in four distinct stages, sketched in Fig. 1.2 and listed below.

1. From the surface to a density of ∼550 kg m^{-3} (the density of randomly packed ice spheres) densification proceeds via particle settling, also called grain-boundary sliding (Alley, 1987; Arnaud and others, 1998b). The rate of settling depends strongly on inter-particle bonds, particle shape and available porespace volume for relative movement of particles. This stage represents roughly one third of the total densification process from firn to ice.

2. After random packing is achieved, the dominant processes are particle sintering (inter-particle bond growth) and deformation in response to the growing overburden load. The end of particle settling significantly decreases the densification rate (Ebinuma and Maeno, 1987). This stage is generally considered to cover the density range 550 to 730 kg m^{-3} (Frolov and Fedyukin, 1998), and therefore represents roughly another third of total densification.

3. Further densification occurs from 730 to 830 kg m^{-3} primarily through particle deformation. Pore closeoff occurs during this stage, generally starting around 780 and completing around 830 kg m^{-3} (Severinghaus and Battle, 2006). At pore closeoff, the air pressure in the bubbles is the local atmospheric pressure. Approximately one sixth of the total densification occurs in this stage.

4. Below pore closeoff, densification slows again as the air bubbles begin to "push back" against the creeping ice. Air bubbles shrink and grow more spherical as the bubble pressure approaches the overburden pressure. Eventually, all air bubbles are converted to clathrate hydrates and the ice is bubble free (Langway, 1958; Lipenkov and others, 1997). The final sixth of total densification is accomplished in this stage.

From this list, we can see that the majority of firn densification occurs in the shallow firn (depths typically < 50 m) where microstructural factors play a role.

The importance of microstructure-dependent densification (MDD) in controlling densification is best illustrated through the somewhat controversial topic of density inversion. MDD can occur without causing a density inversion (Alley and others, 1982), but density inversion requires MDD (Freitag and others, 2004).

1.2.1 Density Inversion

Density inversion has been detected in the past using either a combination of high resolution density data and chemistry data collected from the same core, or high resolution structural data obtained by X-ray computed tomography techniques.

1.2.1.1 Gerland and Others (1999)

The classic study by Gerland and others (1999) showed a change in correlation with depth between the density and electrical conductivity signals in the Berkner Island, Antarctica core. This core demonstrated a marked minimum in density variability at 25 m (see Fig.1.4) which, in conjunction with the density and conductivity data, prompted Gerland to hypothesize that weaker, coarse grained firn (CGF) deposited in the summer compacted faster than stronger, fine grained firn (FGF) deposited in the winter. The data from this study are shown in Fig. 1.3 and 1.4.

The electrical conductivity of the Berkner Island core was determined using the electrical conductivity meter (ECM) method of Hammer (1980). Briefly, this method entails dragging two brass electrodes, held at a 1250 VDC potential difference and separated by 1 cm, down a flat section of core surface. The current flow, in μA, is recorded as a function of depth and is responsive to changes in acidity, or pH of the core but is largely insensitive to the presence of salts (Moore and others, 1992). The acidic layers are associated with summer precipitation (Hammer, 1980; Legrand and

Mayewski, 1997) due to changes in sea ice extent, biological activity in the Southern Ocean and seasonal weather patterns.

Gerland's hypothesis argues that the differential compaction rate *continues* past the point where CGF and FGF densities are equal, the inversion point. Therefore, the surprising part of his hypothesis is this: firn densification depends strongly on some factor *other* than bulk density. That factor has been speculated to be either microstructural (Freitag and others, 2004), chemical (Alley and Woods, 1996) or a combination of both. This implies that understanding firn compaction in general, and MDD/density inversion in particular, must involve simultaneous studies of both microstructure and chemistry in order to separate these effects.

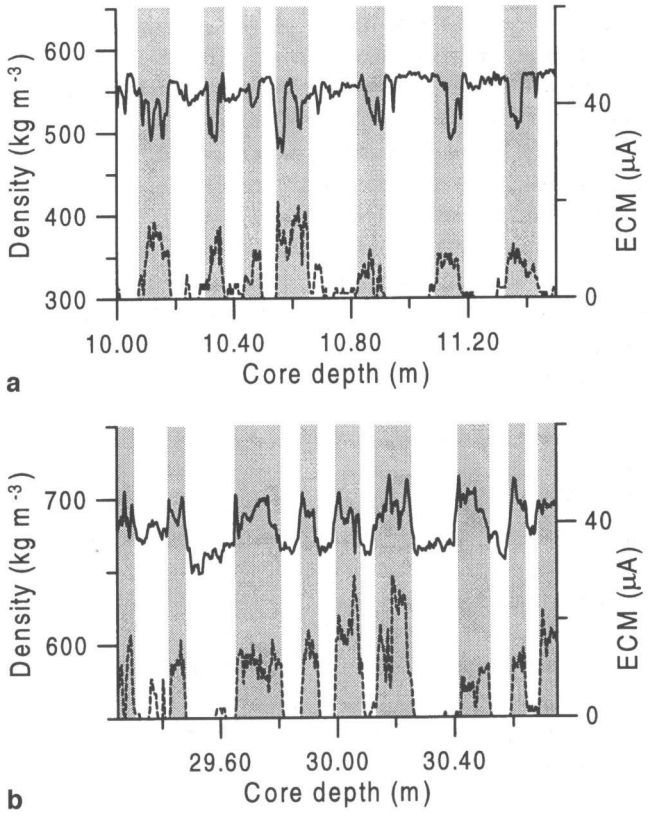

Figure 1.3. Density and ECM data for Berkner Island, Antarctica. Density (upper curves) and ECM current (lower curves) for sections above (a) and below (b) the density inversion. Shaded bands indicate summer layers as determined by ECM readings. From Gerland and others (1999).

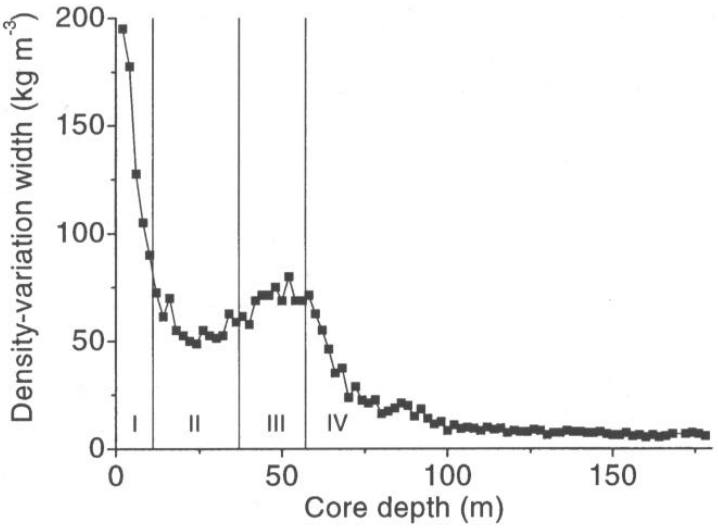

Figure 1.4. Density variability for Berkner Island, Antarctica. Variability calculated over 2 m depth windows as a function of depth in the B25 core. From Gerland and others (1999).

Both Koerner (1971) at Plateau Station and Fujita and others (2009) at Dome Fuji Station found the opposite relationship of firn type with season: strong, fine grained firn formed in the summer while weak, coarse grained firn formed in the winter. These stations are noteworthy in that they are the highest and arguably the coldest stations in East Antarctica, and may represent special conditions not routinely experienced elsewhere in the polar regions (e.g. Gerland's coastal site at Berkner Island).

Li and Zwally (2002), based on their analysis of the density data from Gerland and others (1999), also came to a similar conclusion as Koerner and Fujita (CGF→winter and FGF→summer), but only after interpreting the minimum in density variability (25 m, Fig. 1.4) as "abnormal...possibly due to the interannual changes of the surface weather conditions." We now know that this minimum in density variability is observed in many different cores and is evidence of MDD manifested as density inversion (Horhold and others, 2011). Regardless of the seasonality

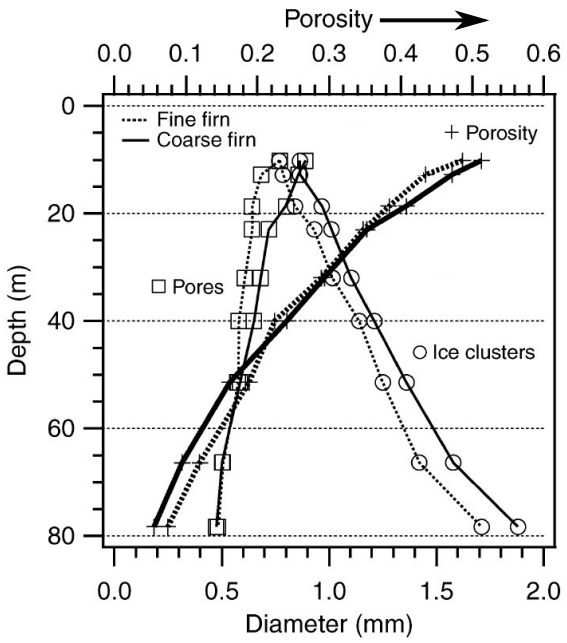

Figure 1.5. Density inversion as revealed by XCT. Thick lines correspond to Depth and Porosity axes, thin lines correspond to Depth and Diameter axes. From 0 to 20 m depth, CGF (solid line) is more porous (less dense) than FGF (dashed line). Deeper than 50 m, the opposite is true. From Freitag and others (2004).

of CGF and FGF, the idea underlying MDD remains the same: CGF is weaker than FGF throughout the firn column.

The theory regarding the density variability minimum (Alley and others, 1982; Horhold and others, 2011) is that if CGF is less dense, but compacting faster than FGF, then at some depth the CGF and FGF densities must be roughly equal, hence the minimum in density variability at that point. Beyond this depth, CGF *continues* its more rapid compaction, and density variability increases to a maximum (about 50 m in Fig. 1.4) until both CGF and FGF begin to approach ice densities. Since the final ice density is the same for both firn types, the variability decreases.

1.2.1.2 Freitag and Others (2004)

Further evidence for density inversion is given by Freitag and others (2004). The B26 core was recovered in northwest Greenland (77°15′N, 49°13′W, 18 cm a^{-1}

accumulation rate and mean firn temperature of -31° C) and measured using the same high resolution density equipment used by Gerland and others (1999). A density variability minimum was observed at 25 m depth. Freitag and coworkers used X-ray computed tomography (XCT) to record 3D images of selected samples of the firn microstructure with $40\times40\times40$ μm^3 resolution. This measurement does not allow the direct measurement of density, but rather determines the porosity n which can be related to the density by $\rho = (1-n)\rho_{\text{ice}}$.

The XCT instrument provided detailed grain size and porespace shape and volume data, and allowed the calculation of separate porosity-depth profiles for CGF and FGF, as shown in Fig. 1.5. The results are a straightforward confirmation of Gerland's hypothesis: CGF is less dense at the surface, passes through a zone where it is equal in density to FGF, and is more dense than FGF at depths greater than 50 m. Most of the densification comes about by volume growth of ice grains. Porespace volume shrinks only slightly with depth.

The XCT method, while providing an unprecedented view of firn microstructure, is often limited to small sample sizes (and therefore requires destructive sample removal from the core) and requires a long time to obtain and post-process the data in order to extract porosity, grain and pore space sizes and other structural parameters. XCT systems have seen use in the field (Freitag and others, 2008), but cannot be adapted for use in a borehole since tomography, by definition, requires access to all sides of the sample.

1.2.1.3 Hawley and Morris (2006)

The in-situ work of Hawley and Morris (2006) very likely observed the start of a density inversion in a 30 m borehole at Summit, Greenland using optical and neutron scattering measurements recorded in the same borehole.

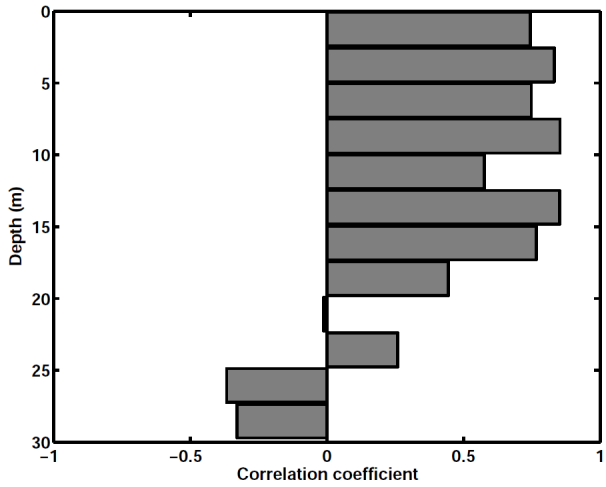

Figure 1.6. Firn density and albedo correlation as a function of depth in a Summit, Greenland borehole. From Hawley and Morris (2006).

Optical firn reflectivity (albedo) data were recorded as a function of depth using Hawley's borehole optical stratigraphy (BOS) system, a small, annular light source and video camera unit that is lowered into the borehole (Hawley, 2005). The vertical resolution of this system is limited by borehole size and multiple light reflections from the borehole walls which tend to smooth out stratigraphy-related albedo variations (Fudge and Smith, 2010).

Firn density was measured using Morris' neutron scattering probe (Morris and Cooper, 2003), an Am-Be fast neutron source mounted to a BF_3 thermal neutron detector which is lowered into the borehole. This system measures density based on the neutron moderation properties of the surrounding firn. A higher firn density implies stronger moderation by the H atoms in the firn, and thus a larger thermal neutron count rate. The neutrons have a $\sim$14 cm radius "sphere of influence" (Morris, 2008) which tends to smooth out stratigraphy-related density variations.

The major result of their study is shown in Fig. 1.6 which shows the firn density-albedo correlation as a function of depth. In the shallow sections of this borehole, FGF is both more dense and more optically reflective than CGF. Passing through

a zone of no correlation at 20–25 m, the correlation then begins to show a negative correlation, likely indicating a density inversion: CGF is now more dense, but still less reflective than FGF. If these results and interpretation are correct, it implies a very interesting behavior for firn: the relative densities of CGF and FGF invert while their relative optical properties do not.

The instruments used in this study are simple, rugged, easily portable and are able to collect their data in a borehole, allowing repeat measurements of the same borehole over time. Repeat, in-situ measurements of the firn are invaluable, since the firn is left to densify undisturbed (other than the borehole itself) in its natural environment. The most significant drawback is the lower vertical resolution when compared with the techniques of Gerland and others (1999) and Freitag and others (2004).

1.3 Hypothesis

We have established the importance of understanding firn densification in the contexts of ice sheet mass balance and ice core paleoclimate reconstruction. Gerland, Freitag and Horhold have established that density inversion exists and is likely a common feature of polar firn in regions with regular annual accumulation. Hawley and Morris have likely shown that density inversion is detectable in the field using a combination of optical and neutron scattering measurements.

In short, we know that density inversion *can* happen and therefore MDD is a significant part of understanding how firn behaves, whether it undergoes density inversion or not. We need to understand the mechanism of MDD to explain not just *where* and *how* density inversion occurs, but also to make useful predictions of future firn densification based on the current microstructural stratigraphy at a given site.

MDD plays a significant, possibly dominating role in the evolution of the upper 50 m of the firn column where two thirds of firn densification occurs. Sites with density inversion provide useful test cases to observe MDD processes operating in a obvious way. If we can objectively and reliably characterize firn microstructure as a function of depth as the density inversion process unfolds, then we can improve our knowledge of firn rheology and adjust our densification models accordingly.

Horhold and others (2011) state, "High resolution grain size data are needed to examine the impact of grain size on the densification of the different layers." We should also add to this the requirement that the methods used must be non-destructive and usable in the field so that our results are not altered by firn metamorphism during the long journey from ice sheet to laboratory (Kaempfer and Schneebeli, 2007). Following the microstructural measurement, the core should still be available for other uses, including chemical analysis to explore the potential impurity-related densification effects on firn. The ideal instrument would provide this microstructural data in-situ via borehole measurements.

The limited throughput, considerable expense and difficulty of deploying an XCT machine into the field makes it unlikely that this will be the method of choice for processing the many hundreds of meters of core required in a study of the full range of MDD/density inversion processes. Furthermore, the XCT system cannot be adapted for deployment in a borehole to provide in-situ data.

Optical scattering methods, while promising, have received limited theoretical and modeling attention. It is supposed (Hawley and Morris, 2006; Fudge and Smith, 2010) that both density and grain size will have effects on the optical scattering properties of firn, but a unified optical model of firn including bubbly ice and measurement geometries other than reflectivity does not yet exist.

Given all of the earlier approaches, we propose to put the most promising methods on a firm theoretical footing by stating the following hypothesis:

Firn densification is a microstructure-dependent process. We will test this hypothesis using only non-destructive, photonic measurement methods.

To test this hypothesis, we must:

1. Design, optimize and develop reliable calibration methods for a non-destructive, high resolution firn/ice core density instrument. This effort is detailed in Chapter 2 which is an expanded version of a published paper (Breton and others, 2009).

2. Develop a complete and unified model of firn optics that includes both firn and bubbly ice, allowing studies of density inversion into and beyond the firn-ice transition. The resulting model and comparison with existing transmission and albedo data are discussed in Chapter 3.

3. Test the predictions of the firn optics model by analyzing a firn/ice core likely to contain density inversion. This work involved the collection of high resolution density and optical scattering data from the top 160 m of the West Antarctic Ice Sheet (WAIS) Divide deep core WDC06A. The methods, analysis and results of this process are described in Chapter 4.

CHAPTER 2
DESIGN, OPTIMIZATION AND CALIBRATION OF A GAMMA-RAY DENSITY GAUGE FOR FIRN AND ICE CORES

> "The [depth-density] function ... has to be continuous and simple in order to be useful. Strictly speaking, this would require that snow falls all the time at a constant rate and constant initial density. Fortunately for the polar traveler, this is not the case."
>
> – Bader (1954)

2.1 Introduction

If we desire to study the densification of polar firn and ice, then we must have the best means possible of measuring the density at high resolution and with high precision. Firn density is usually calculated from measurements of sample volume and mass, quantities which are not only subject to a large measurement uncertainty but must also be sampled at a low vertical resolution to make sample handling practical (Whillans and Bolzan, 1988). High precision measurements are possible on ice samples using the iso-octane differential weight technique discussed in Gow (1970), but it cannot be used on firn, generally requires samples to be removed from the core, and is not suited for high resolution density profiling.

Accurate assessments of inter-annual accumulation variability and firn compaction mechanisms require that a different measurement technique be used. High resolution density gauging systems provide information on physical firn and ice properties that cannot be practically determined any other way (Horhold and others, 2011).

A gamma-ray density gauge (sketched in Fig. 2.1) non-destructively determines the density of a sample of known thickness by comparing the transmission rate or intensity of a beam of γ-rays passing through a sample with the intensity of the same beam passing through air. Provided that the beam is narrow and consists of γ-rays of the same energy, the intensity of the transmitted γ-ray beam follows the Lambert-Beer law:

$$n = n_0 \exp(-\mu_m \rho x) \tag{2.1}$$

where n is the γ-ray intensity (γ-rays s^{-1}) at the detector with a sample present, n_0 is γ-ray intensity at the detector with no sample present, ρ is the average density of the sample along the beam path (g cm^{-3}) and x is the beam path length in the sample (cm). The mass attenuation coefficient μ_m of the sample material (cm^2 g^{-1}) is defined as μ/ρ where μ is the linear attenuation coefficient (cm^{-1}) of the sample material. The linear attenuation coefficient is a function of both the atomic number and density of the material and is a measure of the probability per unit length that a γ-ray will interact in some way with the sample material. The mass attenuation coefficient simply removes the density dependence from μ and provides a way to determine the material density if μ_m is known.

Both n and n_0 are *unscattered* γ-ray intensities, that is, they have passed from source to detector without interacting with anything along the way, arriving at the detector undeflected and with their original energy. Ideally, γ-rays scattering from the sample are either deflected into and absorbed by the Pb detector collimator plate, or have lost sufficient energy in the Compton scattering process to be discarded by the counting system. However, in a real instrument there is some contribution to n from small angle scattering events as discussed in Section 2.2.2.4.

The mass attenuation coefficient is a constant for a given material and γ-ray energy E_γ, so measuring the sample attenuation consists of simply determining n_0

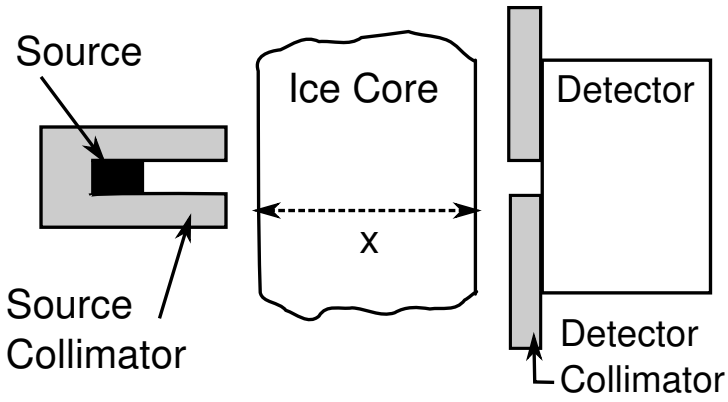

Figure 2.1. Top-down view of a γ-ray density gauge.

and n. In a real measurement, we do not measure intensities directly, but instead determine them from $n_0 = N_0/t_0$ and $n = N/t$ where N_0 and N are the number of unscattered γ-rays arriving at the detection system in a time t_0 and t respectively.

The attenuation measurement alone can only give information about the product ρx which has units of g cm^{-2} and is called the *mass thickness* of the sample. In order to extract a traditional density (g cm^{-3}), we must also measure the diameter of the ice core x. We then determine the density as

$$\rho = -\frac{\ln(n/n_0)}{\mu_m x}. \tag{2.2}$$

Several important aspects of a real density measurement are not captured by this relation:

1. Choice of optimum E_γ for a given material and sample size
2. System dead time losses cause measured intensities m and m_0 to be lower than from the actual intensities n and n_0
3. Choosing an appropriate activity for the γ-ray source
4. Calibrating the device to account for both finite detector energy resolution and departures from the narrow-beam approximation due to finite collimator hole size.

Section 2.2 discusses these issues and our methods of solving them, section 2.3 covers measurement uncertainty, repeatability and throughput while section 2.4 a radiation safety analysis for the instrument. We have named the resulting instrument MADGE: the Maine Automated Density Gauge Experiment.

2.1.1 Previous Instruments

Several instruments of this type have been used in glaciological work before, including the Alfred Wegener Institute (AWI) densimeter (Gerland and others, 1999; Wilhelms, 2000), and the Hokkaido University X-ray device (Hori and others, 1999). These instruments operate at very different photon energies, but both use very intense sources: about 3 Ci of ^{137}Cs (primary energy 661 keV) for the AWI instrument and a 30 kV x-ray tube for the Hokkaido University device. The strength of their sources requires that both detectors operate in *current mode* since the high x or γ-ray intensity makes detecting the arrival or the energy of an individual photon impossible.

This is a potential disadvantage because Eq. 2.1 is valid only for mono-energetic photons. Current mode detection cannot differentiate between unscattered photons (with full energy E_γ) and those that have been Compton scattered to some lower energy. Detectors without energy resolution must either use very tight collimation or correct the measurements using an empirical *buildup factor* which depends on E_γ and both the geometry and density of the sample (Knoll, 1989).

Detector operation in *pulse mode* counts each detected γ-ray individually and analyzes it for E_γ by monitoring the electrical pulse created by the detector. Using pulse mode precludes operation at very high gamma-ray intensities due to dead time losses (Knoll, 1989), but it does improve the statistical accuracy of the measurement and ensures that we are correctly applying Eq. 2.1 by only counting events in a narrow energy range corresponding to unscattered γ-rays. Dead time losses occur

when the γ-ray intensity is so high that it is not possible for the counting system to electronically distinguish the detector pulse of one γ-ray from the next, counting multiple γ-rays as one.

All of the previously mentioned transmission methods acquire ex-situ data from firn/ice cores extracted from the ice sheet. In-situ density data has been acquired in glacial boreholes using the neutron scattering methods pioneered by Morris and Cooper (2003). In this method the density probe (a Wallingford soil-moisture probe, consisting of a fast neutron source and a BF_3 thermal neutron detector) is slowly lowered into a glacial borehole. The fast neutrons are moderated by the surrounding firn and ice, where higher density leads to more effective neutron moderation and therefore a higher thermal neutron count rate. The active detection volume for this instrument is large, a $\sim$ 14 cm radius about the probe center, due entirely to the long range of fast neutrons in firn (Morris, 2008). Nevertheless, this represents the only successful in-situ density measurement technology available to glaciologists today.

2.1.2 MADGE Workbench and Sensor Head

The instrument consists of an aluminum workbench on which ice cores are processed, and an insulated and temperature controlled electronics box. The workbench provides a straight and level surface for supporting the ice core trays and mounting the density profiling hardware. The ice cores are held in adjustable-height core trays and are density-profiled by the sensor head, a π-shaped set of aluminum plates which provide rigid mounting support for the source, γ-ray detector and ice core diameter calipers, shown in Fig. 2.2. The two legs of the π are the source and detector support plates, while the top is the yoke, a plate machined to keep the support plates parallel and properly aligned with each other.

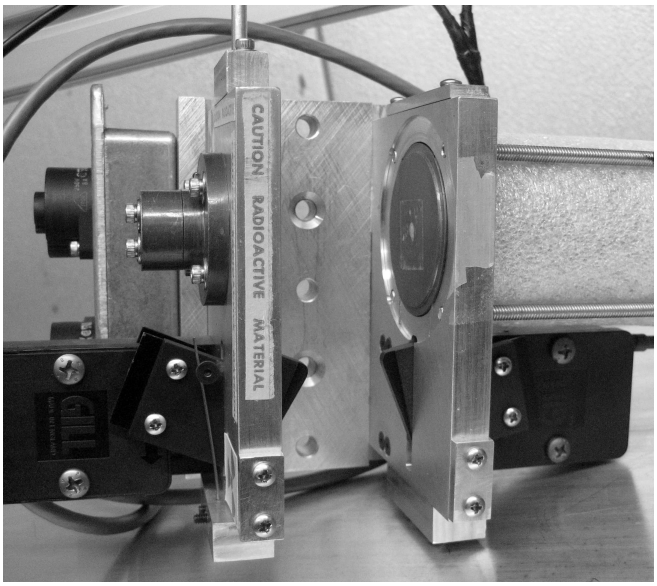

Figure 2.2. Bottom view of the MADGE sensor head. The source and detector support plates are on the left and right, respectively. Core calipers are the black mechanisms at the bottom, designed to contact the core 33.3 mm ahead of the γ-ray beam. The sensor head travel direction is from top to bottom of the photo. For scale, each support plate is 10 cm from top to bottom.

A belt-type linear actuator driven by a stepper motor moves the sensor head in 3.3 mm increments over the ice core. After the sensor head is moved, the core diameter and gamma transmission are measured and stored by a microcontroller. Each such movement and measurement sequence is called an exposure and it takes 303 exposures to produce a continuous profile of a 1 m ice core.

The core diameter calipers are 3.3 mm wide spring-loaded plastic arms which pivot in from both sides of the sensor head to make contact with the ice core. Each arm carries a steel activator which interacts with a Gill* Blade25 eddy-current position detector (`http://www.gillsensors.co.uk`) to provide sub-millimeter position measurements. The core diameter measurement is made 33.3 mm (exactly ten exposures) ahead of the nuclear measurement so that the data can be easily shifted

*Gill Sensors, Saltmarsh Park, 67 Gosport Street, Lymington, Hampshire, United Kingdom, SO41 9EG

during post processing to ensure that the core diameter and gamma transmission data are properly matched.

2.1.3 MADGE Electronics Box and Microcontroller

The insulated electronics box takes 120 VAC, 60 Hz power and contains the microcontroller board, a Canberra* model 1000 portable Nuclear Instrumentation Module (NIM) bin (`http://www.canberra.com`), a ±12 V linear power supply and a Parker† OEMZL6 stepper motor controller (`http://www.parker.com`). A solid state relay controlled resistance heater and an exhaust blower are also installed inside the box to heat or cool as necessary to maintain a stable interior temperature of about 20°C during measurements.

The microcontroller is a Rabbit Semiconductor‡ RCM3720 (`http://www.rabbit.com`) and operates all parts of the instrument through RS-232, Serial Peripheral Interface (SPI) and simple transistor-transistor-logic (TTL) level voltage signals, as shown in Fig. 2.3. The Canberra 512 counter timer and the core diameter calipers are operated via RS-232, while the OEMZL6 stepper motor driver is controlled via TTL-level signals to select movement direction and give stepping commands.

The microcontroller board also has 12-bit analog to digital (A-D) and digital to analog (D-A) conversion capabilities. The A-D converter measurements are used primarily to monitor temperatures while the D-A converter is used to control the lower level discriminator (LLD) setting of the Canberra 2015A SCA so that any drift in the nuclear measurement system can be corrected.

*Canberra Industries Inc., 800 Research Parkway Meriden, Connecticut 06450, USA

†Parker Hannifin Corporation, Electromechanical Automation Division, 5500 Business Park Drive, Rohnert Park, CA 94928

‡Rabbit Semiconductor, 2900 Spafford Street, Davis, CA 95618

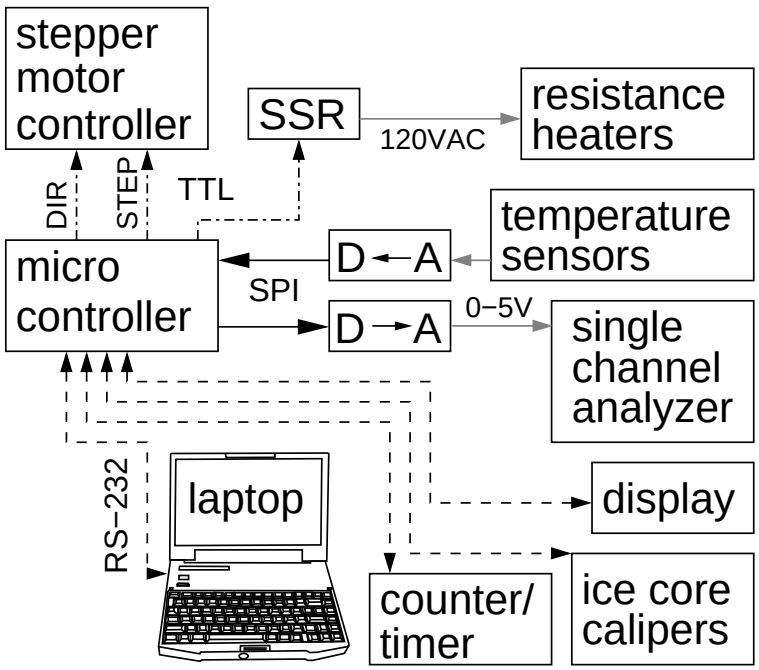

Figure 2.3. MADGE inter-instrument communications. RS-232 shown in dashed lines, TTL-level shown in dash-dot lines, SPI shown in solid lines.

The RCM3720 can be reprogrammed in the field and has an on-board 1MB serial Flash memory to store hundreds of meters of density profiles. The operator can upload data to a laptop via any standard terminal program.

2.2 Measurement Methods

The density gauge makes two simultaneous measurements: sample thickness x determined by calipers, and sample mass thickness ρx determined by γ-ray transmission. In this section we discuss the equipment, the mathematical models for transforming raw data into useful form, and the calibration method for the γ-ray transmission measurement system.

2.2.1 Thickness Measurement

Measurement of the sample thickness determines the path length of the γ-ray beam through the sample and can have an enormous impact on the calculated sample density uncertainty, as shown in Section 2.3.1.

2.2.1.1 Caliper Equipment

Ice core calipers for field use need to withstand low temperatures and blowing snow while providing sub-millimeter precision over the course of several thousand measurements per day. We experimented with non-contact techniques (ultrasonic and optical) and found them unsuitable for rough and porous ice core surfaces, and subject to possible interference by blowing snow. We finally chose a spring loaded caliper design that contacted the core on both sides (designated as source-side and detector-side depending on where the caliper arm was mounted on the sensor head) and measured the caliper arm displacements using a pair of Gill Blade25 eddy current sensors.

A Blade25 sensor reports a digital output code for a given caliper arm displacement, with a resolution of roughly 38 codes mm^{-1} (Gill Sensors, 2004). This output code is converted to an actual displacement measurement (d_{src} or d_{det}) by using the calibration relationship discussed below in section 2.2.1.2. The two Blade25 sensors were controlled directly by the RCM3720 microcontroller via 3-wire RS-232 connections. The RCM3720 then performed the displacement conversion calculation and took the average of 30 measurements from each caliper arm to calculate the core diameter x as

$$x = d_{\mathrm{yoke}} - d_{\mathrm{src}} - d_{\mathrm{det}} \tag{2.3}$$

where d_{src} is the distance between the source support plate and the ice core, d_{det} is detector support plate to ice core distance and d_{yoke} is the inside distance between the source and detector support plates and is equal to 40.64 mm for the WDC06A

core setup. This system allows for correct core diameter measurements even though the core may not be perfectly centered in the gauge.

2.2.1.2 Caliper Calibration

The initial calibration of the ice core calipers compared the Blade25 output to the actual caliper arm displacement. We mounted the sensor head on a vertical mill table equipped with a Mitutoyo* AT715 Absolute Linear Scale (±0.005 mm accuracy) and cycled each caliper arm through its full range of motion (`http://www.mitutoyo.com`). This calibration provided data on the Blade25 sensor response as a function of displacement and also the noise present in the sensor response. We modeled the sensor response as a function of displacement by a third-order polynomial for two reasons:

1. The geometry of the sensor head and the desire for a simple caliper mechanism required that a given caliper arm rotate about an axle. Therefore we used the Blade25, designed as a *linear* displacement sensor, as an angular displacement sensor. For displacements between 0 and 6 mm (where most measurements occur) the sensor output is linear and noise-free, but for larger displacements (around 8 mm or greater, corresponding to small core diameters) the output is less linear and suffers from increased noise (±2 codes ≈ ± 0.05 mm). The polynomial provides good linearity for small to medium displacements and also captures the non-linearity at larger displacements.

2. The RCM3720 microcontroller can easily convert the sensor output codes to real displacements via the polynomial, rather than storing a large onboard lookup table.

*Mitutoyo America Corporation, 958 Corporate Blvd. Aurora, IL 60502

Sensor	A	B	C	D
Source-side	0.0326	-0.2424	38.1960	-0.8828
Detector-side	0.0349	-0.1309	38.0897	-0.3810

Table 2.1. MADGE caliper calibration coefficients.

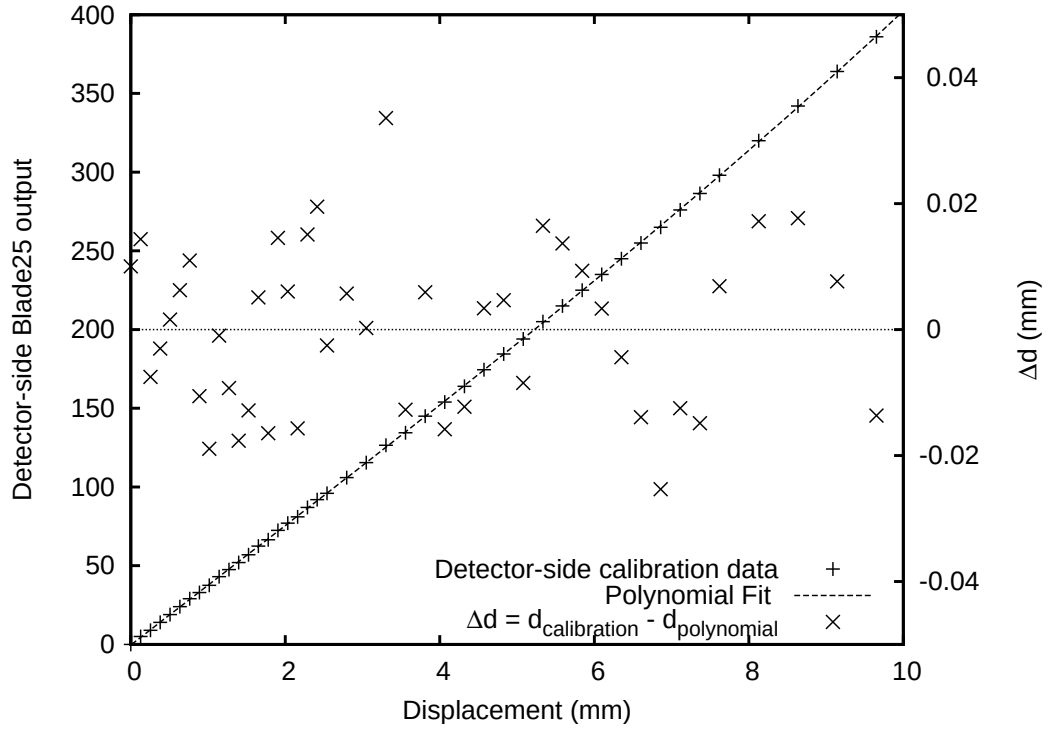

Figure 2.4. Blade25 calibration and uncertainty data. Data shown are for detector-side unit, source-side calibration and uncertainty data are similar.

The general expression is $Ac^3+Bc^2+Cc+D = d$ where c is the output code of the Blade25 and the coefficients are determined by a least squares fit to the calibration data. The same expression is used for both $d_{\rm src}$ and $d_{\rm det}$ though the coefficients have slightly different values as shown in Table 2.2.1.2.

The uncertainty associated with $d_{\rm det}$ can be observed in Fig. 2.4 where the difference Δd between the actual displacement and that calculated by the polynomial fit is shown. These differences are generally ± 0.02 mm or less. Except for large displacement measurements (> 8 mm), the uncertainty of the sensor output is ± 1

code or 0.026 mm. The overall uncertainty of the core diameter measurement is then $\Delta x = \Delta d_{\text{src}} + \Delta d_{det} = 2(0.046) \cong 0.1$ mm.

2.2.2 Gamma-ray Transmission Measurement

We will follow the path of a single γ-ray from its source to its final destination as a count stored in the memory of the microcontroller to discuss all of the equipment used in the transmission measurement.

The γ-ray source, built by Eckert & Ziegler Isotope Products Laboratory* is a sealed stainless steel capsule containing a 3.7 GBq ^{241}Am pellet with a primary E_γ of 59.5 keV. The capsule is housed inside of a small lead shield equipped with a fail-safe, spring-loaded shutter (allowing the source to be turned on or off) and a 3.3 mm diameter collimator hole. The source collimator hole is 10 mm long and confines the radiation to a 36.4° apex-angle cone, aimed directly at the detector collimator hole.

The detector collimator is a flat Pb plate covering the entire detector face except for a 3.3 mm diameter hole in the center. The Pb plate provides radiation shielding for the detector side of the sensor head and prevents the detector from counting any radiation except that passing through the collimation hole. Together, the source and detector collimators define a pencil-shaped measurement beam which passes through the diameter of the ice core.

For the MADGE detection system, we required high speed and good energy resolution at 59.5 keV to match our source. The γ-ray detector was built by Saint-Gobain Crystals† (`http://www.detectors.saint-gobain.com`) and is a 3.8 cm diameter by 3.8 cm tall BrilLanCe$^{\text{TM}}$380 (B380) scintillation crystal mounted to a

*Eckert & Ziegler Isotope Products, 24937 Avenue Tibbitts, Valencia, CA 91355
†Saint-Gobain Crystals, 17900 Great Lakes Pkwy, Hiram, OH 44234-9681

photomultiplier tube (PMT). We chose B380 over the traditional NaI as our scintillator because of the faster response time of the B380 crystal.

The detector requires a high voltage source and electronics to process the output signal pulses. MADGE uses a standard NIM bin to house and power a Canberra model 3102D high voltage power supply, a model 512 dual counter timer and a model 2015A single channel analyzer (SCA) with amplifier.

Signal pulses from the detector are first sent to the SCA. The SCA outputs a single logic pulse only if the input detector pulse voltage falls within a preset voltage window. This voltage window defines the E_γ range that will trigger a count by the counting system. The output logic pulses are sent to the counter/timer which keeps track of both the number of logic pulses (counts) and the elapsed time of the measurement. The microcontroller reads both count and elapsed time data from the counter/timer for storage.

2.2.2.1 Goldilocks' γ-ray

For a given sample size and density, a very high energy γ-ray may not interact with the sample at all and a very low energy γ-ray may not penetrate the sample to be counted. In between these two extremes we expect that there will be an energy which is 'just right'. We want γ-rays with low enough energy to have sufficient interaction with the sample to get a good density measurement but not so much interaction that the count rate is prohibitively low.

We can find this optimum γ-ray energy from Eq. 2.1 by first defining the sensitivity S as the change in intensity n for a given change in sample density ρ:

$$S = \frac{\partial n}{\partial \rho} = -\mu_m x n_0 \exp(-\mu_m \rho x). \tag{2.4}$$

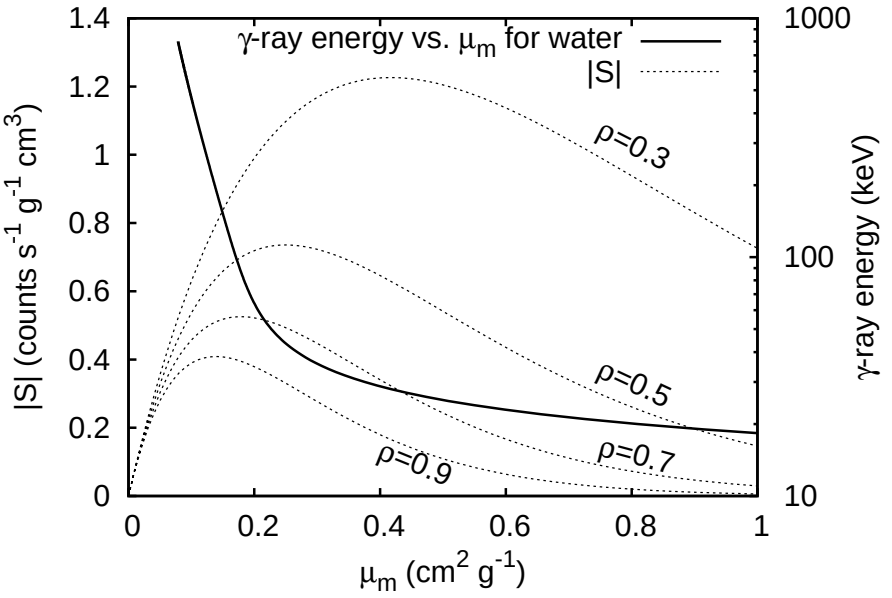

Figure 2.5. Sensitivity $|S|$ versus μ_m. Data are for 8 cm diameter ice cores of indicated densities (in g cm^{-3}). E_γ versus μ_m for water (Brunetti and others, 2004) is plotted to relate the μ_m for optimized S to E_γ for the sample material of interest. $|S|$ shown for a unit sample-free intensity ($n_0 = 1$ count s^{-1}) for simplicity.

Given a sample material, size and range of densities, we can find the value of μ_m which maximizes the sensitivity and then translate that optimum μ_m value into γ-ray energy using the solid curve in Fig. 2.5.

S is a negative number by definition, since n will decrease with increasing ρ, but in Fig. 2.5 we plot the absolute value $|S|$ to visualize the meaning of the maximum: that value of μ_m which achieves the greatest change in output signal (intensity or count rate) for a given change in the input signal (density). Plotting $|S|$ versus μ_m for various values of ρ, we can see in Fig. 2.5 that the sensitivity has a maximum and approaches zero for the two extremes of high and low values of μ_m.

Setting $\partial S/\partial \mu_m$ equal to zero yields a simple relationship between μ_m, x and ρ for optimal sensitivity: $\mu_m = 1/\rho x$. Using this general relationship, we can use estimates of our expected sample size and density range to determine the optimum mass

Sample size x (cm)	Sample density ρ (g cm^{-3})	Optimal μ_m (cm^2 g^{-1})	Optimal E_γ (keV)
5.0	0.2	1.0	18.2
5.0	0.917	0.218	53.6
8.0	0.2	0.625	22.2
8.0	0.917	0.136	203.4

Table 2.2. MADGE sample parameters and resulting optimized mass attenuation coefficients and γ-ray energies for water. Mass thicknesses range from 1.0 to 7.3 g cm^{-2}.

attenuation coefficient, which can then be converted into a corresponding optimal E_γ by choosing a material, and plotting E_γ versus μ_m for that material.

Our criteria for choosing E_γ for MADGE were based on maximizing S for our design core sizes. We needed to process core diameters ranging from 5.0 to 8.0 cm with expected firn and ice densities ranging from 0.2 to 0.917 g cm^{-3}, which together yield mass thicknesses ranging from 1.0 to 7.3 g cm^{-2}. The optimum μ_m values for this range are shown in Table 2.2.2.1. Choosing our material to be water, we can then use the E_γ versus μ_m curve for water to find the optimum E_γ.

Taken together, the data shown in Table 2.2.2.1 suggests that a γ-ray energy between 20 and 100 keV would provide good sensitivity for the expected range of sample size and density, and led us to select ^{241}Am for our source isotope with its primary E_γ of 59.5 keV. This choice is nearly optimal for a 0.917 g cm^{-3}, 5 cm diameter core (ρx = 4.6 g cm^{-2}), which roughly represents the center of our expected sample mass thickness range.

2.2.2.2 Detection System Dead Time

All γ-ray detection systems have a limit on the rate at which they can resolve one γ-ray from another. This limit is generally described using the idea of a system dead time τ: the period of time following the arrival of a γ-ray during which the system is unable to count a newly arriving γ-ray. Dead time losses occur when the

incoming rate of γ-rays is so high that it is not possible for the counting system to electronically distinguish the detector response of one γ-ray from the next, counting multiple γ-rays as one. Two problems arise from this phenomenon:

1. the actual rate of γ-rays incident on the detector n and measured count rate m diverge as the incident intensity increases, making it necessary to perform a dead time correction to determine the correct values of n and n_0

2. the dead time correction is based on the value of the dead time τ which has its own associated uncertainty $\Delta\tau$, introducing additional uncertainty to calculated sample densities.

We needed an appropriate mathematical model for the counting system dead time losses and an experimentally determined value of τ for that model. All subsequent measurements can then be corrected for dead time losses using the model. We briefly discuss three models of interest: the non-paralyzable, the paralyzable and the hybrid.

The simplest model of dead time is the *non-paralyzable* model, which assumes that the detection system is unable to count an additional event if it occurs within a time τ of the previous event (Knoll, 1989). In this model, the relationship between measured count rate m and the actual rate of incident γ-rays n is given by

$$n = \frac{m}{1 - m\tau}. \tag{2.5}$$

It is important to note that n is a function of m and τ only.

The *paralyzable* model is the same as the non-paralyzable model with the additional restriction that the dead time starts over for each additional event occurring during a dead time. In this case, the relationship is

$$m = n \exp(-n\tau). \tag{2.6}$$

Here we cannot solve for n directly as a function of m and τ, so we must find n iteratively. Incorporating this model into the uncertainty propagation of Section 2.3.1 makes it impossible to find an analytical expression for $\Delta\rho$, the uncertainty of the final density measurement.

Finally, a two parameter *hybrid* model combines both of the previous models (Lee and Gardner, 2000; Lee and others, 2007). The hybrid model is given as

$$m = \frac{n \exp(-n\tau_P)}{1 + n\tau_N} \tag{2.7}$$

where the parameter τ_P is the dead time characterizing paralyzable behavior of the detection system and τ_N characterizes the non-paralyzable behavior. Since it includes the paralyzable model, this model also requires that n be determined using an iterative calculation.

For the MADGE detection system, we found that the hybrid model was a good representation of the dead time losses over a wide range of event rates, but the non-paralyzable model was even better for the actual operating range of interest ($n \leq$ 80,000 counts per second). Therefore, we used the non-paralyzable model to simplify the uncertainty calculation for the final density measurement.

We performed a dead time experiment on the MADGE detection system using the following steps:

1. place the source and detector 1 m apart
2. record M, the number of counts measured during an interval t_{dt}
3. move the source 2 cm towards the detector
4. repeat steps 2 and 3 until the source and detector meet
5. calculate the actual event rate n as a function of source-detector separation using an inverse-square relationship

Model Parameter	Value (μs)	Note
Non-paralyzable	τ=2.592 $\pm$ 0.0062	excellent fit for $m < 80{,}000$ cps
Paralyzable	τ=1.579 $\pm$ 0.0285	poor fit for $m > 25,000$ cps
Hybrid	τ_N=1.824 $\pm$ 0.0153	good fit for all m
	τ_P=0.513 $\pm$ 0.0055	good fit for all m

Table 2.3. MADGE dead time model parameters

6. plot measured count rate $m = M/t_{\mathrm{dt}}$ as a function of source-detector separation

7. choose a dead time model and perform least-squares fit to m data.

Since the source is collimated, it is crucial to maintain exactly the same source orientation throughout the experiment. We found that the only satisfactory way to perform this experiment was to rigidly mount the source on a cart and rail system and to use long counting intervals (t_{dt} = 30 s).

The result of this procedure is shown in Fig. 2.6 where we see that the hybrid model nicely describes the MADGE detection system dead time losses over the entire range of measured count rates. The paralyzable model does not fit these data well, but the non-paralyzable model fits extremely well (in fact, better that the hybrid model) in the region where $m <$ 80,000 counts per second (cps). The results of the curve fitting are shown in Table 2.2.2.2.

We can define an operating range for the density gauge where dead time losses (calculated as $n\tau$) are less than 20%, ensuring that we can assume that the measured γ-ray counts maintain a Poisson distribution (Knoll, 1989). For the non-paralyzable model, $n\tau$ reaches 10% at $n \approx$ 39,000 cps which, by design, is the open gauge event rate n_0 in Eq. 2.1. In this region, the non-paralyzable model with τ=2.592 μs is the best characterization of the MADGE detection system behavior and therefore

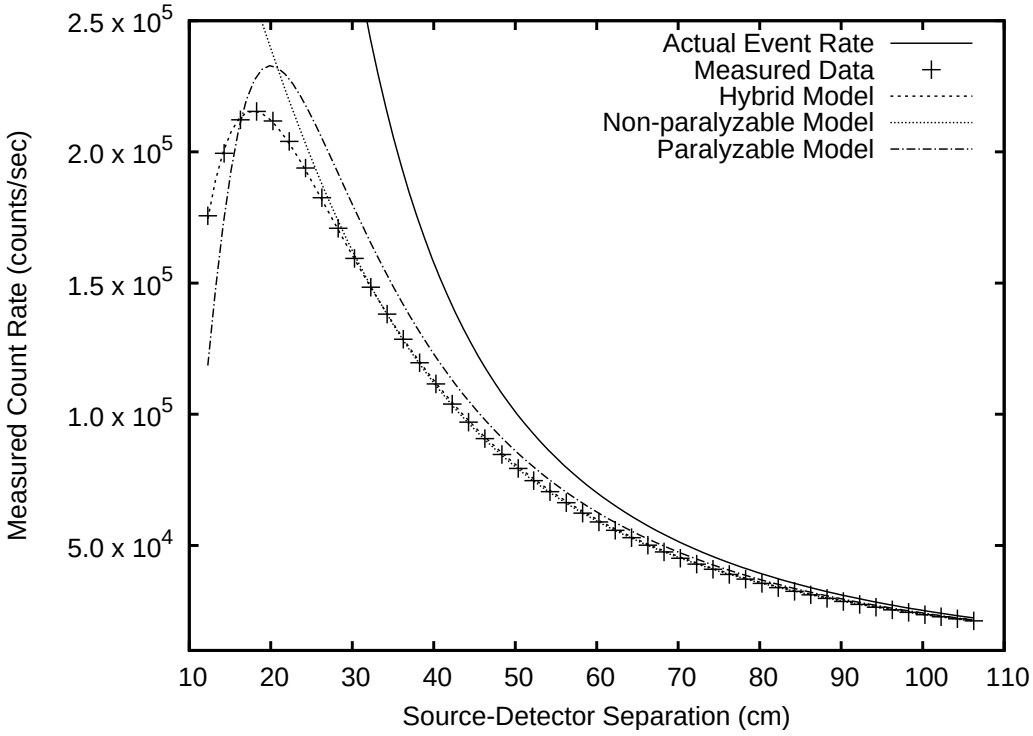

Figure 2.6. MADGE dead time experimental data and various dead time models.

it is the model used for all subsequent dead time corrections. This also gives us a fundamental understanding of the capacity of our detection and counting system so that we can properly choose the γ-ray source activity.

2.2.2.3 Source Activity

The primary limitation on the activity of the source is the collimation and dead time characteristics of the detection system to which it is coupled. A source with excessive activity requires very large dead time corrections, increasing the influence of the dead time uncertainty $\Delta\tau$ on the final density uncertainty $\Delta\rho$ to unacceptable levels. On the other hand, a weak source will require far greater time to achieve a given density uncertainty goal. We sought to find an n_0 which satisfies $n_0\tau \approx 10\%$, a compromise between throughput and dead time losses.

We calculated n_0 to be $0.1/2.592 \times 10^{-6}$ s $\approx$ 39,000 cps. We then determined the source activity which would deliver n_0 gamma-rays sec^{-1} to the detector given the geometry of the gauge and fixed absorbers (collimators, source and detector window materials) in the beam path.

The required source activity $A_{\rm src}$ can be calculated as

$$A_{\rm src} = \frac{n_0}{(\epsilon_{\rm geom})(\epsilon_{\rm det})(B_{E_\gamma})(T_{\rm fixed})(f_{\rm self})} \tag{2.8}$$

where $\epsilon_{\rm geom}$ is the geometric efficiency of the source-detector pair, $\epsilon_{\rm det}$ is the efficiency of the detector, B_{E_γ} is the branching ratio of the source isotope at E_γ, $T_{\rm fixed}$ is the γ transmission through all fixed materials in the beam path and $f_{\rm self}$ is the fraction of 59.5 keV γ-rays which are not lost to self absorption within the source pellet. All of these factors are functions of E_γ except the geometric efficiency. All of these factors except $f_{\rm self}$ are discussed at length in Knoll (1989). In our case $\epsilon_{\rm det} = 1$ because the 59.5 keV γ-rays, once inside the detector, are virtually guaranteed to interact with the scintillation crystal due to its size, density and high atomic number.

For the MADGE prototype operating on a 5 cm diameter core, we used the following values to determine the required source activity:

$$\frac{39,000}{(1.16 \times 10^{-4})(1.0)(0.36)(0.7501)(0.33)} = 3.77 \times 10^9 \text{ Bq}. \tag{2.9}$$

Density scanning of the West Antarctic Divide WDC06A core (in the form of 3 cm $\times$ 3 cm $\times$ 100 cm firn/ice sticks) required a smaller source-to-detector plate separation than the 5 cm cores. Reduction of the source - detector distance increased n_0 beyond the desired operating range. The installation of an aluminum absorber plug into the detector collimator hole maintained $n_0 \sim 43$ kcps, higher that the 5 cm setup but still within the operating range.

A difficult problem is the absorption of γ-rays within the source pellet itself, quantified by $f_{\rm self}$. This is a significant problem for ^{241}Am because E_γ is relatively

low (easily absorbed) and Am itself has a very high atomic number (a strong absorber) and is distributed throughout the volume of the source pellet. Our only successful calculation of f_{self} was a Monte Carlo approach which indicated that nearly 67% of the 59.5 keV γ-rays are lost to self absorption in the source pellet, yielding $f_{\text{self}} = 0.33$ used in the calculation above.

2.2.2.4 Mass Attenuation Coefficient Calibration

The nuclear instrument calibration is the determination of μ_m for a given γ-ray energy, detection system energy window width, detection system dead time and source-detector-collimator geometry. In essence, the calibration consists of multiple γ-ray transmission measurements measured with varying absorber thicknesses. When these data are plotted as the natural logarithm of counts versus mass thickness of absorber, the slope of the resulting line yields μ_m.

There are many sources in the literature for very precise values of μ_m, determined using experimental setups as close to the narrow-beam ideal as possible. These values represent the *maximum* value of μ_m attainable by any density gauge system. However, two factors cause real systems to achieve a lower μ_m than the maximum, ideal value: finite detector and counting system energy resolution, and finite size collimator holes.

The B380 detector has an energy resolution of 10.8% at 59.5 keV (Saint-Gobain Crystals, 2008), meaning that the measured energy of many 59.5 keV γ-rays would yield a Gaussian distribution (called a photopeak) centered at 59.5 keV with FWHM of 6.4 keV. Since the photopeak has a finite width in energy, the user must adjust the counting system energy window width (via the single channel analyzer) to count the events in the photopeak.

The finite energy window width allows some unwanted scattered γ-rays to be counted: those that have Compton scattered through a small angle such that they fall within the energy window *and* still pass through the detector collimator.

The end result of the additional scattered counts is to make it appear that the calibration absorber is absorbing fewer γ-rays than predicted by Eq. 2.1. The apparent reduction in absorbing power results in a lower μ_m value than the maximum, demonstrating that calibration is a necessary process for all real instruments in order to properly account for the various non-ideal aspects of a given system.

Both the energy window and collimator hole size can be made smaller in an attempt to minimize the number of scattered γ-rays counted, but at the cost of decreased count rate of both scattered and unscattered γ-rays, which then reduces the instrument throughput since the device must spend more time on a single exposure.

For γ-ray energies less than the pair-production threshold at 1022 keV, a density gauge is really an *electron* density gauge, since all photon absorption and scattering is due to either photoelectric absorption or Compton scattering interactions with electrons in the sample. This allows us to perform the μ_m calibration on the material regardless of whether it is a gas, liquid or solid (Knoll, 1989), since the number of electrons per molecule is constant regardless of the phase of the material. Liquid water is an ideal calibration absorber in that the bulk density is spatially uniform.

The MADGE calibration equipment consists of a plastic cylinder to contain the water, a syringe, an electronic scale to measure the mass of the cylinder, and a source of deionized water. The calibration begins with the sensor head mounted vertically (source on bottom, detector on top) and leveled so that the cylinder can be centered over the beam path. The mass and inner diameter of the empty cylinder are recorded and then a gamma transmission measurement is performed with the empty cylinder in the beam path. This not only provides a zero water thickness data point, but also ensures that the attenuation effect of the cylinder is the same

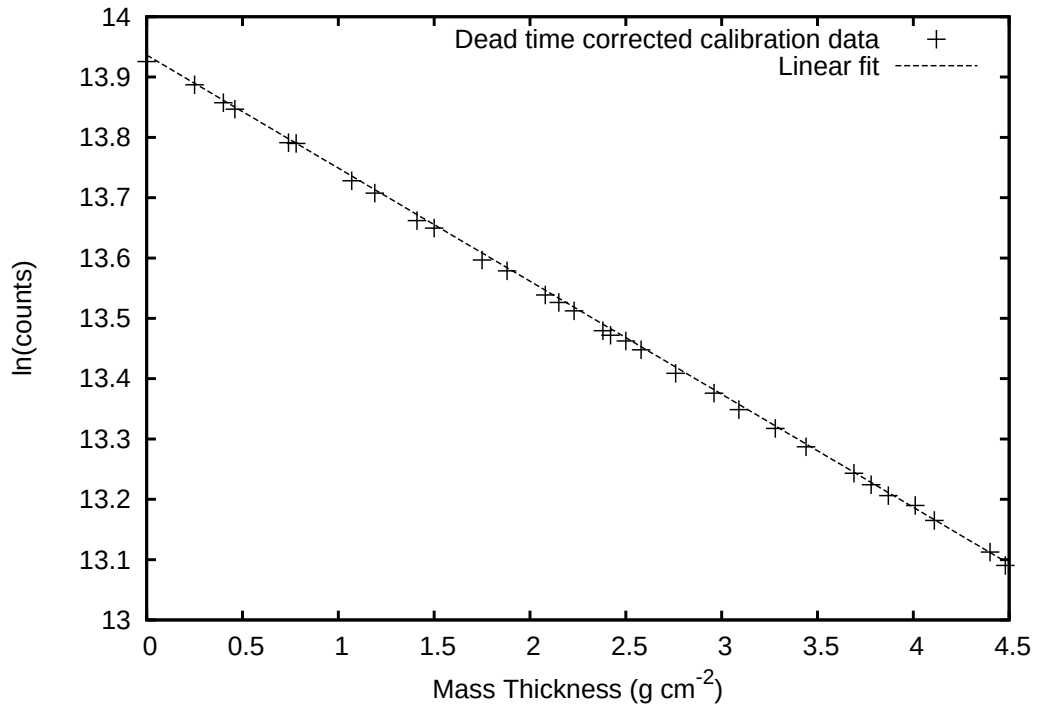

Figure 2.7. Typical μ_m calibration curve. Data for the MADGE 3 cm (for the WDC06A core) sensor head. $\mu_m = 0.1810 \pm 0.0004$.

for all data points. Since μ_m is determined by the slope of the plotted data, the presence of the cylinder does not affect the calibration results.

A small amount water is then added to the cylinder and the water mass thickness is calculated by dividing the total mass of water by the cross sectional area of the cylinder opening. Note that the water density is not required for the mass thickness determination. A gamma transmission measurement is performed with the cylinder centered in the beam path and the process is repeated for many different mass thicknesses, ideally covering the same range of mass thickness expected for real samples.

After performing dead time corrections for all data points, plotting the natural logarithm of corrected counts versus mass thickness of water yields a straight line whose slope is μ_m. A calibration curve is shown in Fig. 2.7.

Element	Pure Water $\mu_m = 0.2058$	Impure Water $\mu_m = 0.2059$	Seawater $\mu_m = 0.2111$
H	0.1119	0.1118	0.1083
O	0.8881	0.8879	0.8586
Na	0	50×10^{-6}	0.0109
Mg	0	10×10^{-6}	0.0014
S	0	10×10^{-6}	0.0009
Cl	0	100×10^{-6}	0.0195
K	0	10×10^{-6}	0.0004
Ca	0	10×10^{-6}	0.0004

Table 2.4. Calculated μ_m (at E_γ = 60 keV) for water with varying major ion concentrations and the weight fractions of hydrogen, oxygen and the major ions used in the calculation.

MADGE has been calibrated for 3 and 5 cm core diameter setups with μ_m of 0.1810±0.0004 and 0.1874 ± 0.0005 cm^2 g^{-1} respectively. The longer source to detector distance of the 5 cm setup eliminates more of the small angle Compton scattered photons discussed above, resulting in a larger μ_m.

2.2.2.5 Effects of Impurities on μ_m

Our development of the μ_m calibration has assumed that both the sample cores and calibration absorber are the same material: pure water. Real firn and ice cores do contain impurities, typically in the 1 part per 10^9 range for the major ions. To evaluate the effects of these impurities, we analyzed hypothetical samples of impure water (representing an "impure" ice core) and seawater.

In Table 2.2.2.5, we have calculated the mass attenuation coefficients at 60 keV for pure water, impure water, and 35 part-per-thousand salinity seawater to demonstrate the effects of increasing impurity concentrations. The mass attenuation coefficients for these mixtures were calculated as $\mu_m = \sum_i w_i \mu_{m,i}$ where w_i is the weight fraction of element i and $\mu_{m,i}$ is the mass attenuation coefficient of element i. The elemental $\mu_{m,i}$ data were taken from Saloman and others (1988).

We chose the impure water concentrations to be at least an order of magnitude greater than those observed at the coastal Wilson Piedmont Glacier site of Bertler and others (2004). Even at these exaggerated impurity concentrations, the change in μ_m is significantly less than the uncertainty of the μ_m calibration. Therefore, for the purposes of γ-ray density gauging, treating firn and ice cores as pure water is well justified.

2.2.3 Photomultiplier Fatigue

The scintillation crystal in the MADGE detector converts ionizing radiation into visible light. This light signal is very small and must be amplified using a photomultiplier tube (PMT). The signal amplification for these devices is huge ($10^6 - 10^9$) and is accomplished using high voltage to force individual electrons to impact the dynodes with enough energy to liberate more electrons. This electron multiplication process proceeds through the PMT, eventually resulting in a measurable (mV) signal at the PMT output which is then sent to still more amplifiers in the Nuclear Instrumentation system.

Photomultiplier fatigue is a term used to describe the change in detector output pulse height in response to sudden changes in input count rate (Cantarell, 1964; Cantarell and Almodovar, 1965; Zhong and others, 1989). PMT fatigue is largely believed to be caused by *space charge* effects on the dynodes of the device, and recovering from those effects takes significant amounts of time. For MADGE, this means that the *measured* 60 keV photopeak for ^{241}Am shifts slightly in energy after large count rate changes, and then slowly recovers. The source E_γ does not change, but our ability to correctly measure E_γ is degraded. An example of this is shown in Fig. 2.8 where

1. a background energy spectrum was recorded with the source shutter closed,

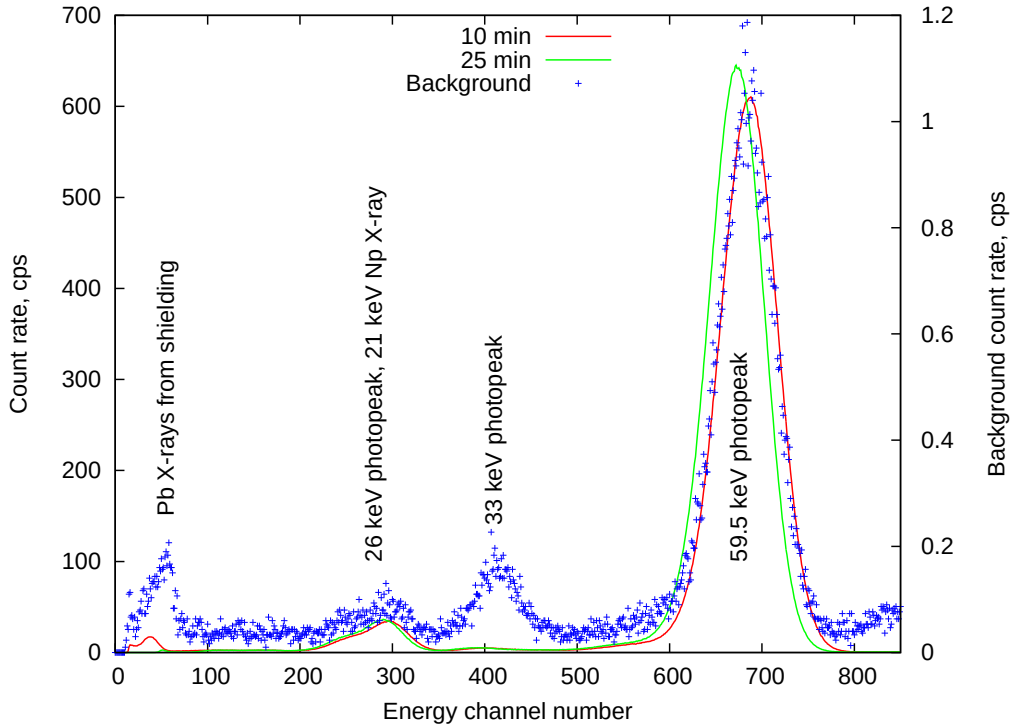

Figure 2.8. γ-ray spectra (300 sec recording time) at various times in a low to high CR transition.

2. the source shutter was opened at t=0 minutes,

3. a 300 sec spectrum was started at t=10 minutes, and

4. a 300 sec spectrum was started at t=25 minutes.

This is an example of PMT fatigue response for a low to high count rate (CR) transition: the photopeak maintains the same area (i.e. PMT sensitivity stays constant) but the center of the photopeak first shifts quickly towards a lower detected energy, reaches a minimum around 25 minutes and then very slowly recovers over several hours.

Because the energy window of the SCA is fixed, movement of the photopeak within the energy window can cause significant changes in the CR reported by MADGE. This usually causes abnormally high density readings on the first part of an ice core, as shown in Fig. 2.9.

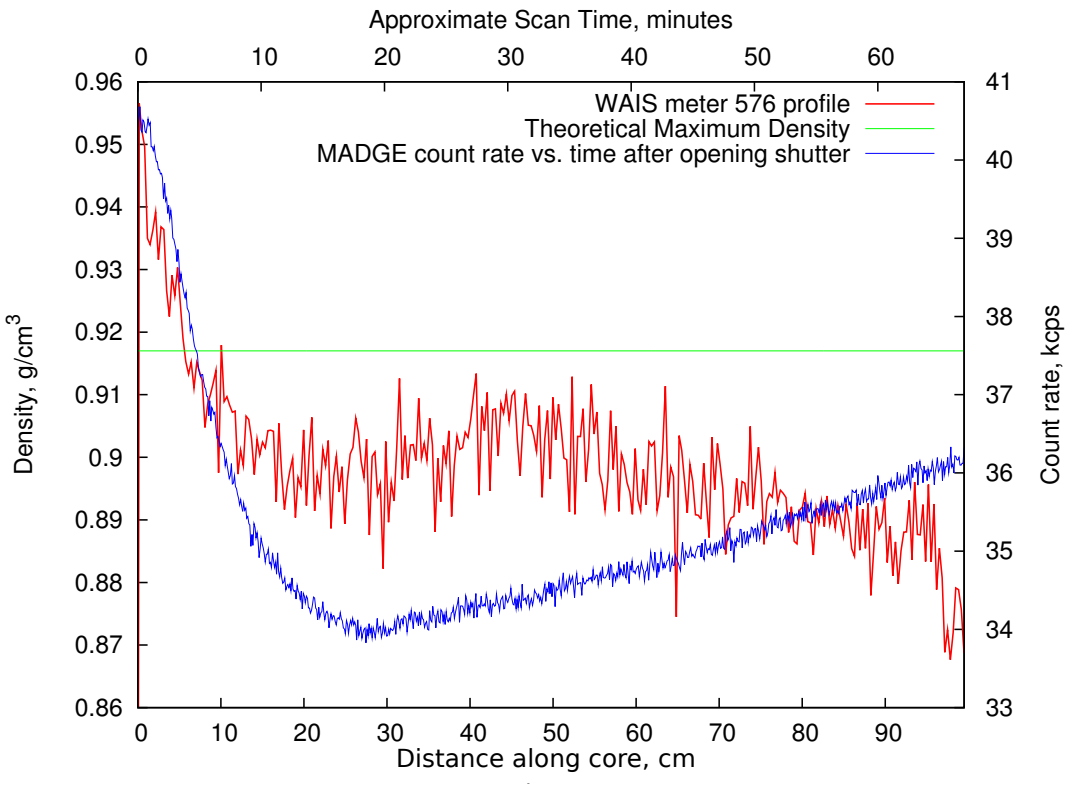

Figure 2.9. Counting effects of PMT fatigue. Density profile of deep WAIS ice compared with typical open gauge CR following shutter opening. Reported densities for this core section are incorrect due to PMT fatigue. Note that the open gauge CR has not recovered even after a full hour.

Fig. 2.9 requires some explanation. The CR vs. time curve (blue) was recorded immediately following opening the source shutter. Here we see the CR falling off rapidly with time as the photopeak shifts towards lower energies; since less of the photopeak lies within the SCA energy window, the SCA reports a decreasing CR. At $\sim$25 minutes, the photopeak reaches its minimum energy (CR stabilizes), and then the photopeak slowly creeps back up towards the SCA energy window.

The ice core used in this study was from 576 m deep and we expect the density profile to be quite flat and centered at 917 kg m^{-3}, therefore the problems with PMT fatigue are shown especially well here. The ice core density profile (red) was also recorded shortly after opening the shutter. In this case, MADGE measured n_0 early in the CR transient, resulting in a very high n_0. As the density profile proceeded

in time, PMT fatigue was artificially driving CR down throughout the early section of the core, resulting in artificially high density measurements. After CR stabilizes near 40 cm, the fatigue recovery now begins to artificially increase CR, causing the decrease in density as the core scan goes on.

There are three aspects to implementing anti PMT fatigue features in MADGE: procedurally implementing an open shutter PMT warm-up period, widening the SCA energy window, and implementing a CR monitoring section of code in the MADGE operating system. The single largest correction can be made simply by choosing an SCA energy window that is large enough to account for PMT fatigue effects, but not so large that other extraneous peaks (namely the 21 keV Np X-ray) are included in the window. Of course, any change to the SCA window width will require recalibration of μ_m. Widening the SCA window corrected much of the problem, but some drift still remained for very large changes in CR (typcially at air-ice interfaces like core ends and core breaks). The MADGE operating software was re-written to carefully monitor CR to force re-measurement of any exposures which were greater than 10% different from the previous exposure. In some cases, this results in multiple re-measurements before CR stabilizes, but this does not seem to have any significant effect on the core throughput.

The results of these features are shown in Fig. 2.10 where plastic absorber blocks and the lead shutter itself are used to cause large and rapid CR variations. The data clearly show that the PMT fatigue problem has been eliminated.

2.3 Uncertainty and Throughput

Having discussed all of the measurement systems, calibrations and individual uncertainties, we now need to combine them through Eq. 2.2 to determine the final 1-σ uncertainty in the density measurement, denoted as $\Delta\rho$.

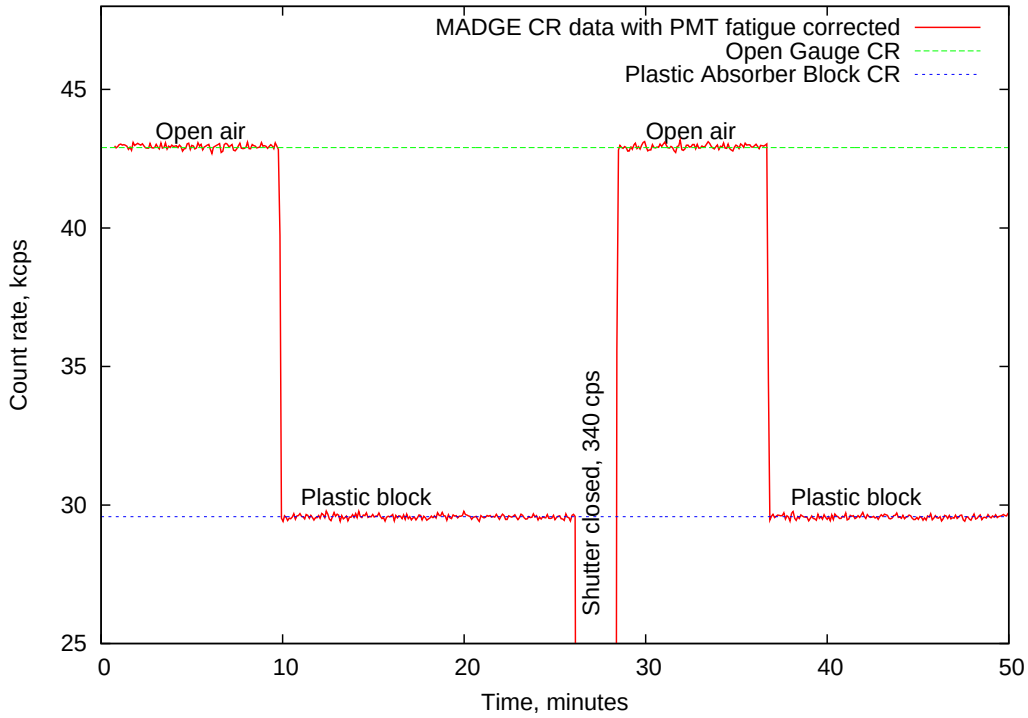

Figure 2.10. Testing the anti-PMT fatigue features of MADGE. Testing performed by rapidly inserting and removing plastic absorber blocks and cycling the source shutter. PMT fatigue is still occurring, but the SCA energy window is wide enough to accomodate energy shifts, and MADGE performs repeat measurements until CR is steady.

2.3.1 Uncertainty Propagation

Applying the error propagation formula (Bragg, 1974) to Eq. 2.2, we obtain three terms which describe the contributions of the nuclear counting, the core diameter and the mass-attenuation coefficient respectively, to the overall uncertainty in the calculated density:

$$\begin{aligned}[\Delta\rho]^2 &= \left(\frac{\partial\rho}{\partial\ln(n/n_0)}\right)^2[\Delta\ln(n/n_0)]^2 \\ &\quad + \left(\frac{\partial\rho}{\partial x}\right)^2[\Delta x]^2 + \left(\frac{\partial\rho}{\partial\mu_m}\right)^2[\Delta\mu_m]^2. \end{aligned} \tag{2.10}$$

Here, Δx and $\Delta\mu_m$ are the measurement uncertainties of the core diameter and the mass-attenuation coefficient respectively.

Δx (cm)	Nuclear Term	Diameter Term	μ_m Term	Timing Term	$\Delta\rho$ (g cm^{-3})
0.01	74.2%	8.9%	16.9%	$< 10^{-12}$ %	0.004
0.02	58.6%	28.1%	13.3%	$< 10^{-12}$ %	0.004
0.05	23.7%	70.9%	5.4 %	$< 10^{-13}$ %	0.006
0.10	7.6%	90.7%	1.7%	$< 10^{-13}$ %	0.011

Table 2.5. Contributions to overall uncertainty in the calculated density $\Delta\rho$ for typical MADGE operating parameters and several different values for x uncertainty: $N = 1.5 \times 10^5$, $t = 7.0 \pm 10^{-7}$ sec, $N_0 = 1.5 \times 10^6$, $t_0 = 42.0 \pm 10^{-7}$ sec, $\mu_m = 0.187 \pm 0.001$ cm^2 g^{-1} and $x = 5.0$ cm.

Terms involving Δt are ignored because the time base (internal clock) in a modern nuclear counter/timer instrument is very accurate, with Δt and Δt_0 around $\pm 0.1\mu$s (Canberra Industries, 2002). Therefore, the contribution of the timing uncertainty to the overall density uncertainty is negligible in comparison to the other measurements (see Table 2.3.1).

Performing the indicated derivatives in Eq. 2.10, we obtain the following final expression:

$$
\begin{aligned}
[\Delta\rho]^2 \;=\; & \frac{1}{x^2\mu_m^2 n^2}\left\{\left(\frac{1}{1-m\tau}+\frac{m\tau}{(1-m\tau)^2}\right)^2\left[\frac{m}{t}\right]\right. \\
& \left.+\left(\frac{m^2}{(1-m\tau)^2}\right)^2[\Delta\tau]^2\right\} \\
& +\frac{1}{x^2\mu_m^2 n_0^2}\left\{\left(\frac{1}{1-m_0\tau}+\frac{m_0\tau}{(1-m_0\tau)^2}\right)^2\left[\frac{m_0}{t_0}\right]\right. \\
& \left.+\left(\frac{m_0^2}{(1-m_0\tau)^2}\right)^2[\Delta\tau]^2\right\} \\
& +\left(\frac{\ln(n/n_0)}{x^2\mu_m}\right)^2[\Delta x]^2 \\
& +\left(\frac{\ln(n/n_0)}{x\mu_m^2}\right)^2[\Delta\mu_m]^2 \qquad (2.11)
\end{aligned}
$$

where $n = m/(1-m\tau)$ and $n_0 = m_0/(1-m_0\tau)$.

The uncertainty calculated by Eq. 2.11 depends on the values chosen by the operator for N and N_0, as well as using proper values for Δx, $\Delta \mu_m$ and $\Delta \tau$. We tested Eq. 2.11 by conducting sets of 100 repeat measurements on the same location of a firn core and varying N for each set. The results of this testing are shown in Fig. 2.11 and demonstrate the close relationship between N, throughput and $\Delta \rho$.

Note that the *observed* standard deviation shown above each box plot is not the same as the calculated standard deviation $\Delta \rho$ from Eq. 2.11. The calculated values are larger the observed standard deviation by $\sim$0.001 g cm^{-3} for all values of N. Therefore, Eq. 2.11 slightly overestimates the uncertainty in the density measurements and can be confidently and conservatively applied to MADGE density data.

We also tested the repeatability of the instrument by performing repeated density scans of the same 1 m section of core and observing the variability, shown in Fig. 2.12. The average standard deviation of all 303 measurements was 0.0082 while the calculated $\Delta \rho$ was 0.009 g cm^{-3}, showing again that Eq. 2.11 provides a conservative estimate for the measurement uncertainty for varying densities and core diameters observed over the length of a core segment.

The WAIS Divide WDC06A core provided a unique opportunity to compare MADGE data against both manual and iso-octane density measurements. The manual measurements were made in the field by Dr. Todd Sowers of Penn State, by weighing 1 m sections of the core and calculating a volume based on the cylindrical dimensions of the core section. The iso-octane measurements were performed by Dr. Joan Fitzpatrick of the USGS, by computing the differential weight of 10 cm long sections cut from the core weighed in air, and then weighed immersed in an iso-octane bath (J. Fitzpatrick, personal communication). Uncertainties for the manual measurement were not available, but the iso-octane uncertainty is $\pm$0.0003 g cm^{-3} (Gow, 1970), an order of magnitude better than typical MADGE data. However,

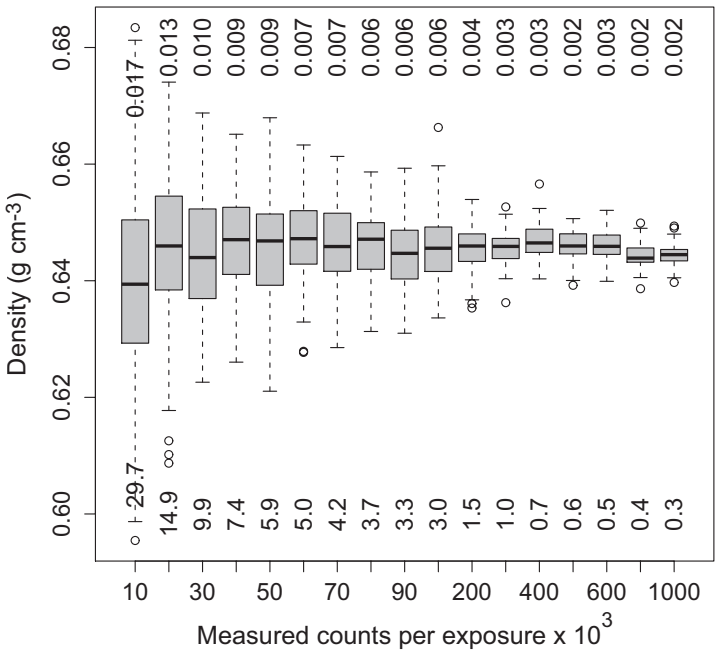

Figure 2.11. MADGE density measurement uncertainty vs. N. Box-and-whisker plots for repeated density measurements of the same location on a 3 cm wide firn core for various exposure counts N. Measurements were repeated 100 times for each exposure count setting. The observed standard deviation (g cm^{-3}) and average throughput (m h^{-1}) are shown above and below each box plot, respectively. The lower axis scale changes at $N = 100 \times 10^3$.

iso-octane density methods cannot be applied to firn since it would infiltrate the firn porespace and contaminate the core.

Comparision of MADGE and manual data show a systematically 2% lower manual density over the entire 93 m record from Sowers. This is, to some extent, expected since precise evaluation of the core section volume is difficult and cannot reliably account for any flaws within the recovered core. Deeper in the core where the iso-octane data begin, MADGE data (averaged over the applicable 10 cm of core) and iso-octane data agree very well, typically within 0.5%. This level of agreement provides evidence that the liquid water μ_m calibration procedure developed for MADGE is correct.

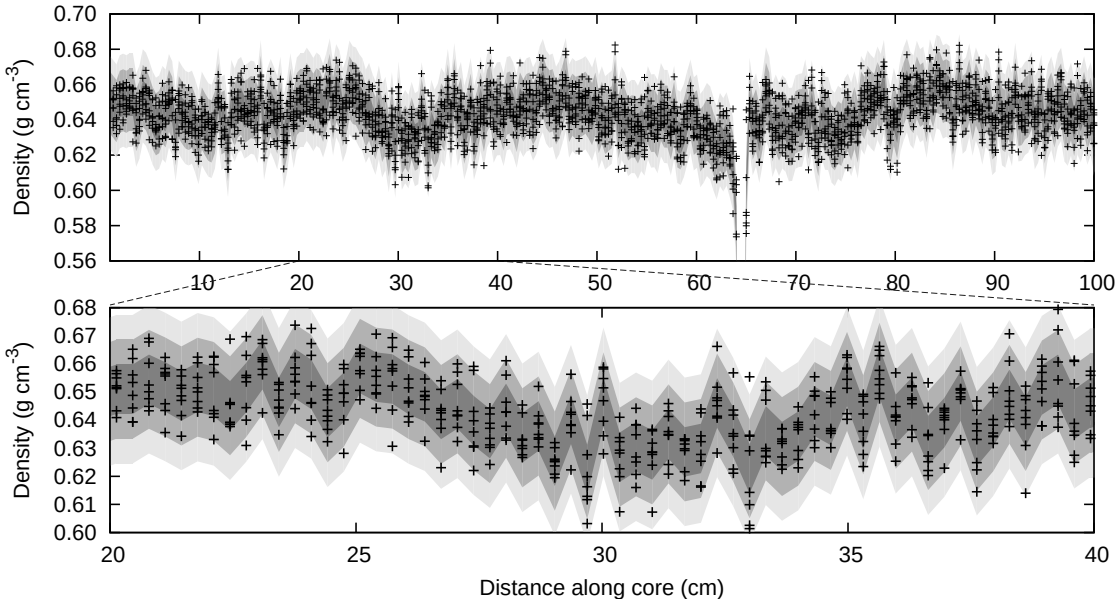

Figure 2.12. Eight repeated density scans of a South Pole firn core. Sample was a 3 cm wide core collected from South Pole at $N = 50 \times 10^3$, yielding a calculated $\Delta\rho = 0.009$ g cm^{-3}. Upper plot shows entire core with core break at 64 cm. Lower plot gives close up view of 20-40 cm section. Dark gray indicates $\pm\Delta\rho$, gray indicates $\pm 2\Delta\rho$ and light gray indicates $\pm 3\Delta\rho$ bands about the mean density. The data spread over these bands demonstrates that $\Delta\rho$ calculated by Eq. 2.11 is correctly accounting for γ-ray counting, μ_m and core diameter uncertainties.

2.3.2 Throughput

Throughput is the rate at which the instrument can density-profile a unit length of core. The desired level of measurement uncertainty, source activity, dead time and the mass thickness of the sample all affect the throughput. The desired measurement uncertainty will determine N, the number of γ-rays that need to be counted during each exposure to achieve the measurement uncertainty goals, as shown in Fig. 2.11. The rate of γ-ray transmission n for a given sample mass thickness determines the average time (in seconds) required for an exposure: $t = N/n$. The instrument

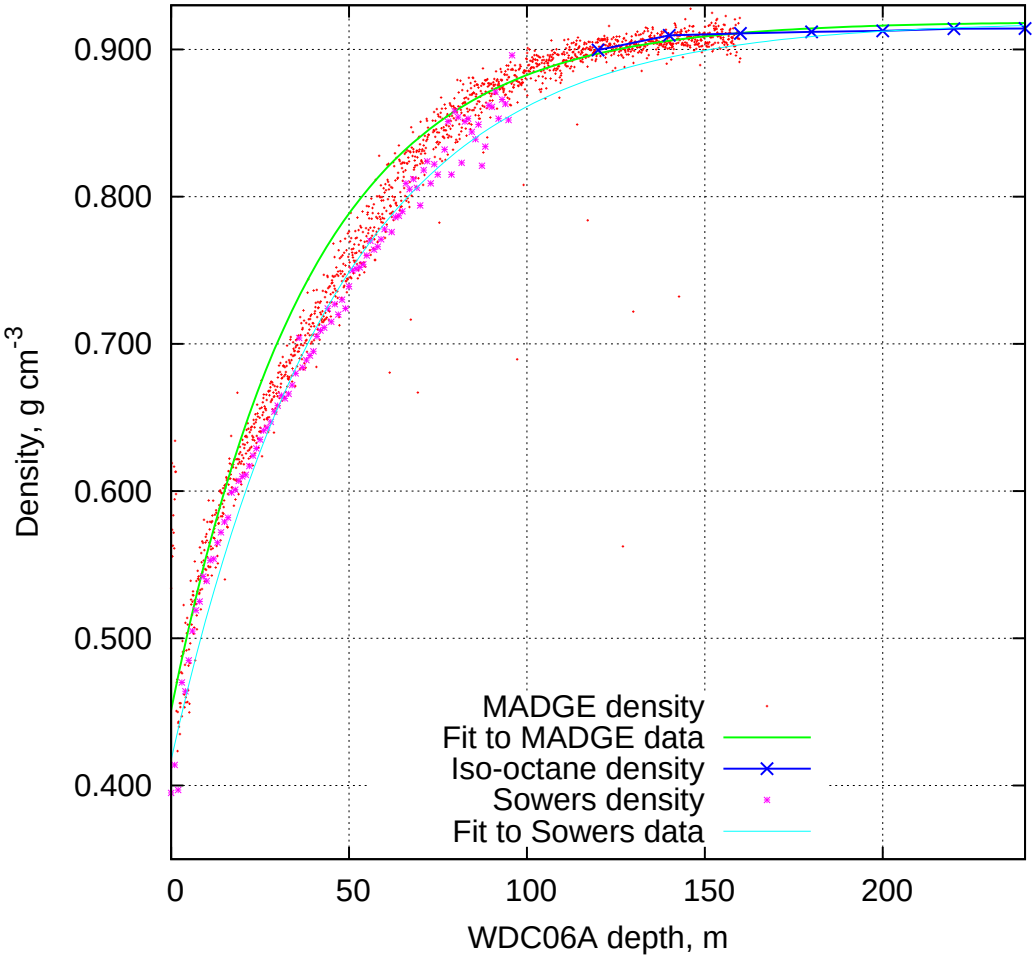

Figure 2.13. Intercomparsion of three density data sets. MADGE (0 to 160 m), manual measurements by T. Sowers (0 to 93 m) and iso-octane densities by J. Fitzpatrick (120 to 250 m).

throughput T (in m h^{-1}) can then be calculated as $T = 3600/\alpha t$ where α is the number of exposures per meter.

We chose $N = 1.5 \times 10^5$ and $N_0 = 1.5 \times 10^6$ counts for field operation of MADGE on 5 cm diameter cores, resulting in a $\Delta\rho$ of about 0.004 g cm^{-3}. These values yield T=1.5 m h^{-1} at an average sample density of 0.5 g cm^{-3}.

2.4 Exposure and Dose Estimation

Radiation safety is very important both for safe operation and for safe source transport when the instrument is deployed to the field. We can calculate the radiation exposure and dose rates based on the source activity A_{src}, the geometry of the density gauge and the design of the shield, shutter and collimator. The first task is to calculate the specific gamma ray emission Γ for ^{241}Am and compare this with the value provided by Eckert & Ziegler Isotope Products (Valencia, CA), the manufacturer of the source.

Cember (1992) gives the calculation for Γ as

$$\Gamma = (1.043 \times 10^{-6}) \sum_i E_i B_i \mu^{\text{e}}_{\text{air},i} \tag{2.12}$$

where the leading constant incorporates several different constants for the conversion of joules to MeV, seconds to hours, joules of energy deposited per kilogram of air to the charge in Coulombs of ion pairs created per kilogram of air, and to account for the spherical spreading of radiation at 1 m away from a point source. B_i is the branching ratio for the ith gamma line, while E_i and μ^{e}_i are the energy (MeV) and the energy absorption coefficient in air (m^{-1}) for the ith gamma line. Equation 2.12 gives Γ in units of $\frac{\text{C/kg}}{\text{MBq-h}}$ at 1 m, which we will then convert to the more familiar $\frac{\text{R}}{\text{Ci-h}}$ at 1 m. Table 2.6 shows calculations for each gamma line including transmission through the 0.25 mm thick stainless steel window of the source housing, denoted as T_w.

Using the relations 1 C/kg = 3881 Roentgen and 1 MBq = 2.70×10^{-5} Ci, the value of Γ for this source is 9.22×10^{-3} $\frac{\text{R}}{\text{Ci-h}}$ or $9.22 \frac{\text{mR}}{\text{Ci-h}}$ at 1 m. To compare this number to the manufacturer's figure which is given in terms of a dose equivalent rate at 1 m, we must convert the exposure rate $\dot{X}$ in mR into soft tissue dose equivalent rate $\dot{D}$ in mrem at the dominant gamma-ray energy of 59.5 keV which has a quality

E (MeV)	B	$\mu^{\mathrm{e}}_{\mathrm{air}}$	T_w	Γ_i $\frac{\mathrm{C/kg}}{\mathrm{MBq-h}}$ at 1 m
0.0595	0.360	3.56×10^{-3}	0.780	6.20×10^{-11}
0.0264	0.024	4.04×10^{-2}	0.004	9.62×10^{-13}
0.0208	0.049	6.30×10^{-2}	0.001	6.97×10^{-13}
0.0178	0.194	6.30×10^{-2}	1.98×10^{-3}	9.62×10^{-13}
0.0139	0.133	1.57×10^{-1}	8.27×10^{-6}	2.51×10^{-15}
			Total	6.42×10^{-11}

Table 2.6. Specific gamma-ray emission for gamma lines of ^{241}Am.

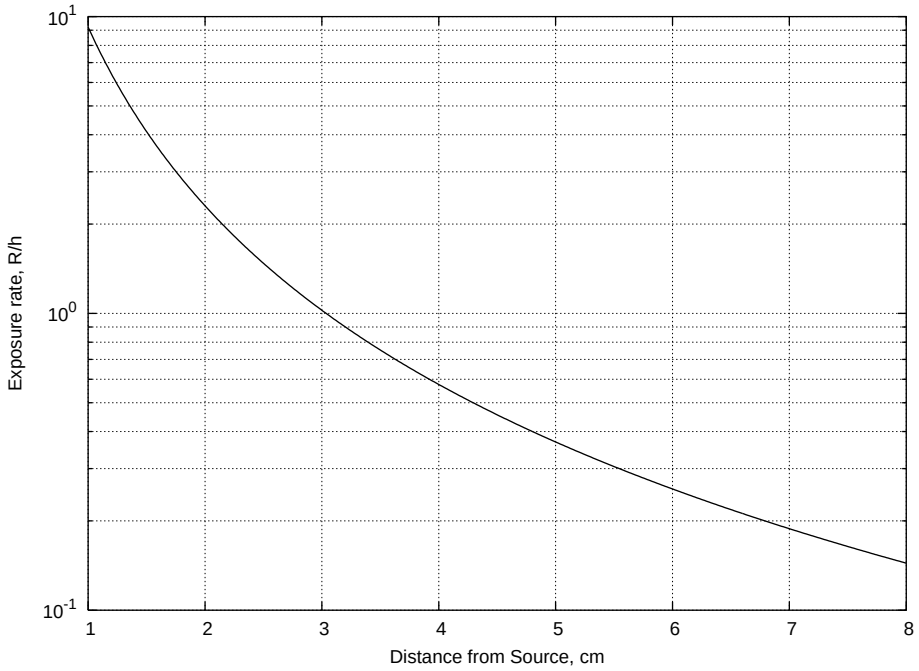

Figure 2.14. Exposure rate vs. distance from 100 mCi ^{241}Am source.

factor $QF = 1$.

$$\dot{D} = \dot{X} \left[\frac{\mu^{\mathrm{e}}_{\mathrm{tissue}} \rho_{\mathrm{tissue}}}{\mu^{\mathrm{e}}_{\mathrm{air}} \rho_{\mathrm{air}}} \right]_{\text{at 59.5 keV}} [QF] = 1.41 \dot{X} \tag{2.13}$$

This yields a value of 1.30 $^{\mathrm{mrem}}/_{\mathrm{h}}$ at 1 m for a 100 mCi source. The manufacturer lists a value of 4 $^{\mathrm{mrem}}/_{\mathrm{h}}$ for a 300mCi source, therefore the value for a 100mCi source would be 1/3 of this value, or 1.33 $^{\mathrm{mrem}}/_{\mathrm{h}}$. This compares well with the previous calculation. Exposure rate as a function of distance from the unshielded source is shown in Fig. 2.14.

2.4.1 Shield, Collimator and Shutter Design

The gamma rays of ^{241}Am are of low energy and are therefore easily shielded by thin layers of lead. Our shielding goal is to reach < 2 mR/h at the surface of the shield which is shown in Appendix A.4.a. The endcap and collimator always remain mounted together, while the frontcap is put in place for transport in case the shutter bumps open. Important shielding data for lead is shown in Table 2.7.

Property	Value	Units
Density	11.38	g cm^{-3}
μ_m	4.87	cm^2 g^{-1}
μ	55.4	cm^{-1}
HVL	0.0125	cm

Table 2.7. Properties of lead at 60 keV gamma energy. HVL is half value layer thickness, defined as the thickness of lead required to reduce the radiation intensity by 50%.

To properly calculate the required shielding thickness $t_{\rm sh}$, we must account for the effects of buildup, which is a function of $\mu\ t_{\rm sh}$, called the relaxation length (Cember, 1992). The thickness dependence of the buildup factor β means that the calculation normally requires an iterative process, however, lead shielding is so effective for the low energy ^{241}Am gammas that this is not necessary. The shielded exposure rate 1 cm away from the source surrounded by a shield 0.25 cm thick is calculated from

$$\begin{aligned} \dot{X}_{\rm sh} &= \dot{X}_{\rm unsh}\ \beta e^{-\mu t_{\rm sh}} \\ &= (9.22{\rm R/h})(2.0)(e^{-(55.4)(0.25)}) \\ &= 17.8\mu{\rm R/h} \end{aligned} \tag{2.14}$$

where $\beta = 2.0$ comes from Fig 10.9 of Cember (1992). This tiny thickness of lead is more than sufficient to achieve our shielding goal, however, the actual shield will be larger than this to make the actual machining process easier.

The collimator length $l_c = 1$ cm and beam diameter $d_{\rm beam} = 0.33$ cm implies that the radiation field will be a cone with an apex angle $\alpha = 2\tan^{-1}(d_{\rm beam}/l_c)$. For

this design, $\alpha = 36.4°$ which means that the base of the radiation cone will have a diameter of 2 cm at the midpoint of the density gauge and a diameter of 4.4 cm at the detector side. At this distance, the exposure rate is 212 mR/h, therefore we use a 1 mm thick lead foil with a 5 cm diameter around the detector collimator. The 1 mm lead foil reduces the exposure rate to 1.7 mR/h and the aluminum detector support plate itself will further reduce it to 0.8 mR/h.

The shutter is a spring-loaded pin with a lead plug on the end. The shutter is therefore always forced closed unless held open by a red-flagged shutter pin which fits into the 2mm hole drilled in the pin. The lead plug has a minimum thickness of 1.6 mm which reduces the radiation field (using Eq. 2.14) at the source collimator exit (1 cm away from source) from 9.22 R/h to

$$(9.22)(1.5)e^{-(55.4)(0.16)} = 1.9 \times 10^{-3} \text{ R/h} \tag{2.15}$$

This 1.9 mR/h represents the worst case exposure rate from any part of the instrument with the shutter closed.

2.4.2 Direct Beam Estimates

The exposure rate anywhere inside the radiation cone will vary as a function of position away from the source. This is the same calculation shown in Fig. 2.14 and is given by the inverse square law for radiation spreading from a point source:

$$\dot{X}(d) = \dot{X}_{\text{ref}} \left[\frac{d_{\text{ref}}}{d} \right]^2 \tag{2.16}$$

where $\dot{X}_{\text{ref}}$ and d_{ref} are a known, reference exposure rate and distance from the point source, typically derived from the specific gamma ray emission of the isotope used.

Clearly, the exposure rate at the source collimator exit is the most intense with $\dot{X} = 9.22$ R/h or 2.56 mR/sec. It is not possible to physically access the collimator exit with a hand or finger when an ice core is present since the air gap is only 2.5 mm

between the ice core and the source collimator. The exposure rate with the shutter closed is 1.9 mR/h, so it is therefore procedurally very important to close the shutter when no sample is present. However, the worst case exposure for a momentary (3 second) exposure to an extremity like a finger or hand inside the density gauge with the shutter open is 7.7 mR which represents a dose of 10.8 mrem to soft tissue.

2.4.3 Scattered Beam Estimates

The calculation of the exposure due to the scattering of radiation in the sample is necessarily complicated. The primary interaction of 60 keV gamma rays in a low Z material like ice is Compton scattering, so it is worth the effort to estimate the scattered exposure. We have performed three different estimates, the first two involving Thomson and Compton scattering cross sections, and the third using a Monte Carlo simulation of the density gauge and ice core. These estimates will be presented in order of increasing accuracy, so we will begin with the Thomson scattering calculation. A summary of scattered exposures calculated by each method is presented at the end of this section.

2.4.3.1 Thomson Scattering Estimate

Thomson scattering is the low energy analog of Compton scattering. It describes the coherent scattering of photons from free electrons. The differential Thomson scattering cross section (cross section expressed on a per unit solid angle basis) has the form

$$\frac{d\sigma_0}{d\Omega} = \frac{r_0^2}{2}(1 + \cos^2\theta) \tag{2.17}$$

where r_0 is the classical electron radius and θ is the scattering angle. The angular dependence here slightly favors forward and backward scattering and slightly disfavors side scattering. However, for ease of calculation, we will ignore this angular dependence and assume that the scattering is isotropic. The total Thomson

ρ_{ice} $^{\text{g}}/_{\text{cm}^3}$	$\dot{X}$ at core surface with no attenuation	$\dot{X}$ at core surface with attenuation	$\dot{X}$ 1 cm above core with attenuation
0.917	27.19 mR/h	16.83 mR/h	8.66 mR/h
0.2	5.44 mR/h	4.90 mR/h	2.52 mR/h

Table 2.8. Results of Thomson scattering calculations.

scattering cross section is found by integrating Eq. 2.17 over all directions:

$$\int_0^{2\pi} \int_0^{\pi} \frac{r_0^2}{2}(1+\cos^2\theta)\sin\theta \; d\theta \; d\phi = \frac{8\pi}{3} r_0^2 = \sigma_0 \tag{2.18}$$

This σ_0 is the total Thomson scattering cross section and has a value of 0.66525 barns per electron (where 1 barn = 10^{-24} cm^2).

To find the number of gamma rays that undergo Thomson scattering, we perform the following calculation (Johns and Cunningham, 1983):

$$N_{\text{scat}} = \sigma_0 N_e \phi_{\text{inc}}(3.8\text{cm}) A_{\text{beam}}(3.8\text{cm}) \tag{2.19}$$

where N_e is the number of electrons per cm^2 in the target, ϕ_{inc}(3.8cm) is the gamma ray flux in $^{\gamma}/_{\text{cm}^2\text{sec}}$ evaluated at 3.8 cm from the source (at the center of the ice core) and A_{beam}(3.8cm) is the area of the base of the gamma ray radiation cone, also evaluated at the center of the ice core.

Spreading the scattered radiation isotropically, we calculate the scattered flux as $\phi_{\text{scat}} = N_{\text{scat}}/(4\pi d^2)$ for a given distance d from the scattering center at the center of the ice core. From this flux, we can calculate (Cember, 1992) the exposure at d by

$$\dot{X}_{\text{scat}} = [3881^{\text{R}}/_{(\text{C/kg})}] \frac{\phi_{\text{scat}}(d) \; E_\gamma [1.6 \times 10^{-13\text{J}}/_{\text{MeV}}] \mu^e_{\text{air}}}{[\rho_{\text{air}}{}^{\text{kg}}/_{\text{cm}^3}][34^{(\text{J/kg})}/_{(\text{C/kg})}]} \tag{2.20}$$

The results of this calculation are listed in Table 2.8. Attenuated exposure values were calculated by transporting the scattered gamma rays from the center of the ice core to the surface.

2.4.3.2 Compton Scattering Estimate

The Compton scattering calculation is exactly the same as the Thomson scattering calculation with two changes. First, Compton scattering describes the interaction of a photon and an electron which can absorb energy in the interaction, making this an incoherent scattering process. This also means that there is a stronger preference for forward scattering as the gamma ray energy increases. Secondly, the differential Compton scattering cross section is related to the Thomson by

$$\frac{d\sigma_{cs}}{d\Omega} = \frac{d\sigma_0}{d\Omega} F_{KN} \tag{2.21}$$

where

$$F_{KN} = \left[\frac{1}{1+\alpha(1-\cos\theta)}\right]^2 \left[1 + \frac{\alpha^2(1-\cos\theta)^2}{(1+\alpha(1-\cos\theta))(1+\cos^2\theta)}\right] \tag{2.22}$$

Again, θ is the scattering angle and α = photon energy / rest mass energy of the electron. This relationship was derived by Klein and Nishina (1929) by taking into account the recoil energy absorbed by the electron. F_{KN} is always less than 1, and therefore the Compton scattering cross section is always less than the Thomson cross section (Johns and Cunningham, 1983).

With this in mind, we perform the same analysis (ignoring angular dependence) as the previous section except that the total scattering cross section σ_0 is replaced by σ_{cs} evaluated at 60 keV which is 0.5456 barns. The results are shown in Table 2.9.

ρ_{ice} g/cm^3	$\dot{X}$ at core surface with no attenuation	$\dot{X}$ at core surface with attenuation	$\dot{X}$ 1 cm above core with attenuation
0.917	22.32 mR/h	13.81 mR/h	7.11 mR/h
0.2	4.46 mR/h	4.02 mR/h	2.07 mR/h

Table 2.9. Results of Compton scattering calculations.

2.4.3.3 Monte Carlo Estimate

Now we arrive at what we believe to be our best estimate of the scattered exposure rate. A Monte Carlo simulation code begins by specifying the geometry, materials, and any desired detectors in a 3-D description of the problem. An imaginary gamma ray source of specified energy is placed in the proper location within this geometry and allowed to emit gamma rays in random directions, thus simulating a real isotropically radiating source. Using the interaction cross sections for the materials in the problem, the program walks the gamma rays through the geometry and simulates the life of one gamma ray at a time. By simulating many millions of imaginary gamma rays, the program can build up a statistically valid simulation of how the geometry would transport gamma rays in the real world.

The code we used to perform this simulation is MCNP5 (Briesmeister, 1993), an electron, photon and neutron Monte Carlo code distributed by Oak Ridge National Laboratory through the Radiation Safety Software and Information Center. This code is an industry standard, is well documented and provides statistical analysis of the results to show any problems such as poorly defined geometry, too few simulated particles run, or abnormal detector behavior.

Our input file, shown in Appendix A, set up the shield, collimators, and ice core with the actual dimensions and geometry of our design. A typical simulation run used 12 h of computer time and ran approximately 3.06×10^8 virtual particles through the design. We placed 9 detectors in a grid pattern 1 cm above the ice core to measure the scattered radiation flux as a function of position, which was then converted to exposure to produce Fig. 2.15.

Putting all of the scattering estimates together, we obtain Table 2.10. The results are all in line with physical intuition: the more dense the sample, the more scattered exposure we expect. Both the Thomson and Compton calculations con-

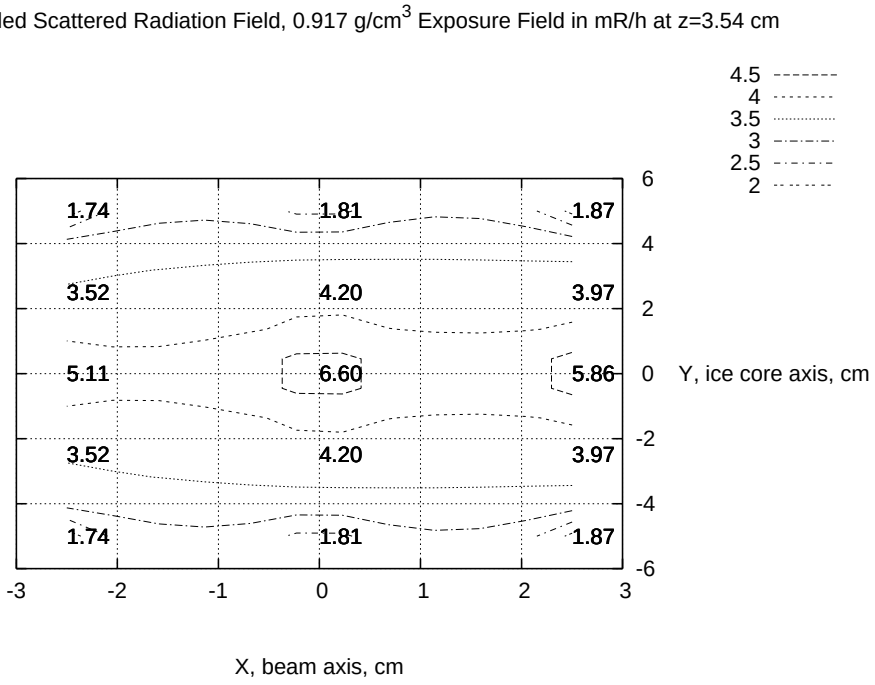

Figure 2.15. MCNP5 scattering calculation results. Source is located on the left at $x = -3$ and the detector is located on the right at $x = +3$. The contour lines give some intuitive feeling about the results but do not reflect any additional data. All data points are shown numerically on the plot.

servatively assumed that no energy was lost in the photon-electron collision, and that all scattering was isotropic. By looking at Fig. 2.15, we can see that these were poor assumptions because the exposure rates are not symmetric about the y axis. They show that the gamma rays tended to be more forward scattered than isotropic. Also of note is the maximum exposure rate located above the axis of the ice core, due to the combined effects of forward scattering from the left and backscattering from the right.

The Monte Carlo simulation provides reasonable exposure estimates and does so in a much more rigorous manner than the Thomson or Compton estimates we used, and therefore we believe that the MCNP5 estimates are the best available.

Method Used	ρ_{ice} g/cm^3	$\dot{X}$ at core surface with no attenuation	$\dot{X}$ at core surface with attenuation	$\dot{X}$ 1 cm above core with attenuation
Thomson	0.917	27.1 mR/h	16.8 mR/h	8.6 mR/h
Compton	0.917	22.3 mR/h	13.8 mR/h	7.1 mR/h
MCNP5	0.917	-	7.7 mR/h	3.9 mR/h
Thomson	0.2	5.4 mR/h	4.9 mR/h	2.5 mR/h
Compton	0.2	4.4 mR/h	4.0 mR/h	2.0 mR/h
MCNP5	0.2	-	2.8 mR/h	1.4 mR/h

Table 2.10. Comparison of scattering calculations.

The scattered exposure rates are not zero, but are far from dangerous and do not extend any farther than 2-3 cm outside of the sample. The real risk of exposure from the density gauge is a direct beam exposure which is prevented both procedurally and by a mechanically fail-safe shutter system. Operators need not touch or be near the density gauge when measurements are taken because the instrument operates automatically except for the manual opening and closing of the shutter, which only requires a few seconds to accomplish.

2.5 Conclusions

The density gauging system described in this chapter provides significant benefits over existing firn and ice density gauging systems:

1. Measurements are non-destructive, automated, highly accurate and recorded at high spatial resolution.

2. The calibration of the instrument is straightforward, repeatable and uses the actual measurand (water) as its standard.

3. Operating on 3-8 cm diameter cores allows the use of lower source activity, thereby lowering operator radiation exposure and making shipment of the instrument easier and less expensive.

4. Optimizing E_γ for the sample mass thickness provides the best density measurement and allows simple, lightweight shielding because the optimal E_γ is relatively low.

5. Using a pulse mode γ-ray counting system with energy discrimination ensures that we are correctly applying the Lambert-Beer law.

6. The measurement uncertainty analysis for a pulse mode instrument is well developed and easily calculated for each exposure.

7. The instrument is field portable and field proven in an Antarctic traverse setting.

In answering the central questions posed in the Hypothesis (see Chapter 1), understanding and quantifying microstructure-dependent densification (MDD) processes requires that we follow density variations at the mm scale. Manual gravimetric methods are fundamentally limited by their low resolution and therefore cannot sample the density profile frequently enough to develop a meaningful picture of the firn column.

Only automated density scanning provides the sampling frequency required to analyze MDD compaction rate differences between coarse and fine grained firn, or to meaningfully explore inter-annual accumulation variability at a given coring site. This chapter has described the basic physics and measurement uncertainties associated with the instrument, including intercomparsion of three independent density profiles of the same core, to demonstrate the high confidence that we place in MADGE results. MADGE data for the WDC06A core have been archived at `http://www.waisdivide.unh.edu` and are used extensively in Chapter 4 which compares MADGE density data with the optical properties of the WDC06A core at mm scales.

CHAPTER 3
MODELING OPTICAL SCATTERING IN POLAR FIRN CORES, ICE CORES AND BOREHOLES

"Essentially, all models are wrong, but some are useful."

– George E. P. Box

3.1 Introduction

Characterizing microstructure-dependent densification in firn demands an instrument which can acquire objective, high resolution data about the physical structure of the firn. This chapter details the theory and modeling results for understanding the relationship between the microstructural and optical properties of polar firn and ice. The theory and models presented here will provide a unified view of multiple-scattering firn and ice optics to aid in developing novel optical scattering microstructure instrumentation and better understanding existing instruments.

Objectively measuring the microstructure (defined here as the ice grain or air bubble sizes and the mean distances between them) of firn and ice is not a simple task. Various forms of microscopy (Baker and others, 2007; Kipfstuhl and others, 2006; Spaulding and others, 2010), computed tomography (Freitag and others, 2008, 2004; Kerbrat and others, 2007; Lundy and others, 2002), and optical scattering (Alley and others, 1997; Arnaud and others, 1998a; Gallet and others, 2009; Hawley and others, 2008, 2003; Kaempfer and others, 2007; Kinnard and others, 2008; Sjogren and others, 2007; Svensson and others, 2005) measurements have been made of firn microstructure, with varying degrees of success.

Firn and ice density have interesting and significant effects on the optical scattering properties of firn and ice, related both to changes in the density of scatterers

and the size of the grains and bubbles doing the scattering (Bohren and Beschta, 1979; Grenfell and Warren, 1999; Kokhanovsky and Zege, 2004; Kaempfer and others, 2007; Fudge and Smith, 2010). Optical scattering methods have two significant advantages in that they can be (1) non-destructive and (2) applicable to in-situ borehole measurements of firn structure. However, optical scattering techniques have also been confounded by the lack of a unified framework for understanding the three fundamental optical scattering measurement geometries:

1. backscattering, also known as reflectivity or albedo measurements, often performed in glacial boreholes and snow pits

2. transmission measurements, often performed on firn/ice cores

3. measurement of light scattered perpendicular to the incident beam, which we will call *emergence*, often performed on firn/ice cores using linescan camera systems.

We begin the Chapter with a brief discussion of instruments utilizing the three fundamental optical measurement geometries for firn and ice structure, including visual stratigraphy (Alley and Bentley, 1988; Meese and others, 1997; Alley and others, 1997) and modern video and photographic methods (Kinnard and others, 2008; Sjogren and others, 2007; Hawley and Morris, 2006; Hawley and others, 2008) and a linescan imaging system. The linescan system used for the collection of optical scattering data on the WDC06A core is the Optical Imaging System (OIS) installed at the National Ice Core Laboratory in Denver, Colorado by McGwire and others (2008a).

Next, we develop and present results from two different numerical firn and ice optics models. The model predictions are then used to understand both the large scale (tens of meters of depth) and small scale (centimeter) changes in firn and ice

optical properties due to firn densification and variability in firn microstructure for all three of the fundamental geometries. The different optical measurement geometries manifest firn/ice microstructural effects differently, resulting in distinctive, yet complementary measurements of the optical properties of firn and ice. Therefore, the contents of this chapter lay important theoretical groundwork for testing the Hypothesis of Chapter 1. The optical models described here must make testable predictions about the optical properties of firn and ice as functions of density and microstructure.

We use, modify and extend both the radiative transfer approach of Fudge and Smith (2010) and the geometric optics approach of Picard and others (2009) to calculate photon transport within firn and ice, using the simplifying assumption of spherical ice grains and air bubbles. The models provide a unifying view of the various measurement techniques and explains the large and small scale correlation patterns between optical scattering and firn/ice density characteristic to each measurement technique.

We conclude the chapter with a brief list of improvements for the optical determination of firn microstructure, giving the basic form and design requirements for a new instrument specifically adapted for firn physical property measurements.

Chapter 4 takes the results developed here and compares the experimental WDC06A results with the model predictions. We show that the OIS, despite being originally designed only for deep ice core photography, collects compelling data demonstrating that important aspects of firn and ice microstructure can be quantitatively measured using optical scattering techniques.

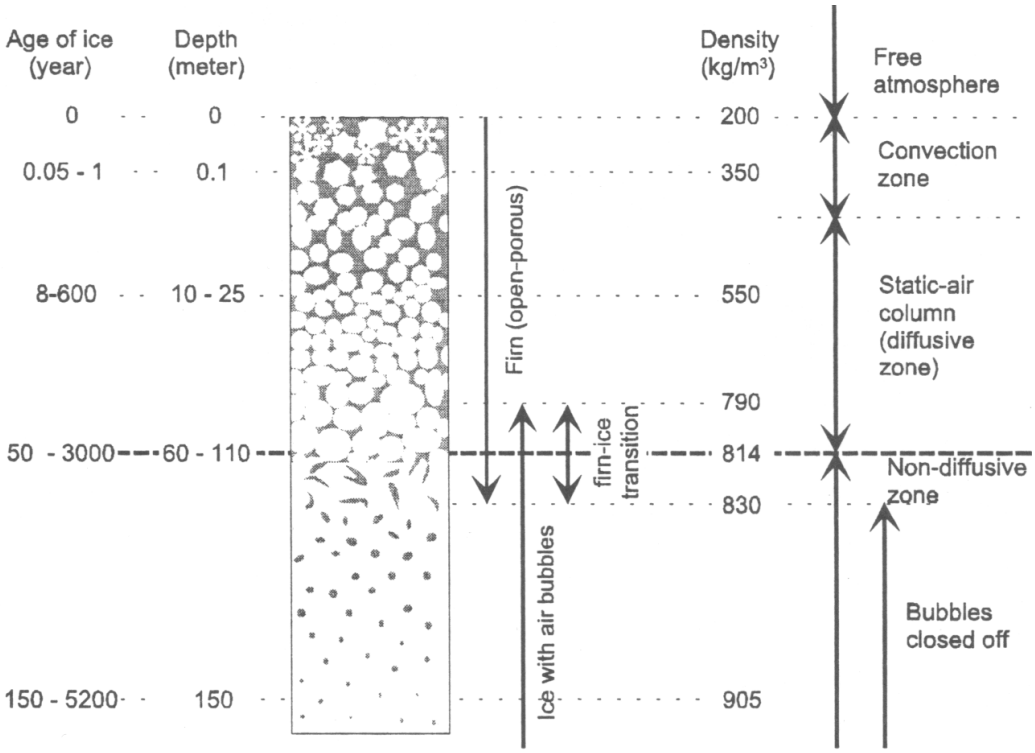

Figure 3.1. Diagram of showing important depths, ages, and densities in a typical, idealized polar firn column. From Blunier and Schwander (2000).

3.2 Firn and Optical Measurements of Firn Structure

Firn is highly variable, containing a wide range of densities, ice grain sizes, coordination numbers (number of points of contact with other particles) and bonding strengths (Alley, 1988; Braithwaite and others, 1994; Colbeck, 1991; Faria and others, 2010; Horhold and others, 2011). These parameters change with depth (illustrated in Fig. 3.1) as the ice grains become larger, more rounded and more interconnected (Lundy and others, 2002; Freitag and others, 2008). In the firn-ice transition, we reach a zone where the distinction between individual ice grains becomes difficult, and we begin to distinguish instead between individual air bubbles. As these bubbles close off, the air inside is captured at atmospheric pressure. Increasing firn and ice load above the bubbles serves to compress the air bubbles, reducing their size, but maintaining a relatively constant bubble number density (BND) (Spencer

and others, 2006). At roughly 1200 m depth, all air bubbles have vanished under the extreme pressure, and the air they once contained is stored within the ice as clathrate hydrates (Lipenkov, 2000).

3.2.1 Firn Types

Alley and others (1982) carefully studied the extremes of polar firn behavior, and describes two bounding firn types:

1. Coarse grained firn (CGF) is composed of large irregular grains with relatively low coordination number. The porespace in CGF is also large, implying a low density. The combination of low coordination number and low density ensures that CGF is physically weak and highly permeable to air flow (Frolov and Fedyukin, 1998; Golubev and Frolov, 2000; Horhold and others, 2009; Schneebeli and Johnson, 1998).

2. Fine grained firn (FGF), composed of smaller, rounded grains which are sintered together due to wind packing, is generally much stronger, denser and less permeable to air compared to CGF (Rick and Albert, 2004; Courville and others, 2007).

Alley and others (1990) use data from Summit, Greenland to argue that the CGF layers are generally created during late summer / autumn due to formation and subsequent burial of a thick near-surface hoar layer. Contrary to Alley, Fujita and others (2009) and Koerner (1971) use data from high elevation sites in East Antarctica to contend that CGF is a winter phenomenon, and that FGF is produced due to solar input during the summer months. Whatever the source of the differing firn types, there is wide agreement that they can be easily discerned using the oldest optical instrument of all, the human eye.

3.2.2 Visual Stratigraphy

Visual stratigraphy (VS), the inspection of the layering and grain structure of a snow pit or ice core by a human observer, is a technique that is as old as ice coring itself (Langway, 2008). This is traditionally done using *transmitted* light. When performed on ice cores, VS has traditionally been done on cores cut in half along the core axis, providing a flat viewing surface which is illuminated from underneath using low temperature fluorescent lights. A typical transmission setup (without the core axis cut) is shown in Fig. 3.2 where a digital camera or human observer could be used to analyze the core. The observer stands above the core and notes changes in transmitted visible light intensity resulting from changes in density, snow or firn grain size, and the presence of melt layers. In firn, the general relationship in transmission VS is simple: low density firn is less transmissive and therefore appears dark to the observer, while high density firn is more transmissive and appears bright. High density (bubble-free) ice appears brighter than lower density bubbly ice. In short, the more ice-like the core, the greater is the transmitted intensity (Langway, 1962; Alley and others, 1997).

Transmission VS shows us that the number density of ice grains in firn or air bubbles in ice play a large role in the scattering characteristics of a given firn/ice sample. The firn microstructure parameter we will use to analyze this and other scattering measurements is the specific surface area (SSA), which characterizes the concentration of scatterers (in our case, air-ice interfaces) within the sample. SSA is discussed in detail in Section 3.3.3 on page 73.

Our modeling methods use a 4 cm $\times$ 4 cm $\times$ 4 cm cube of firn/ice as the sample volume. Granted, firn/ice cores are not cubes, but the dimensions involved are directly comparable to small diameter cores.

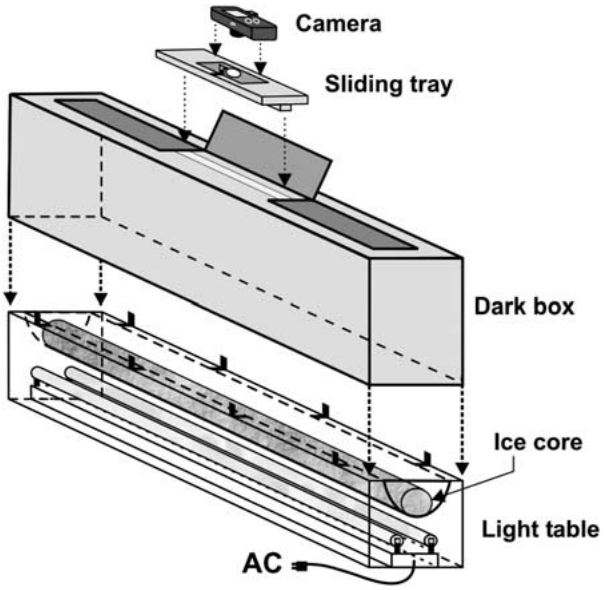

Figure 3.2. Sketch of the transmission optical imaging setup used by Kinnard and others (2008).

3.2.3 The Borehole Optical Stratigraphy (BOS) System

Measurements of reflectivity or albedo have been performed both on ice cores (Sjogren and others, 2007) and inside of boreholes Hawley and others (2003). The in-situ borehole albedo data from Hawley's BOS system are collected using a small video camera centered in the borehole and an annular, white LED light source used to uniformly illuminate the borehole wall (Hawley, 2005). A sketch of the setup is shown in Fig. 3.3.

After the BOS instrument has traversed and recorded the borehole wall, the resulting video is post-processed to extract the average reflected intensity from the borehole wall as a function of depth. Fudge and Smith (2010) created a radiative transfer model of this instrument to estimate the vertical resolution and determine the effects of firn grain size and density on the reflectivity signal. We subsequently modified this model to work with our finite, cubical geometry, additional absorbing boundary conditions and photon tallies.

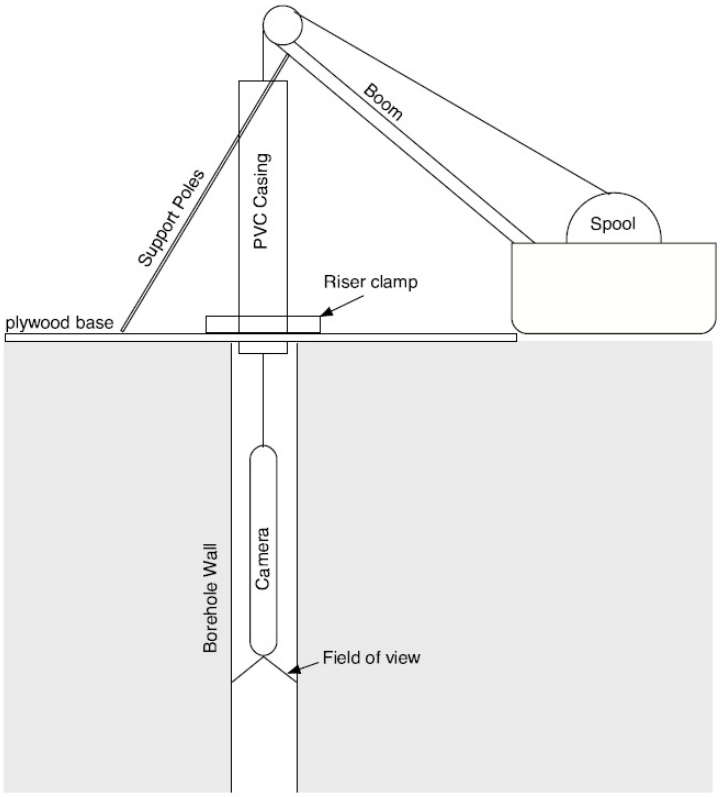

Figure 3.3. Sketch of the Borehole Optical Stratigraphy system, from Hawley (2005).

The finite firn/ice volume used in our model is not a good representation of the semi-infinite curved slab viewed by the BOS system, but should capture the essential behavior of albedo as a function of grain/bubble size and density.

3.2.4 Linescan Imaging Systems

Linescan (1-D) imaging of ice cores is useful because it eliminates the parallax problems associated with normal, 2-D imaging cameras (Svensson and others, 2005; McGwire and others, 2008b). A linescan camera is very similar to modern photo-copier or image scanner in that it takes many 1-D images along the length of the sample, and then assembles them into a parallax-free 2-D image.

A sketch of the OIS is shown in Fig. 3.4 which shows the unique side illumination setup. Svensson and others (2005) used a slightly different illumination method,

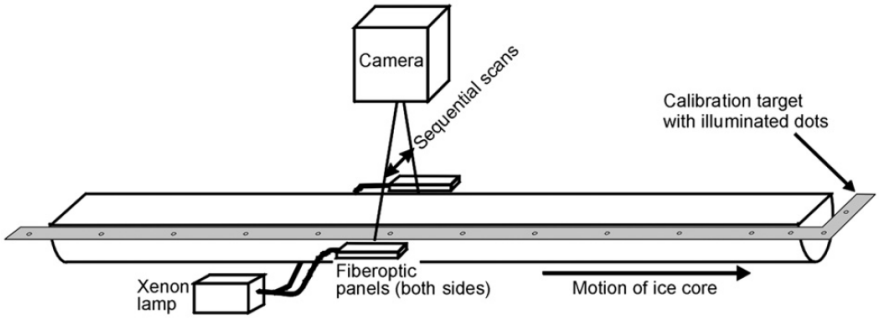

Figure 3.4. Sketch of the Optical Imaging System (OIS) geometry, from McGwire and others (2008a).

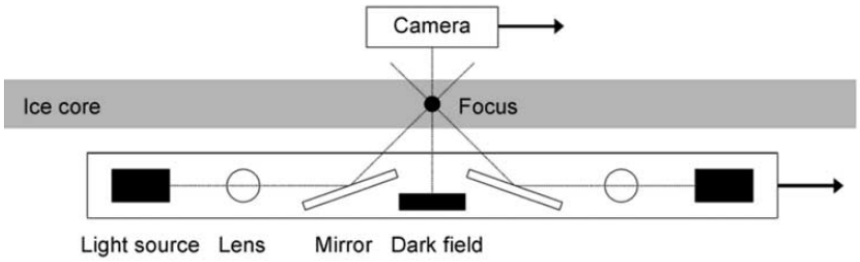

Figure 3.5. A side-view sketch of the linescan camera system constructed by Svensson and others (2005).

shown in Fig. 3.5, but the concept is the same: avoid placing the camera in direct view of the light source.

By recording the light scattered through 90°, the OIS is measuring what we will call the *emergence*, the scattered light emerging from the sample along a direction orthogonal to the input light beam. The fiber optic panels extend for several centimeters down each side of the core, thus illuminating large volumes of the core with broad spectrum light from a 1 kW Xe light bulb. The OIS can operate at either 1 pixel/1 mm or 1 pixel/0.1 mm resolution. The 45° scattering angle shown in Fig. 3.5 achieves the same goal, but makes for a more complicated analysis of the photon scattering, since the input beams must traverse core depths other than the one being photographed.

Arguably, neither method is perfect, since the emergence measured at a given depth is at least somewhat dependent on the optical properties of firn/ice *adjacent* to the section imaged by the camera. The relatively small firn/ice volume used in the model ignores the effects of illumination scattered into the volume of interest from adjacent core sections. This simplification and the fact that the model is illuminated from only one side saves a great deal of computational effort while still providing essential information about emergence and its dependence on grain/bubble size and density.

3.3 Radiative Transfer

Optical scattering in snow, firn and bubbly ice is dominated by refraction at air-ice interfaces (Barkstrom and Querfeld, 1975; Bohren, 1987), while absorption is generally small and occurs only within ice (Wiscombe and Warren, 1980; Warren, 1982). Modeling photon transport through these highly scattering media is difficult because the scattering is strongly anisotropic. At least two approaches have been used: radiative transfer and geometric optics.

The theory of radiative transfer accepts the fact that solving Maxwell's equations for N randomly located and shaped scatterers is intractable (and unneccessary) for many systems, and therefore attempts to treat the scattering problem in an *average* and phenomenological sense (Mobley and Preisendorfer, 1994).

Because radiative transfer theory is an approximate solution for Maxwell's equations in the limit of large numbers of scatterers, several assumptions regarding the scattering medium must be made. In atmospheric and astrophysical scattering problems, where radiative transfer theory was developed (Henyey and Greenstein, 1941; Chandrasekhar, 1950), these assumptions are generally well founded. They are less appropriate for dense and closely packed scattering media like firn and bubbly ice.

1. The scattering medium is locally (i.e. on length scales much larger than a typical photon mean free path) homogeneous. Therefore, in a small macroscopic volume, the density and optical properties of the scatterers within are constant (Prahl, 1988).

   This assumption is not particularly good for firn and ice. Typical mean free pathlengths at optical wavelengths (400-800 nm) are on the order of 1 mm, comparable to ice grain and bubble sizes (Domine and others, 2008). This is no coincidence: the scattering in firn and ice occur at air-ice interfaces, not within the ice grains and certainly not within the air in the pore space.

2. The scatterers are sufficiently far apart and randomly spaced so that wave interference effects are insignificant. Said another way, the scattering pattern of the medium is the simple superposition of the scattering pattern of each scatterer, ignoring phase differences between the outgoing waves of the various scatterers (Grenfell and Warren, 1999; Wiscombe and Warren, 1980).

   This assumption is valid for firn and ice at optical wavelengths given that the size of a typical scatterer is much larger than the wavelength, and that the location and shape of the scatterers is random (Bohren, 1987; Kokhanovsky, 2004).

3.3.1 The Radiative Transfer Equation

The radiative transfer equation is an integro-differential expression relating the spatial rate of change of radiance L (often called the specific intensity or simply intensity) to the various photon loss and gain mechanisms within the study volume (Kokhanovsky, 2004). The radiance has units of W m^{-2} sr^{-1} and is specified here for unpolarized light of a given wavelength. The steady-state, unpolarized,

monochromatic photon transport equation is

$$(\hat{s} \cdot \nabla) L(\vec{r}, \hat{s}) = S(\vec{r}, \hat{s}) - \mu_t L(\vec{r}, \hat{s}) + \mu_s \int_{4\pi} p(\hat{s}, \hat{s}') L(\vec{r}, \hat{s}') d\Omega'. \tag{3.1}$$

Solutions to this equation yield the radiance distribution as a function of position and viewing direction $\hat{s}$. It depends on the photon source S, the nature of the scatterers themselves (characterized by the wavelength-dependent scattering, absorption and extinction coefficients μ_a, μ_s and $\mu_t = \mu_a + \mu_s$, respectively), and the geometry, and the boundary conditions of the problem. The term on the LHS represents the spatial rate of change of radiance at position $\vec{r}$, in direction $\hat{s}$, hence the directional derivative. On the RHS, the first term (labeled Term 1 in Fig. 3.6) specifies the photon source distribution while the second term (Term 2) represents radiance loss per unit distance due to absorption and scattering.

The final RHS term (Term 3) of Eq. 3.1, the most difficult to evaluate, is the gain of radiance per unit distance due to scattering photons scattering back into the region of interest from a differential solid angle $d\Omega'$ about the direction $\hat{s}'$ from other parts of the problem geometry.

3.3.2 Phase Function

The function $p(\hat{s}, \hat{s}')$ is called the phase function and describes the probability of a photon reaching point $\vec{r}$ from direction $\hat{s}$ to be scattered into the direction $\hat{s}'$. Despite its name, it has nothing to do with wave phase, but rather characterizes the scattering pattern from a single scatterer (Prahl, 1988). A purely isotropic scatterer would have a phase function $p(\hat{s}, \hat{s}') = 1/4\pi$ because the phase function must be normalized over all directions. Anisotropic scatterers like ice grains and air bubbles have more complicated phase functions, but because radiative transfer theory is a phenomonelogical theory, the choice of phase function is largely determined by how

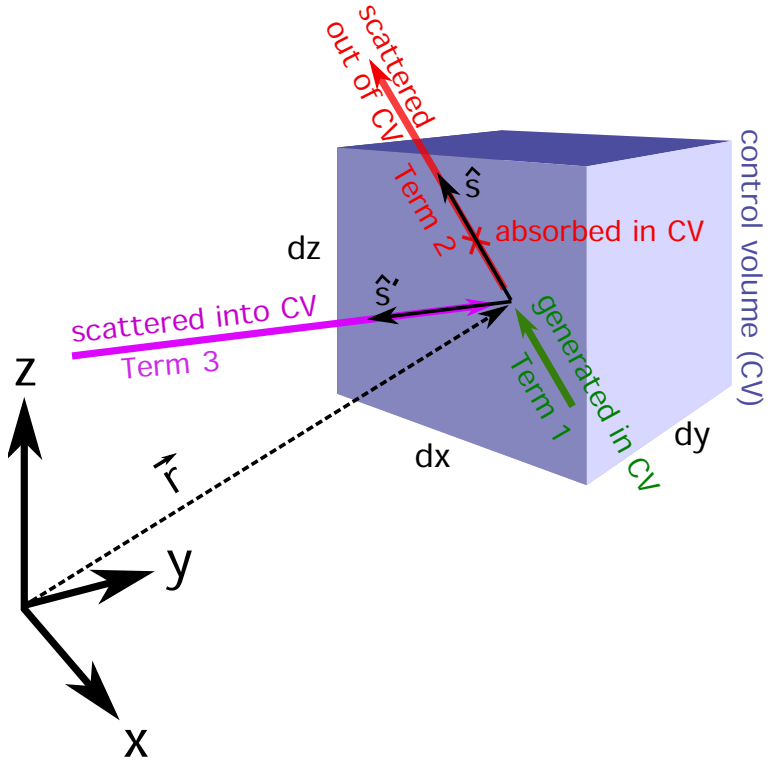

Figure 3.6. Sketch of a differential control volume (CV) centered at $\vec{r}$ for the radiative transfer equation. Arrows indicate the sources and sinks of radiance identified in Eq. 3.1. Term 1 quantifies sources of radiance within the CV, Term 2 quantifies losses due to both absorption within the CV and scattering out of the CV into other parts of the problem geometry, and Term 3 quantifies radiance scattered in to the CV from other parts of the problem geometry. All $\hat{s}$ and $\hat{s}'$ directions are required for the complete solution, but only one direction of each is shown here for clarity.

well it fits the observed scattering pattern, not by the physical characteristics of the scatterers themselves.

The Henyey-Greenstein phase function (Henyey and Greenstein, 1941) has been widely used in many geophysical radiative transfer applications, despite its original astrophysical purpose (Haltrin, 2002). It contains a parameter called the asymmetry parameter ($-1 \leq g \leq +1$) which is used to adjust the scattering pattern from isotropic ($g = 0$) to fully forward ($g = +1$) or backward ($g = -1$) scattering. Here θ is the angle between the incident and scattered photon direction.

$$p(\cos\theta) = \frac{1 - g^2}{4\pi(1 + g^2 - 2g\cos\theta)^{3/2}} \tag{3.2}$$

The asymmetry parameter for ice grains in air is around 0.89 and around 0.85 for air bubbles in ice (Fudge and Smith, 2010; Mullen and Warren, 1988; Wiscombe and Warren, 1980). The bubbles are slightly more isotropic due to total internal reflection at scattering angles larger than about 49.7° (Fowles, 1989). It is unclear how best to make the transition from the ice-grains-in-air (GA) to the air-bubbles-in-ice (BI) values for g through the firn-ice transition so we, like Fudge and Smith (2010), simply use the GA value in all of our calculations.

3.3.3 Specific Surface Area

Ice grains (index of refraction $n_{\text{ice}} = 1.31$) in air ($n_{\text{air}} = 1.00$) and air bubbles in ice are both considered optically "hard" particles, meaning that there is a large difference between the index of refraction of the particle and the medium in which the particle is embedded. For a given particle size and geometry, optically hard particles are more effective scatterers because of the larger intensity of Fresnel reflections and larger angles of refraction (Kokhanovsky, 2004). In the previous section, we saw that both ice grains and air bubbles alter the optical properties of an ice core, demonstrating that it is the density of the air-ice interfaces within the core that control the propagation of light via refraction and/or reflection. This interface density is called the specific surface area (SSA) and can be expressed in two ways:

1. The total air-ice surface area per unit volume, SSA_v, has units of $\text{m}^2\ \text{m}^{-3}$. SSA_v is generally more useful for characterizing the optical scattering properties and microstructure of snow, firn or ice (Kokhanovsky and Zege, 2004; Freitag and others, 2004).

2. The total air-ice surface area per unit mass, SSA_m, has units of $\text{m}^2\ \text{kg}^{-1}$. This representation of SSA is more often seen in the cryosphere literature where the emphasis is on snow photochemistry and gas paleoclimate reconstructions,

both of which measure chemical or gas concentrations (Domine and others, 2008; Gallet and others, 2009).

The two representations of SSA are related by $\mathrm{SSA_v} = (\rho \times \mathrm{SSA_m})$ where ρ is the density of the snow, firn or ice. In this chapter, SSA_v will be used most often since it describes the number density (per unit volume) of scatterers which is the fundamental parameter for modeling and understanding light transport.

A simple way to model SSA is to assume that both ice grains and air bubbles are *spherical*:

$$\mathrm{SSA}_v = \begin{cases} \frac{3\rho}{r_g\,\rho_{\mathrm{ice}}} & \text{for ice grains in air,} \\ \frac{3}{r_b}(1 - \frac{\rho}{\rho_{\mathrm{ice}}}) & \text{for air bubbles in ice} \end{cases} \tag{3.3}$$

where r_g and r_b are the grain and bubble radii respectively, and ρ_{ice} is the density of pure ice (0.917 g cm^{-3} at 273 K). Later in the chapter we will use the generic scatterer radius a to describe both r_g and r_b, especially in cases where it is unclear whether GA or BI is a more appropriate representation of firn structure.

The maximum density range for ice spheres is 586 kg m^{-3} for a random packing and 680 kg m^{-3} for a face centered cubic packing (Golubev and Frolov, 1998), so the ice "spheres" at densities above this value *must* have suffered some type of deformation, and have inter-grain bonds of significant volume. The minimum density for ice spheres is about 200 kg m^{-3} when *carefully stacked* to have a coordination number (number of contacts with surrounding particles) $j = 3$ (Arons and Colbeck, 1998). As shown by typical surface firn densities of 300 to 400 kg m^{-3}, this rarely lasts for long in nature (Colbeck, 1983). In polar regions, typical firn grain sizes r_g are 0.2 to 0.3 mm and increase with depth (Freitag and others, 2008).

For air bubbles in ice, the minimum density for face centered cubic packing is 240 kg m^{-3} and 330 kg m^{-3} for random packing. The maximum density is of

course bounded by the density of solid ice (917 and 920 kg m^{-3} at 273 and 248 K respectively) (Gow, 1970).

Choosing between the grains-in-air (GA) and bubbles-in-ice (BI) scenarios is difficult near the firn porespace closeoff depth where both grains and bubbles coexist. Firn porespace closeoff (where air bubbles are sealed off from the surrounding air in the firn) is generally considered to begin around 780 kg m^{-3} and complete closeoff is achieved by 830 kg m^{-3} (Domine and others, 2008).

It is important to note that a given value of SSA_v is not unique to a particular firn or ice type. For example, large grained firn with $r_g = 0.7$ mm has an SSA_v = 7000 m^{-1}, as does very bubbly ice at ρ=700 kg m^3, $r_b = 0.2$ mm. The SSA_m values for the large grains and bubbly ice are 9.3 and 9.9 m^2 kg^{-1} respectively. SSA_m values need not be unique either, showing that a unique description of the firn or ice type requires both density and grain/bubble size. Despite the non-uniqueness, SSA_v values range from zero in solid ice, roughly 4500 near the firn-ice transition and over 25,000 m^{-1} for very small grained surface snow.

3.3.4 Analytical Solutions of Radiative Transfer Equation

For large scale and far field calculations (albedo from a 1 m deep snowpack, for example) solutions to Eq. 3.1 can be obtained using a diffusion approximation (Giddings and LaChapelle, 1961) with simple, perfectly absorbing boundary conditions. Other analytical solutions have been obtained by Kokhanovsky and Zege (2004) and Zege and others (2008) for semi-infinite slabs of snow in the low absorption limit of the radiative transfer equation. The results for the spherical albedo R (defined as the fraction of light energy reflected from a diffusely illuminated semi-infinite scattering medium) are quite simple:

$$R = \exp(-y), \qquad y = 4\sqrt{\frac{\mu_a}{3\mu_t(1-g)}} \tag{3.4}$$

Taking the absorption coefficient $\mu_a = 1/L_{\text{abs}}$ as constant and the attenuation coefficient μ_s from Eq. 3.5, Eq. 3.4 shows the expected relationship between albedo, asymmetry parameter and SSA_v: for a given absorption coefficient, albedo is higher for more isotropic scattering (smaller values of g) and for higher specific surface area (larger values of μ_t).

3.3.5 Monte Carlo Approach for Radiative Transfer Equation

For smaller scattering volumes such as firn or ice core samples, the diffusion and semi-infinite slab approximations are inappropriate since the measurement of the radiance distribution will, by necessity, be made near the boundaries of the sample where the both approximations are poor. In this section, we follow the work of Fudge and Smith (2010) and Prahl (1988) by modifying their Monte Carlo radiative transfer code to suit the OIS geometry and provide relatively correct radiance distributions near the perfectly absorbing boundaries of the firn/ice core.

The Monte Carlo method takes a very literal and probabilistic approach to solving transport equations (Metropolis and Ulam, 1949). It models the propagation of photon packets in the sample by choosing scattering angles from a probability distribution derived from Eq. 3.2 and propagation distances from an exponential probability distribution with an average value equal to the mean free path for scattering L_{scat}.

Fudge and Smith (2010) characterize the scattering and absorption coefficients for the GA and BI cases with the following equations.

$$\frac{1}{\mu_s^{\text{GA}}} = L_{\text{scat}}^{\text{GA}} = \frac{4\rho_{\text{ice}} r_g}{3Q_{\text{scat}}\rho} = \frac{4}{\text{SSA}_v^{\text{GA}} Q_{\text{scat}}} \tag{3.5}$$

$$\frac{1}{\mu_s^{\text{BI}}} = L_{\text{scat}}^{\text{BI}} = \frac{4\rho_{\text{ice}} r_b}{3Q_{\text{scat}}(\rho_{\text{ice}} - \rho)} = \frac{4}{\text{SSA}_v^{\text{BI}} Q_{\text{scat}}} \tag{3.6}$$

The scattering efficiency (the ratio of the effective scattering cross section to the geometrical cross section of the scatterer) is $Q_{\text{scat}} \cong 2$ at optical wavelengths due

to diffraction effects near the edges of the ice grain or air bubble (Brillouin, 1949; Grenfell and Warren, 1999; Fu and Sun, 2001; Sudiarta and Chylek, 2001).

Absorption is incorporated into the model using absorption data from Warren (1984) and Warren and Brandt (2008) which show that ice is extraordinarily transparent in the optical range. For our modeling at λ=600 nm, $L_{\text{abs}} = 1/\mu_a = 8.3$ m, meaning that on average, a photon will travel 8.3 m through solid ice between absorption events. In the Monte Carlo model, absorption is calculated in two different ways, depending on whether the GA or BI scenario is assumed. For the GA scenario, a single scattering albedo ω is calculated from

$$(1 - \omega) \approx 0.85 r_g / L_{\text{abs}} \tag{3.7}$$

which is then used to determine the loss of radiance from the photon packet per scattering event. ω is formally defined as the ratio of the total scattering cross section to the total extinction (scattering + absorption) cross section, but can also be thought of as the probability that a photon will *not* be absorbed in a single scattering event (Mishchenko and others, 2000).

The constant factor of 0.85 in Eq. 3.7 was derived by Warren and others (2006) from Mie scattering models run for a wide range of grain radii, where the factor was near 0.88 for r_g=0.04 mm and 0.85 for r_g=0.2 mm. We use the higher value because the grains encountered in the firn column are at least this large (Freitag and others, 2008). It is unclear if 0.85 is appropriate for deep firn where r_g can be an order of magnitude larger.

For an initial photon packet radiance L_0, the final photon packet radiance in the GA scenario is

$$L^{\text{GA}} = L_0 \omega^{N_{\text{scat}}} \tag{3.8}$$

where N_{scat} is the total number of scattering events experienced by the photon packet from its start at the source to its exit from the model geometry.

For the BI scenario, the total photon transport length ℓ is scaled by the relative density (ρ/ρ_{ice}) to estimate the total in-ice path length. In this case, the final photon packet radiance is

$$L^{\text{BI}} = L_0 \exp\left[-\frac{\ell(\rho/\rho_{\text{ice}})}{L_{\text{abs}}}\right]. \tag{3.9}$$

With the connections made between firn and ice microstrutural parameters and optical parameters, we can now simulate the resulting radiance distribution for the sample geometry. Note that the radiative transfer approach does not require an explicit description (i.e. sizes, shapes and locations of individual grains and/or bubbles) of the scattering medium, thereby making this approach quite economical in terms of computer memory. This contrasts strongly with the geometric optics modeling described later in this chapter.

We ran the model to cover physically reasonable values of density and grain/bubble sizes. The firn/ice core geometry, shown in Fig. 3.7, was modeled as a 4 cm $\times$ 4 cm$\times$ 4 cm cube with perfectly absorbing boundary conditions on each face of the cube. The point source was located 2 cm below the upper surface of the core and produced $\lambda = 600$ nm photons in the $+x$ direction. This is therefore a model for a very tightly collimated red laser, and is not truly representative of the wide spectrum Xe-bulb light source, nor the large fiber optic panels used by the OIS. As we shall see, the important firn optics are well captured using this simpler light source, and are much closer in spirit to the proposed optical scattering physical properties instrument discussed at the close of this chapter.

The model propagates the photon packets through the problem geometry until they reach one of the boundaries. The photon packets that cross the boundaries are stopped (thereby imposing perfectly absorbing boundary conditions) and their location, total path length traveled ℓ and total number of scatterings N_{scat} are

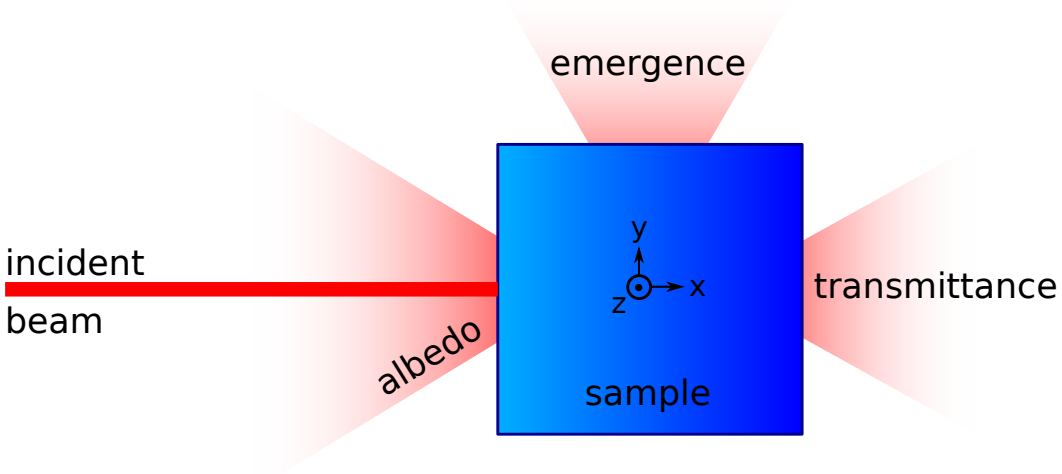

Figure 3.7. The geometry used in the Monte Carlo radiative transfer simulation. The z-axis is along the firn/ice core axis. The coordinate system origin is actually located at the beam/sample interface, but is drawn in the center of the sample for clarity.

recorded in an output file. Subsequent post-processing of the output file applies the appropriate absorption calculation (Eq. 3.8 or Eq. 3.9) for that particular packet.

The model provides the radiance escaping from the three core faces of interest: the radiance backscattered toward the source (the ratio of this radiance to the input radiance is called the albedo A), the radiance forward scattered across the core to the face opposite the source (the ratio of this radiance to the input radiance is called the transmittance T), and the radiance emerging from the top face of the core (the ratio of this radiance to the input radiance we have called the emergence E).

3.3.6 Monte Carlo Radiative Transfer Model Results

The model results are shown in Fig. 3.8, with A, E and T plotted versus SSA_v for both BI and GA scenarios. Each data point is the result of simulating the transport of 10^6 photon packets through the model geometry. They are generally in line with our intuition: $\mathrm{SSA}_v \to 0$ (solid air or solid ice) $T = 1$, $A = 0$ and $E = 0$, while $\mathrm{SSA}_v \to \infty$ tends towards $T = 0$, $A = 1$ and $E = 0$. In between, E passes through a

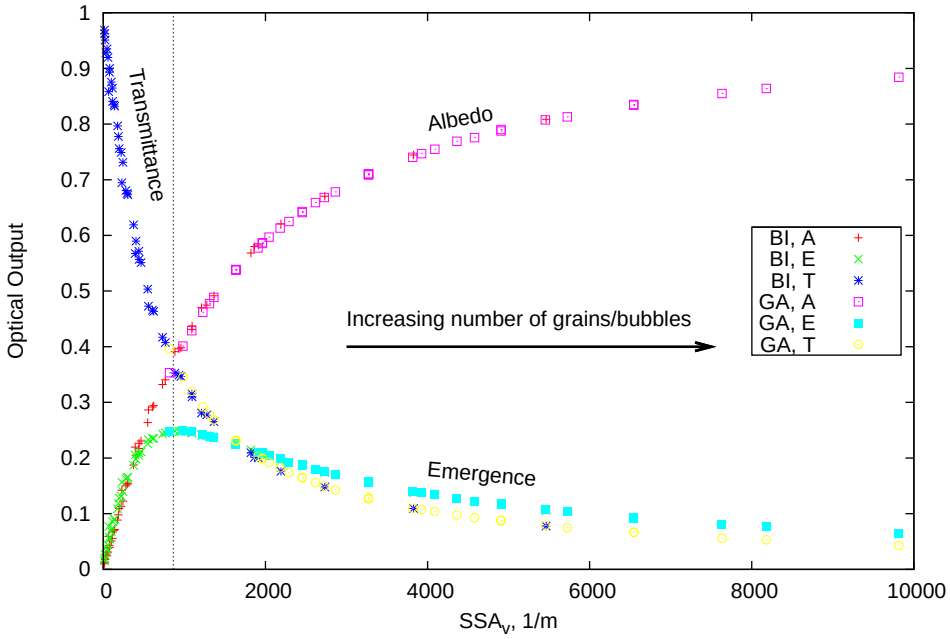

Figure 3.8. Results of the Monte Carlo radiative transfer model. $4 \times 4 \times 4$ cm^3 sample at λ =600 nm with $a = 0.2$ mm. The dashed line at 880 m^{-1} indicates the emergence maximum for this geometry and a value.

maximum at about 880 m^{-1}. Note that we replace r_g and r_b with a generic scatterer radius a from this point forward to simplify the plots and diagrams. Zones of GA and BI will be clearly marked on the plots where appropriate.

The most obvious comment is that there is little difference between the BI and GA results when plotted versus SSA$_v$. This is expected since the same value of $g = 0.89$ was used for both scenarios, but also partially unexpected since absorption was calculated in different ways (see Eqns 3.8 and 3.9. The similarity shows

1. that SSA$_v$ is the fundamental quantity for characterizing the scattering properties of firn and ice and

2. absorption does not play a significant role in centimeter-scale firn optics at $\lambda = 600$ nm.

Plotting the same data (shown on page 82) at various grain/bubble radii a versus density shows a very different picture, one that will help us understand the behavior of the optical measurement geometries for albedo, transmittance and emergence.

For all three plots, we see that the GA scenario makes intuitive sense at low densities. Fine ice grains ($a = 0.2$ mm) in air have a very high albedo which, for a constant grain size, increases with density due to the increased scatterer density. The high albedo ensures that both transmittance and emergence will be small for fine grained firn due to energy conservation. The opposite is true for coarse firn ($a = 0.4$ mm). Expressed on an equal ice content (density) basis, many small grains are more effective at scattering than a few large grains.

The BI scenario also makes intuitive sense at high densities. Expressed on an equal air content (density) basis, many small bubbles are more effective at scattering than a few large bubbles. As density increases, fewer and fewer bubbles are allowed until the ice is bubble free and transparent.

The emergence curves still have the maximum shown in Fig. 3.8, though now we can see that this maximum is only applicable to the BI scenario where the number of bubbles is getting small. The emergence maximum in the GA scenario occurs at densities close to zero which are not physically realizable for either snow or firn. We also note that the magnitude of the emergence maximum appears to be dependent only on air content (density), and independent of bubble size a. An image of a typical spatial distribution for emergence is shown in Fig. 3.10.

3.3.7 Discussion of Radiative Transfer Model Results

In all of the plots in Fig. 3.9, we note that the GA and BI scenarios fail to match up for a given grain or bubble size. This is not suprising since $\mathrm{SSA}_v^{GA} \neq \mathrm{SSA}_v^{BI}$ for a given value of a, but we do expect the optical outputs of the sample to vary smoothly

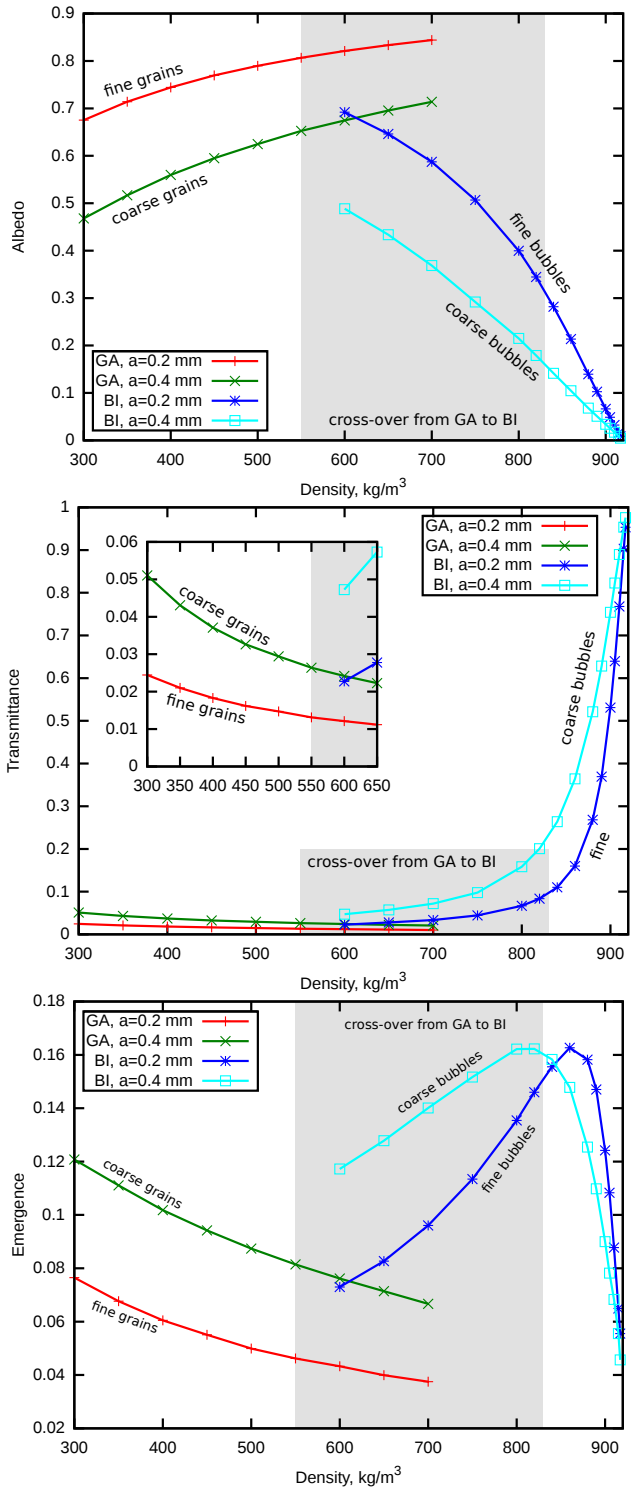

Figure 3.9. Albedo, transmittance and emergence for the Monte Carlo radiative transfer model. $4 \times 4 \times 4$ cm^3 sample at λ =600 nm and grain/bubble radii a. Note differing scales for the vertical axes.

and continously with density. We would therefore like to avoid the discontinuty by finding and justifying a continous path from GA to BI to solid ice.

One problem is the fact that we used a constant g for both scenarios because we do not know how it should vary with density. Wiscombe and Warren (1980) discuss a density dependence where g increases with density in the GA scenario to g=0.965 for $\rho = 0.5$ g cm^{-3}, but this analysis stops at this density because it is "near the upper limit for the density of a surface snow layer". This trend cannot continue much further since polar firn at $\rho = 0.750$ g cm^{-3} would have $g \to 1$ and would therefore be nearly transparent, contrary to observations. Even if we could somehow determine $g^{GA}(\rho)$, we must still figure out how to smoothly transition to $g^{BI}(\rho)$ which is at least 15% smaller than the GA version.

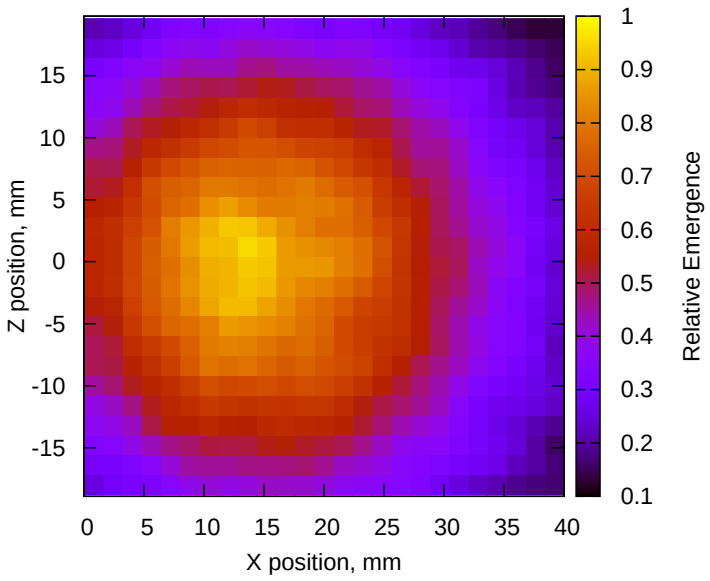

Figure 3.10. Relative emergence pattern on the top face of 4 × 4 × 4 cm^3 cube of bubbly ice. ρ=750 kg m^{-3}, a=0.4 mm. Illumination source at z=0 and centered in the $y - z$ plane, sending photon packets into the cube in $+x$ direction.

The other problem is the fact that the GA and BI firn and ice models only apply at low and high densities, respectively. It is an open question what combination of these models is appropriate in the "cross-over" region, or if an entirely different model is needed to connect the firn microstructure to the optical properties in this region. However, it does seem that the GA and BI curves should provide upper and lower bounds on where real firn and ice could possibly exist on our "map" of optical properties and firn/ice density and structural properties.

What we *do* know is that firn begins in the GA scenario, and moves towards bubbly ice in the BI scenario, and ends up as solid ice. The exact path taken by the firn in (ρ, a) (density, grain/bubble size) space determines the observed optical outputs, but we can, guided by the GA and BI bounds in the cross-over region, make a reasonable guess about this path given the following:

1. Ice grain size increases with time and depth (Alley and others, 1982; Freitag and others, 2004; Rick and Albert, 2004).

2. After porespace closeoff, there are about 2 bubbles formed per ice grain (Spencer and others, 2006). This is crucial because it (and the ice grain size data from Freitag and others (2004)) demonstrates that the relative SSA_v difference between FGF and CGF *persists* through and beyond the firn-ice transition.

3. Bubbles are compressed and shrink after porespace closeoff due to the differential pressure between the bubble (atmospheric pressure at closeoff) and the pressure imposed by the $\sim$100 m deep column of firn and ice (Alley and others, 1997; Lipenkov, 2000).

4. Porespace closeoff is the endpoint of ambiguity over which firn/ice structural model (GA or BI) to use. According to the radiative transfer model results

for densities < 900 kg m^{-3}, the transition from GA to BI structure is *certain* to cause a decrease in A and increases in both E and T.

Using this guidance, we can move along a hypothetical (ρ, a) path to estimate the change in optical output as a function of depth, density and grain/bubble size for transmittance (Kinnard and others (2008)), albedo (Hawley and others (2003)) and emergence (Arnaud and others (1998a), McGwire and others (2008b)) instruments. For each instrument, we will first analyze the expected optical output for a conjectured mean (average of fine and coarse) (ρ, a) path to determine the overall expected trend for polar firn. Then we will analyze the optical effects of FGF and CGF variations about the mean trend.

3.3.7.1 Analysis for Transmittance Instruments

We will follow the mean path shown in Fig. 3.11. Starting at point A at the surface, we expect T to slowly increase with depth since the increasing density and increasing grain size effects are competing. According to the data presented in Kinnard and others (2008), the grain growth slightly dominates in this region. At point B, transmittance begins increasing more rapidly with density since, for the same density, we expect BI to be more transmissive than GA. Point C is the end of pore closeoff, and therefore we are fully within the BI regime with transmittance increasing rapidly with density.

Superimposed on this mean trend, we have variability of firn types. At the surface, FGF has higher density and is composed of small, well rounded, sintered grains. CGF has a lower density and is composed of large, irregular and poorly connected grains with large porespaces. The density, grain size and optical effects of the two firn types are summarized by the double ended arrows: near the surface, CGF will have a lower density and larger grain size, resulting in a higher T. The opposite is

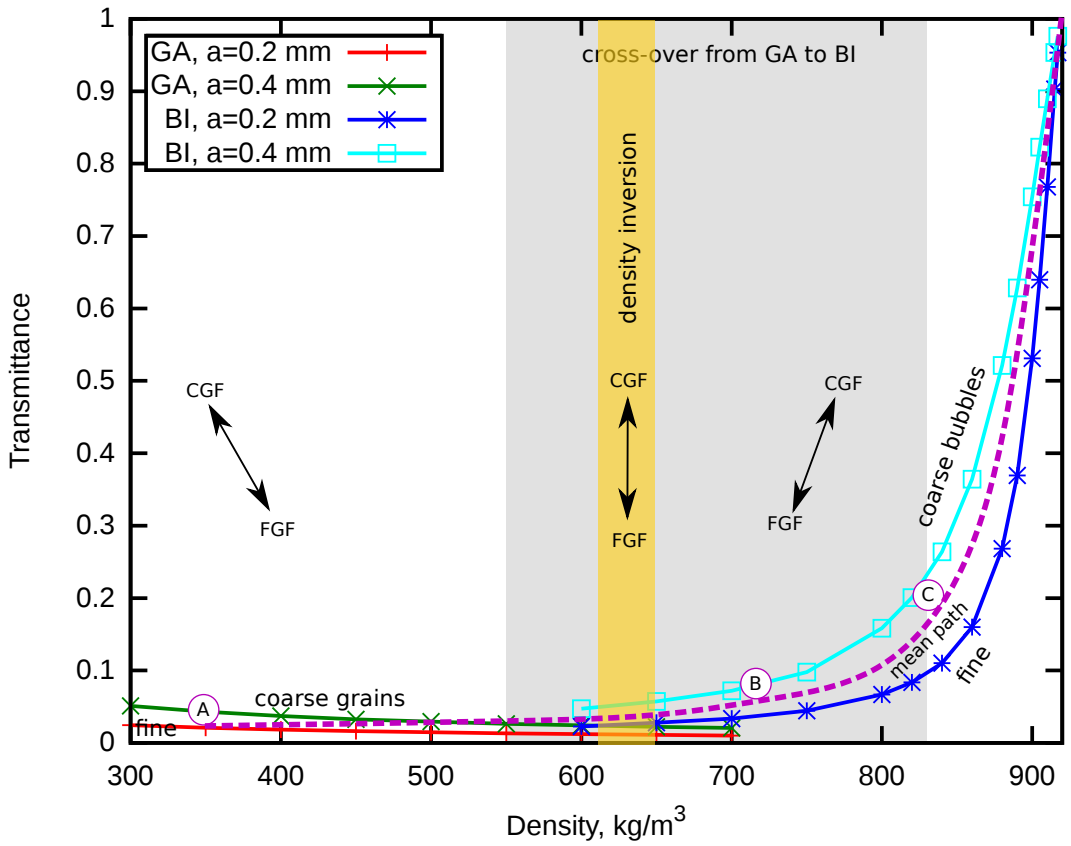

Figure 3.11. Transmittance as a function of depth and firn type for a hypothetical firn/ice core. Double ended arrows show the expected optical effects for CGF and FGF variations about the mean (ρ, a) path.

true for FGF. Therefore, near the surface, we expect density and transmittance to be *negatively* correlated.

The CGF is generally believed to compact faster (per unit time and therefore also, on average, per unit depth) than the FGF, resulting in a density inversion at approximately 650 kg m^{-3} (Alley and others, 1982; Freitag and others, 2004; Fujita and others, 2009; Gerland and others, 1999). If density inversion happens, there will be a zone of *no* correlation. CGF will still yield a higher T, but CGF and FGF densities are approximately equal in the region of density inversion, hence the vertical arrows and lack of density-T correlation.

Beyond the density inversion, CGF is now more dense than FGF, and this difference in density is maintained through the remainder of the firn into bubbly ice. Note that a density inversion does not necessarily imply an SSA_v inversion: according to Spencer and others (2006) approximately 2 bubbles are created per ice grain, therefore CGF must retain its smaller SSA_v relative to FGF through the densification and eventual pore closeoff process. Therefore our model predicts that density and T will be *positively* correlated from the density inversion point and deeper. The positive correlation will slowly diminish as the difference in CGF and FGF densities becomes small, since both firn types asymptotically approach the maximum density of solid ice.

There are two possibilities for failure of this correlation prediction:

1. If density inversion does not happen, then density and T will be negatively correlated throughout the entire core.

2. If, contrary to Spencer and others (2006), both density *and* SSA_v invert at the same time, then the original negative correlation observed at the surface would again persist throughout the core.

Kinnard and others (2008) provide density-transmittance data, shown in Fig. 3.12. However, they do not calculate cm-scale density-transmittance correlation data (i.e. the bottom plot of Fig. 3.14), so it is difficult to test the density-T correlation predictions of the analysis for microstructural variations about the mean. However, the overall trend for the mean (ρ, a) path is quite good and explains why the simple exponential light attenuation model fails to fit the data for low densities: the competing effects of increasing density and increasing a cause very little change in T for large changes in density.

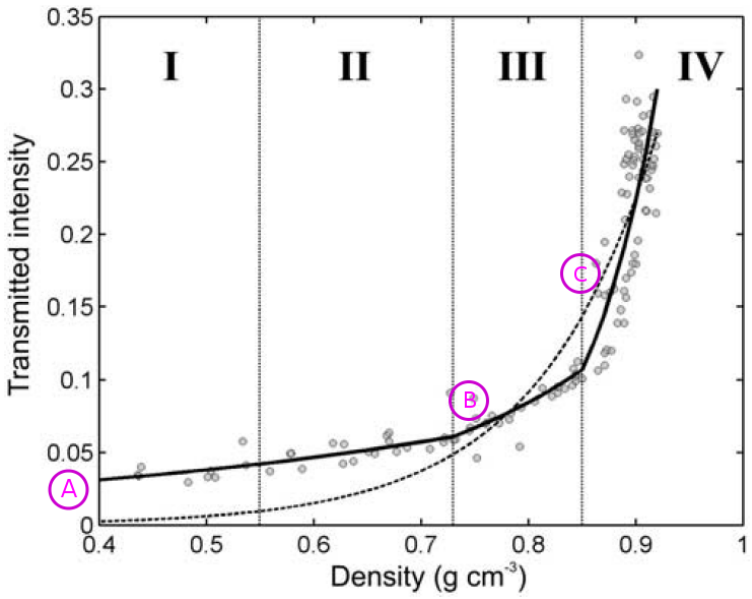

Figure 3.12. Optical transmission vs. density for an Arctic ice core. From Kinnard and others (2008). The dotted line represents a simple exponential model for transmission. The marked points A-C correspond to those in Fig. 3.13.

3.3.7.2 Analysis for Albedo Instruments

Following the mean (ρ, a) path in Fig. 3.13, we begin in the fine grained surface firn at point A. Grain size and density are both increasing with depth. The former tends to reduce albedo, while the latter tends to increase it, resulting in a very modest increase in albedo with depth until point B. At point B we reach the maximum albedo where density is high and grain sizes are small - therefore, we expect this maximum to occur in FGF. Going deeper, we see a rapidly diminishing albedo through point C at the end of the density inversion. Albedo continues to decrease with depth, past point D at porespace closeoff and down into solid ice.

Albedo variability due to firn type is exactly the opposite of the transmittance case: above the density inversion, FGF will have a higher density and albedo and therefore we predict a positive density-albedo correlation in this region. Through the density inversion, FGF will still have a higher albedo than CGF, but there is no significant density difference between the two, so we predict no correlation. Below

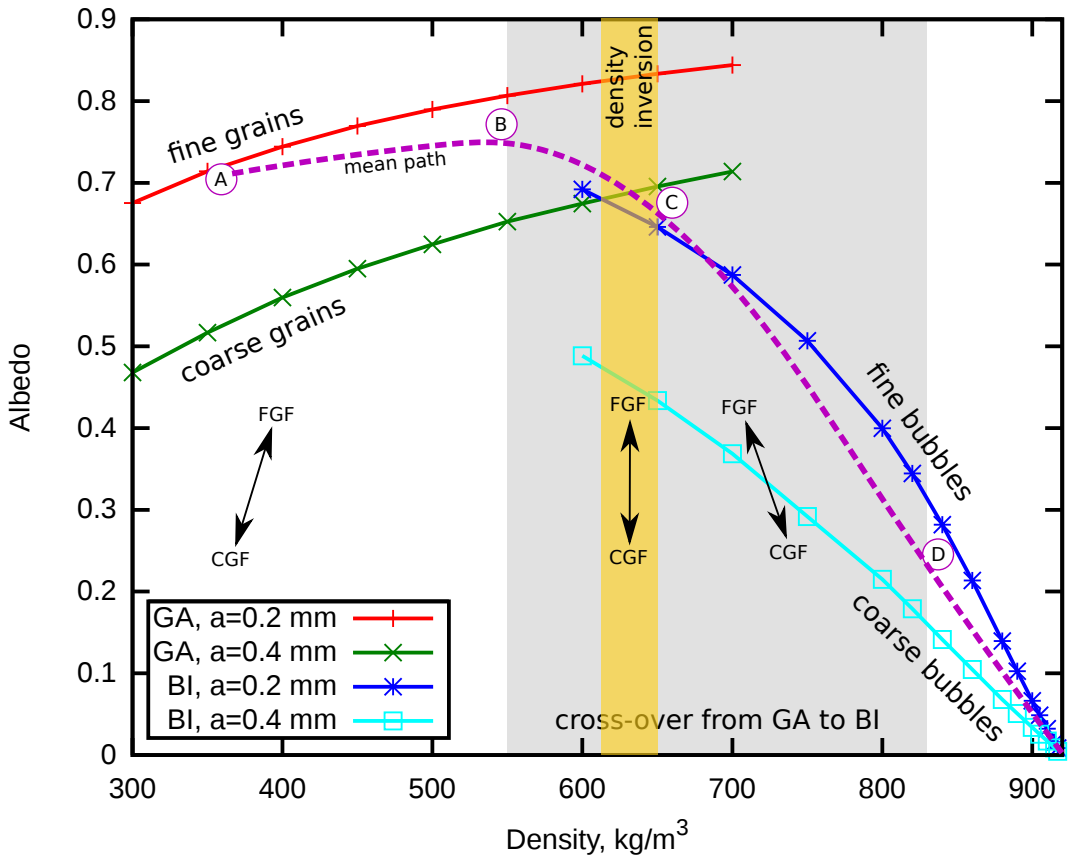

Figure 3.13. Albedo as a function of depth and firn type for a hypothetical firn/ice core or borehole.

the density inversion, CGF still has a lower albedo, but now has a higher density, therefore we expect a negative density-albedo correlation from point C down towards solid ice. Eventually, the density differences between CGF and FGF grow small, so the negative correlation will eventually fade in the deep ice.

Hawley and Morris (2006) collected in-situ density and albedo data from a 30 m borehole at Summit, Greenland. The density, albedo and correlation are shown in the plots of Fig. 3.14 which have been annotated to show where the preceding analysis falls on Hawley and Morris's data.

From the surface to point B, the observed borehole albedo is highly variable and slowly increasing with depth, reaching a maximum around 550 kg m^{-3}. From the surface to 17 m depth, the density-albedo correlation is strongly positive and then

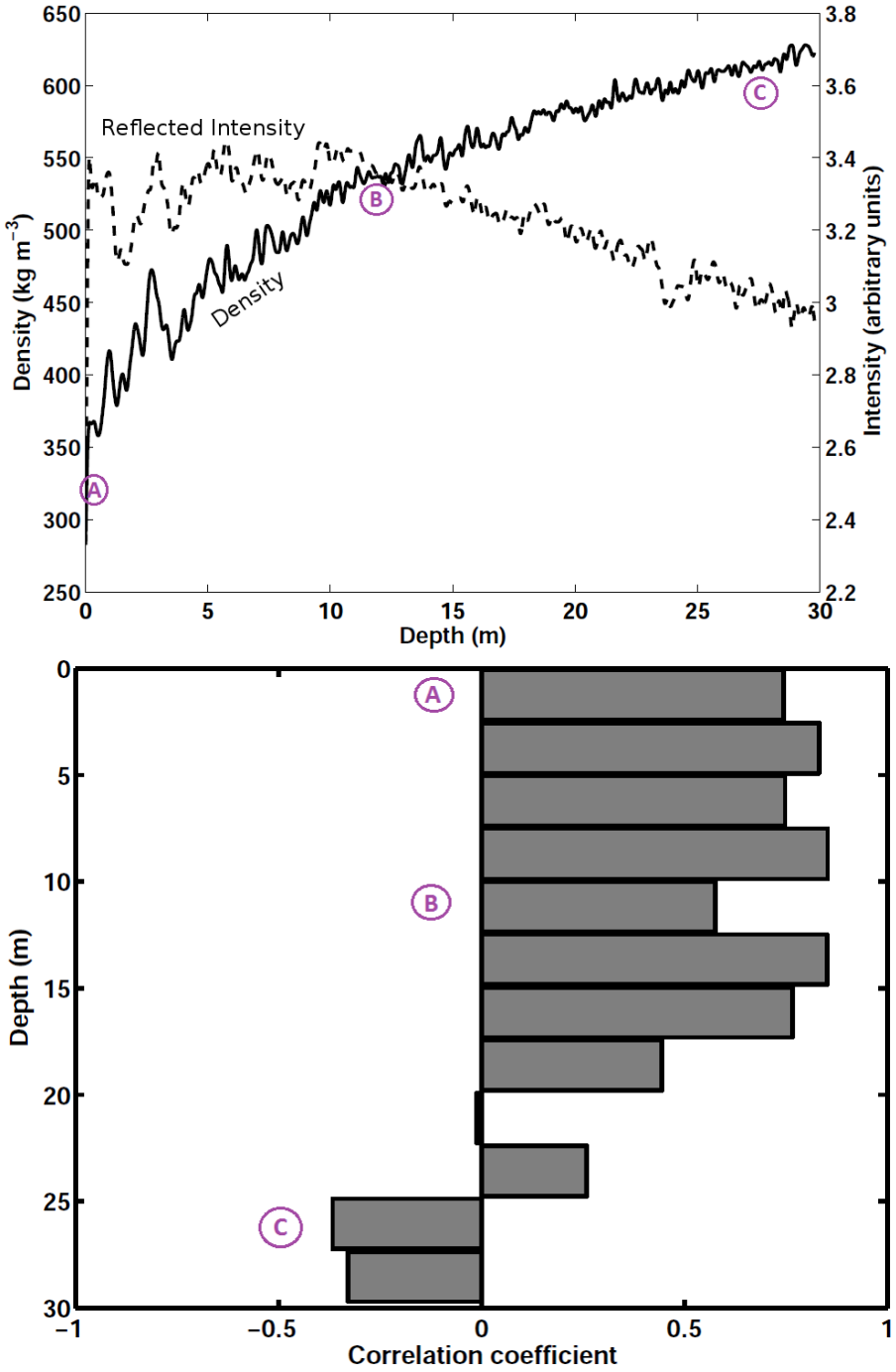

Figure 3.14. Density and albedo data from Hawley and Morris (2006). Top: density (solid line) and borehole albedo (dotted line) from Hawley and Morris (2006). Bottom: density-albedo correlation coefficients as a function of depth. Corresponding points on Fig. 3.13 are marked by circled letters on both plots. Point D is not shown since data collection ended at 30 m depth, well above pore closeoff for Summit, Greenland.

quickly swings to a negative correlation by 25 m. Unfortunately, the data from this borehole stops at 30 m, but the data that we have suggest that our radiative transfer model results and hypothesized (ρ, a) path are at least qualitatively correct when compared with field data.

At the conclusion of their paper, Hawley and Morris (2006) relate that, based on the density and the firn core chemistry profiles, a density inversion *did not* occur at the Summit site. However, the pattern of density-albedo correlation with depth suggest that density inversion *did* occur at Summit between 20 and 25 m depth. Similar to the transmittance case, if density inversion did not occur, then we would expect positive density-albedo correlation throughout the core. The difference in vertical resolution between the neutron-scattering density probe ($\sim$ 14 cm, Morris (2008)) and the firn core chemistry analysis ($\sim$ 2 cm, McConnell and others (2002)) may have made it difficult to confidently discern a density inversion, especially with the borehole extending only a few meters deeper than the inversion zone.

3.3.7.3 Analysis for Emergence Instruments

Transmittance and albedo measurements are relatively straightforward to understand and could be viewed as perfectly complementary to each other if firn and ice cores were of infinite optical size. Of course, they are not, and therefore the emergence (or leakage) becomes important for measurements on finite-sized cores.

Illumination sources must be located outside of the firn/ice core. Therefore, the core albedo controls how much light is available *inside* the core for emergence and transmission. The radiative transfer model shows that the division of internal core light between E and T depends on the optical properties of the core.

In Fig. 3.15, the mean (ρ, a) path begins at point A, the surface. Core albedo is high here, so there is little light available in the core interior for either T or E. For our 4×4 cm^2 core size, $E \approx T$ at point A and both increase slowly with depth

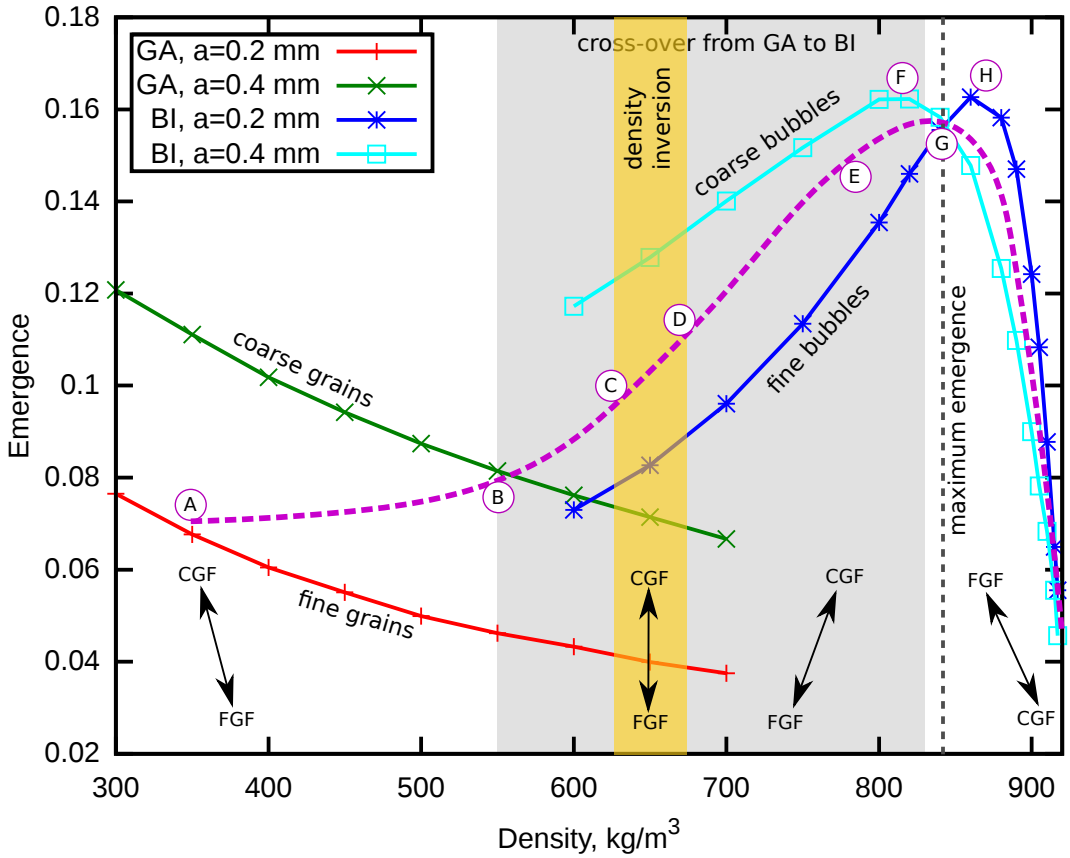

Figure 3.15. Emergence as a function of depth and firn type for a hypothetical firn/ice core. Note that the maximum E for coarse bubbles occurs within the expected porespace closeoff zone, while the maximum for fine bubbles occurs at higher densities.

from the surface. At point B, around 550 kg m^{-3} where A has its maximum, E and T begin to increase more rapidly with depth. Firn with large bubbles (CGF) will pass through the E maximum first (point F), while FGF will pass through the E maximum slightly deeper (point H). Therefore, we predict an overall E maximum for the mean (ρ, a) path at point G, somewhere between the CGF and FGF maxima. Deeper than this, E should decrease steadily with depth until fully transparent, bubble-free ice is reached.

The E variability due to firn type is more complicated than the albedo or transmittance cases. At the surface (point A), CGF has a lower density and higher E than the higher density FGF, therefore we predict a negative density-E correlation.

At point B, we expect a weakening negative correlation which moves towards *no* correlation in the density inversion zone between points C and D. From point D to the emergence maximum at point G, we expect a positive density-E correlation that grows stronger with depth. CGF and FGF reach their E maxima at points F and H, respectively. The mean (ρ, a) path E maximum occurs between these at point G, about 840 kg m^{-3}.

Also at point G we predict, for the same density, that $E_{\mathrm{CGF}} \approx E_{\mathrm{FGF}}$. Beyond this point, $E_{\mathrm{FGF}} > E_{\mathrm{CGF}}$ for the same density, though the post-inversion differences in density still persist. Therefore we expect the positive density-E correlation to diminish with depth and eventually (beyond point H) become negative. At very high densities, the negative correlation should fade as the density difference between CGF and FGF becomes small.

If no density inversion occurs, then based on our model, we predict the following:

- a negative density-E correlation from the surface down to the E maximum at point G,
- below point G, the correlation would become positive, and
- at densities greater than 900 kg m^{-3} the correlation would become small.

We also plot the emergence results in the (ρ, a) plane so that the mean (ρ, a) path and variations about that path can be better visualized. The data shown here are from the geometric optics model (Section 3.4 below) but the results of the RT model are similar. The lower (upper) part of this plot was calculated using the GA (BI) microstructural model and the dividing line between them is shown around 500 kg m^{-3}. At the density inversion (point D) there is (theoretically) no density difference between CGF and FGF, therefore only differences in a can cause changes in E (i.e. a double-ended arrow indicating the E effects of microstructure type would be parallel to the a-axis).

The conjectured mean (ρ, a) path starts with small ice grains which grow with depth. The applicable firn microstructural model must then transition from GA to BI, though the details of this transition are unknown at present. Between points D and E the dominant scatterer (grain, bubble or both) size a reaches a maximum and then begins to decrease to match the bubble sizes reported by Lipenkov (2000). Eventually, emergence and a approach zero as the path approaches solid ice.

Along the way, the mean (ρ, a) path crosses contours of constant E and the angle at which they intersect has an important effect on the expected variability of E in response to firn microstructural changes. When the mean (ρ, a) path crosses perpendicular to a contour, the double-ended arrow will be parallel to the contour - hence the minimum in emergence variability at point C: changes in microstructure cause (theoretically) no change in emergence. Similarly, the maximum emergence variability (point E) occurs where the mean path is parallel to the emergence contour, therefore the double-ended arrow will be perpendicular to the contour: changes in microstructure cause large changes in emergence.

We reserve the comparison of prediction with experiment for Chapter 4 where we have collected both high resolution density and emergence data on the WAIS Divide WDC06A core using MADGE and the OIS.

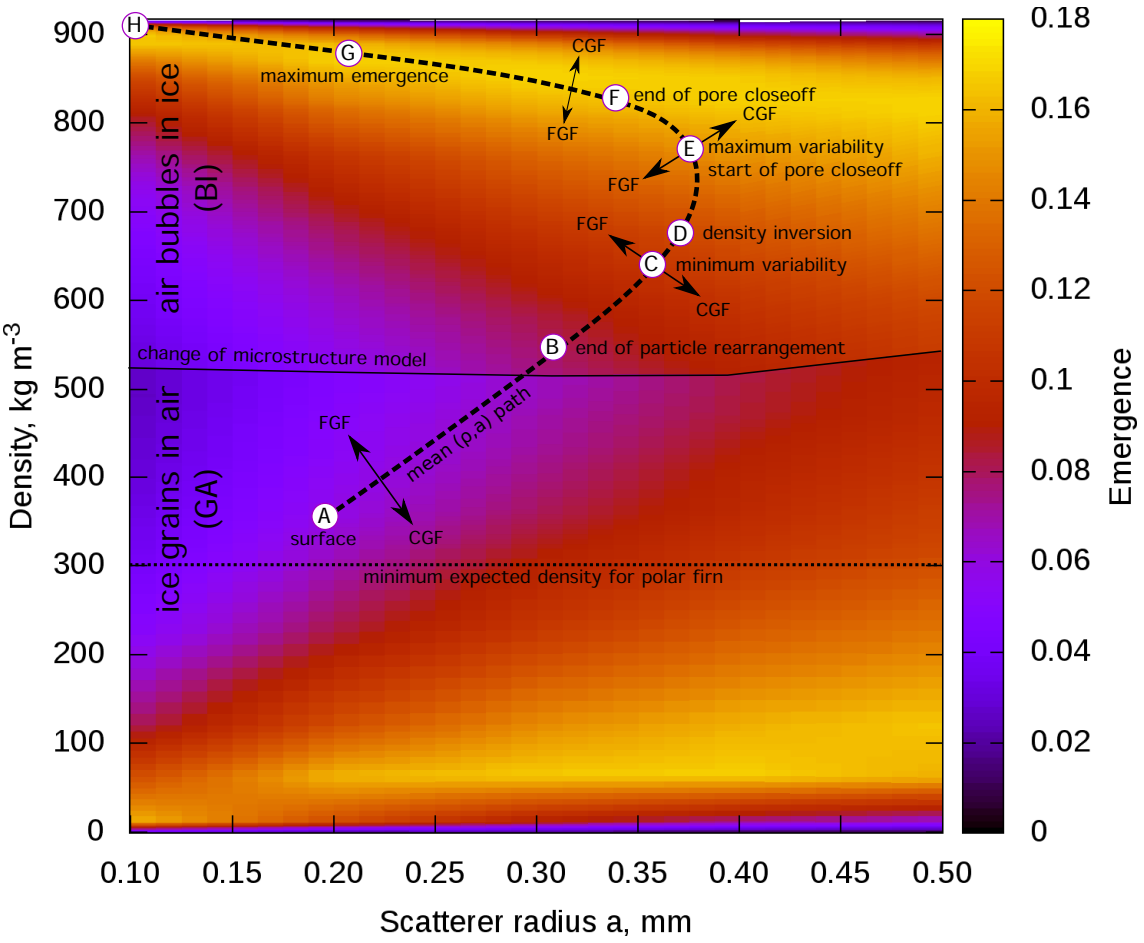

Figure 3.16. Plot of emergence in (ρ, a) space. A conjectured mean (ρ, a) path for polar firn undergoing density inversion is superimposed on the emergence plot. Contours of constant E are roughly "$>$" shaped and centered around 500 kg m^{-3}. The double-ended arrows indicate the expected E effects for firn microstructure variations about the mean (ρ, a) path: FGF always lives on the small a side of the path, CGF always lives on the large a side. Double-ended arrows are parallel to constant E contours at point C, the E-variability minimum, and perpendicular to E contours at point E, the E-variability maximum.

3.3.8 Conclusions from the Radiative Transfer Model

The radiative transfer model presented in this section provides us with clear albedo, transmittance and emergence predictions for mean (ρ, a) paths in polar firn and ice. The model also yields expected correlation patterns with density and depth for both density-inversion and non-density-inversion cases.

We have two cases where complete datasets exist to test these predictions:

1. Hawley and Morris (2006) gives low resolution, in-situ density, albedo and density-albedo correlation data for a 30 m borehole. The optical and density data from this work strongly suggest that a density inversion did occur at their site, while the firn chemistry and density data suggest that density inversion did *not* occur.

2. The data presented in Chapter 4 which provides high resolution (3.3 mm) density data collected on the WDC06A core using MADGE and the optical emergence data collected via image analysis on core photographs (1.0 mm) recorded by the OIS on the same core. The density profile stretches from the surface to 160 m and therefore provides the deepest, highest resolution comparison between density and firn/ice optical properties to date.

The results of the radiative transfer modeling have enabled us to form a self consistent theory of firn/ice optics, and now we must rely on the experimental results of Chapter 4 to show us if this theory is correct from the surface to the firn-ice transition and beyond.

The most significant shortcoming of the radiative transfer model is the unknown variation of the asymmetry parameter g through the porespace closeoff and into the bubbly ice regime. This could have significant effects on all of the optical outputs, especially the existence and location in (ρ, a) space of the emergence maximum for bubbly ice. The few experimental data that we do have (Mullen and Warren,

1988; Warren, 1982) suggest that the constant g approach used here and by Fudge and Smith (2010) should be verified using an alternative method. The next section details the use of geometric optics simulations to provide verification of the radiative transfer model results.

3.4 Geometric Optics Solutions of the Photon Transport Equation

In snow photochemistry studies, recent progress has been made in estimating and measuring SSA_m using infrared albedo measurements both in snow pits (Painter and others, 2007) and inside boreholes (Arnaud and others, 2011). To more fully understand the effect of grain *shape* on the measured albedo, Picard and others (2009) developed SNOWRAT, a geometric optics (GO) modeling code for snow composed of grains of various sizes and shapes, including spheres, cylinders, cubes, rectangular prisms and so on. The study concluded that, in a worst case scenario, the albedo could vary as much as $\pm 20\%$ based on differences in grain shape alone.

The geometric optics approach has the significant advantage that no average quantities (asymmetry parameters, scattering lengths, etc.) or assumed phase functions are used in the model at all. Photon packets are propagated through the sample by ray tracing, with photon-ice grain interactions determined from an explicitly described geometry of ice grains in air. Scattering directions are determined using the two basic tools of geometric optics: reflection and refraction calculated via Fresnel's equations and Snell's law (Fowles, 1989; Kaempfer and others, 2007; Picard and others, 2009). Use of the geometric optics approximation requires that the size of the scattering particles a is much larger than the wavelength λ of illumination used, which is certainly true for ice grains and air bubbles (~ 0.1 mm minimum) illuminated in the optical (~ 600 nm) and infrared (~ 1300 nm) wavelengths.

The SNOWRAT code was originally designed to model snow and shallow firn so that snow pit or borehole wall albedos could be predicted in the infrared (λ =1300 nm) where both scattering and absorption are significant. The SNOWRAT code base is substantial but modifying this code to correctly handle spherical bubbles in ice (BI) involved only five changes:

1. SNOWRAT creates "objects" of various sizes and shapes within a designated problem geometry. In normal operation, these objects would be ice, and the remaining space in the problem geometry is specified as air. To implement the BI scenario, we exchanged the indices of refraction for the objects and problem geometry space, so that the objects were now composed of air, and the remaining space composed of ice. This change was made in the `raytracer.cxx` module.

2. The geometric optics code originally calculated absorption when photon packets traveled *inside* objects (ice grains). The BI scenario required that we calculate absorption only when photon packets travel outside of objects (air bubbles). This change was made in the `raytracer.cxx` module.

3. SNOWRAT was originally designed for very high SSA models, and therefore ignored photons which passed through the sample without scattering. Of course, for high density ice, there may be significant sample regions with no bubbles at all. SNOWRAT originally discarded these photon packets as "mistakes". The code was altered for high density BI work by properly collecting these unscattered packets and counting them (after applying the appropriate amount of absorption) in the transmittance tally. This change was made in the `raytracer.cxx` module.

4. The number of ice grains to place in the sample geometry for a given density and grain radius a is *not* the same number of air bubbles for the same density and bubble radius a. The equation to calculate the number of bubbles $N_{\text{bub}} = \frac{V_{\text{sample}}}{(4/3)\pi a^3}\left(1 - \frac{\rho}{\rho_{\text{ice}}}\right)$ was implemented in the `randomspheres.cxx` module.

5. SNOWRAT uses stereological techniques (Underwood, 1970) to determine the final density and SSA_m of the sample geometry. The code draws 1000 virtual lines through the sample geometry and, in the original calculation, determines SSA_m as $\langle 2I/L \rangle_{\text{lines}}/\rho$ where I is the number of ice/air intersections and L is the total length of line falling *inside* ice grains. This was changed so that L was the total length of line falling *outside* the air bubbles.

   The density was originally calculated as $\rho_{\text{ice}}\langle L/L_{\text{total}} \rangle_{\text{lines}}$ where L_{total} is the overall length of line within the sample geometry. Again, the code was changed such that L was the total length of line falling *outside* the air bubbles.

   Both of these changes were made in the `world.cxx` module.

We chose to use only spherical shapes so that the assumptions involved in calculating SSA_v and grain size would be consistent between the radiative transfer (RT) and GO model runs. Additionally, we used a random placement of spheres which allowed the spheres to overlap. This feature provides a more realistic simulation of true firn and ice structure which often has extensive bonding between grains and bubbles, especially near the firn-ice transition. All of the models were run at $\lambda = 600$ nm using realistic grain/bubble sizes and firn/ice densities.

The sample geometry was a $4{\times}4{\times}4$ cm^3 firn/ice cube, with a light source incident on the center ($y = 2$ cm, $z = 2$ cm) of the $x = 0$ face of the cube. Because the resulting propagation depends entirely on the microstructural sample geometry, the input beam cannot intercept the sample at a single point, otherwise all subsequent photon packets would follow the same path, defeating the purpose of the simulation.

Therefore the launching point of the photon packets is distributed over a square aperture of side length 2 cm so that the packets have an opportunity to sample many different regions of the geometry. Each simulation used 20×10^3 photon packets.

3.4.1 Results of Geometric Optics Modeling

In shape and general magnitude, the GO results are similar to those obtained with RT methods (see Fig. 3.8). At $\mathrm{SSA}_v = 5000$ m^{-1}, albedos agree within 8% ($A_{\mathrm{GO}} > A_{\mathrm{RT}}$), transmittances differ by 1% ($T_{\mathrm{RT}} > T_{\mathrm{GO}}$), and the emergences differ by 2.5% ($E_{\mathrm{RT}} > E_{\mathrm{GO}}$). The emergence maxima are within 200 m^{-1} of each other and agree within 2%. Specific comparision plots for T, A and E vs. SSA_v for each modeling method are shown in following subsections.

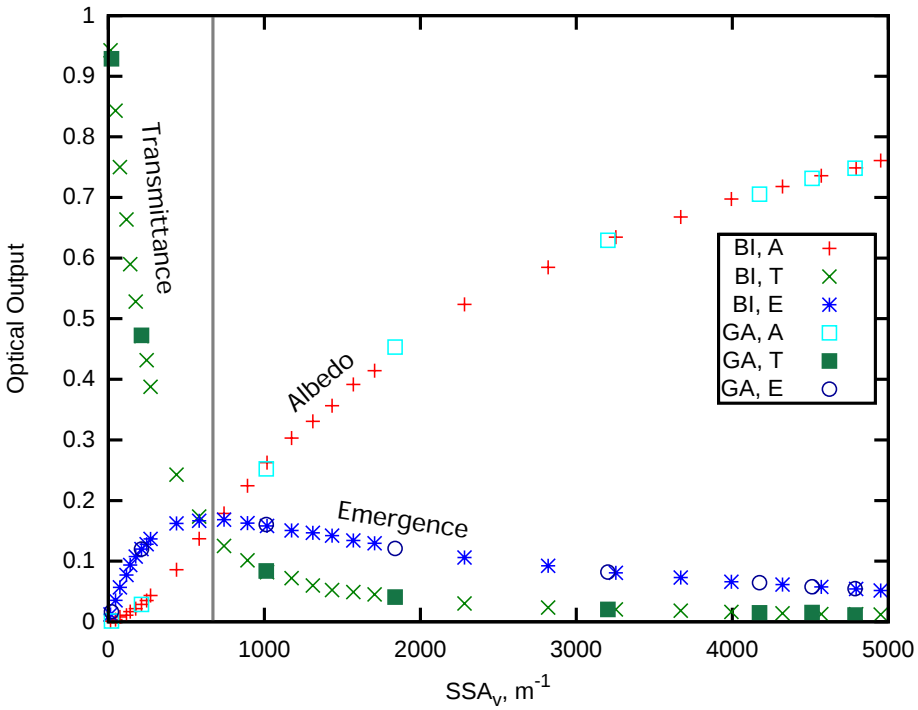

Figure 3.17. Overall geometric optics model output. Simulated at $\lambda = 600$ nm and $a = 0.2$ mm. The grey line at 670 m^{-1} indicates the emergence maximum for this geometry and a value.

All of the essential features of the RT model are reproduced in the GO model ($SSA_v \to 0$ (solid air or solid ice) $T = 1$, $A = 0$ and $E = 0$, while $SSA_v \to \infty$ tends towards $T = 0$, $A = 1$ and $E = 0$), but the differences deserve some discussion. The photon sources were quite different: a perfectly collimated beam for the RT model, versus a 2 cm $\times$ 2 cm square beam used for the GO model. Also, the methods for calculating absorption were different between GO and RT models, but also between the GA and BI scenarios within the RT model (see Eqs. 3.8 and 3.9). Considering these differences and the assumption of a constant asymmetry parameter $g = 0.89$ in the RT model, we do not expect exact agreement.

The overall magnitude of the optical output and trends with SSA_v are consistent between the two different models. The model differences do not require us to change any of our predictions regarding optical outputs or expected density-optical correlation patterns.

3.4.1.1 Analysis for Transmittance

The overall shape and analysis for the GO transmittance results are the same as for the RT model (see Figures 3.18 and 3.19): for a given grain/bubble size, transmittance increases with density as the sample becomes more and more transparent. Here and in subsequent plots, we extended the region of overlap between the GA and BI scenarios since this was more straightforward to do with GO methods.

3.4.1.2 Analysis for Albedo

Albedo as determined by GO follows the RT results nicely as shown in Figures 3.20 and 3.21. The predictions for the mean (ρ, a) path and firn type variability about that path are the same.

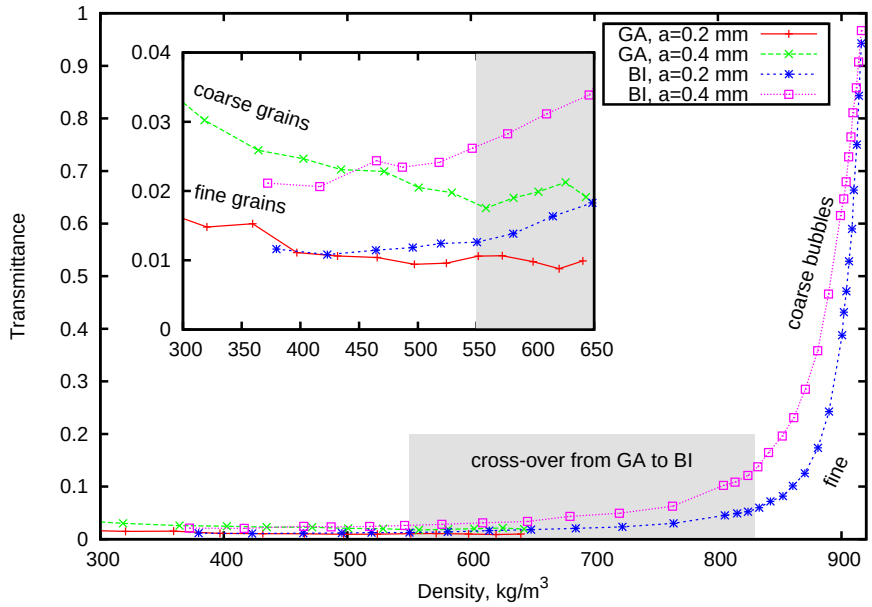

Figure 3.18. Geometric optics result for transmittance. Plotted as a function of firn/ice density and grain/bubble radius a. The inset plot in the upper right shows a close up view of the decreasing T for fine and coarse grains in the GA scenario.

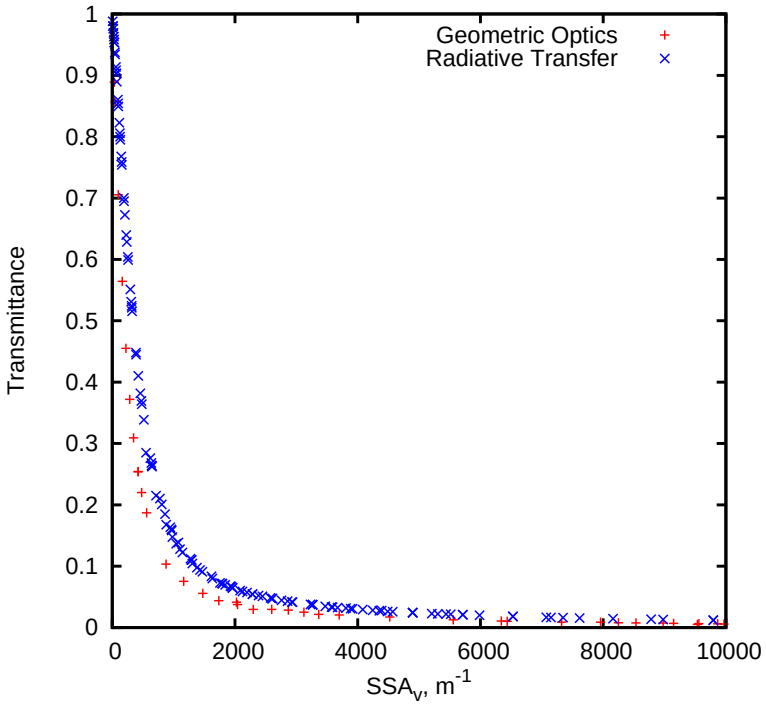

Figure 3.19. Comparison of transmittance for GO and RT models.

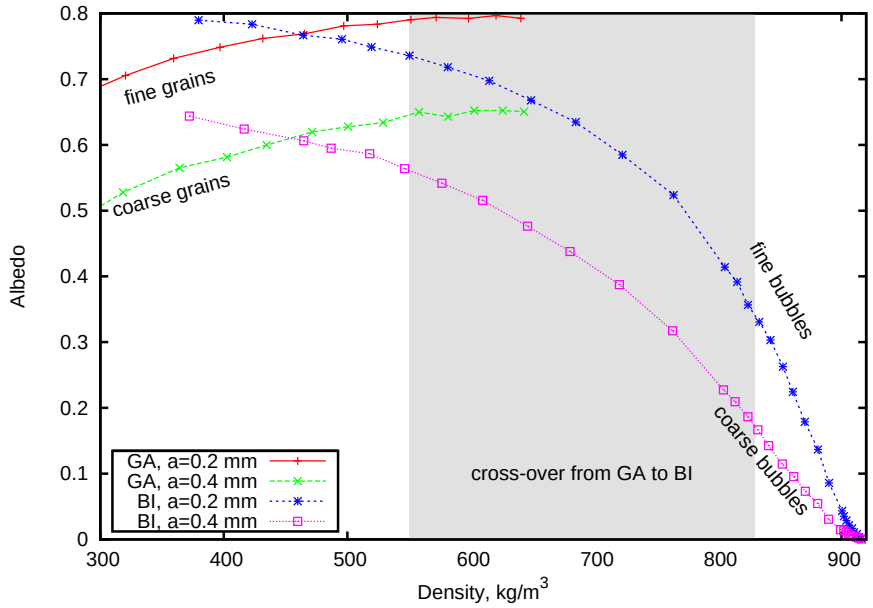

Figure 3.20. Geometric optics result for albedo as a function of firn/ice density and grain/bubble radius a.

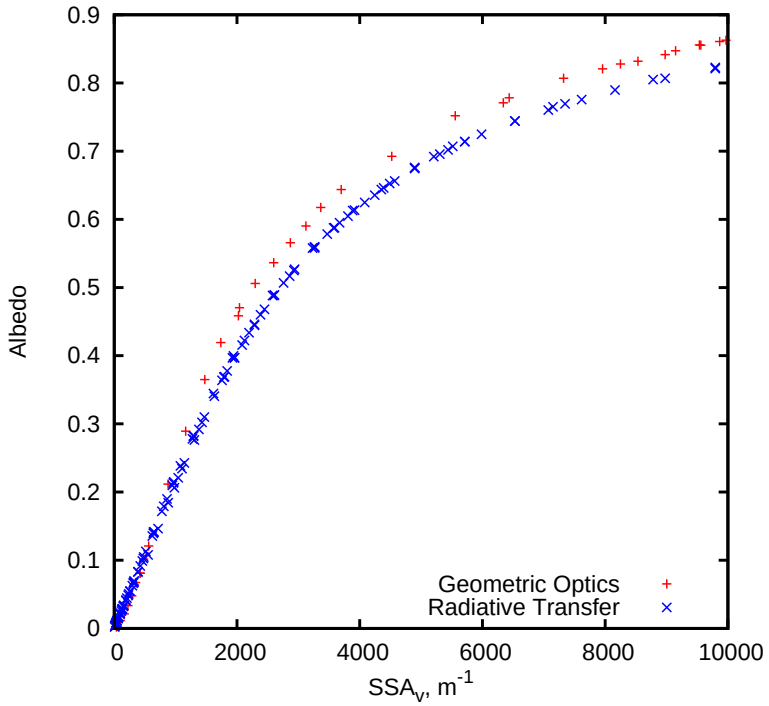

Figure 3.21. Comparison of albedo for GO and RT models.

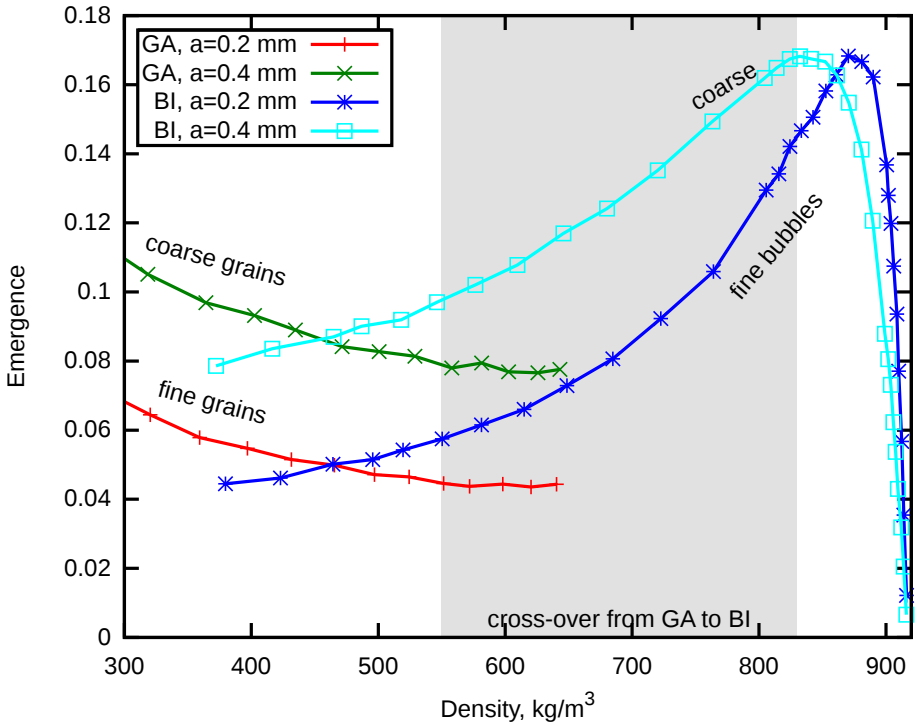

Figure 3.22. Geometric optics result for emergence as a function of firn/ice density and grain/bubble radius a.

3.4.1.3 Analysis for Emergence

Emergence results for the GO model are shown in Fig. 3.22 and are compared with RT results in Fig. 3.23. The emergence maxima determined by the GO model are slightly closer towards solid ice than the RT model, 880 versus 840 kg m^{-3}. The emergence for the RT model is generally higher than that of the GO model, but otherwise the results are comparable and predictions are the same for both models.

3.4.2 Conclusions from Geometric Optics Modeling

The geometric optics approach is an even more literal interpretation of the photon transport equation than the Monte Carlo RT approach. Explicitly modeling the firn and ice microstructure is computationally intensive, but provides us with high confidence that our model is making correct predictions regarding the optical prop-

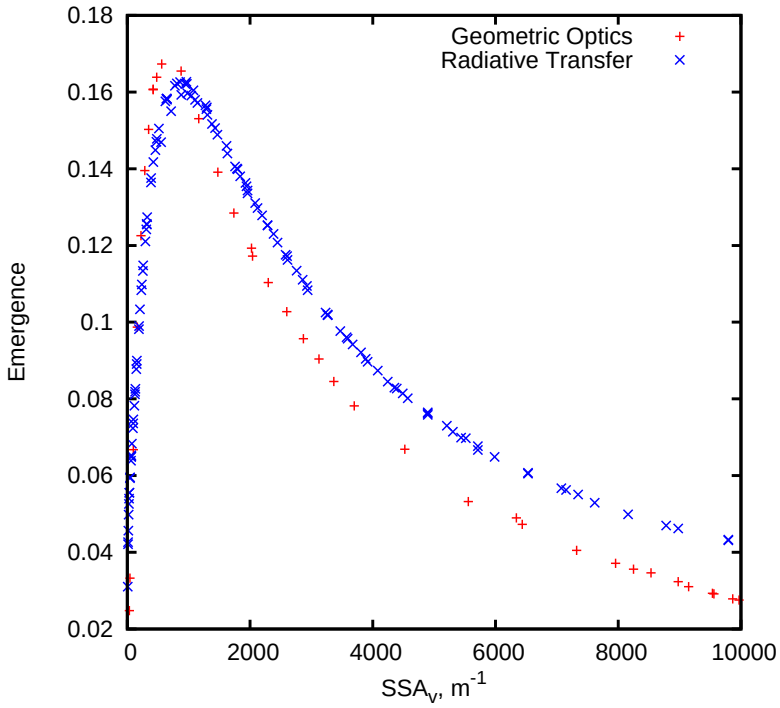

Figure 3.23. Comparison of emergence for GO and RT models.

erties of real samples. The agreement of this model with both the RT model and the transmittance and albedo data of Kinnard and others (2008) and Hawley and Morris (2006) is encouraging, especially in light of the differences between models and experimental setups.

As with the RT results, we have two datasets available to test the veracity of the GO models: Hawley and Morris (2006) and the data presented in the next chapter.

3.5 Conclusion

The theoretical and model results presented in this chapter make clear predictions regarding the relationship between firn microstructure and optical properties for each of the three fundamental measurement geometries. The predictions can be divided into two categories: predictions for the optical characteristics of the mean

(ρ, a) path of firn evolution, and predictions for variations in microstructure *about* the mean path.

In this chapter, we have compared transmission and albedo measurements with the model predictions with favorable results. In the next chapter, we compare emergence data collected from the WAIS Divide core WDC06A with a high resolution density profile of the same core to test the model predictions. If the emergence model predictions are correct, then we can test the Hypothesis of microstructure-dependent densification by separating the density profile based on microstructural type.

3.6 Suggested Improvements for Optical Scattering Measurements

The transmission- and albedo-based optical instruments described in Sections 3.2.2 and 3.2.3 take existing photographic equipment and use it for the extraction of high resolution firn/ice physical properties data. The OIS is designed for high resolution emergence photography of cores for archival purposes, and makes no attempt to derive physical properties data from the images. These systems share share two fundamental problems.

- **Illumination:** The goal of photography is to image a large section of core or borehole wall using uniform illumination. Conversely, the goal of extracting physical properties at high resolution requires a very small viewing area and a well collimated illumination source. Broadly (both spatially and wavelength-wise) illuminated samples make it difficult to avoid scattering effects from adjacent firn/ice sections, and make it impossible to separate the subtle changes in absorption from physical changes in the firn/ice.

- **Location in (ρ, a) space:** An optical measurement at a single wavelength provides a measurement of SSA_v (see Fig. 3.17 for example) which is a func-

tion of both ρ and a. SSA_v is not necessarily unique to a given firn or ice type, prompting many researchers to associate an optical measurement with an SSA_m (SSA_v normalized by ρ) value (Domine and others, 2007; Painter and others, 2007; Picard and others, 2009; Taillandier and others, 2007). This is valid only in the GA scenario since SSA_m is a function only of a there. Deeper in the core, we must consider the BI scenario in which SSA_m becomes a function of both ρ and a. In short, if we desire an instrument that can determine a from the surface down to solid ice, then we must acquire both optical *and* density data at the same time.

Noting these issues, we propose a firn/ice microstructure instrument that simultaneously collects high resolution density and optical data on the same core. High resolution density is generally only available from scanning γ- or X-ray density transmission instruments (see Chapter 2), and so we propose that these instruments be augmented with an optical scattering experiment.

The light source should be small and well collimated, preferably with multiple illumination positions and/or wavelengths so that multiple measurements of SSA_v can be made on the same section of core. The photodetectors should be small, collimated and easily *calibrated*. Specifically, we recommend the measurement of both emergence and transmission since our models show that the ratio E/T scales nearly linearly with SSA_v and avoids the mechanical problems associated with both injecting light into the side of the core, and simultaneously measuring the albedo at the same location.

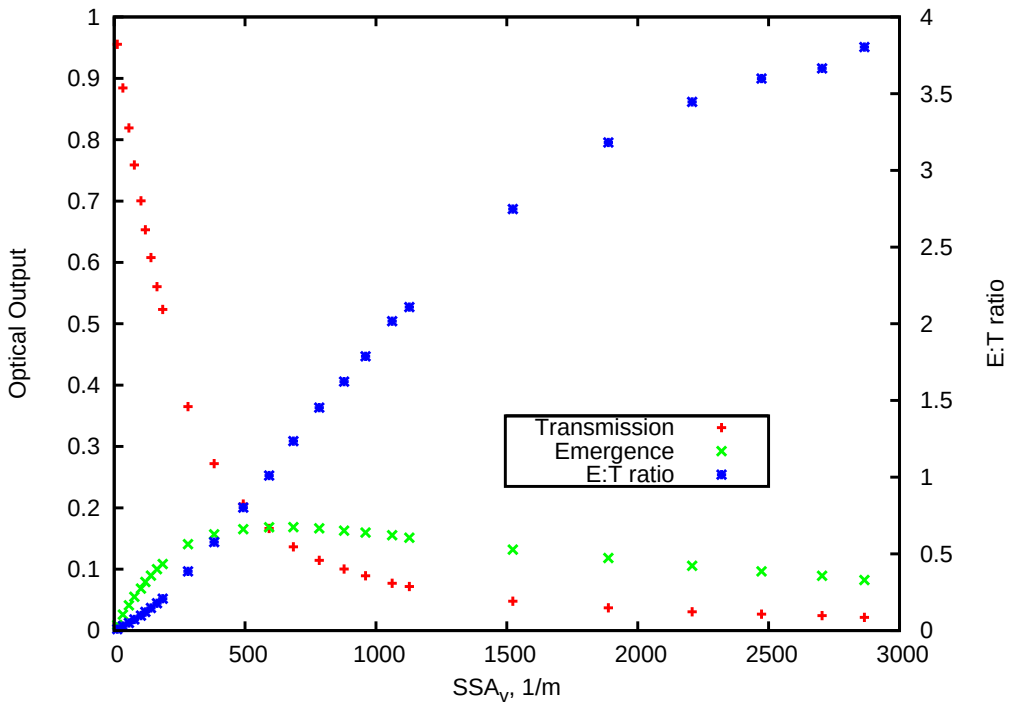

Figure 3.24. Emergence, transmittance and $E{:}T$ ratio for bubbly ice at $a = 0.3$ mm.

CHAPTER 4
ANALYSIS OF MICROSTRUCTURE-DEPENDENT DENSIFICATION IN THE WAIS DIVIDE WDC06A CORE

"One day I touched it with my hands,

And it scattered like scared birds."

– The Gourds, "Plaid Coat"

4.1 Introduction

In this chapter, we use experimental data collected from the West Antarctic Ice Sheet (WAIS) Divide WDC06A ice core to first verify that the models developed in Chapter 3 are correct and then test the Hypothesis of Chapter 1 by analyzing for microstructure-dependent densification (MDD). This core is expected (based on annual temperature and accumulation rate) to exhibit density inversion (a phenomenon discussed in Chapter 1), a direct result of MDD.

The models developed in Chapter 3 predict the expected optical scattering behavior as a function of density and grain/bubble size in firn/ice, and we use density and optical scattering profiles from the WDC06A core to verify these predictions. Should the model predictions prove correct, we can then use MADGE density and OIS emergence data to generate a firn/ice microstructure profile for the WDC06A core. The microstructure profile will allow us to separate the overall density dataset by microstructure type and therefore analyze the core for signs of MDD.

We begin by outlining firn densification models, including a brief analysis of the potential for density inversion at the WAIS Divide site. The next section presents the WDC06A density profile data collected by MADGE and discusses density variability as related to density inversion. Details of the image processing methods and results

for the emergence measurement are given in the next section. Following this, a comparison is made of the density and emergence data, discussed in the context of the model predictions of Chapter 3. The comparision demonstrates that the model correctly captures all of the observed scattering phenomenon in the real core. Finally, we separate the density data according to microstructural type and explictly show MDD and density inversion in the WDC06A core.

4.2 Models of Firn Densification

4.2.1 Early Models

One of the earliest theories regarding firn and ice densification was proposed by Ernest Sorge in 1931 and more fully developed in the language of calculus by Bader (1954). Sorge's law of firn densification states that under conditions of constant temperature and accumulation rate, the depth-density profile $\rho(z)$ (using the snow surface as the reference point) is invariant in time. This law does not allow the derivation of a theoretical function for $\rho(z)$, but given a profile, it can yield useful relationships between density, densification rate and accumulation rate. Bader (1954), in reference to the differences in density between summer and winter snow, states

> "Summer and winter snow accumulation will furthermore have to be treated separately because they go through different paths in their early stages of metamorphism. The new depth-density curve will then consist of alternating segments of two slowly converging curves, one for summer and one for winter snow. These curves should no longer be of empirical form, but must be formulated in terms of pertinent facts of snow mechanics."

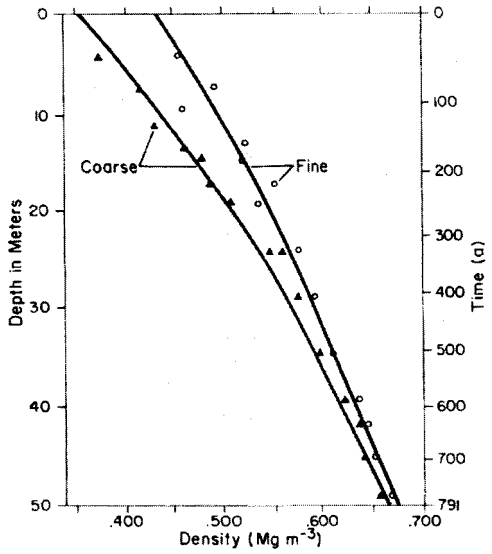

Figure 4.1. Differences in densification rate observed by Alley and others (1982) at Dome C, Antarctica.

Nearly 60 years later, we are still searching for a complete, non-empirical explanation of firn compaction.

The next step in modeling firn compaction was made by Schytt (1958) who assumed that the porosity $S(z) = \frac{\rho_{\text{ice}} - \rho(z)}{\rho_{\text{ice}}}$ of the firn was directly determined by the load $\sigma_z = \int_0^z \rho(h)dh$ of firn above a depth z. This results in a differential equation whose solution is a simple "build-up" curve with two parameters: the density at the surface $\rho_{\text{surf}} = \rho(z = 0)$ and characteristic compaction length z_ρ.

$$\rho(z) = \rho_{\text{ice}} - (\rho_{\text{ice}} - \rho_{\text{surf}}) \exp(-z/z_\rho) \tag{4.1}$$

This equation allows empirical fits to a wide variety of polar density profiles. In general, colder and lower accumulation sites will have larger values of z_ρ compared to lower elevation, warmer or more coastal sites (Cuffey and Paterson, 2010).

4.2.2 Differential Firn Compaction at Dome C, Antarctica

Alley and others (1982) used Eq. 4.1 in their study of coarse and fine grained firn types at Dome C, Antarctica. The core used in this study was 50 m deep and, as

Firn Type	ρ_{surf}	z_ρ
Fine grained	431 kg m^{-3}	75.2 m
Mean Dome C	358 kg m^{-3}	60.6 m
Coarse grained	349 kg m^{-3}	61.4 m

Table 4.1. Numerical parameter values in Eq. 4.1 for firn at Dome C, Antarctica. From Alley and others (1982).

can be seen in Fig. 4.1, no density inversion is observed within this depth interval. However, we should note that Dome C is very high (3240 m elevation), very cold (mean average temperature -54° C) and has a very low accumulation rate (3.7 cm a^{-1} water equivalent), so we expect all compaction processes to be very slow. The values used for depth-density curves in Fig. 4.1 are shown in Table 4.1.

The data collected by Alley at Dome C demonstrates that coarse grained firn (CGF) has a lower starting density ρ_{surf} and compacts more rapidly than fine grained firn (FGF) of similar density. We can also see that the firn component with the most rapid compaction tends to dominate the mean compaction. This is not surprising if we consider a system of two springs (firn types) of different spring constants arranged in series. Under a given load, the softer spring (CGF) deforms more than the harder spring (FGF), and therefore the overall system deformation should be dominated by the softer spring (Frolov and Fedyukin, 1998; Golubev and Frolov, 2000).

4.2.3 Estimates of Differential Firn Compaction for WDC06A

Following Horhold and others (2011), we can make a crude estimate of *if* and *where* a density inversion might occur in the WDC06A core. We fit Eqn. 4.1 to the density trend, and then used variations in ρ_{surf} and z_ρ comparable to those listed in Alley and others (1982) to estimate CGF and FGF behavior. The result is shown in Fig. 4.2 using the fitting values shown in Table 4.2.

Firn Type	ρ_{surf}	z_ρ
Fine grained	480 kg m^{-3}	53.0 m
Mean WDC06A	440 kg m^{-3}	41.0 m
Coarse grained	400 kg m^{-3}	41.0 m

Table 4.2. Estimated numerical parameter values in Eq. 4.1 for firn at WAIS Divide.

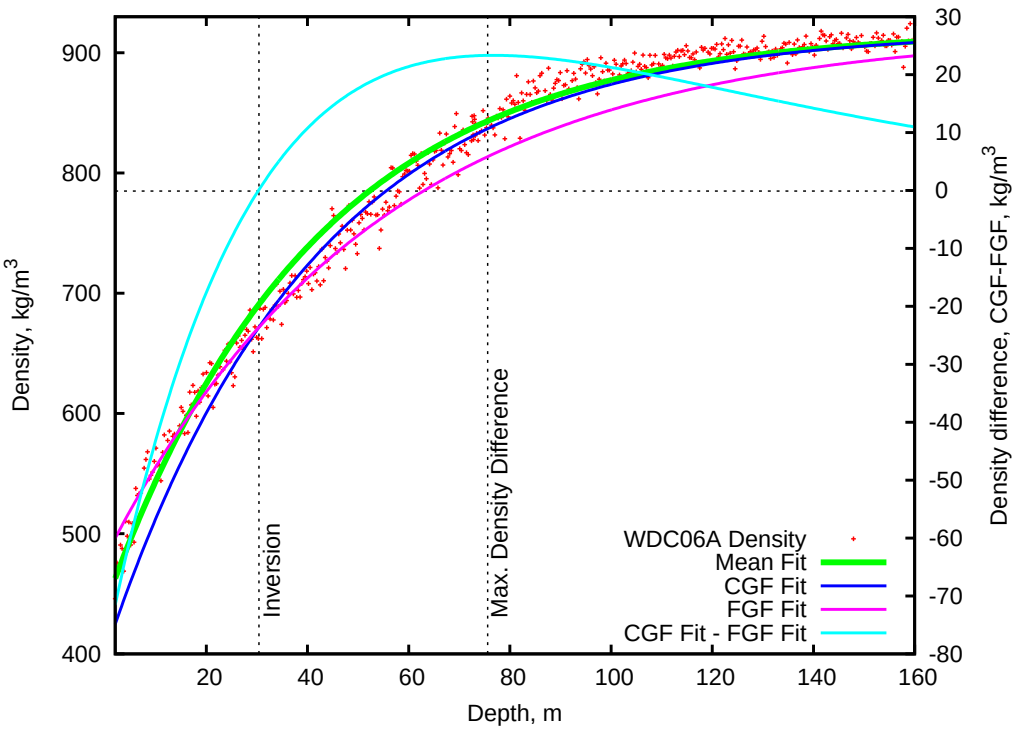

Figure 4.2. WDC06A density vs. depth and estimates for coarse and fine grained firn density profiles. WDC06A density vs. depth plotted along with the overall fit to Eqn. 4.1 and separate estimates for coarse and fine grained firn density profiles. The difference in density between CGF and FGF is plotted against the right-hand y-axis.

From these crude estimates, a density inversion seems possible around 25-30 m depth and a density near 660 kg m^{-3}. We also expect that CGF and FGF density difference will pass through a maximum around 70-75 m depth and near a density of 830 kg m^{-3}. We note that all of these fitted surface densities are higher than the $\sim$380 kg m^{-3} actually observed at the WAIS Divide site (M. Battle, 2011, pers. comm.).

4.2.4 Modern Firn Densification Models

Modern firn densification models attempt to include the effects of temperature, load or overburden, and the microstructure (grain size and geometry, coordination number, bonding strength) of the firn. Many researchers have pursued both empirical and theoretical work on this problem because it has an effect on ice core paleoclimate record interpretation (Lipenkov and others, 1997; Spencer and others, 2001) as well as remotely-sensed observations of surface elevation change (Wingham and others, 1998).

Empirical approaches (Herron and Langway, 1980; Kameda and others, 1994; Spencer and others, 2001) typically take depth-density profiles (often determined by low resolution, gravimetric methods) from many sites and adjust various fitting parameters to best match the data. The most significant problem with an empirical approach is that the best fit parameters today need not be the same 1000 or 10,000 years ago under possibly very different climatic conditions (Salamatin and others, 2009). The Herron-Langway model and actual WDC06A density are plotted in Fig. 4.3 to illustrate the differences between empirical models and high resolution density datasets. Other comparisons can be found in Freitag and others (2004) and Horhold and others (2011).

Theoretical approaches have focused on understanding firn compaction in the framework of hot-sintering of metallurgical powders described by Arzt (1982). The comparison of firn with hot metallic powders is apt since the ice grains are, relatively speaking, quite close to their melting point. The many different theoretical approaches (Golubev and Sokratov, 2004; Salamatin and others, 2009; Arnaud and others, 1998b) use idealized particles and bond geometries (Arons and Colbeck, 1998), various power-law approximations for ice creep and include Arrhenius-type formulations ($d\rho/dt \propto \exp\left(-E_{\text{act}}/RT\right)$) for the temperature dependence. The ac-

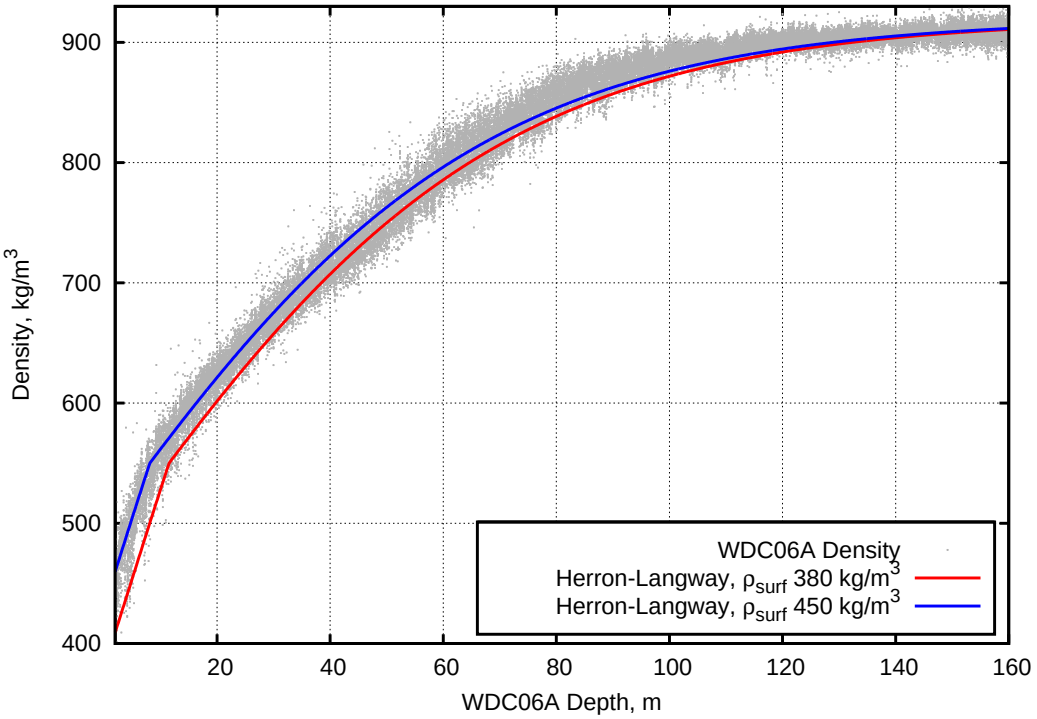

Figure 4.3. Plot of WDC06A density and empirical density-depth profiles using the Herron and Langway (1980) model. Model inputs for the WAIS Divide site: water equivalent accumulation rate of 20.2 cm a^{-1}, surface densities of 380 (observed at site) and 450 (best fit to data) kg m^{-3}.

tivation energy E_{act} in the temperature dependence is generally set around 45.6 kJ mol^{-1} (Gow, 1969; Herron and Langway, 1980; Alley and others, 1982; Alley and Woods, 1996; Spencer and others, 2001; Cuffey and Paterson, 2010; Spaulding and others, 2010), though this value may vary for different firn microstructural types (Salamatin and others, 2009).

The existing models do not include the concept underlying density inversion: multiple firn types with differential densification rates *within the same firn column.* Salamatin and coworkers (Salamatin and Lipenkov, 2008; Salamatin and others, 2009) come the closest, but instead of designating multiple *firn* types, they instead designate multiple *coring site* types to include specific firn microstructural effects on compaction. In comparing their model results to density-depth profiles of actual ice

cores, they separate the coring sites into "L" and "H" groups, roughly corresponding to low temperature, low accumulation sites with low densification rates and high temperature, high accumulation sites with higher densification rates respectively.

4.3 Density Analysis of the WAIS Divide WDC06A Core

At the National Ice Core Laboratory in Denver, Colorado, the WDC06A core was carefully sawed into many different pieces for various types of physical and chemical analyses. The samples provided to the University of Maine were 3×3× ∼100 cm "sticks" of firn and ice from the surface down to 577 m depth, and were intended for melting to obtain high resolution dust size distribution, dust chemistry and electrical conductivity measurements.

Prior to melting, the upper 160 m of this core were density scanned using MADGE, the γ-ray density gauge described in Chapter 2. MADGE was set up inside a small (2 m × 4 m) sample storage freezer set at -20° C. A clean "tent" was set up over the MADGE workbench, using High Efficiency Particulate Air (HEPA) filtered air to maintain positive pressure within the tent. The tent was installed to minimize particulate contamination of the core during the density measurement and core handling. In addition, the core trays used to support the core during density measurement were constructed from high-density polyethylene plastic to minimize chemical contamination of the cores.

Most of the density scans ran for about an hour, yielding a typical 1-σ density uncertainty of ± 4 kg m^{-3}. The record was collected at 3.3 mm resolution (the diameter of the detector collimator hole) and was therefore continuous with the exception of one meter from 72 to 73 m depth which was accidentally deleted.

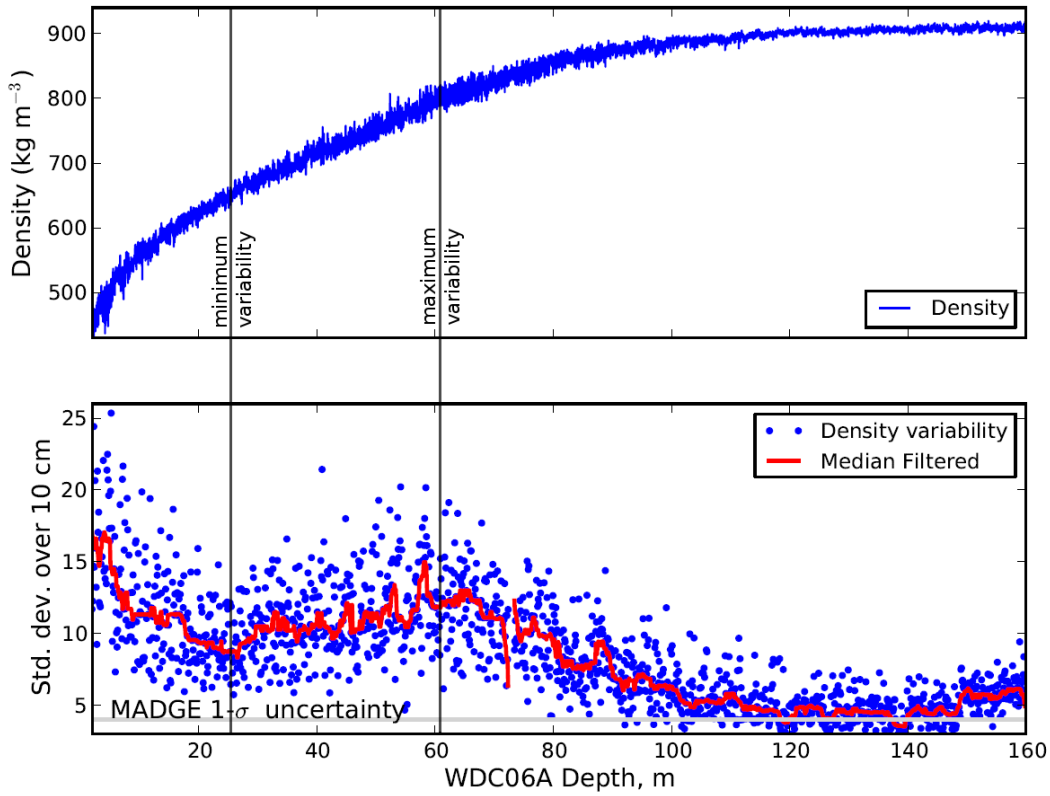

Figure 4.4. WDC06A density and density variability. Top: WDC06A density versus depth. Bottom: one standard deviation of density calculated over 10 cm intervals. Variability minimum near 25 m and maximum near 60 m are likely due to density inversion. The second apparent minimum near 150 m is due to increased MADGE profiling rate for the bottom 10 m. Gap in the median filtered data is due to lost data from 72 to 73 m.

4.3.1 Density Results

The overall density trend and density variability of the WDC06A core are comparable to other polar cores (Gerland and others, 1999; Hori and others, 1999; Horhold and others, 2011). In particular, the variability has the classic minimum at $\sim$ 25 m which some authors see as evidence for a density inversion (Freitag and others, 2004; Horhold and others, 2011). The variability maximum near 60 m is also related to density inversion - this is expected to be the point of maximum density difference between CGF and FGF. We note here that this depth is about 15 m shallower than the maximum density difference estimated by the crude model of Sec. 4.2.3 above.

Fig. 4.4 shows WDC06A density and variability (quantified as one standard deviation of density calculated over a 10 cm depth interval) as a function of depth. The density and variability pass through two minima. The first, near 25 m depth, is due to the density inversion effects discussed above. The second is due to a change in MADGE profiling speed for the last 10 m of core, and is not due to any change in core structure. The majority of the core was set to collect 3×10^5 counts for each exposure, but the bottom 10 m were profiled using half this amount to avoid delaying melting operations. Therefore, the uncertainty in the density measurement for this bottom section is larger, ± 6 instead of ± 4 kg m^{-3} for the upper 150 m. Regardless, below 120 m the natural density variability is of comparable magnitude to MADGE uncertainty and therefore the reported variability in this region simply reflects the limitations of the instrument, not variability in core structure.

4.4 Image Analysis of the West Antarctic Divide WDC06A Core

Images of the upper 577 m of the WDC06A core were recorded in 2009 at the National Ice Core Laboratory in Boulder, Colorado using the Optical Imaging System (OIS) discussed in Chapter 3. The imaged core sections were split, planed flat and polished for good image quality. The rounded outer surface of the core was left in its as-drilled state, possibly having an effect on the emergence data. We downloaded and used the 1 pixel / 1 mm resolution dataset instead of the 1 pixel / 0.1 mm resolution since 1 mm more closely matches the MADGE resolution of 3.3 mm. McGwire and others (2008a) also provided IceImageJ, a customized version of the ImageJ program (Rasband, 1997) which allows image processing with an absolute core depth referencing system.

Extracting emergence from the core images is straightforward and was done manually for all 160 m corresponding to the MADGE density record. A $\sim$1 m long

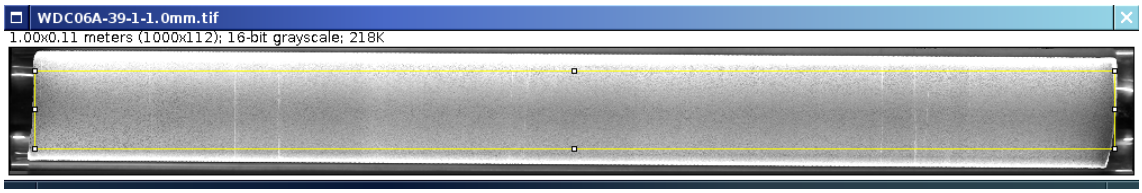

Figure 4.5. Example of core image processing. We used IceImageJ to determine emergence as a function of depth. The yellow box indicates an example analysis region, chosen to avoid the very bright core edges. Note the darkening effect of core ends on image intensity.

core image file is loaded into IceImageJ. We then select a region of interest (ROI) covering the center third of the core for analysis, since the image intensity there was most representative of the core structure and avoided the large cross-core brightness variation due to the dual side-lighting system used by the OIS (see Fig. 4.5). Image intensity (reported in digital values from 0 to $2^{16} - 1$) is averaged in the cross-core direction across the ROI, and this average is reported every pixel (1 mm in our case) along the core axis. The cross core averaging eliminates the effects of any particular grain or bubble in the analysis path.

4.4.1 Image Quality

Core ends, due to their strongly absorbing boundary conditions, caused significant darkening of the image for ∼5 cm near the edges. The core end emergence data are masked to the best of our ability, but core end artifacts remain throughout the record as repeated zones of low emergence with a 1 m periodicity. Therefore, it is important to note that roughly 10% of each core image is unusable due to core end effects. Despite the issues with core end intensity, direct comparison of the emergence and density data as a function of depth was possible because of the absolute core depths reported by the IceImageJ for each image pixel. We estimate that the worst-case uncertainty in co-registration of OIS and MADGE core depths is ±5 mm since an unlucky MADGE exposure could place the start of the core section ∼3 mm

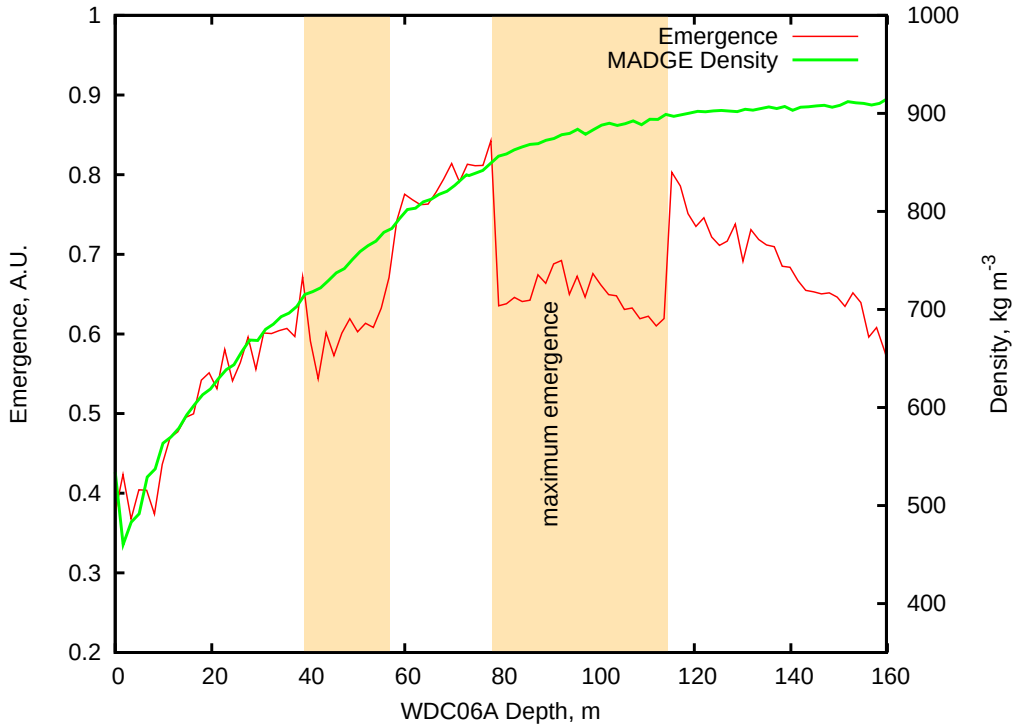

Figure 4.6. Raw emergence and density for the WDC06A core. Adjustments to camera exposure settings or illumination source are evident in the shaded regions, though the emergence maximum is preserved because it was recorded under consistent imaging conditions. Density data have been smoothed for clarity.

off of the actual start, plus two pixels of uncertainty in locating the core edge in the digital image.

Overall, the image quality is good in an archival, photographic sense. However, for the purposes of extracting physical properties, the images lack consistency in illumination. Emergence tends to decrease along each core segment in a semi-linear fashion, probably related to misalignment between the core and the fiber-optic light panel axes. More important are the large adjustments to either the camera exposure settings or illumination source made at various points in the photography (possibly different core processing days), leading to discontinuities in the emergence data shown in Fig. 4.6 that are clearly not related to any physical change in the cores. The true emergence maximum at 90 m is still evident in the raw data and we are

fortunate that this maximum occurred in the middle of a scanning day, not at the start or end of a new scanning day.

After nearly abandoning the OIS data because of these problems, we reasoned that contiguous sections of core with smoothly varying density should also have smoothly varying emergence intensity. Using the shallowest section (0–38 m) of "normal" data as our base, the raw emergence in the discontinuous sections were adjusted to produce the final emergence dataset. Note that even if this adjustment procedure is incorrect, it will not change the overall correlation pattern since the correlation coefficients are calculated over 16.5 cm windows, not the entire core. The procedure could produce a false mean (ρ, a) path emergence signal, but we think this is unlikely since the emergence maximum was preserved in the raw data.

The emergence intensities are normalized to the highest digital value of the camera system, but because of the adjustment procedure discussed above and the lack of calibration data, we should not attempt to compare absolute values of OIS emergence with the model predicted emergences from Chapter 3. The OIS data are relative emergences only, and have no specific relation to the source intensity that produced them.

4.4.2 Emergence Results

The mean (ρ, a) path emergence results are presented in Fig. 4.7 where excerpts of selected high resolution WDC06A images are shown in order of increasing depth. We can see by visual inspection that the emergence passes through a maximum somewhere between 60 and 100 m depth and that different grain sizes yield different emergences.

Emergence and its variability are plotted in graphical form in Fig. 4.8. Density and emergence both increase with depth and share a similar trend until 90 m, where emergence begins to abruptly decrease. The lower plot shows that emergence has

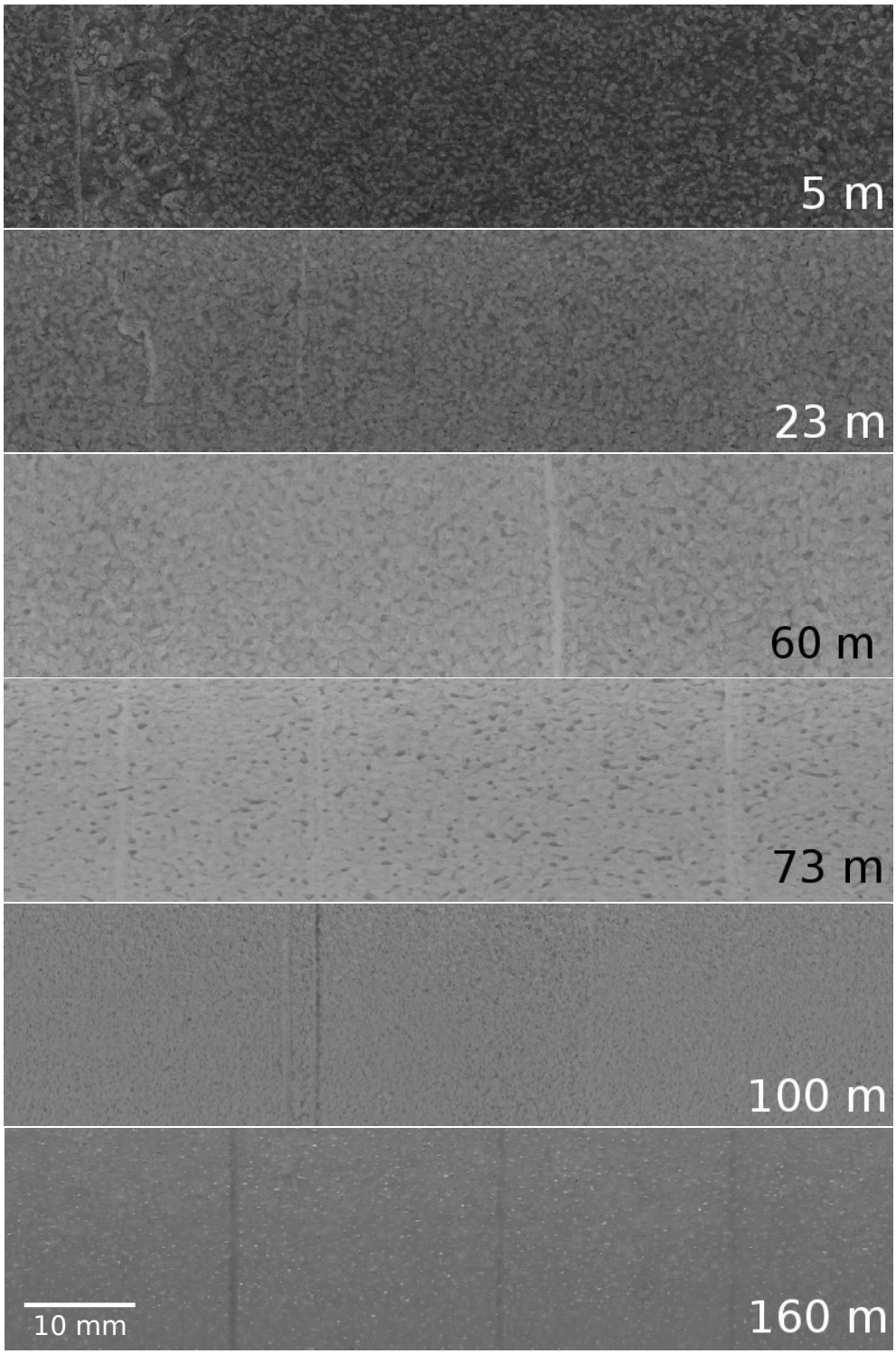

Figure 4.7. High resolution images of the WDC06A core. Selected high resolution (0.1 mm / pixel) OIS images of the WDC06A core. Images courtesy of the National Snow and Ice Data Center and McGwire (2009). Orientation for all images is: surface ← bedrock.

a similar pattern of variability as density and Fig. 3.16 shows why. The variability minimum at 25 m (point C) is due to the mean (ρ, a) path perpendicular crossing of a constant emergence contour just prior to the density inversion at point D: changes in microstructure will be along the contour, resulting in little change in emergence.

At the actual density inversion, CGF and FGF densities are approximately equal. If firn microstructural differences did not persist through the density inversion, then we would expect uniform grain sizes and very low emergence variability beyond the inversion point. The observation that emergence variability increases and reaches a maximum near point F at 62 m depth (similar to the density data in Fig. 4.4) indicates that the differences in microstructure survive and, coupled with density variations, continue to drive significant emergence variability to $\sim$120 m depth. Again, Fig. 3.16 illustrates why emergence variability is a maximum here: the mean (ρ, a) path is now parallel to a constant emergence contour and therefore microstructural changes will cause significant changes in emergence.

Comparing Fig. 4.4 and Fig. 4.8, we see that density and emergence follow a similar pattern until an emergence maximum is reached at 90 m and ρ=880 kg m^{-3}, in excellent agreement with the GO model prediction.

Fig. 4.9 plots the measured E versus ρ and shows that the GO model predictions for fine and coarse scatterers provided reasonable boundaries for the real data across the entire density range. The measured E signal is dominated by the coarse grained/bubbled material from the surface down to 750 kg m^{-3} ($\sim$50 m), after which E begins to trend towards finer grained/bubbled material. Since grain growth is well documented (Alley and Woods, 1996; Gow, 1969) to monotonically increase with depth and age, we believe that this shift in a is an indication of one or more of the following:

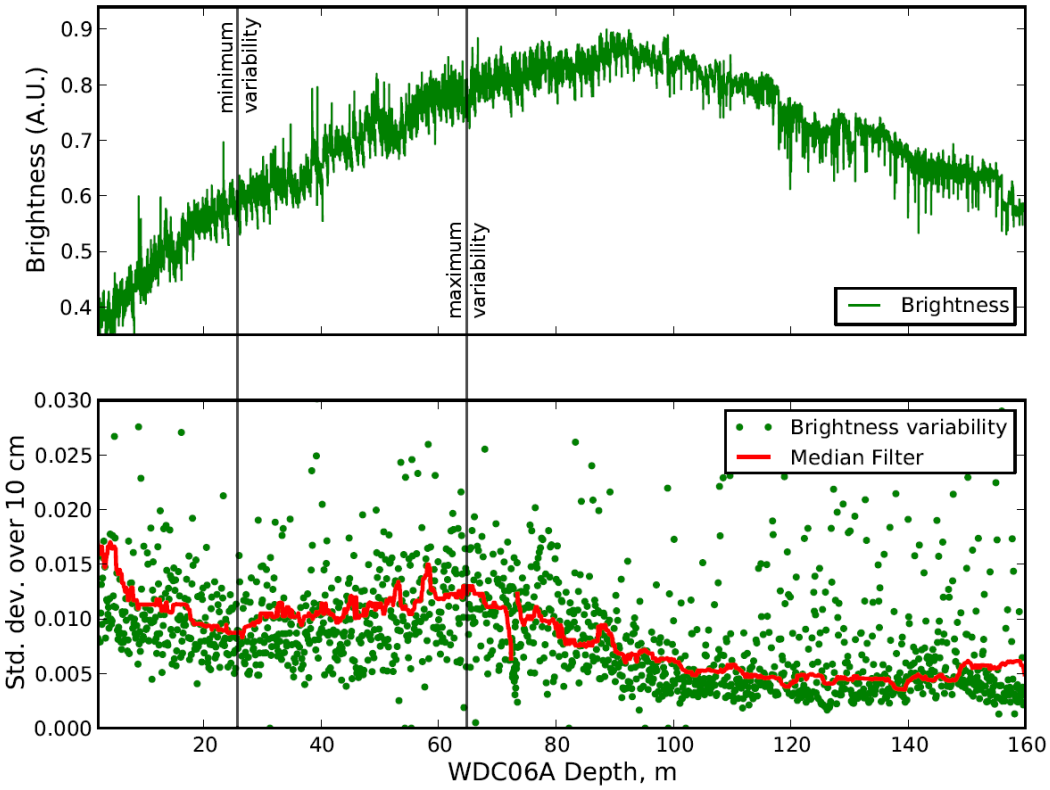

Figure 4.8. Emergence and emergence variability versus depth.

1. Reaching the maximum scatterer size between points D and E in Fig. 3.16. Beyond this point, scatterer size is thought to decrease due to compression of bubbles due to increasing overburden.

2. The initiation of pore closeoff in FGF prior to (shallower than) CGF closeoff (Schwander, 1989; Schwander and others, 1988; Severinghaus and Battle, 2006; Spencer and others, 2006; Stauffer and others, 1985). The idea here is that firn with fully formed bubbles will have a higher E than firn still consisting of a mixture of grains and bubbles. The shallower FGF closeoff is thought to happen due to the higher coordination number in FGF, leading to pore closeoff at a lower density and shallower depth than CGF.

3. The splitting of large bubbles in CGF to yield a higher bubble number density of finer bubbles as discussed in Spencer and others (2006). Bubbles in CGF have a high surface area and irregular shape and are therefore more likely to split into smaller, more regular bubbles during the pore closeoff process. Note that the air content (density) does not change in this process, only the bubble sizes.

Fujita and others (2009) argue that pore closeoff occurs first in CGF, and data supporting this position is given in Section 4.5.2. At the moment, it is not clear if optical scattering data will provide answers regarding the role played by firn microstructure in the pore closeoff process.

The results presented in this section are encouraging in terms of validating the performance of the models, but are not sufficient to show that microstructure-dependent densification (demonstrated by density inversion) occurred at WAIS Di-

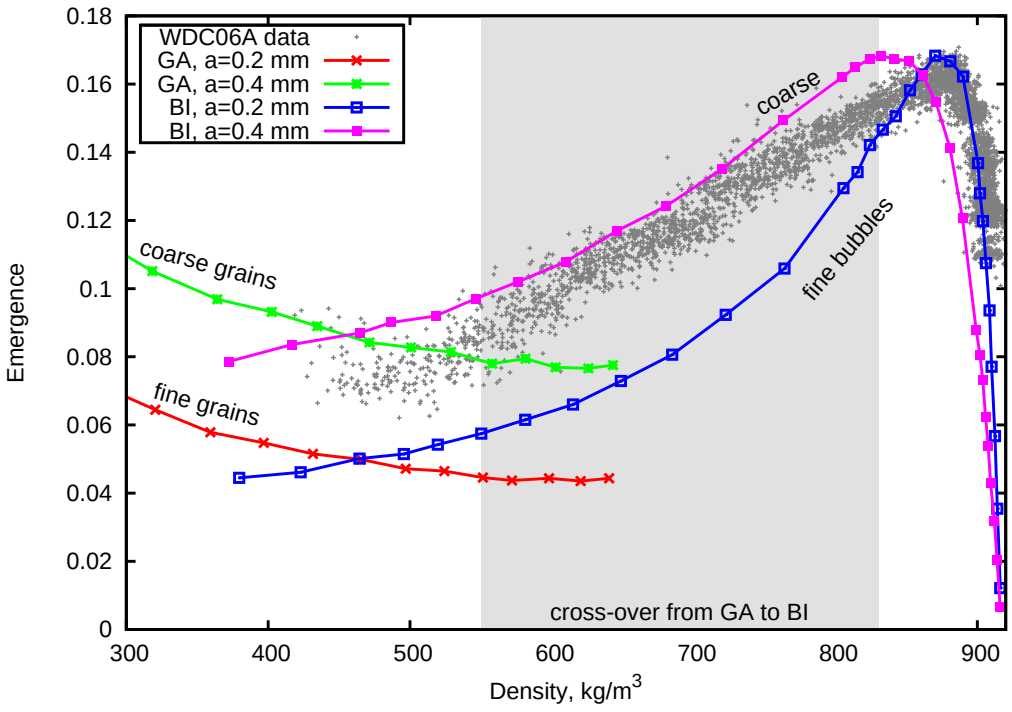

Figure 4.9. WDC06A emergence plotted with GO model results.

vide. Both density inverted and non-inverted sites would show similar mean (ρ, a) emergence pattern. The density inversion is only revealed by the correlation pattern discussed in the next section.

4.5 Density-Emergence Correlation Patterns

We report detailed results on density-emergence correlation and its relation to model predictions made in Chapter 3 and above in Section 4.2.3.

Stated briefly, the models predicted that

- Emergence for the mean (ρ, a) path should increase with depth until the emergence maximum is reached at densities between 840 (RT model) and 880 (GO model) kg m^{-3}. It should then decrease steadily toward zero for pristine, bubble-free ice.

- CGF emergence will be larger than that for FGF from the surface to the emergence maximum. The opposite will be true beyond the maximum.

- Shallower than the density inversion at approximately 30 m, we expect density and emergence to have a negative correlation. In the inversion zone, we expect no correlation. Deeper than the inversion, but shallower than the emergence maximum, we expect a positive density-emergence correlation. We expect the maximum positive correlation at the maximum CGF-FGF density difference, around 60 m (according to density variability) or 70-75 m (according to the crude estimate of Section 4.2.3). After the maximum density difference, the positive correlation should weaken.

- Beyond the emergence maximum, we expect a weakly negative density-emergence correlation to develop and then fade as the CGF-FGF density difference grows small.

4.5.1 Emergence Results for Firn Type Variations

The variation in ice grain size is apparent within the 5 m and 23 m images in Fig. 4.7. On the left hand side of these images, coarser grains are present and appear brighter in the emergence image, while fine grained regions appear darker. Deeper in the core, variations in grain size become difficult to perceive visually. Individual bubbles are visible only in the deepest image.

We also note the change in relative emergence of ice lenses, the thin (1 mm or thinner) solid ice structures embedded in the firn and bubbly ice: from the surface down to at least the 73 m image, the lenses appear brighter than the surrounding material. From the 100 m image and deeper, the ice lenses appear darker. We can understand this by referring to Fig. 3.15 on page 92. In the shallow part of the core (from point A to point D) moving from the mean (ρ, a) path over to an ice lens location of ($\rho \sim 900\text{kg m}^{-3}, a < 0.2$ mm) yields a higher emergence. Around point E, the difference in emergence between the surrounding material and the ice lens will be small, suggesting that it will be difficult to detect ice lenses in this region. Near the emergence maximum, moving over to ice lens density will yield a lower emergence, so the ice lenses appear darker than the surrounding bubbly ice. Deeper still, there is little density difference between the ice lens and the now largely bubble-free ice, so ice lenses again become difficult to detect.

With the images of Fig. 4.7 setting the stage, we now take a detailed look at the coupled effects of density and firn microstructure on the development of the density-emergence ($\rho - E$) correlation pattern shown in the lower plot of Fig. 4.10. This large scale plot is annotated and labeled at particular points of significance along the core. The labeled points also correspond to the labels on Fig. 3.15 which summarizes the model results.

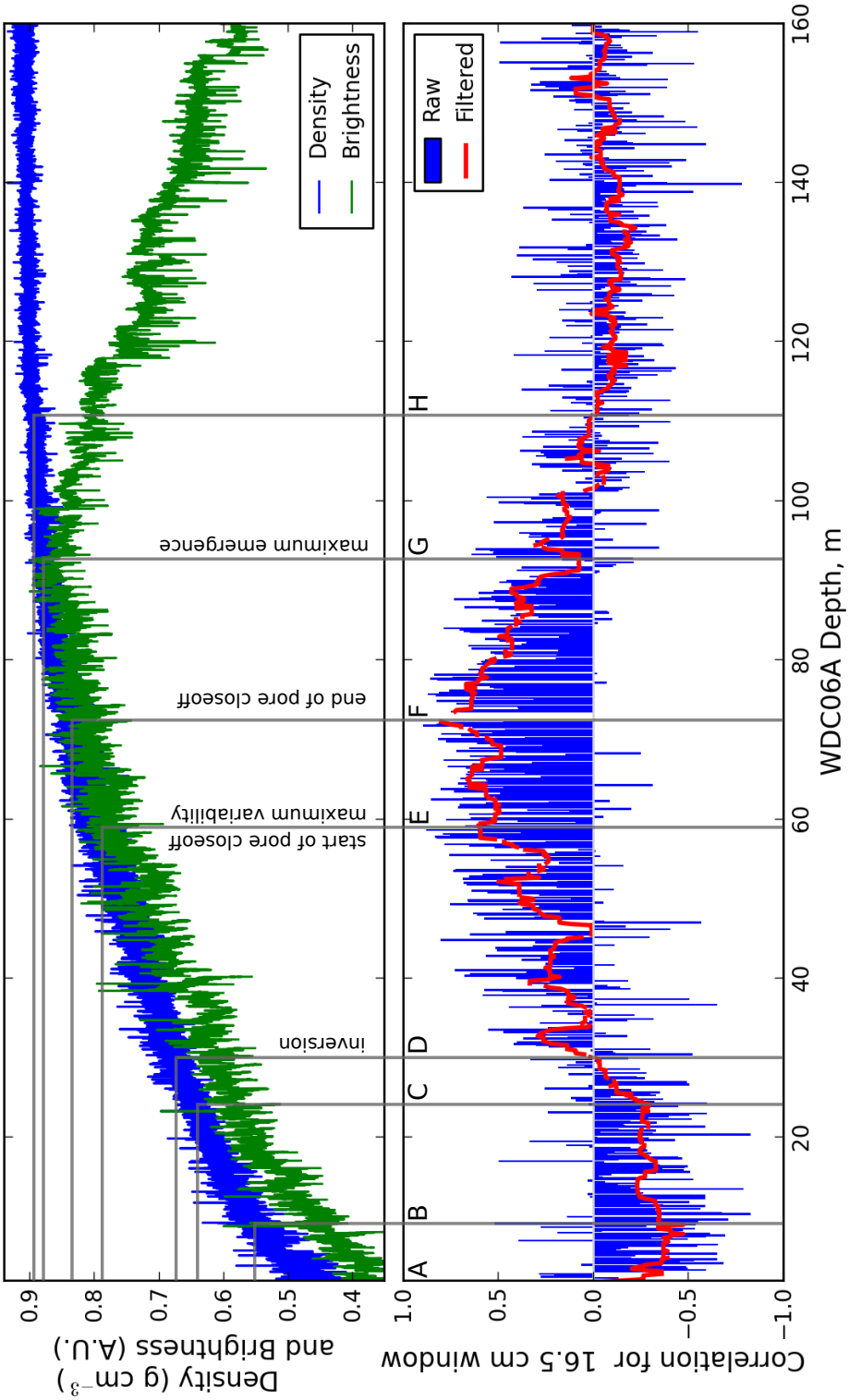

Figure 4.10. Large scale relationship between density and emergence. Data recorded by MADGE and the OIS. The lower plot shows density-brightness correlation coefficients calculated over 16.5 cm windows.

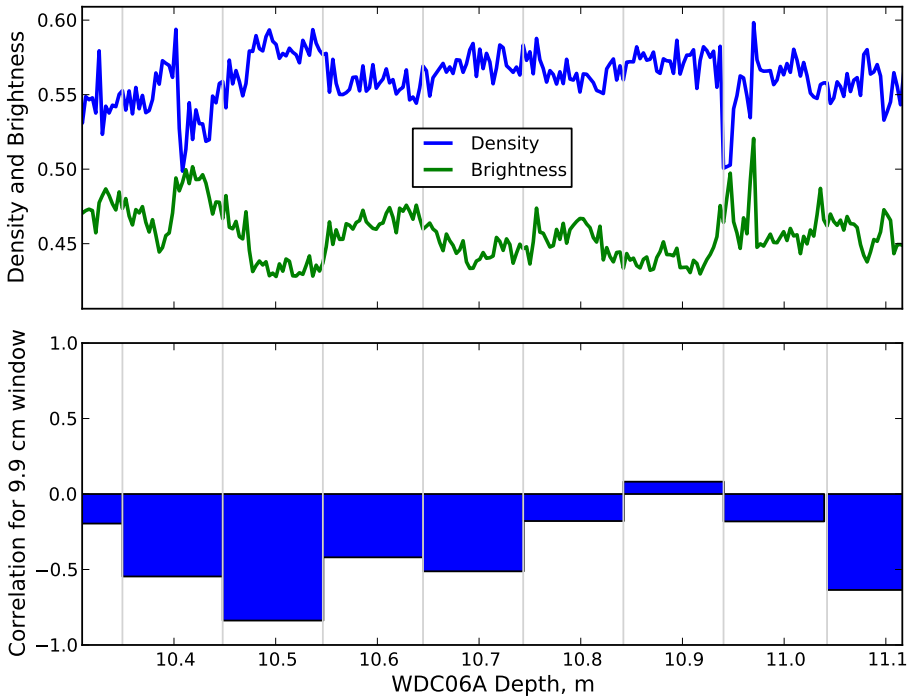

Figure 4.11. Shallow density, emergence and correlation. Top: Density in g cm^{-3} and emerged brightness vs. depth for firn above the density inversion zone ($<$ 25 m depth). Bottom: Density-emergence correlation coefficent vs. depth. Correlation window widths shown by vertical lines.

4.5.1.1 Shallow

In shallow regions (0–22 m) of the core, Fig. 4.11 shows that density and emergence are negatively correlated. Manually measured (Alley and others, 1982) and machine measured (Freitag and others, 2004) densities show that CGF has lower densities than FGF near the surface, therefore we identify regions of high emergence/low density with CGF, and low emergence/high density with FGF. Ice lenses are an exception to this rule: at this point on the (ρ, a) path, they have a high density and therefore a high emergence relative to the firn. The surface is point A (0 m, 400 kg m^{-3}) and point B (10 m, 550 kg m^{-3}) marks the expected end of

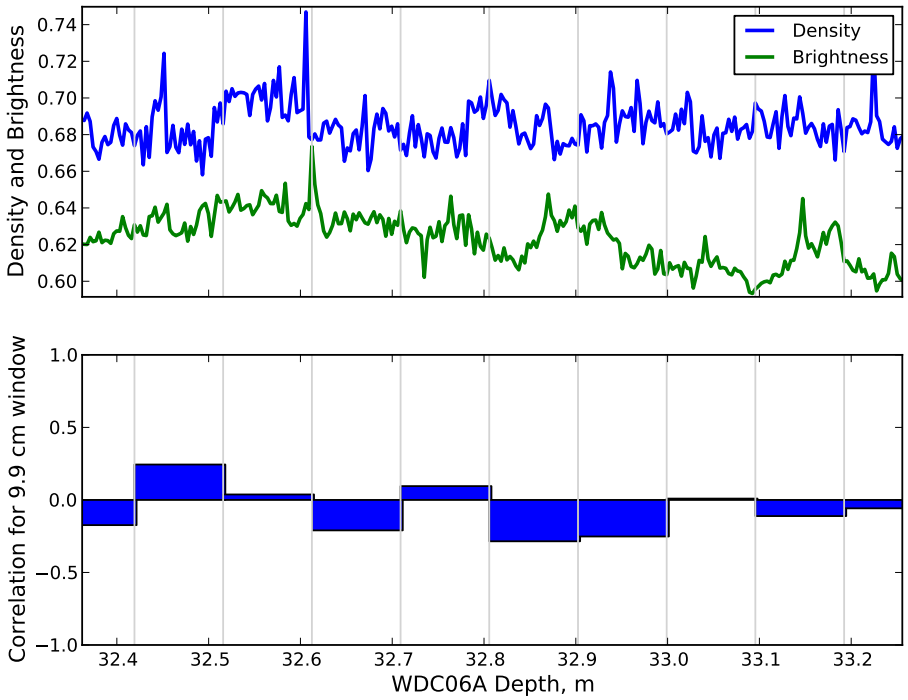

Figure 4.12. Density, emergence and correlation in the inversion zone. Top: Density in g cm^{-3} and emerged brightness vs. depth for firn in the density inversion zone (approximately 25 m to 35 m depth). Bottom: Density-emergence correlation coefficient vs. depth.

densification by particle rearrangement. Point C (22 m, 640 kg m^{-3}) marks the start of the density inversion zone as the negative correlation begins to rapidly decay.

4.5.1.2 Density Inversion Zone

In the density inversion zone, Fig. 4.12 shows interspersed regions of negative, positive and no correlation. The large scale view (Fig. 4.10) shows the cross-over point from negative to positive density-emergence correlation occurs at point D (30 m, and 670 kg m^{-3}) at the minimum of both density and emergence variability. We point out here that differential compaction processes are not done yet, and we follow them deeper in the next section.

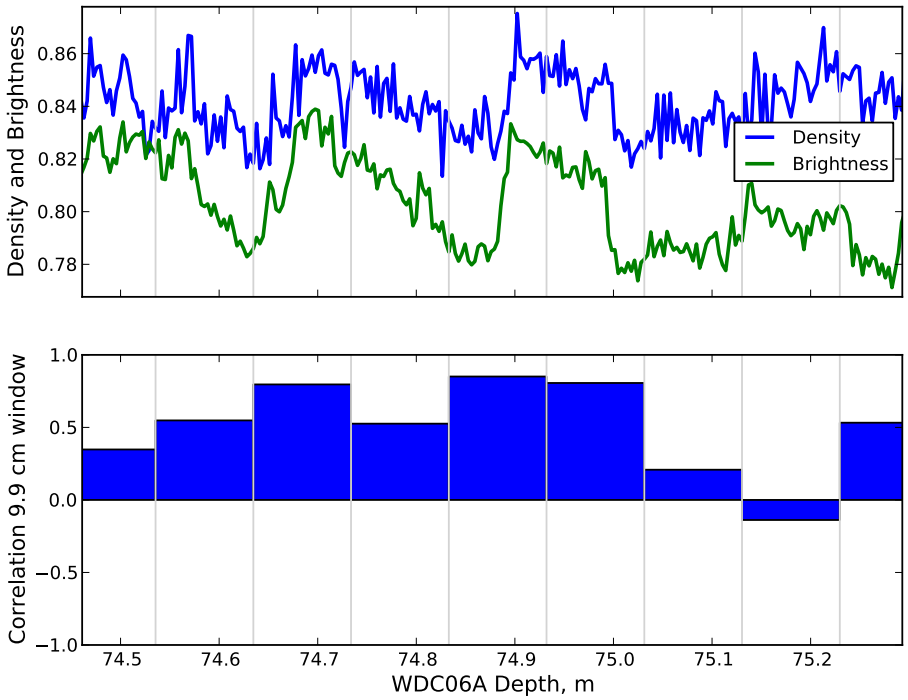

Figure 4.13. Density, emergence and correlation below the density inversion zone. Top: Density in g cm^{-3} and emerged brightness vs. depth below the density inversion zone ($>$ 35 m). Bottom: Density-emergence correlation coefficient vs. depth.

4.5.1.3 Pore Closeoff and Bubbly Ice

As the differential compaction continues through 30–75 m depth, we see a steady increase in positive density-emergence correlation, shown in detail in Fig. 4.13. This extraordinary positive correlation is the result of the large CGF-FGF density and emergence differences in this region. The emergence and density profiles match each other down to cm-scale features in many cases.

If density inversion did *not* happen, the observed correlation in this region would be *negative* since CGF would have a lower density but retain its higher emergence. The maximum in density and emergence variability occurs around point E (60 m, 780 kg m^{-3}) and Fig.4.10 shows that the $\rho - E$ correlation continues to increase at a somewhat slower rate until point F (72 m, 830 kg m^{-3}), the expected density

Point	a value (mm)	E magnitude	dE/dρ
E	0.4 (CGF)	large	+
E	0.2 (FGF)	medium	+
E	0.1	small	+
F	0.4 (CGF)	large	$0 \rightarrow -$
F	0.2 (FGF)	medium	+
F	0.1	small	+
G	0.4 (CGF)	medium	−
G	0.2 (FGF)	large	$0 \rightarrow -$
G	0.1	medium	+
H	0.4 (CGF)	small	−
H	0.2 (FGF)	small	−
H	0.1	large	$0 \rightarrow -$

Table 4.3. Emergence magnitude and slope for various firn types at analysis points E–H for Fig. 4.14.

for the completion of pore closeoff. In section 4.5, we predicted that the maximum positive $\rho - E$ correlation would occur at point E, not point F. The explanation is that we only considered *two* firn types, CGF and FGF, in our earlier predictions.

In an actual core, there is a *distribution* of grain and bubble sizes, not just the two bounding firn types upon which we base our predictions. Due to the nature of the E measurement, coarse grain/bubble sizes tend to dominate the signal. But eventually, as shown in Fig. 4.14, the emergence curves pass through a maximum, and the coarse bubbled material does so at a lower density than fine bubbled material. Extending our range of $a = 0.1$ mm to include compressed bubbles, we can explain the correlation pattern using the summary listed in Table 4.3.

At point E, we have a strong positive $\rho - E$ correlation (due to $dE/d\rho > 0$ for all firn types) which slowly approaches a maximum at point F where we reach the maximum E_{CGF}. Beyond F, $dE_{\mathrm{CGF}}/d\rho$ becomes negative, meaning that CGF is now contributing a small amount of negative $\rho - E$ correlation, weakening the positive contributions from FGF and very fine $a = 0.1$ mm bubbles. As we pass point G and the E_{FGF} maximum, both CGF and FGF are contributing negative $\rho - E$ correlation.

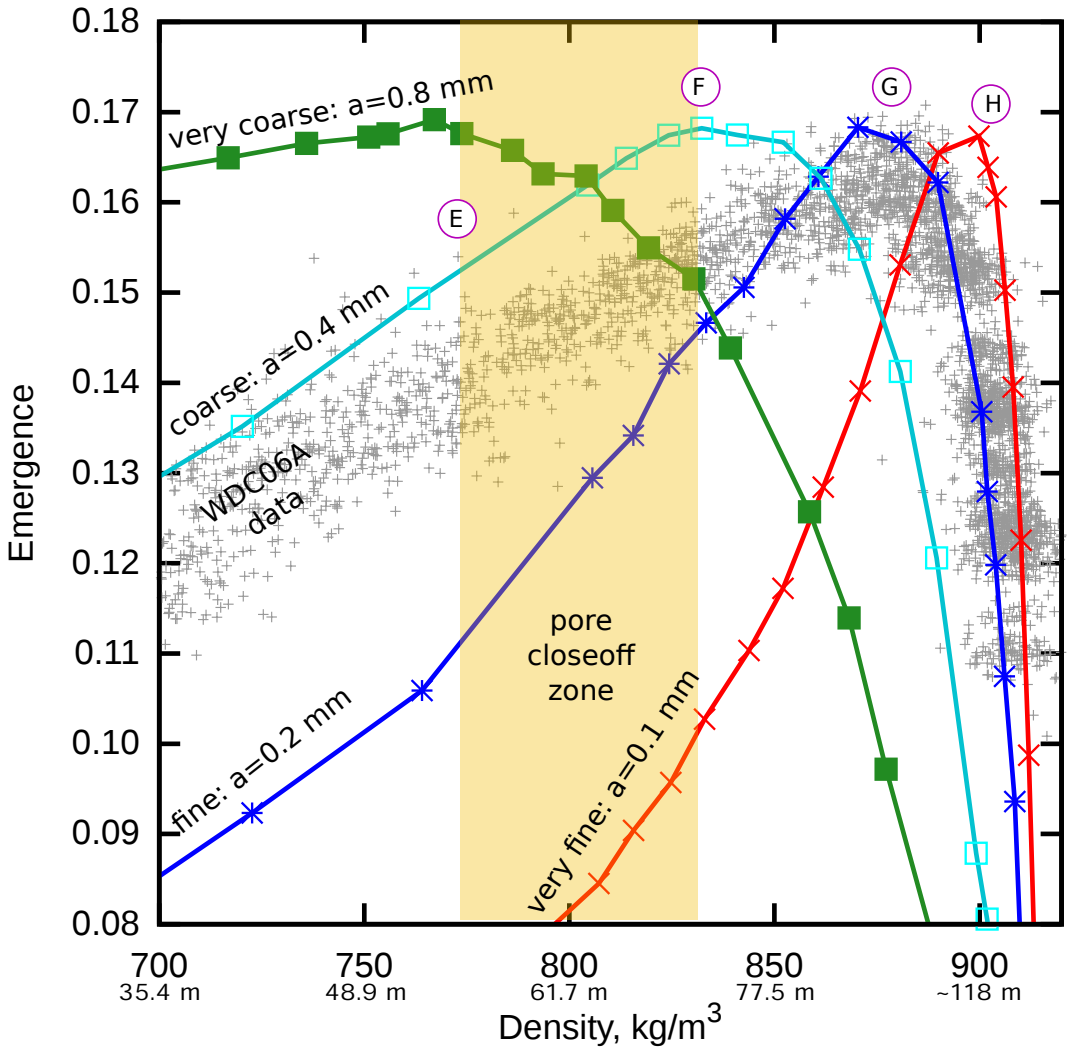

Figure 4.14. WDC06A and GO model emergence maxima for coarse, fine and very fine grained firn types. The measured E response is the result of a *distribution* of a values within the core. Approximate depth corresponding to the density are shown below each of the density-axis labels.

Finally, passing point H we cross over the $E_{a=0.1\text{ mm}}$ maximum and now all three firn types are contributing to the negative $\rho - E$ correlation. At this depth, the CGF-FGF density difference is quite small, so the negative correlation is weak, and disappears entirely as the density difference vanishes.

Given the bubble size data of Lipenkov (2000), it is not surprising that our deepest data trend closer to the $a = 0.1$ mm model predictions. The CGF and FGF

designations serve well from the surface, through pore closeoff and slightly beyond, but passing 900 kg m^{-3} we must include the effects of air bubble compression. The model result curve plotted for very coarse bubbles ($a = 0.8$ mm) shows that there were no bubbles of this size in the actual core. Had the core contained bubbles of this size, they would have dominated the emergence signal until the maximum at roughly 770 kg m^{-3}.

4.5.1.4 Validity of the Emergence Model

The observed mean (ρ, a) path shown in Fig. 4.9 is consistent with predictions made both in $(E - \rho)$ space (see Fig. 3.15) and in (ρ, a) space (see Fig. 3.16). The model also correctly predicts the differences in firn and ice lens emergence shown in Fig. 4.7. At the WAIS Divide site, we expect to see microstructure-dependent densification (MDD) manifested as a density inversion and the measured $E - \rho$ correlation data are all consistent with the model predictions for a density inversion.

In short, our simplified firn optics model correctly predicted both the mean emergence in firn and ice, and also correctly described the microstructure-driven variability in firn and ice emergence. From this, we conclude that the model is valid, and can be used to classify firn microstructural types in the WDC06A core.

4.5.2 Density as a Function of Microstructure Type

We now use the emergence data to separate various firn microstructure types into three simple categories: CGF, FGF and other. This analysis, similar to the approach taken by Freitag and others (2004), is the method we use to compare the densification rate of these firn types as a function of depth and to explicitly show the density inversion process in the WDC06A core. The methods developed in this and earlier chapters can be used to produce millimeter-scale firn and ice

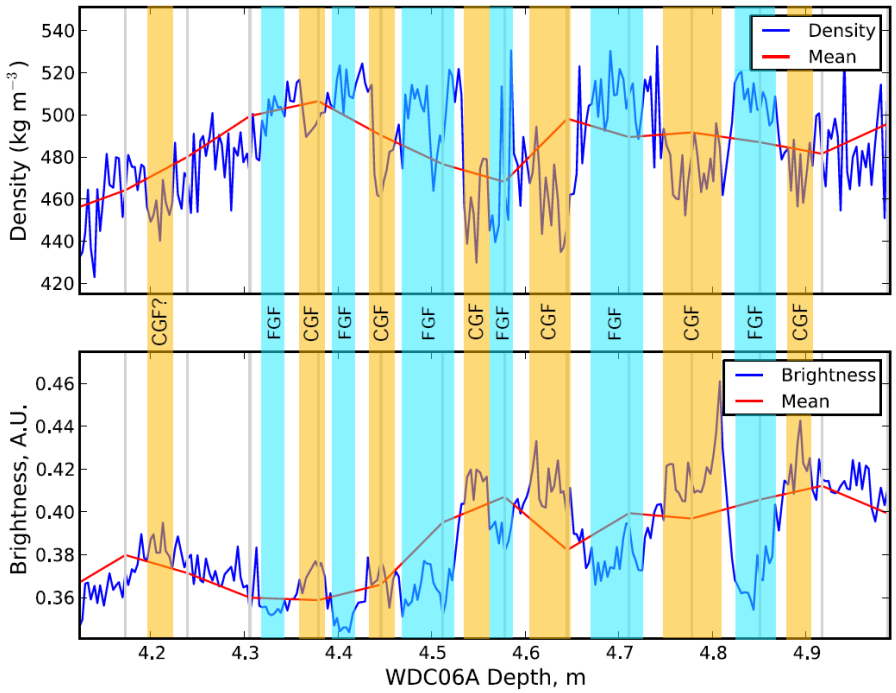

Figure 4.15. Sorting of firn microstructure types based on emergence. Separate means of density and emergence (plotted in red) were calculated over 10 cm windows (delimited by grey vertical lines). The mean value curves help to show where density and emergence have significant variation from the mean, and thus extract information about firn microstructure type.

microstructure profiles, but we do not do this for WDC06A because the emergence data are uncalibrated and of mediocre quality.

Based on the results of Section 3.3.7.3, Fig. 3.16 and Fig. 3.15, we expect $E_{\mathrm{CGF}} > E_{\mathrm{FGF}}$ from the surface down to a density of $\sim$ 880 kg m^{-3}, and $E_{\mathrm{FGF}} > E_{\mathrm{CGF}}$ at higher densities. Our microstructural analysis of the WDC06A core was based on locating and recording the average density for high and low E layers within the core.

Fig. 4.15 shows the general approach for collecting the data. Data collection was performed manually and only on those layers which had easily identifiable emergence stratigraphy. Thus the microstructure specific depth-density profiles plotted in Fig. 4.16 are clustered more thickly (in depth) in regions of the core with obvious E stratigraphy and are sparse elsewhere. The density inversion zone and regions

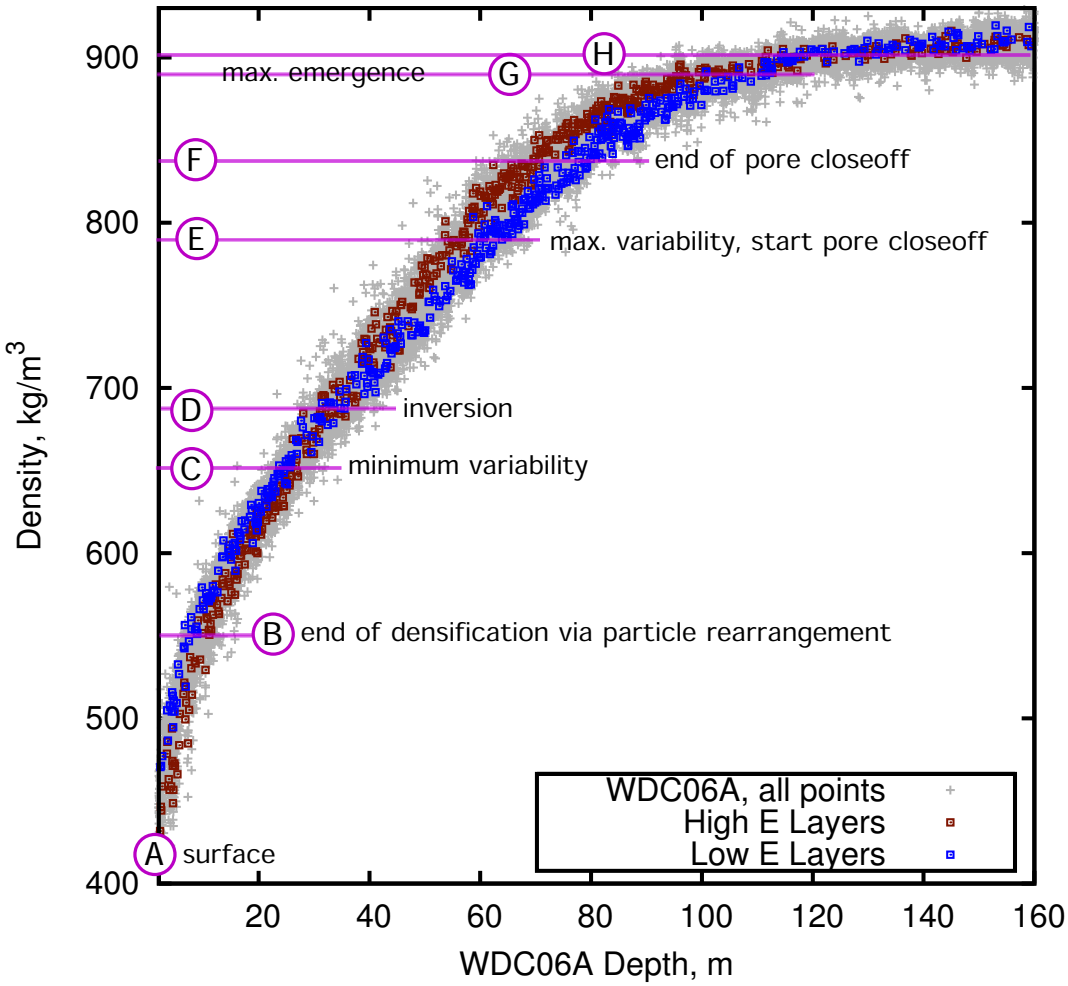

Figure 4.16. WDC06A density plotted for high and low emergence layers. Labeled points correspond to those on Fig. 4.10 and Fig. 3.15.

deeper than $\sim$ 100 m (regions with relatively low density and E variability) had the least obvious stratigraphy.

Organizing the density data into high and low E depth-density profiles shows a similar density inversion process as Freitag and others (2004) for the 0-80 m interval. The high E data correspond to CGF and low E data correspond to FGF for the majority of the 160 m core (shallower than point H). Density inversion occurs $\sim$ 30 m depth (as demonstrated in the correlation data) and is maintained to the point where we are limited by our instrumentation accuracy. We presume that these subtle density differences (of comparable magnitude to the 1-σ uncertainty

Firn Type	ρ_{surf}	z_ρ
Fine grained	467 kg m^{-3}	47.2 m
Mean WDC06A	440 kg m^{-3}	41.0 m
Coarse grained	421 kg m^{-3}	40.1 m

Table 4.4. Measured values in Eq. 4.1 for firn at WAIS Divide.

of MADGE) based on firn microstructure persist to substantial depths and would likely be revealed as small scale changes in air bubble volume and number density.

Our data continue deeper and show that the CGF and FGF depth-density profiles reach their largest separation near point F, the end of pore closeoff. Beyond this depth, the profiles begin to approach each other and eventually overlap near the overall emergence maximum at point G. The firn optics model suggests that at point H and deeper the emergence pattern should switch ($E_{\text{FGF}} > E_{\text{CGF}}$), but both these data and the $\rho - E$ correlation data are not particularly convincing. The standard accuracy of the density gauge is likely insufficient to reveal the subtle density variations at these depths, though longer MADGE exposure times could remedy this to some extent.

We fit empirical Schytt curves to the CGF and FGF density data to characterize the differences in densification between the firn types. The results are shown in Table 4.4. The fitted curves place the density inversion near 26 m depth, but do not predict equal densities again until nearly 200 m depth, far deeper than was observed experimentally. However, the fitted parameters do suggest that the overall densification of the firn column is still dominated by CGF as discussed in Section 4.2.2.

The differences in densification rate with respect to depth also clearly show microstructure-dependent effects, as shown in Fig. 4.17. CGF starts at a lower surface density, but maintains a higher densification rate than FGF from the surface (point A) down to the end of pore closeoff (point F). At pore closeoff, densification

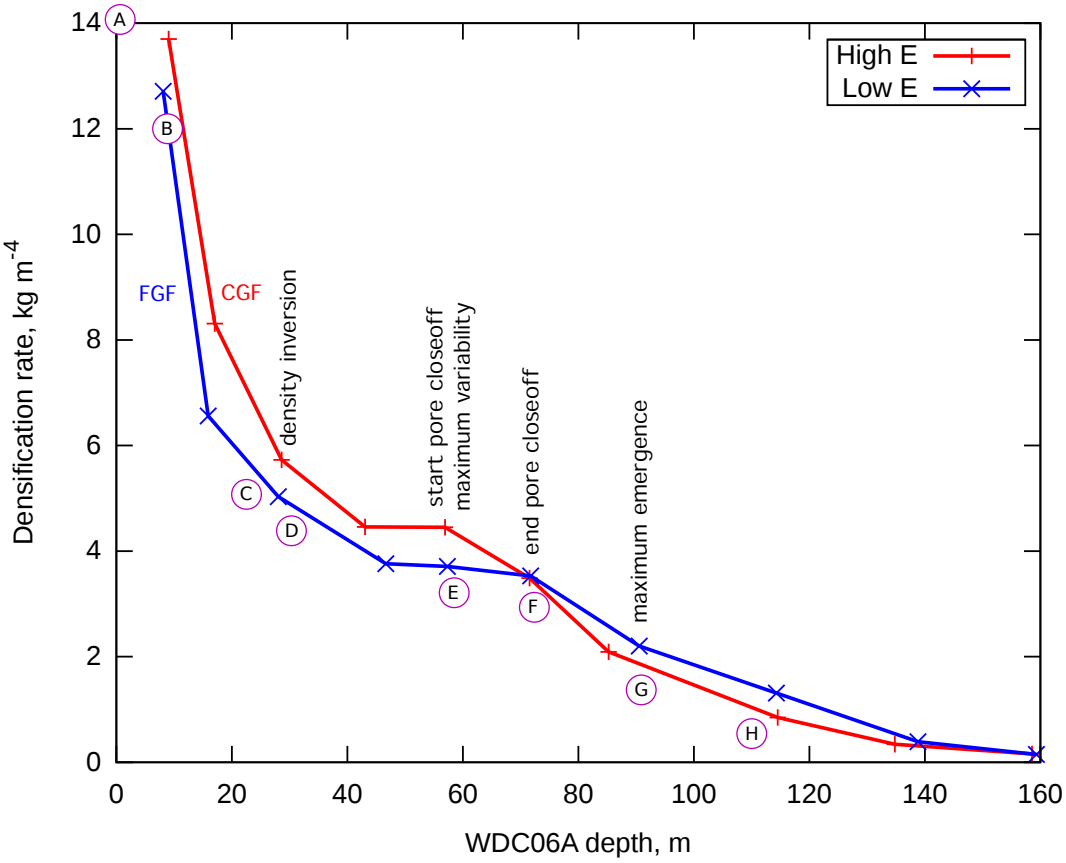

Figure 4.17. Densifcation rates of the WDC06A core. Data separated by optically-derived firn microstructure type. Labeled points correspond to those on Fig. 4.10 and Fig. 3.15.

rates are about equal, and deeper than this FGF has a slightly higher densification rate than CGF as it "catches up" on its approach to solid ice.

Both microstructural types seem to reach a plateau of constant densification rate near 50 m, though this plateau is longer for FGF. The reduction in densification rate beyond the plateaux (i.e. deeper than point E for CGF, deeper than point F for FGF) could be interpreted as evidence of pore closeoff. The mechanical argument for this interpretation is that resistance supplied by the increasing air bubble pressure serves to stiffen the firn and reduce the densification rate (Arnaud and others, 2000).

If this interpetation is correct, Fig. 4.17 shows CGF pore closeoff (point E) occuring at a shallower depth than FGF (point F), in accord with Fujita and others

(2009) and contrary to Severinghaus and Battle (2006). A coordinated high resolution microstructure and permeability study of the same core would seem to be required to resolve this question.

In the analysis of this section, no attempt is made at actually determining the average a for each layer because of the mediocre quality of the optical data. Were we more confident of this data, the procedure would be as follows:

1. Use E (or preferably E:T ratio) to determine SSA_v. Fig. 3.17 (or Fig. 3.24) shows how this would be done.

2. Use ρ, SSA_v and Eq. 3.3 to determine a for appropriate (GA or BI) scenario. The majority of the firn column (i.e. deeper than $\sim$25 m) seems to be best analyzed using the BI scenario: $a = r_b = \frac{3}{\mathrm{SSA}_v}(1 - \rho/\rho_{\mathrm{ice}})$, but further study of this is needed.

This analysis is not limited to only coarse and fine layers, but can be applied to all of the density and optical data available, thus producing a microstructure profile of the entire core.

The largest uncertainty in this scatterer size analysis is, of course, the validity of the GA/BI characterization of firn structure, especially between points B and E where the firn could simultaneously contain both grains and bubbles.

4.6 Conclusions

Much of this chapter was devoted to verification of the optical models described in Chapter 3. The agreement of the geometric optics model with experiment is striking, considering the sub-optimal optical scattering data and the many simplifying assumptions made in the model. The radiative transfer model also performed well, but placed the emergence maximum closer to pore closeoff than was actually ob-

served. Though more computationally intensive, we recommend the use of geometric optics methods for future exploration of firn optics.

The data collected from the core demonstrate that the models correctly predict the optical scattering properties of both the mean path of firn evolution and microstructural variations about the mean as indicated by the ρ-E correlation pattern.

There are four possibilities regarding the ρ-E correlation.

1. Neither density nor optical inversion occurs: CGF always has lower ρ and higher E compared to FGF. If this is the case, then we expect to observe ρ-E anti-correlation throughout the core.

2. Density inversion does occur, optical inversion does not: CGF starts shallow with lower ρ and higher E and finishes deep with higher ρ and higher E compared to FGF. If this is the case, then we expect a distinctive (-+-) ρ-E correlation pattern.

3. Optical inversion does occur, density inversion does not: CGF starts shallow with lower ρ and higher E and finishes deep with lower ρ and lower E compared to FGF. If this is the case, then we again expect a distinctive (-+-) ρ-E correlation pattern.

4. Both density *and* optical properties invert: CGF starts shallow with lower ρ, higher E and finishes deep with higher ρ, lower E compared to FGF. If this is the case, then we expect to observe ρ-E anti-correlation throughout the core.

Our observed ρ-E correlation data support both possibilities 2 and 3. However, the data of Gerland and others (1999) and Freitag and others (2004) and the clear minimum in density variability at the inversion point of the WDC06A core shown in Fig. 4.4 all point towards the inversion of density, not optical properties, as the the most likely interpretation. This implies that the microstructural differences in

firn types are *preserved* through the density inversion and beyond, in support of the ∼2 bubbles-per-grain found by Spencer and others (2006).

With experimental confirmation that our model results were correct, we then separated the density data by microstructural type to explicitly show MDD and density inversion occurring in the WDC06A core. It seems that conditions for density inversion have generally prevailed over the past 600 years covered by our 160 m analysis. It seems possible that the strength of density inversion (i.e. the difference in CGF and FGF densification rates) may have varied with time given changes in accumulation rate and temperature, but the low quality of our optical data prevents us from going beyond speculation. We simply note here that density inversion is likely not a binary "on/off" phenomenon, but may change in intensity according to different climate conditions. Further studies with deep firn cores from low accumulation sites would help in our understanding of the temperature and accumulation rate thresholds involved.

Microstructure-dependent densification is easily, and probably best detected by comparison of optical scattering and high resolution density data. The photonic methods described here will, pending implementation and testing of the instrumental improvements outlined at the end of Chapter 3, provide a non-destructive, field-deployable means of objectively characterizing firn and ice macro- and microstructure at millimeter resolution.

CHAPTER 5
CONCLUSIONS

> "There are two possible outcomes: if the result confirms the hypothesis, then you've made a measurement. If the result is contrary to the hypothesis, then you've made a discovery."
>
> – Enrico Fermi

5.1 The Hypothesis

The Hypothesis in Chapter 1 stated:

Firn densification is a microstructure-dependent process. We will test this hypothesis using only non-destructive, photonic measurement methods.

Testing this Hypothesis involved three interrelated projects: constructing a high resolution density instrument, developing a unified model of firn optics, and testing the predictions of the firn optics model using real data from the WAIS Divide WDC06A core. The model predictions were found to be correct and were therefore used to guide our classification of firn microstructural types within the core. Separating the density data by microstructure type allowed us to explicitly demonstrate microstructure-dependent densification (MDD) and density inversion in the WDC06A core.

5.1.1 Density Instrument

We successfully designed and built a novel pulse-mode gamma-ray density gauge for firn and ice cores. Operating the instrument in pulse-mode introduced some difficulties with regard to dead time losses and photomultiplier tube fatigue, but we

were able to resolve these issues, resulting in an instrument with a well documented, modeled and tested measurement uncertainty.

The liquid water calibration procedure developed for this instrument is able to characterize the non-ideal aspects of a real density gauge: finite beam size and finite detector and counting system energy resolution. For typical operating conditions, the instrument has a one-σ measurement uncertainty of ± 4 kg m^{-3} at a throughput of roughly 1 m h^{-1}, taking continuous density measurements every 3.3×10^{-3} m along the core.

The instrument is field deployable and was successfully operated in summer Antarctic plateau conditions on the 2006–2007 U.S. ITASE traverse from Taylor Dome to South Pole. This instrument uses low energy 60 keV gamma-rays to optimize density sensitivity, simplify international shipping requirements for polar deployment and enhance field portability since lightweight shielding was sufficient to ensure operator safety.

With respect to the data collected on the WDC06A core, the data compared very well with iso-octane density measurements of the same core, and with the general characteristics of other high resolution density profiles of other cores. These data represent the deepest high resolution density profile of an ice core produced by the United States ice coring program.

5.1.2 Optical Models

The radiative transfer models of photon propagation in firn agreed well with similar models by Fudge and Smith (2010) and with the expected behavior for limiting cases (solid air, solid ice, etc.). The models allowed for simultaneous simulation of albedo, transmittance and emergence as functions of SSA$_v$, bulk density and optical scatterer radius a. The most significant drawback to the RT approach was uncer-

tainty in how best to vary the asymmetry parameter g in the firn-ice transition zone and deeper into bubbly ice.

The geometric optics model, based on the SNOWRAT ray tracing code by Picard and others (2009), allowed the explicit modeling of air bubbles and avoided the asymmetry parameter issue altogether. We used the "random spheres" method (i.e. the spheres were allowed to overlap) of creating simulated firn and ice microstructure, and this seems to have worked quite well in terms of comparing model with experiment. The most significant differences between RT and GO models occurred in our determination of the emergence maximum, with GO correctly placing the maximum closer to pure ice.

Overall, the results of these models form a consistent picture of firn optics which allows us to understand the differences between transmittance, albedo and emergence measurements made on the same core or borehole. Albedo, whether measured at the surface of an ice core or the wall of a borehole, controls the amount of light available to scatter within the core or borehole wall. Therefore, simultaneous measurements of emergence and transmittance and bulk density can yield microstructural information about the core, without having to measure albedo.

The models also show that a purely optical measurement can only yield SSA_v. Bulk density must be measured along with the optical output in order to make any kind of prediction about mean optical scatterer size a. This is problematic for borehole albedo studies since there is no existing in-situ instrument which can measure bulk density at a comparable resolution to the optical measurement.

5.1.3 Comparison of Measured Data with Model Predictions

The comparison between the WDC06A density and emergence E profiles matched the model predictions very well, despite mediocre quality optical data and a simplified firn optics model. The E versus ρ data was surprisingly linear from 400 to

850 kg m^{-3} and fell largely within the bounds of the somewhat arbitrarily assigned "coarse" and "fine" scatterer sizes. At very high densities, the emergence data suggest that the actual bubbles were smaller still, thus the $a = 0.1$ mm analysis in Fig. 4.14.

In terms of firn/ice type variability, all of the changes in density-E correlation pattern were consistent with density inversion. The peak in density-E correlation continued deeper than expected, but this is because we had assumed a binary (coarse or fine) distribution in a, the scatterer size. The real data, as we might expect, seems to have a continuous distribution of a, and so the positive correlation continues as smaller and smaller scatterers pass through their emergence maxima on the way down to solid ice.

The continuous a distribution is also related to the significant (nearly 20 m) depth difference between the peak in density-E correlation and the maximum E for the mean (ρ, a) path. Only if our sample had mono-disperse scatterers (i.e. a had only one value), would we expect these maxima to coincide.

The final point to make is that the air bubbles-in-ice (BI) representation of a and SSA_v seems to fit the majority of the data best, even down to 550 kg m^{-3} where no actual bubbles would be expected. We suspect this is due to the fact that in the BI representation, SSA_v is a function of both bubble size a and firn/ice density. For ice grains in air (GA), SSA_v is a function only of the grain size and is likely better suited to characterizing the optical properties of snow rather than firn.

5.1.4 Overall Conclusion

The photonic methods developed in this dissertation are capable of non-destructively characterizing polar firn microstructure on large and small scales. Microstructure-dependent densification was clearly detected in the WDC06A core in the form of

density inversion, and evidence for long term persistence of this phenomenon was visible down to the uncertainty limits of the density instrument.

The theoretical and experimental foundations have been laid for a novel photonic instrument to non-destructively characterize firn microstructure in the field at high resolution. This is important for a number of glaciological applications.

1. Enhanced utility for linescan imaging systems. Several major ice core analysis laboratories have linescan imaging systems installed which can, with proper calibration and a high resolution core density profile, be used for firn microstructural profiling.

2. Alternative to X-ray computed tomography (XCT). High resolution microstructure profiling has previously been performed via XCT, but the techniques described in this chapter provide a less expensive and non-destructive alternative.

3. Potentially adaptable for in-situ measurements. XCT requires a view of all sides of a sample and is thus not practical for borehole-based microstructure measurements. Hawley and Morris (2006) have shown that in-situ albedo and density measurements can be made. Improving the vertical resolution of this approach will be the key to producing in-situ firn and ice microstructural profiles.

5.2 Future Work

5.2.1 Combined Photonic Instrument

A significant issue is depth co-registration of the density and emergence data. That the data generally lined up so well for WDC06A is a testament to careful laboratory work both here at the University of Maine and at the National Ice Core

Laboratory. Some of the variations in the density-E correlation profile could indicate either important changes in the intensity of the density inversion mechanism due to climate changes, or subtle errors in depth assignment between two very different instruments measuring different pieces of the same core.

The MADGE platform already has a very precise and automated sensor head positioning system. Therefore we propose upgrading MADGE with an optical scattering measurement system such that density, emergence and transmittance are all measured on the same piece of core, and measured at a fixed distance apart. This would greatly simplify data comparison and increase the accuracy of the optical measurement. The new optical system should include the suggested improvements discussed in Section 3.6 and strive to field deployable.

5.2.2 Optical Models

The optical models were crucial in correctly interpreting the emergence and density-E correlation data. Now that they have been established experimentally, there is plenty of opportunity to explore important topics such as poly-disperse scatterers, non-spherical scatterers, modeling the effects of stratigraphy, and assessing and improving the vertical resolution of optical scattering techniques, etc. The most important issue, however, is to determine the best way to represent firn structure around the firn-ice transition where neither GA or BI representations seem realistic.

REFERENCES

Albert, M., C. Shuman, Z. Courville, R. Bauer, M. Fahnestock and T. Scambos, 2004. Extreme firn metamorphism: impact of decades of vapor transport on near-surface firn at a low-accumulation glazed site on the East Antarctic plateau, *Annals of Glaciology*, **39**(1), 73–78.

Alley, R.B., 1987. Firn densification by grain-boundary sliding: a first model, *Le Journal de Physique Colloques*, **48**(C1), 249–256.

Alley, R.B., 1988. Concerning the deposition and diagenesis of strata in polar firn, *Journal of Glaciology*, **34**(1), 18.

Alley, R.B. and C.R. Bentley, 1988. Ice-core analysis on the Siple Coast of West Antarctica, *Annals of Glaciology*, **11**, 1–7.

Alley, R.B., J.F. Bolzan and I.M. Whillans, 1982. Polar firn densification and grain growth, *Annals of Glaciology*, **3**, 7–11.

Alley, R.B., E.S. Saltzman, K.M. Cuffey and J.J. Fitzpatrick, 1990. Summertime formation of depth hoar in central Greenland, *Geophysical Research Letters*, **17**(13), 2393–2396.

Alley, R.B., C.A. Shuman, D.A. Meese, A.J. Gow, K.C. Taylor, K.M. Cuffey, J.J. Fitzpatrick, P.M. Grootes, G.A. Zielinski, M. Ram and others, 1997. Visual-stratigraphic dating of the GISP2 ice core: Basis, reproducibility, and application, *Journal of Geophysical Research*, **102**(C12), 26367.

Alley, RB and GA Woods, 1996. Impurity influence on normal grain growth in the GISP2 ice core, Greenland, *Journal of Glaciology*, **42**(141), 255–260.

Alley, Richard B., 2000. Ice-core evidence of abrupt climate changes, *Proceedings of the National Academy of Sciences of the United States of America*, **97**(4), 1331–1334.

Arnaud, L., J. Barnola and P. Duval, 2000. Physical modeling of the densification of snow/firn and ice in the upper part of polar ice sheets, Physics of Ice Core Records, Hokkaido University Press, 285–305.

Arnaud, L., M. Gay, J.M. Barnola and P. Duval, 1998a. Imaging of firn and bubbly ice in coaxial reflected light: a new technique for the characterization of these porous media, *Journal of Glaciology*, **44**(147), 326–332.

Arnaud, L., V. Lipenkov, JM Barnola, M. Gay and P. Duval, 1998b. Modelling of the densification of polar firn: characterization of the snow-firn transition, *Annals of Glaciology*, **26**, 39–44.

Arnaud, L., G. Picard, N. Champollion, F. Domine, JC Gallet, E. Lefebvre, M. Fily and JM Barnola, 2011. Measurement of vertical profiles of snow specific surface area with a 1 cm resolution using infrared reflectance: instrument description and validation, *Journal of Glaciology*, **57**(201), 17.

Arons, E.M. and S.C. Colbeck, 1998. Effective medium approximation for the conductivity of sensible heat in dry snow, *International Journal of Heat and Mass Transfer*, **41**(17), 2653–2666.

Arzt, E., 1982. Influence of an increasing particle coordination on the densification of spherical powders, *Acta Metallurgica*, **30**(10), 1883–1890.

Bader, H., 1954. Sorge's Law of densification of snow on high polar glaciers, *Journal of Glaciology*, **2**, 319–323.

Baker, I., R. Obbard, D. Iliescu and D. Meese, 2007. Microstructural characterization of firn, *Hydrological processes*, **21**(12), 1624–1629.

Barkstrom, B.R. and C.W. Querfeld, 1975. Concerning the effect of anisotropic scattering and finite depth on the distribution of solar radiation in snow, *Journal of Glaciology*, **14**, 107–124.

Bertler, N.A.N., P.A. Mayewski, P.J. Barrett, S.B. Sneed, M.J. Handley and K.J. Kreutz, 2004. Monsoonal circulation of the McMurdo Dry Valleys, Ross Sea Region, Antarctica: signal from the snow chemistry, *Annals of Glaciology*, **39**, 139–145.

Blunier, T. and J. Schwander, 2000. Gas enclosure in ice: age difference and fractionation, *The Physics of Ice Core Records*, 307–326, Hokkaido University Press.

Bohren, C.F., 1987. Multiple scattering of light and some of its observable consequences, *American Journal of Physics*, **55**(6), 524–533.

Bohren, C.F. and R.L. Beschta, 1979. Snowpack albedo and snow density, *Cold Regions Science and Technology*, **1**(1), 47–50.

Bragg, G. M., 1974. Principles of experimentation and measurement, Prentice-Hall, Englewood Cliffs, N.J.

Braithwaite, R.J., M. Laternser and W.T. Pfeffer, 1994. Variations of near-surface firn density in the lower accumulation area of the Greenland ice sheet, Pâkitsoq, West Greenland, *Journal of Glaciology*, **40**(136), 477–485.

Breton, D.J., G.S. Hamilton and C.T. Hess, 2009. Design, optimization and calibration of an automated density gauge for firn and ice cores, *Journal of Glaciology*, **55**(194), 1092–1100.

Briesmeister, E J F, 1993. MCNP - A General Monte Carlo N-Particle Transport, Report LA-12625-M, Los Alamos National Laboratory.

Brillouin, L., 1949. The Scattering Cross Section of Spheres for Electromagnetic Waves, *Journal of Applied Physics*, **20**, 1110.

Brunetti, A., M.S. del Rio, B. Golosio, A. Simionovici and A. Somogyi, 2004. A library for X-ray-matter interaction cross sections for X-ray fluorescence applications, *Spectrochimica Acta Part B*, **59**, 1725–1731.

Canberra Industries, 2002. Canberra Model 512 Dual Counter/Timer User's Manual, 800 Research Parkway, Meriden, CT 06450, USA.

Cantarell, I., 1964. Theoretical and Experimental Study of Fatigue in Photomuliplier Tubes, *Nuclear Science and Engineering*, **18**, 31–48.

Cantarell, I. and I. Almodovar, 1965. Prediction, acceleration and correction of fatigue effects in photomultiplier tubes, *The International Journal of Applied Radiation and Isotopes*, **16**(2), 91 – 95.

Cember, H., 1992. Introduction to Health Physics, McGraw-Hill, second ed.

Chandrasekhar, S., 1950. Radiative Transfer, Oxford University Press.

Colbeck, SC, 1983. Theory of metamorphism of dry snow, *Journal of Geophysical Research*, **88**(C9), 5475–5482.

Colbeck, SC, 1991. The layered character of snow covers, *Reviews of Geophysics*, **29**(1), 81–96.

Courville, ZR, MR Albert, MA Fahnestock, LM Cathles IV and CA Shuman, 2007. Impacts of an accumulation hiatus on the physical properties of firn at a low-accumulation polar site, *Journal of Geophysical Research*, **112**(F2), F02030.

Craven, M. and I. Allison, 1998. Firnification and the effects of wind-packing on Antarctic snow, *Annals of Glaciology*, **27**, 239–245.

Cuffey, K.M. and WSB Paterson, 2010. The Physics of Glaciers, Butterworth-Heinemann.

Domine, F., M. Albert, T. Huthwelker, H.W. Jacobi, AA Kokhanovsky, M. Lehning, G. Picard and WR Simpson, 2008. Snow physics as relevant to snow photochemistry, *Atmospheric Chemistry and Physics*, **8**(2), 208.

Domine, F., AS Taillandier and WR Simpson, 2007. A parameterization of the specific surface area of seasonal snow for field use and for models of snowpack evolution, *Journal of Geophysical Research*, **112**, F02031.

Ebinuma, T. and N. Maeno, 1987. Particle Rearrangement and Dislocation Creep in a Snow-Densification Process, *Le Journal de Physique*, **48**(C1), 263–269.

Faria, S.H., J. Freitag and S. Kipfstuhl, 2010. Polar ice structure and the integrity of ice-core paleoclimate records, *Quaternary Science Reviews*, **29**(1-2), 338–351.

Fowles, G.R., 1989. Introduction to Modern Optics, Dover.

Freitag, J., S. Kipfstuhl and SH Faria, 2008. The connectivity of crystallite agglomerates in low-density firn at Kohnen station, Dronning Maud Land, Antarctica, *Annals of Glaciology*, **49**(1), 114–120.

Freitag, J., F. Wilhelms and S. Kipfstuhl, 2004. Microstructure-dependent densification of polar firn derived from X-ray microtomography, *Journal of Glaciology*, **50**(169), 243–250.

Frolov, A.D. and I.V. Fedyukin, 1998. Elastic properties of snow-ice formations in their whole density range, *Annals of Glaciology*, **26**, 55–58.

Fu, Q. and W. Sun, 2001. Mie theory for light scattering by a spherical particle in an absorbing medium, *Applied Optics*, **40**(9), 1354–1361.

Fudge, T.J. and B.E. Smith, 2010. Light propagation in firn: application to borehole video, *Journal of Glaciology*, **56**(198), 614.

Fujita, S., J. Okuyama, A. Hori and T. Hondoh, 2009. Metamorphism of stratified firn at Dome Fuji, Antarctica: A mechanism for local insolation modulation of gas transport conditions during bubble close off, *Journal of Geophysical Research*, **114**(F3), F03023.

Gallet, JC, F. Domine, CS Zender and G. Picard, 2009. Rapid and accurate measurement of the specific surface area of snow using infrared reflectance at 1310 and 1550 nm, *The Cryosphere Discussions*, **3**(1), 33–75.

Gerland, S., H. Oerter, J. Kipfstuhl, F. Wilhelms, H. Miller and W.D. Miners, 1999. Density log of a 181 m long ice core from Berkner Island, Antarctica, *Annals of Glaciology*, **29**, 215–219.

Giddings, JC and E. LaChapelle, 1961. Diffusion theory applied to radiant energy distribution and albedo of snow, *Journal of Geophysical Research*, **66**(1), 181–189.

Gill Sensors, 2004. Blade Sensor Technical Manual, Document 1484-007, www.gillsensors.co.uk.

Giovinetto, MB and HJ Zwally, 2000. Spatial distribution of net surface accumulation on the Antarctic ice sheet, *Annals of Glaciology*, **31**(1), 171–178.

Golubev, V.N. and A.D. Frolov, 1998. Modelling the change in structure and mechanical properties in dry-snow densification to ice, *Annals Of Glaciology*, **26**, 45–50.

Golubev, V.N. and A.D. Frolov, 2000. Model of structure and mechanical properties of dry granular snow, *Annals of Glaciology*, **31**(1), 434–438.

Golubev, V.N. and S.A. Sokratov, 2004. Regular packing of grains as a model of snow structure, *Annals of Glaciology*, **38**(1), 25–29.

Gow, A.J., 1969. On the rates of growth of grains and crystals in South Polar firn, *Journal of Glaciology*, **8**, 241–252.

Gow, A. J., 1970. Preliminary Results of studies of ice cores from the 2164 m deep drill hole, Byrd Station, Antarctica, International Symposium on Antarctic Glaciological Exploration (ISAGE), Hanover, NH, Septermber 1968, International Association of Scientific Hydrology, no. 86.

Grenfell, T.C. and S.G. Warren, 1999. Representation of a nonspherical ice particle by a collection of independent spheres for scattering and absorption of radiation, *Journal of Geophysical Research*, **104**(D24), 31697–31709.

Haltrin, V.I., 2002. One-parameter two-term Henyey-Greenstein phase function for light scattering in seawater, *Applied Optics*, **41**(6), 1022–1028.

Hamilton, G.S. and I.M. Whillans, 2000. Point measurements of mass balance of the Greenland Ice Sheet using precision vertical Global Positioning System (GPS) surveys, *Journal of Geophysical Research*, **105**(B7), 16295–16.

Hamilton, G.S., I.M. Whillans and P.J. Morgan, 1998. First point measurements of ice-sheet thickness change in Antarctica, *Annals of Glaciology*, **27**, 125–129.

Hammer, CU, 1980. Acidity of polar ice cores in relation to absolute dating, past volcanism, and radio-echoes, *Journal of Glaciology*, **25**, 359–372.

Hawley, R.L., 2005. Borehole investigations of firn processes, Ph.D. thesis, University of Washington.

Hawley, R.L., O. Brandt, E.M. Morris, J. Kohler, A.P. Shepherd and D.J. Wingham, 2008. Techniques for measuring high-resolution firn density profiles: case study from Kongsvegen, Svalbard, *Journal of Glaciology*, **54**(186), 463–468.

Hawley, R.L. and E.M. Morris, 2006. Borehole optical stratigraphy and neutron-scattering density measurements at Summit, Greenland, *Journal of Glaciology*, **52**(179), 491–496.

Hawley, R.L., E.D. Waddington, R.B. Alley and K.C. Taylor, 2003. Annual layers in polar firn detected by Borehole Optical Stratigraphy, *Geophysical Research Letters*, **30**(15), 1788.

Hawley, R.L., E.D. Waddington, G.W. Lamorey and K.C. Taylor, 2004. Vertical-strain measurements in firn at Siple Dome, Antarctica, *Journal of Glaciology*, **50**(170), 447–452.

Henyey, L. C. and J. L. Greenstein, 1941. Diffuse radiation in the galaxy, *Astrophysical Journal*, **93**, 70–83.

Herron, M.M. and C.C. Langway, 1980. Firn densification: an empirical model, *Journal of Glaciology*, **25**, 373–385.

Horhold, M.W., M.R. Albert and J. Freitag, 2009. The impact of accumulation rate on anisotropy and air permeability of polar firn at a high-accumulation site, *Journal of Glaciology*, **55**(192), 625–630.

Horhold, MW, S. Kipfstuhl, F. Wilhelms, J. Freitag and A. Frenzel, 2011. The densification of layered polar firn, *Journal of Geophysical Research*, **116**(F1), F01001.

Hori, A., K. Tayuki and 10 others, 1999. A detailed density profile of the Dome Fuji (Antarctica) shallow ice core by X-ray transmission method, *Annals of Glaciology*, **29**, 211–214.

Johns, Harold and John Cunningham, 1983. The Physics of Radiology, Charles C. Thomas, fourth ed.

Kaempfer, TU, MA Hopkins and DK Perovich, 2007. A three-dimensional microstructure-based photon-tracking model of radiative transfer in snow, *Journal of Geophysical Research*, **112**(D24), D24113.

Kaempfer, TU and M. Schneebeli, 2007. Observation of isothermal metamorphism of new snow and interpretation as a sintering process, *Journal of Geophysical Research*, **112**(D24), D24101.

Kameda, T., H. Shoji, K. Kawada, O. Watanabe and H.B. Clausen, 1994. An empirical relation between overburden pressure and firn density, *Annals of Glaciology*, **20**(1), 87–94.

Kaspari, S., P.A. Mayewski, D.A. Dixon, V.B. Spikes, S.B. Sneed, M.J. Handley and G.S. Hamilton, 2004. Climate variability in West Antarctica derived from annual accumulation-rate records from ITASE firn/ice cores, *Annals of Glaciology*, **39**(1), 585–594.

Kerbrat, M., B. Pinzer, T. Huthwelker, HW G
"aggeler, M. Ammann and M. Schneebeli, 2007. Measuring the specific surface area of snow with X-ray tomography and gas adsorption: comparison and implications for surface smoothness, *Atmospheric Chemistry and Physics Discussions*, **7**(4), 10287–10322.

Kinnard, C., R.M. Koerner, C.M. Zdanowicz, D.A. Fisher, J. Zheng, M.J. Sharp, L. Nicholson and B. Lauriol, 2008. Stratigraphic analysis of an ice core from the Prince of Wales Icefield, Ellesmere Island, Arctic Canada, using digital image analysis: High-resolution density, past summer warmth reconstruction, and melt effect on ice core solid conductivity, *Journal of Geophysical Research*, **113**(D24), D24120.

Kipfstuhl, S., I. Hamann, A. Lambrecht, J. Freitag, S.H. Faria, D. Grigoriev and N. Azuma, 2006. Microstructure mapping: a new method for imaging deformation-induced microstructural features of ice on the grain scale, *Journal of Glaciology*, **52**(178), 398–406.

Klein, O. and T. Nishina, 1929. Uber die Streuung von Strahlung durch freie Elektronen nach der neuen relativistischen Quantendynamik von Dirac, *Zeitschrift fur Physik A*, **52**(11), 853–868.

Knoll, Glenn F., 1989. Radiation detection and measurement, Wiley, New York, 2nd ed.

Koerner, R.M., 1971. A stratigraphic method of determining the snow accumulation rate at Plateau station, Antarctica, and application to South Pole-Queen Maud Land traverse 2, 1965-1966, Crary, A.P., ed., Antarctic Snow and Ice Studies II, American Geophysical Union, vol. 16 of *Antarctic Research Series*, 225.

Kokhanovsky, A.A., 2004. Light Scattering Media Optics: Problems and Solutions, Springer Verlag.

Kokhanovsky, A.A. and E.P. Zege, 2004. Scattering optics of snow, *Applied Optics*, **43**(7), 1589–1602.

Langway, C.C., 1958. Bubble pressures in Greenland glacier ice, Symposium of Chamonix, France, 336–349.

Langway, C.C., 1962. Some physical and chemical investigations of a 411 meter deep Greenland ice core and their relationship to accumulation, International Assoc. Scientific Hydrology. Commission of Snow and Ice. Symposium of Obergurgl (publication No. 58), 101–18.

Langway, C.C., 2008. The history of early polar ice cores, *Cold Regions Science and Technology*, **52**(2), 101–117.

Lee, S.H. and R.P. Gardner, 2000. A new G-M counter dead time model, *Applied Radiation and Isotopes*, **53**, 731–737.

Lee, S.H., M. Jae and R.P. Gardner, 2007. Non-poisson counting statistics of a hybrid G-M counter dead time model, *Nuclear Instruments & Methods B*, **263**(1), 46–49.

Legrand, M. and P. Mayewski, 1997. Glaciochemistry of polar ice cores: a review, *Reviews of Geophysics*, **35**(3), 219–243.

Li, J. and H.J. Zwally, 2002. Modeled seasonal variations of firn density induced by steady-state surface air-temperature cycle, *Annals of Glaciology*, **34**(1), 299–302.

Lipenkov, V., 2000. Air bubbles and air-hydrate crystals in the Vostok core, Hondoh, T., ed., Physics of Ice Core Records, Hokkaido University Press, 327–358.

Lipenkov, V.Y., A.N. Salamatin and P. Duval, 1997. Bubbly-ice densification in ice sheets: II. Applications, *Journal of Glaciology*, **43**(145), 397–407.

Lundy, C.C., M.Q. Edens and R.L. Brown, 2002. Measurement of snow density and microstructure using computed tomography, *Journal of Glaciology*, **48**(161), 312–316.

McConnell, JR, RJ Arthern, E. Mosley-Thompson, CH Davis, RC Bales, R. Thomas, JF Burkhart and JD Kyne, 2000. Changes in Greenland ice sheet elevation attributed primarily to snow accumulation variability, *Nature*, **406**(6798), 877–879.

McConnell, Joseph R., Gregg W. Lamorey, Steven W. Lambert and Kendrick C. Taylor, 2002. Continuous Ice-Core Chemical Analyses Using Inductively Coupled Plasma Mass Spectrometry, *Environmental Science & Technology*, **36**(1), 7–11.

McGwire, K., 2009. WAIS Divide ice core images, Antarctica, Digital media, National Snow and Ice Data Center.

McGwire, K.C., G.M. Hargreaves, R.B. Alley, T.J. Popp, D.B. Reusch, M.K. Spencer and K.C. Taylor, 2008a. An integrated system for optical imaging of ice cores, *Cold Regions Science and Technology*, **53**(2), 216–228.

McGwire, K.C., J.R. McConnell, R.B. Alley, J.R. Banta, G.M. Hargreaves and K.C. Taylor, 2008b. Dating annual layers of a shallow Antarctic ice core with an optical scanner, *Journal of Glaciology*, **54**(188), 831–838.

Meese, DA, AJ Gow, RB Alley, GA Zielinski, PM Grootes, M. Ram, KC Taylor, PA Mayewski and JF Bolzan, 1997. The Greenland Ice Sheet Project 2 depth-age scale: methods and results, *Journal of Geophysical Research*, **102**(C12), 26411.

Metropolis, N. and S. Ulam, 1949. The Monte Carlo Method, *Journal of the American Statistical Association*, **44**(247), 335–341.

Mishchenko, M. I., J.W. Hovenier and L.D. Davis, eds., 2000. Light Scattering by Nonspherical Particles, Acadamic Press.

Mobley, C.D. and R.W. Preisendorfer, 1994. Light and Water, Acadamic Press.

Moore, J.C., E.W. Wolff, H.B. Clausen and C.U. Hammer, 1992. The Chemical Basis for the Electrical Stratigraphy of Ice, *Journal of Geophysical Research*, **97**(B2), 1887–1896.

Morris, EM, 2008. A theoretical analysis of the neutron scattering method of measuring snow and ice density, *Journal of Geophysical Research*, **113**(F3), F03019.

Morris, E.M. and J.D. Cooper, 2003. Instruments and methods - Density measurements in ice boreholes using neutron scattering, *Journal of Glaciology*, **49**(167), 599–604.

Mullen, P.C. and S.G. Warren, 1988. Theory of the optical properties of lake ice, *Journal of Geophysical Research*, **93**(7), 8403–8414.

Painter, T.H., N.P. Molotch, M. Cassidy, M. Flanner and K. Steffen, 2007. Contact spectroscopy for determination of stratigraphy of snow optical grain size, *Journal of Glaciology*, **53**(180), 121–127.

Peltier, WR and A.M. Tushingham, 1989. Global sea level rise and the greenhouse effect: might they be connected?, *Science*, **244**(4906), 806.

Picard, G., L. Arnaud, F. Domine and M. Fily, 2009. Determining snow specific surface area from near-infrared reflectance measurements: numerical study of the influence of grain shape, *Cold Regions Science and Technology*, **56**(1), 10–17.

Prahl, S.A., 1988. Light transport in tissue, Ph.D. thesis, University of Texas, Austin).

Rasband, W.S., 1997. ImageJ software.

Rick, U.K. and M.R. Albert, 2004. Microstructure and permeability in the near-surface firn near a potential US deep-drilling site in West Antarctica, *Annals of Glaciology*, **39**(1), 62–66.

Saint-Gobain Crystals, 2008. 17900 Great Lakes Parkway Hiram, OH 44234 USA, www.detectors.saint-gobain.com.

Salamatin, A.N. and V.Y. Lipenkov, 2008. Simple relations for the close-off depth and age in dry-snow densification, *Annals of Glaciology*, **49**(1), 71–76.

Salamatin, A.N., V.Y. Lipenkov, J.M. Barnola, A. Hori, P. Duval and T. Hondoh, 2009. Snow-firn densification in polar ice sheets, *Physics of Ice Core Records*, **2**, 195–222, Hokkaido University Press.

Saloman, E.B., J.H. Hubbell and J.H. Scofield, 1988. X-ray Attenuation Cross Sections for Energies 100 eV to 100 keV and Elements Z = 1 to Z = 92, *Atomic Data and Nuclear Data Tables*, **38**(1), 1–196.

Schneebeli, M. and J.B. Johnson, 1998. A constant-speed penetrometer for high-resolution snow stratigraphy, *Annals of Glaciology*, **26**, 107–111.

Schwander, J., 1989. The transformation of snow to ice and the occlusion of gases, The environmental record in glaciers and ice sheets: report of the Dahlem Workshop on the Environmental Record in Glaciers and Ice Sheets, Berlin, 1988 March 13-18, John Wiley & Sons, 53.

Schwander, J., B. Stauffer and A. Sigg, 1988. Air mixing in firn and the age of the air at pore close-off, *Annals Of Glaciology*, **10**, 141–145.

Schytt, V., 1958. The inner structure of the ice shelf at Maudheim as shown by core drilling, *Norwegian-British-Swedish Antarctic Expedition, 1949-1952, Scientific Results* **4**, *Glaciology* 2, Norsk Polarinstitutt, Oslo, 115–151.

Severinghaus, J.P. and M.O. Battle, 2006. Fractionation of gases in polar ice during bubble close-off: New constraints from firn air Ne, Kr and Xe observations, *Earth and Planetary Science Letters*, **244**(1-2), 474–500.

Sjogren, B., O. Brandt, C. Nuth, E. Isaksson, V. Pohjola, J. Kohler and R.S.W. Van De Wal, 2007. Determination of firn density in ice cores using image analysis, *Journal of Glaciology*, **53**(182), 413–419.

Spaulding, NE, DA Meese, I. Baker, PA Mayewski and GS Hamilton, 2010. A new technique for firn grain-size measurement using SEM image analysis, *Journal of Glaciology*, **56**(195), 12–19.

Spencer, MK, RB Alley and TT Creyts, 2001. Preliminary firn-densification model with 38-site dataset, *Journal of Glaciology*, **47**(159), 671–676.

Spencer, MK, RB Alley and JJ Fitzpatrick, 2006. Developing a bubble number-density paleoclimatic indicator for glacier ice, *Journal of Glaciology*, **52**(178), 358–364.

Stauffer, B., J. Schwander and H. Oeschger, 1985. Enclosure of air during metamorphosis of dry firn to ice, *Annals Of Glaciology*, **6**, 108–112.

Sudiarta, I. Wayan and Petr Chylek, 2001. Mie scattering efficiency of a large spherical particle embedded in an absorbing medium, *Journal of Quantitative Spectroscopy and Radiative Transfer*, **70**(4-6), 709 – 714.

Svensson, A., S.W. Nielsen, S. Kipfstuhl, S.J. Johnsen, J.P. Steffensen, M. Bigler, U. Ruth and R. Rothlisberger, 2005. Visual stratigraphy of the North Greenland Ice Core Project (NorthGRIP) ice core during the last glacial period, *Journal of Geophysical Research*, **110**(D2), D02108.

Taillandier, A.S., F. Domine, W.R. Simpson, M. Sturm and T.A. Douglas, 2007. Rate of decrease of the specific surface area of dry snow: Isothermal and temperature gradient conditions, *Journal of Geophysical Research*, **112**(3), F03003.

Thomas, R., C. Davis, E. Frederick, W. Krabill, Y. Li, S. Manizade and C. Martin, 2008. A comparison of Greenland ice-sheet volume changes derived from altimetry measurements, *Journal of Glaciology*, **54**(185), 203–212.

Underwood, E.E., 1970. Quantitative stereology, Addison-Wesley.

Vaughan, D.G., J.L. Bamber, M. Giovinetto, J. Russell and A.P.R. Cooper, 1999. Reassessment of net surface mass balance in Antarctica, *Journal of Climate*, **12**(4), 933–946.

Warren, S.G., 1982. Optical properties of snow, *Reviews of Geophysics and Space Physics*, **20**(1), 67–89.

Warren, S.G., 1984. Optical constants of ice from the ultraviolet to the microwave, *Applied Optics*, **23**(8), 1206–1225.

Warren, S.G. and R.E. Brandt, 2008. Optical constants of ice from the ultraviolet to the microwave: A revised compilation, *Journal of Geophysical Research*, **113**(D14), D14220.

Warren, S.G., R.E. Brandt and T.C. Grenfell, 2006. Visible and near-ultraviolet absorption spectrum of ice from transmission of solar radiation into snow, *Applied Optics*, **45**(21), 5320–5334.

Whillans, I.M. and J.F. Bolzan, 1988. A method for computing shallow ice-core depths, *Journal of Glaciology*, **34**(118), 355–357.

Wilhelms, F., 2000. Messung dielektrischer Eigenschaften polarer Eiskerne, *Ber. Polarforsch*, **367**.

Wingham, D.J., A.J. Ridout, R. Scharroo, R.J. Arthern and CK Shum, 1998. Antarctic elevation change from 1992 to 1996, *Science*, **282**(5388), 456.

Wiscombe, W.J. and S.G. Warren, 1980. A model for the spectral albedo of snow. I: Pure snow, *Journal of the Atmospheric Sciences*, **37**(12), 2712–2733.

Zege, E., I. Katsev, A. Malinka, A. Prikhach and I. Polonsky, 2008. New algorithm to retrieve the effective snow grain size and pollution amount from satellite data, *Annals of Glaciology*, **49**(1), 139–144.

Zhong, C., H. Zhengde and C. Qun, 1989. Gain stability of photomultipliers at high variable counting rates, *Nuclear Instruments and Methods in Physics Research Section A: Accelerators, Spectrometers, Detectors and Associated Equipment*, **281**(2), 384 – 387.

APPENDIX A

MADGE OPERATING CODE, ELECTRICAL SCHEMATICS AND MECHANICAL DRAWINGS

A.1 Operating Code

```
//MADGEauto14w.c    Updated MADGE OS for WAIS divide core  14 May 2009
//Daniel J. Breton, University of Maine

//WAIS change: adjusted inner yoke distance to reflect WAIS yoke.


//Must compile this code with the
//SEPARATE Instruction & Data Spaces option to ensure that we dont run out
//of root code space.

#nodebug         //important for operation of data upload via serial port A, comment out
                 //if you need Dyn C debugging or printf to stdio

#use "MADGE.LIB"

#define SHOWTEMP_INT    5

#define MANUAL  0
#define AUTO    1

//////////////////////////////////////////INITIAL CONFIG//////////////////////

#define C0PRE       1500    //preset in kcts
#define CPRE        150 //preset in kcts
#define C0TM        5       //preset in sec
#define CTM         5       //preset in sec
#define DIST        10      //run distance in cm
#define MOVE        3.3   //mm to move per meas cyc
#define POST_AUTO_MOVE  50  //mm to move after done with core
#define CORE_L_INIT 100//length in cm of core segment to measure
#define L_OFST      3       //extra length in cm to ensure full core_d profile is captured
#define INIT_MODE   1       //fix ct
#define DAC_INIT    2700    //initial SCA setting in mV
#define TBOX_INIT 10.0  //BOX temp setpoint in deg C
#define TDET_INIT -20.0 //DET temp setpoint in deg C
#define CDR         -6.0    //cooldown rate in deg C per hour
#define HUR         6.0 //heatup rate in deg C per hour
#define TMSTEP  60  //time step for adjusting detector temp in seconds

//////////////////////////////////////////END INIT CONFIG////////////////////



int main(void)
{
    //flag variable declarations
    auto char flagHUR, flagSHOWTEMPS, flagDET_TCC, flagBOX_TCC;
   auto char flagMANUAL, flagAUTO, flagMAINMENU, flagNUKEMENU;
   auto char flagTEMPMENU, flagFILEMENU, flagMEASMENU, flagUPLOAD;
   auto char flagFIX_COUNT, flagFIX_TIME, flagpreAUTO, flagpostAUTO;

   //other variables
    auto int yr, oday, hr, min, mode, i, sel, xfer, hu_counter, count, fmcycles;
   auto int q, hur_inc;
   auto long int menu, junk, C, C0, dac_set, end_index;
   auto float Tbox, Tdet, TdetOW, fjunk, box_set_temp, det_set_temp;
   auto float Tmtr, deltaT, Tdeti, Tdetf, hur;
   auto float Cpreset, C0preset, Ctmpreset, C0tmpreset, pre, pre0, core_d;
   auto float core_l, move, pos0, m0, b0, d0, pos1, m1, b1, d1;
   auto char txt[41], dts[9], mcdata[80], button, buf[80];
   auto double boxPID[7], detPID[7], index, pos, C0time, Ctime;

   //file stuff
```

```
   File ramf, flashf, f;
   FileNumber ramfn, flashfn, nextfn, fnum;

    MADGE_init();           //initializes MADGE in general
   MADGE_fs_init(0);        //initializes filesystem, does not format lx's

   //assign initial config values here
    button = 0;
   index = 0;
   hur = HUR;           //initialize hur to safe value
   det_set_temp = TDET_INIT;
   box_set_temp = TBOX_INIT;
   mode = INIT_MODE;
   C0preset = C0PRE;
   Cpreset = CPRE;
   dac_set = DAC_INIT;
   move = MOVE;
   core_l = CORE_L_INIT;
   pre0 = C0PRE;
   pre = CPRE;
   //caliper inital calibration, constants in MADGE_CALIPER.LIB
   m0 = K_0;
   b0 = B_0;
   m1 = K_1;
   b1 = B_1;

   //nuke_init(mode, pre);  //initialize 512CT to some default values

    //initialize all flags
   flagMAINMENU = 1;    //execute MAIN menu on startup
   flagNUKEMENU = flagTEMPMENU = flagFILEMENU = flagMEASMENU =0;
   flagHUR = flagSHOWTEMPS = flagDET_TCC = flagBOX_TCC = 0;
   flagMANUAL = flagAUTO = flagUPLOAD = flagpreAUTO = flagpostAUTO = 0;

   hur_inc=1;   //initialize hur counter
   box_set_temp = TBOX_INIT;    //initialize box temp setpt
   det_set_temp = get_rtd(DET, V_REF);  //initialize detector temp setpt

   VFD_CMD(CLS, NONE, NONE);  //clear display

   //initialize both temperature control channels
   temp_control_init(boxPID, box_TCC, box_set_temp);
   temp_control_init(detPID, det_TCC, det_set_temp);

   //get date-time-stamp
   get_dts(&yr, &oday, &hr, &min);
   sprintf(dts, "%03d %02d:%02d\n", oday, hr, min);
   //printf(dts);
    ui_display(dts);

   ui_display("MADGEauto ver 1.4");
   ui_beep(3);  //powerup indication

//WELCOME to the BIG LOOP
    loopinit(); //initalize scofunction structures
    while(1)
    {
    loophead(); //something else to deal with scofunctions

        costate // MAIN menu costate
      {
            if(flagMAINMENU)
        {
```

```
    sel = 0;
    VFD_CMD(CLS, NONE, NONE);   //clear display
        ui_display("MAIN:    <U/D>\n");

    for(;;){    //endless loop
    //for a given selection, print menu choice and then return
    //cursor to bottom left of display

    if(sel < 0) sel = 6;    //wrap around menu
    if(sel > 6) sel = 0;    //wrap around menu
        if(sel == 0) ui_display("> NUKE CONFIG\xFE\x47\x01\x02");
        if(sel == 1) ui_display("> TEMP CONFIG\xFE\x47\x01\x02");
        if(sel == 2) ui_display("> FILE CONFIG\xFE\x47\x01\x02");
        if(sel == 3) ui_display("> MEAS CONFIG\xFE\x47\x01\x02");
        if(sel == 4) ui_display("> MADGEauto  \xFE\x47\x01\x02");
    if(sel == 5) ui_display("> MADGEmanual\xFE\x47\x01\x02");
    if(sel == 6) ui_display("> UPLOAD-> PC\xFE\x47\x01\x02");
        //printf(" main menu 2, sel %d ", sel);

    waitfor( button_press(&button) );
    waitfor( DelayMs(PAUSE) );

    if(button == UP) sel++;
    if(button == DOWN) sel--;
    if(button == ENTER)
    {
            ui_beep(1);
       button = 0;  //reset button press
       VFD_CMD(CLS, NONE, NONE);

            switch (sel)
       {
         case 0: {flagNUKEMENU = 1; flagMAINMENU = 0; abort;}
         break;

         case 1: {flagTEMPMENU = 1; flagMAINMENU = 0; abort;}
         break;

         case 2: {flagFILEMENU = 1; flagMAINMENU = 0; abort;}
         break;

         case 3: {flagMEASMENU = 1; flagMAINMENU = 0; abort;}
         break;

         case 4: {flagpreAUTO = 1; flagMAINMENU = 0; abort;}
              break;

         case 5: {flagMANUAL = 1; flagMAINMENU = 0; abort;}
         break;

         case 6: {flagUPLOAD = 1; flagMAINMENU = 0; abort;}
              break;

         default:
         {flagMAINMENU = 1; abort;} //get out and try again
       } //sw
            //abort;  //get out and go to new function
    } //if
        yield; //yield control after once thru
        }   //for
    }// if flagMAINMENU
} //main menu costate
```

```
  costate //NUKE CONFIGURATION
{
      if(flagNUKEMENU)
   {

      sel = 0;
      VFD_CMD(CLS, NONE, NONE);   //clear display
          ui_display("NUKE CONFIG:   <U/D>\n");

      for(;;){    //endless loop
      //for a given selection, print menu choice and then return
      //cursor to bottom left of display
          if(sel < 0) sel = 7;    //wrap around menu
      if(sel > 7) sel = 0;    //wrap around menu
          if(sel == 0) ui_display("> SET C COUNT  \xFE\x47\x01\x02");
          if(sel == 1) ui_display("> SET C0 COUNT \xFE\x47\x01\x02");
          if(sel == 2) ui_display("> SET C TIME   \xFE\x47\x01\x02");
          if(sel == 3) ui_display("> SET C0 TIME  \xFE\x47\x01\x02");
          if(sel == 4)
      {
          if(mode == FIX_CT) ui_display(">*SET FIX COUNT\xFE\x47\x01\x02");
              else ui_display("> SET FIX COUNT\xFE\x47\x01\x02");
      }

          if(sel == 5)
      {
          if(mode == FIX_TM) ui_display(">*SET FIX TIME \xFE\x47\x01\x02");
         else ui_display("> SET FIX TIME \xFE\x47\x01\x02");
      }
          if(sel == 6) ui_display("> SET Vdac (mV)\xFE\x47\x01\x02");

          if(sel == 7) ui_display("> SAVE & EXIT  \xFE\x47\x01\x02");

      waitfor(button_press(&button));
      waitfor(DelayMs(PAUSE));
      if(button == UP) sel++;
      if(button == DOWN) sel--;
          if(button == BACK) { flagNUKEMENU = 0; flagMAINMENU = 1; abort;}

      if(button == ENTER)
      {
              ui_beep(1);
         button = 0;  //reset
         VFD_CMD(CLS, NONE, NONE);
              switch (sel)
         {
           case 0:
           {
                     ui_display("\nC preset(kcts):\n>");
               ui_get_number(&junk, &Cpreset, FULL);
               break;
           }

           case 1:
           {
                     ui_display("\nC0 preset(kcts):\n>");
               ui_get_number(&junk, &C0preset, FULL);
                  break;
            }

           case 2:
           {
```

```
            ui_display("\nCtime preset:\n>");
        ui_get_number(&junk, &Ctime, FULL);
           break;
         }

      case 3:
      {
            ui_display("\nC0time preset:\n>");
        ui_get_number(&junk, &C0time, FULL);
           break;
         }

      case 4:
      {
            ui_display("\nFix Count SET\n>");
        mode = FIX_CT;
        waitfor(PAUSE);
           break;
         }

      case 5:
      {
            ui_display("\nFix Time SET\n>");
        mode = FIX_TM;
        waitfor(PAUSE);
           break;
         }

         case 6:
      {
            ui_display("\nDAC setting (mV):\n>");
        ui_get_number(&dac_set, &fjunk, FULL);
        clear_dac();
        set_dac((int)dac_set);
           break;
      }


      case 7:
      {
            if(mode == FIX_CT)
        {
                pre = Cpreset;
           pre0 = C0preset;
        }
        else
        {
           mode = FIX_TM;
                   pre = Ctime;
                   pre0 = C0time;
        }

        flagNUKEMENU = 0; //get out of NUKE CONFIG
        flagMAINMENU = 1; //and return to MAIN menu

            abort;  //after saving settings, get out of NUKE CONFIG

        break;
      }

      default:
      {flagNUKEMENU = 1; abort;} //get out and try again
    } //sw
```

```
            //abort;  //get out and go to new function
      } //if ENTER
          yield; //yield control after once thru
          }   //for
      }// if flagNUKEMENU
} //NUKE CONFIG costate

  costate //TEMP CONFIG menu costate
{
      if(flagTEMPMENU)
   {

      sel = 0;
      VFD_CMD(CLS, NONE, NONE);   //clear display
          ui_display("TEMP CONFIG:    <U/D>\n");

      for(;;)
      {   //endless loop
          //for a given selection, print menu choice and then return
          //cursor to bottom left of display
              if(sel < 0) sel = 4;    //wrap around menu
          if(sel > 4) sel = 0;    //wrap around menu
              if(sel == 0) ui_display("> SET TDET       \xFE\x47\x01\x02");
              if(sel == 1) ui_display("> SET TBOX       \xFE\x47\x01\x02");
              if(sel == 2)
          {
              if(flagDET_TCC) ui_display("> DISABLE DET TCC\xFE\x47\x01\x02");
                  else                ui_display("> ENABLE DET TCC \xFE\x47\x01\x02");
          }

              if(sel == 3)
          {
              if(flagBOX_TCC) ui_display("> DISABLE BOX TCC\xFE\x47\x01\x02");
                  else                ui_display("> ENABLE BOX TCC \xFE\x47\x01\x02");
          }

              if(sel == 4) ui_display("> SHOW TEMPS     \xFE\x47\x01\x02");

              if(sel == 5) ui_display("> EXIT to MAIN   \xFE\x47\x01\x02");

          waitfor(button_press(&button));
       waitfor(DelayMs(PAUSE));
        if(button == UP) sel++;
         if(button == DOWN) sel--;
              if(button == BACK) { flagTEMPMENU = 0; flagMAINMENU = 1; abort;}

          if(button == ENTER)
       {
                ui_beep(1);
            button = 0;   //reset
             VFD_CMD(CLS, NONE, NONE);
                switch (sel)
             {
                case 0:
                {
                    Tdeti = get_rtd(DET, V_REF);
                sprintf(txt, "Tdet=%.1f  Setpt:\n", Tdeti);
                        ui_display(txt);
                ui_get_number(&junk, &Tdetf, FULL);
                hu_counter = 0;
                    VFD_CMD(CLS, NONE, NONE);   //clear display
                        ui_display("TEMP CONFIG:    <U/D>\n");
                break;
```

```
  }

   case 1:
{
            ui_display("Tbox setpt:\n>");
      ui_get_number(&junk, &box_set_temp, FULL);
          VFD_CMD(CLS, NONE, NONE);   //clear display
              ui_display("TEMP CONFIG:    <U/D>\n");
          break;
        }

   case 2:
{
     flagDET_TCC = !flagDET_TCC;  //change state

    if(flagDET_TCC)
     {
                 sprintf(txt, "Det TCC ENABLED\nSetpt %.1f", det_set_temp);
                 ui_display(txt);

      Tdeti = get_rtd(DET, V_REF);
      hu_counter = 0; //initialize counter
          //initialize temp control channel, but assign current
          //temperature as setpoint-- this lets code under det temp
      //control costate safely control HUR
      temp_control_init(detPID, det_TCC, Tdeti);
          deltaT = hur/3600.0 * TMSTEP;
              }

       if(!flagDET_TCC)
    {
          pwm_set(det_TCC, 1*1024, 0);    //det htr OFF
                  ui_display("Det TCC DISABLED\n");
       }
      break;
          }

   case 3:
{
      flagBOX_TCC = !flagBOX_TCC; //change state

    if(flagBOX_TCC)
     {
                 sprintf(txt, "Box TCC ENABLED\nSetpt %.1f", box_set_temp);
                 ui_display(txt);
      PIDSetpoint(boxPID, box_set_temp);
              }

       if(!flagBOX_TCC)
    {
              pwm_set(box_TCC, 1*1024, 0);    //box htr OFF
                  ui_display("Box TCC DISABLED\n");
       }
          break;
        }

        case 4:
{
              flagSHOWTEMPS = 1;
              flagTEMPMENU = 0;
      break;
        }
```

```
            case 5:
           {
                flagTEMPMENU = 0; //get out of TEMP CONFIG
                 flagMAINMENU = 1; //and return to MAIN menu
                 abort;

                    break;
                  }

            default:
           {flagTEMPMENU = 1; abort;} //get out and try again
          } //sw
       button = 0;
            //abort;  //get out and go to new function
     } //if ENTER
         yield; //yield control after once thru
     }//for loop

  }//if flagTEMPMENU
}//temp config costate

//file config costate goes here
  costate //file config
{
     if(flagFILEMENU)
  {
     VFD_CMD(CLS, NONE, NONE);
         ui_display("FILE CONFIG:\n");
         button = 0;

     for(;;)
     {   //endless loop
     //for a given selection, print menu choice and then return
     //cursor to bottom left of display

         if(sel < 0) sel = 4;    //wrap around menu
     if(sel > 4) sel = 0;    //wrap around menu
         if(sel == 0) ui_display("> File list    \xFE\x47\x01\x02");
         if(sel == 1) ui_display("> Delete file  \xFE\x47\x01\x02");
         if(sel == 2) ui_display("> Format RAM  \xFE\x47\x01\x02");
         if(sel == 3) ui_display("> Format Flash\xFE\x47\x01\x02");
         if(sel == 4) ui_display("> Exit to MAIN\xFE\x47\x01\x02");

     waitfor( button_press(&button) );
     waitfor( DelayMs(PAUSE) );
     if(button == UP) sel++;
     if(button == DOWN) sel--;
     if(button == BACK) { flagFILEMENU = 0; flagMAINMENU = 1; abort;}
     if(button == ENTER)
     {
            ui_beep(1);
        button = 0;  //reset button press
        VFD_CMD(CLS, NONE, NONE);

            switch (sel)
        {
          case 0:    //list files
          {
                for( fnum=1, count = 0 ; fnum < MAX_RAM_FILES ; ++ fnum )
           {
                    if( 0 == fopen_rd( &f, fnum ) )
                {
                        fclose( &f );
```

```
                count++;
            }
        }

 sprintf(txt, "\nRAM: %d of %d used", count, MAX_RAM_FILES);
 ui_display(txt);

        for( fnum=FLASH_FILE_OFST, count = FLASH_FILE_OFST - 1 ; fnum < FS_MAX_FILES ; ++
fnum )
 {
            if( 0 == fopen_rd( &f, fnum ) )
        {
                fclose( &f );
                count++;
            }
        }

   sprintf(txt, "\nFLS: %d of %d used", count-FLASH_FILE_OFST, FS_MAX_FILES-
FLASH_FILE_OFST);
 ui_display(txt);

 waitfor( button_press(&button) ); //show info until button push
}
break;

case 1:    //delete file
{
            ui_display("\nFile# to delete?\n");
    ui_get_number(&junk, &fjunk, FULL);

            if( !fdelete((FileNumber)junk) )
            {
       sprintf(txt, "\nFile %d deleted", junk);
       ui_display(txt);
       waitfor(DelaySec(1));
    }
    else
    {
       sprintf(txt, "\nFile %d can't be\ndeleted...", junk);
       ui_display(txt);
       waitfor(DelaySec(1));
    }
    break;
}

case 2:    //format RAM
{
            lx_format(RAM_LX, 0);
    ui_beep(1);
    ui_display("RAM formatted\n");
    waitfor(DelaySec(1));
    break;
}

case 3:    //format FLASH
{
            lx_format(FLASH_LX, 0);
    ui_beep(1);
    ui_display("Flash formatted\n");
    waitfor(DelaySec(1));
    break;
}
```

```
          case 4:    //exit
          default:
          {
                    flagFILEMENU = 0;
              flagMAINMENU = 1;
              abort;
              break;
          }

        }//sw
      }//if enter
          yield;
      }//for
   }//if fileconfig
}//fileconfig costate

costate   //measurement config
{
  if(flagMEASMENU)
   {
      VFD_CMD(CLS, NONE, NONE);
          ui_display("MEAS CONFIG:\n");
          button = 0;

      for(;;)
      {   //endless loop
      //for a given selection, print menu choice and then return
      //cursor to bottom left of display

          if(sel < 0) sel = 5;    //wrap around menu
      if(sel > 5) sel = 0;    //wrap around menu
          if(sel == 0) ui_display("> SET MOVE     \xFE\x47\x01\x02");
          if(sel == 1) ui_display("> Show Blade0  \xFE\x47\x01\x02");
          if(sel == 2) ui_display("> Show Blade1  \xFE\x47\x01\x02");
          if(sel == 3) ui_display("X SET Caliper m\xFE\x47\x01\x02");
          if(sel == 4) ui_display("X SET Caliper b\xFE\x47\x01\x02");
          if(sel == 5) ui_display("> Exit to MAIN \xFE\x47\x01\x02");

      waitfor( button_press(&button) );
      waitfor( DelayMs(PAUSE) );
      if(button == UP) sel++;
      if(button == DOWN) sel--;
      if(button == BACK) { flagMEASMENU = 0; flagMAINMENU = 1; abort;}
      if(button == ENTER)
      {
             ui_beep(1);
         button = 0;  //reset button press
         VFD_CMD(CLS, NONE, NONE);

             switch (sel)
         {
           case 0: //set movement per meas cycle
           {
                    ui_display("\nmm per meas cycle:\n");
               ui_get_number(&junk, &move, FULL);
               break;
           }

           case 1:    //blade0 data display
           {
                  button = 0; //reset button press
                      for(;;) //endless loop until BACK is pressed
               {
```

```
                button_press(&button);
                        core_d = get_core_d(BL_AVG);
                pos0 = get_blade_0(BL_AVG, &d0, m0, b0);
                pos1 = get_blade_1(BL_AVG, &d1, m1, b1);
                        sprintf(txt, "\ncd %.3f p0 %.1f\nd0 %.3f %.3f", core_d, pos0, d0,
                        YOKE_WIDTH-d0-d1);
                ui_display(txt);
                if(button == BACK) abort;
                waitfor(DelayMs(250));  //update display 4x per second
            }
        }
             break;

        case 2:    //blade1 data display
        {
                button = 0; //reset button press
                    for(;;) //endless loop until BACK is pressed
            {
                button_press(&button);
                        core_d = get_core_d(BL_AVG);
                pos0 = get_blade_0(BL_AVG, &d0, m0, b0);
                pos1 = get_blade_1(BL_AVG, &d1, m1, b1);
                        sprintf(txt, "\ncd %.3f p1 %.1f\nd1 %.3f %.3f", core_d, pos1, d1,
                        YOKE_WIDTH-d0-d1);
                ui_display(txt);
                if(button == BACK) abort; //return to MEAS MENU
                waitfor(DelayMs(250));  //update display 4x per second
            }
        }
             break;

        case 3:    //to be written later, enter caliper slope
        case 4:    //to be written later, enter caliper intercept
        case 5:    //exit back to MAIN MENU
        default:
        {
                    flagMEASMENU = 0;
            flagMAINMENU = 1;
            abort;
        }
        break;

       }//sw
       }//if enter
    yield;
   }//for
      }//if flagMEASMENU
}//meas config costate


  costate //madge manual costate
{
  if(flagMANUAL)
  {
      nuke_init(mode, pre);
          button = 0;
      //ui_display("ENTER to begin\nBACK for MENU");

          waitfor(button_press(&button));     //wait until enter is pressed
                                                  //remember enter goes LOW when
                                          //pressed, normally pulled HIGH
          if(button == ENTER)
          {
```

```
            ui_beep(1);
            VFD_CMD(CLS, NONE, NONE);
            ui_display("Measuring...\n");
                //cycles to the other costates until count reported
                wfd C = nuke_count();
           //printf("C= %d ", C);

            //print results to display
            sprintf(txt, "\nC=%ld\n", C);
                ui_display(txt);
           sprintf(txt, "d=%.3f t=%2.4f", get_core_d(BL_AVG), report_time() );
            ui_display(txt);
           button = 0;  //reset
        }
        else if(button == BACK)
        {
            ui_beep(2);
                flagMAINMENU = 1;   //start Main MENU
           flagMANUAL = 0;  //end MADGE manual
           button = 0;  //reset
           abort;
        }
        else    //undefined button was pressed.... do nothing and loop again
        {
            ui_beep(3);
                button = 0; //reset
           abort;
        }
    }//if(flagMANUAL)
    }   //MADGEmanual costate

 costate //Madge auto escape costate
{
     if(flagpreAUTO || flagAUTO)
   {
         button_press(&button);
      if(button == BACK)
      {
             ui_beep(3);
         flagpreAUTO = 0;
         flagAUTO = 0;
         ui_display("\nMADGEauto\nSTOPPED");
         fclose(&ramf);  //close ram file gracefully, if open
             pause(10000);
         flagAUTO = flagpreAUTO = 0;
         flagMAINMENU = 1;
         abort;
      }//if BACK
     }//if preauto or auto
 }//escape costate

costate  //preauto costate
{
     if(flagpreAUTO)
   {
     button = 0;
      ramfn = next_ram_fn();     //get filenumbers for new data
      flashfn = next_flash_fn();
      unlock_stepper(); //unlock stepper motor to allow manual positioning
         nuke_init(mode, pre0);  //intialize 512CT for C0 meas !!!

         make_ram_file(&ramf, ramfn);    //prepare RAM file for use
```

```
     VFD_CMD(CLS, NONE, NONE);
      ui_display("\nEnter core_L(cm):\n");
      ui_get_number(&junk, &core_l, FULL);

      fmcycles = (int) ceil( ( (core_l+L_OFST) * 10) / move) ;

      //waitfor(button_press(&button));
      //if(button == BACK) {flagAUTO=0; flagMAINMENU=1; abort;}

         ui_display("\nCounting C0...");
      wfd C0 = nuke_count();
      C0time = report_time();
      if(C0time == 0) C0time = report_time();    //try again (hack)
      ui_beep(0);
      sprintf(txt, "\nC0=%ld\nt=%f <ENT>", C0, C0time);

         ui_display(txt);
         //printf(" C0time = %f ", C0time);
      nuke_init(mode, pre);  //config 512TC for C meas !!!


      //waitfor(button_press(&button));
      //if(button == BACK) {flagAUTO=0; flagMAINMENU=1; abort;}

      //data file header
      get_dts(&yr, &oday, &hr, &min);

      //write date time stamp
      sprintf(dts, "%03d %02d:%02d\n\r\0", oday, hr, min);
      ram_write(&ramf, dts); //date time stamp for start of recording

      //write C0, C0time, C, DAC
      sprintf(mcdata, "%ld %f %f %ld\n\r\0", C0, C0time, Cpreset, dac_set);
      ram_write(&ramf, mcdata);

      //write Tbox, Tdet
      sprintf(mcdata, "%.1f %.1f\n\r\0", Tbox, Tdet);
      ram_write(&ramf, mcdata);

      //write mode, move, core length
      sprintf(mcdata, "%d %.2f %.2f\n\r\n\r\0", mode, (move/10), core_l);
      ram_write(&ramf, mcdata);

      lock_stepper();    //lock sensor head in preparation for measurement

      ui_beep(3);  //here we go!

      //switch from preAUTO to real AUTO
      flagpreAUTO = !flagpreAUTO;
      flagAUTO = 1;

      abort; //leave costate
   }//if flagpreAUTO
} //flagpreAUTO costate

costate //flagAUTO costate
{
 if(flagAUTO) {
   button = i = 0;   //initialize i
     //maybe include some
   //code to continue if core diameter is still > some minimum
 while(i <= fmcycles)
   {
```

```
         //get core diameter
     core_d = get_core_d(BL_AVG);
         pos = index * (MMPS/10.0);
         sprintf(txt, "\nP  %.2fcm Tbox %.1f\nCD %.2fcm Tdet %.1f", pos, Tbox, core_d, Tdet);
      ui_display(txt);
      //also send via serA
      serAputs(txt);

     //perform nuclear measurement
         wfd C = nuke_count();
         Ctime = report_time();

         if(mode == FIX_CT)
      {
         sprintf(mcdata, "%.0f\t%f\t%.3f\n\r", index, Ctime, core_d);
             ram_write(&ramf, mcdata);
      }

      if(mode == FIX_TM)
      {
         sprintf(mcdata, "%.0f\t%ld\t%.3f\n\r", index, C, core_d);
             ram_write(&ramf, mcdata);
      }

      ui_beep(0);    //warns of next move, also should provide some
                     //comforting indication that MADGEauto is still working
         yield;          //yield control for temp control and other active costates

       //move sensor head away from stepper motor by 3.3mm
    step((int)(move/MMPS), CCW, MED, &index);
         i++;
   }//while

   //done with auto run, now switch to flagpostAUTO
     flagAUTO = !flagAUTO;
   flagpostAUTO = 1;
   }//if flagAUTO
   abort;    //leave costate
} //flagAUTO costate

costate  //flagpostAUTO costate
{
 if(flagpostAUTO) {
   //printf(" flagpostAUTO ");
     nuke_init(mode, pre0);  //intialize 512CT for C0 meas !!!
     ui_display("\nCounting C0...");
   wfd C0 = nuke_count();
   C0time = report_time();
   if(C0time == 0) C0time = report_time();   //try again if necessary
 //sprintf(txt, "\nC0=%ld\nt=%f <ENT>", C0, C0time);
 //ui_display(txt);
     //printf(" C0time = %f ", C0time);

     ui_display("\nMADGEauto done\nWriting data...");

   //data file footer
   get_dts(&yr, &oday, &hr, &min);

   //write date time stamp
   sprintf(dts, "%03d %02d:%02d\n\r\0", oday, hr, min);
   ram_write(&ramf, dts);    //date time stamp for end of recording
```

```
   //write Tbox, Tdet and End of File marker
   sprintf(mcdata, "%.1f %.1f %f\n\rEOF\n\r\0", Tbox, Tdet, C0time);
   ram_write(&ramf, mcdata);

   make_flash_file(&flashf, flashfn);    //open flash file
     //printf(" make flash file ");
   copy_to_flash(&ramf, &flashf);    //copy data to flash file and close
                                                 //both ram and flash files
 //printf(" copy to flash ");
   ui_beep(2);
   sprintf(txt, "\nSaved to file %d\n<ENT> for 5cm move", flashfn);
     ui_display(txt);

     waitfor(button_press(&button));

   step((int)(POST_AUTO_MOVE/MMPS), CCW, MED, &index);
     end_index = (long int)index;
   ui_beep(2);

   sprintf(txt, "\n<ENT> SH to HOME\n");
   ui_display(txt);

     waitfor(button_press(&button));
   step(end_index, CW, FAST, &index);    //move sensor head back to start pos

 flagpostAUTO = 0;
   flagMAINMENU = 1; //exit postAUTO and return to main menu
   } // if
   abort;
}

costate  //detector temp control costate
{
     if(flagDET_TCC)
   {
      if(Tdet+deltaT >= Tdetf) det_set_temp = Tdetf;
      else det_set_temp = Tdeti + (deltaT * hu_counter);

     PIDSetpoint(detPID, det_set_temp);  //update setpoint to maintain safe HUR
      det_temp_ctrl(detPID, &Tdet);

     }//if flagDET_TCC
}

costate  //detector HUR/CDR control costate
{
     if(flagDET_TCC)
   {
     hu_counter++;
     waitfor(DelaySec(TMSTEP));  //increment det_set_temp at proper interval
   }
}

costate  //box temp control costate
{
     if(flagBOX_TCC)
   {
         box_temp_ctrl(boxPID, &Tbox);
     }
}

 costate //monitor other temps roughly every 5 seconds for showtemp
{
```

```
      Tdet = get_rtd(DET, V_REF);
      Tbox = get_rtd(LM19, V_REF);
   waitfor(DelaySec(5));
}

costate  //showtemps costate
{
     if(flagSHOWTEMPS)
   {
         VFD_CMD(CLS, NONE, NONE);
      for(;;)
      {
         button_press(&button);  //look for button press
             if(button == BACK) { flagSHOWTEMPS = 0; flagTEMPMENU = 1; abort;}
             sprintf(txt, "\nTdet %.1f\nTbox %.1f", Tdet, Tbox);
             ui_display(txt);
             waitfor(DelaySec(1));
         }//for
   }//if

}//showtemps costate

costate  //upload data costate
{            //this costate is NOT compatible with Dyn C debugging because it
         //takes control of serial port A to communicate with PC.  if you
         //need Dyn C debugging, comment out this costate AND the #nodebug
         //directive at start of this code.
 if(flagUPLOAD) {
     VFD_CMD(CLS, NONE, NONE);   //clear display
   ui_beep(1);
   ui_display("ENT to start upload\nof Flash FS.");

     waitfor( button_press(&button) );
     if (button == ENTER)
     {
         ui_beep(1);
         //serAopen(19200);
         //serAwrFlush();
         //serArdFlush();

             for(i = FLASH_FILE_OFST; i < 50; i++)
         {
                 xfer = upload_file(i);
                 sprintf(buf, "\n\rFILE %d: %d BYTES UPLOADED.\n\r\0", i, xfer);
             serAputs(buf);
             pause(1000);
         }//for
             ui_beep(2);
         ui_display("\nUpload DONE!");
     }//if button

         // exit costate, or exit costate if any other button pushed
     flagUPLOAD = 0;
      flagMAINMENU = 1;  //go to main menu
         abort;
   }//if flagUPLOAD
}//upload data costate

}    //BIG LOOP while
return(0);
}//main
```

A.2 MCNP Scattered Radiation Model Input

```
MADGE scattered exposure MCNP Model, max density, Daniel J. Breton
c cell cards for problem
1 1 -11.38 (-3 +6 -5):(+2 -3 +5 -4) $src pig/collimator
2 2 -0.917 -1 -11  $max density ice core, 20cm long
3 1 -11.38 (+2 +7 -8 -11 -12) $detector collimator
4 1 -11.38 -3 +9 -10 $detector cell
5 3 -0.0012 #1 #2 #3 #4 -11
6 0 +11 $everything else
c end of cell cards for problem

c surface definitions
1 CY  2.54 $ice core
2 CX  0.33 $collimator hole
3 CX  1.16 $collimator body
4 PX -2.79 $src side collimator inner wall
5 PX -4.0  $src side collimator outer wall
6 PX -5.79 $src pig outer wall
7 PX +2.79 $det side collimator inner wall
8 PX +3.29 $det side collimator outer wall
9 PX +3.3  $det plane
10 PX +3.8 $det plane
11 SO +10  $edge of simulation
12 CX +5.0 $det side coll outer edge

MODE P
IMP:P 1 1 1 1 1 0
SDEF POS= -3.95 0 0 ERG=.0595 WGT=1 TME=0 PAR=2
F1:P 9 11
E1 0.01 10I 0.06
F15:P -2.5 0 3.54 0
E15 0.01 5I 0.06
F25:P -2.5 0 3.54 0
E25 0.01 5I 0.06
F35:P 0 0 3.54 0
E35 0.01 5I 0.06
F45:P 2.5 0 5.0 0
E45 0.01 5I 0.06
F55:P -2.5 2.5 3.54 0
E55 0.01 5I 0.06
F65:P 0 2.5 3.54 0
E65 0.01 5I 0.06
F75:P 2.5 2.5 3.54 0
E75 0.01 5I 0.06
F85:P -2.5 5.0 3.54 0
E85 0.01 5I 0.06
F95:P 0 5 3.54 0
E95 0.01 5I 0.06
F105:P 2.5 5.0 3.54 0
E105 0.01 5I 0.06
M1 82000 1 $natural lead
M2 1000 2 8000 1 $water
M3 7000 0.8 8000 0.2 $air
ctme 720
```

A.3 Electrical Schematics

A.3.a Board Overview and Interconnection

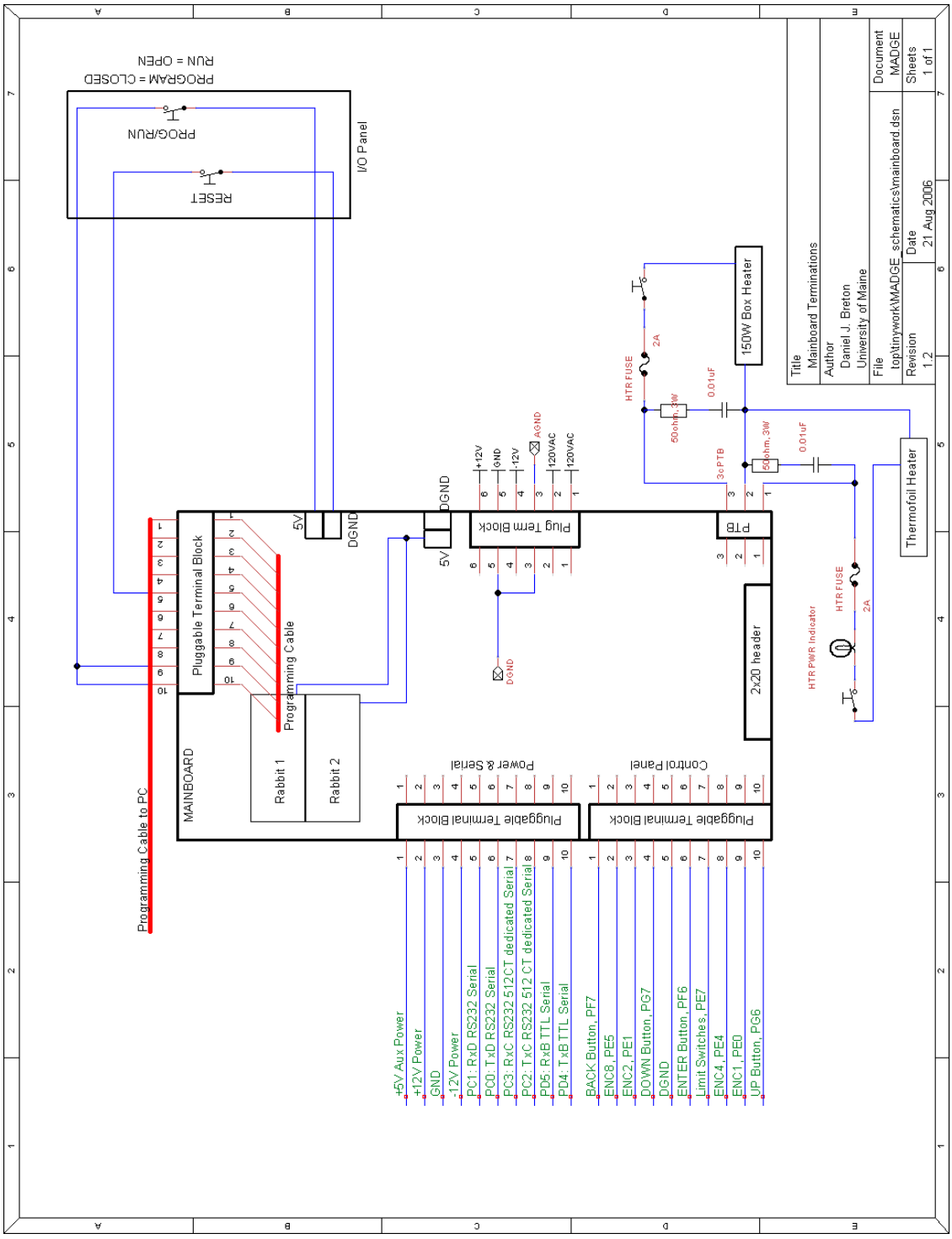

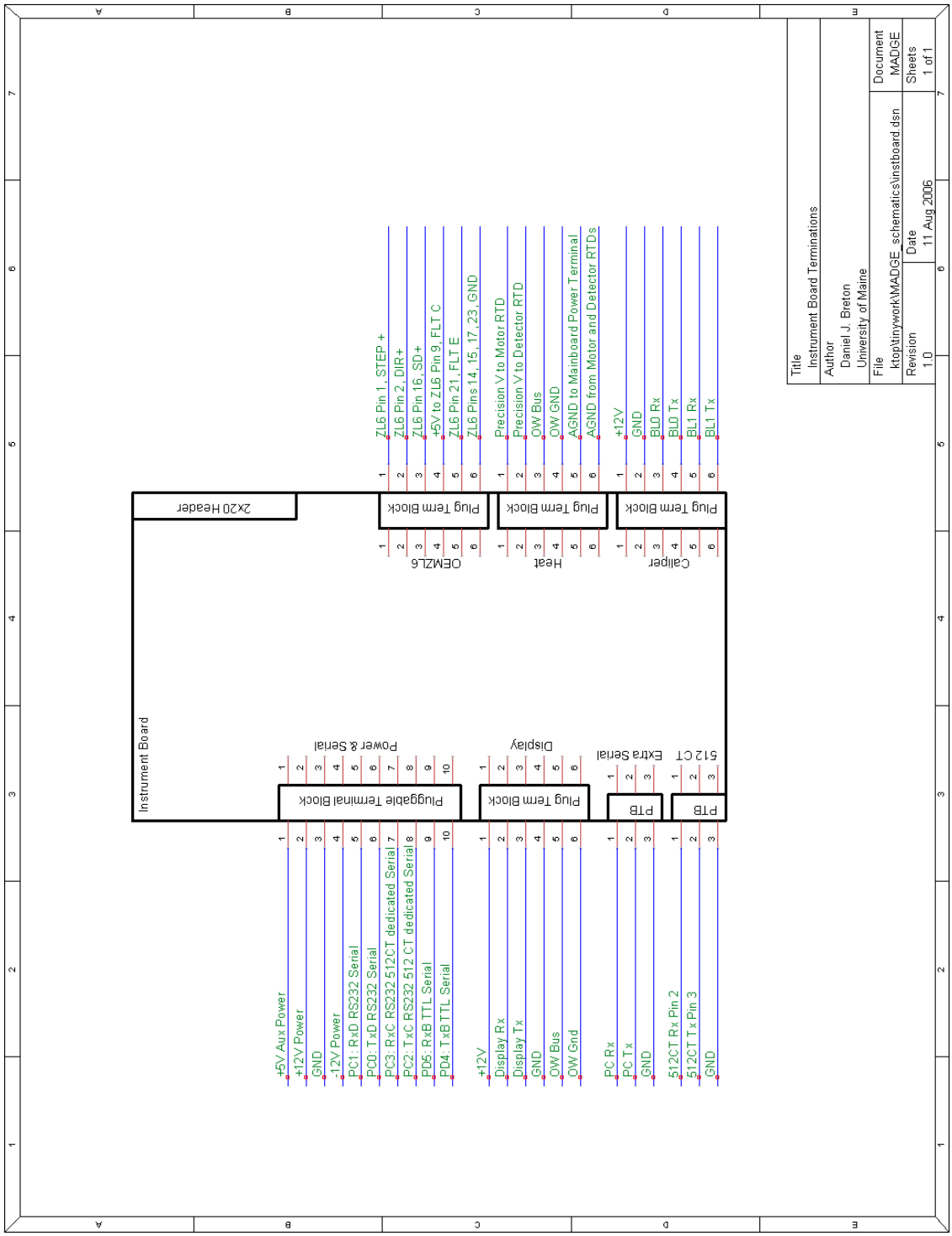
Instrument Board
2x20 Header
Plug Term Block
OEMZL6
Heat
Caliper
ZL6 Pin 1, STEP +
ZL6 Pin 2, DIR+
ZL6 Pin 16, SD+
+5V to ZL6 Pin 9, FLT C
ZL6 Pin 21, FLT E
ZL6 Pins 14, 15, 17, 23, GND
Precision V to Motor RTD
Precision V to Detector RTD
OW Bus
OW GND
AGND to Mainboard Power Terminal
AGND from Motor and Detector RTDs
+12V
GND
BL0 Rx
BL0 Tx
BL1 Rx
BL1 Tx
Pluggable Terminal Block
Power & Serial
Plug Term Block
Display
PTB
Extra Serial
512 CT
+5V Aux Power
+12V Power
GND
-12V Power
PC1: RxD RS232 Serial
PC0: TxD RS232 Serial
PC3: RxC RS232 512CT dedicated Serial
PC2: TxC RS232 512 CT dedicated Serial
PD5: RxB TTL Serial
PD4: TxB TTL Serial
+12V
Display Rx
Display Tx
GND
OW Bus
OW Gnd
PC Rx
PC Tx
GND
512CT Rx Pin 2
512CT Tx Pin 3
GND
Title
Instrument Board Terminations
Author
Daniel J. Breton
University of Maine
File
ktop\tinywork\MADGE_schematics\instboard.dsn
Document
MADGE
Revision
1.0
Date
11 Aug 2006
Sheets
1 of 1

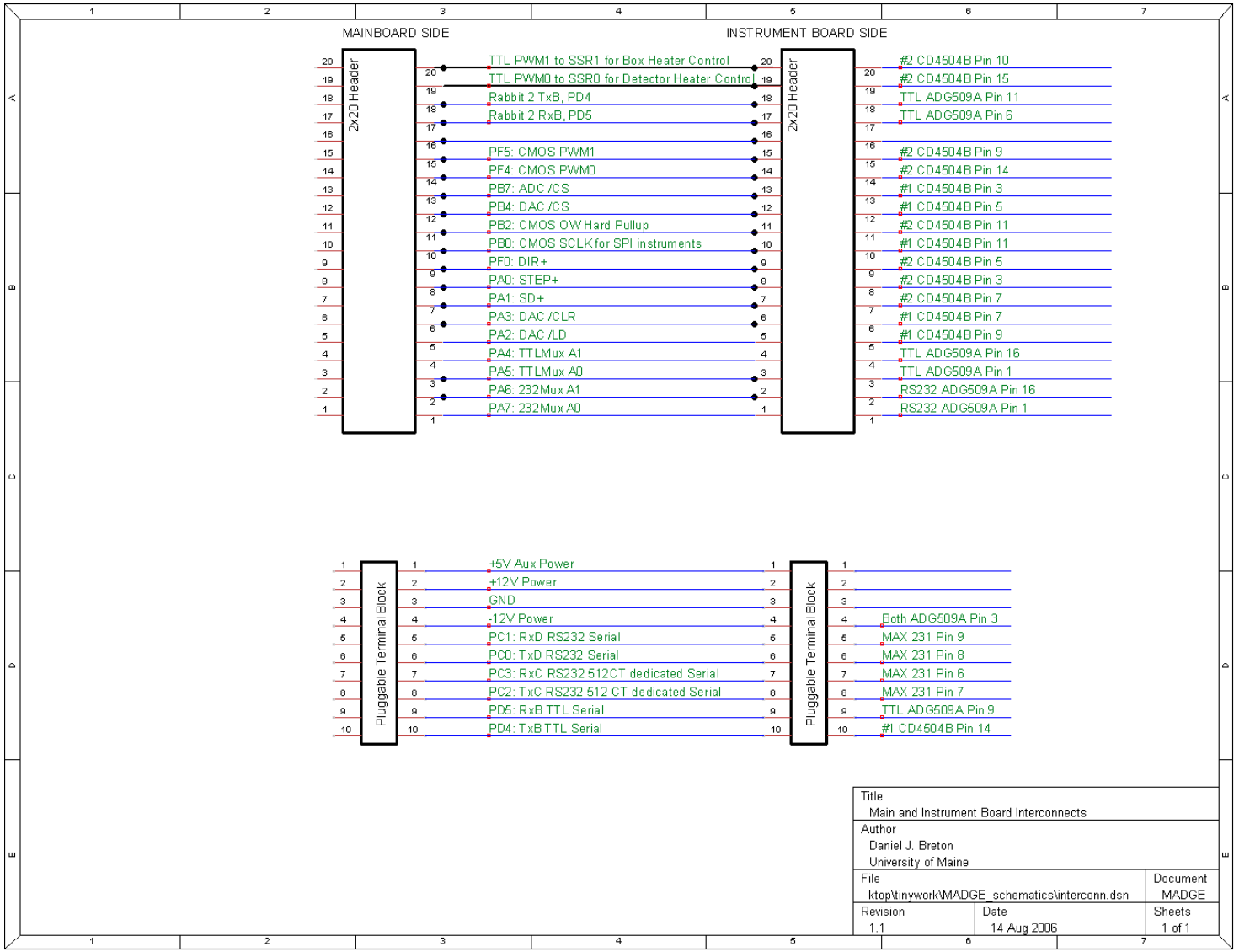
MAINBOARD SIDE
INSTRUMENT BOARD SIDE
2x20 Header
2x20 Header
TTL PWM1 to SSR1 for Box Heater Control
TTL PWM0 to SSR0 for Detector Heater Control
Rabbit 2 TxB, PD4
Rabbit 2 RxB, PD5
PF5: CMOS PWM1
PF4: CMOS PWM0
PB7: ADC /CS
PB4: DAC /CS
PB2: CMOS OW Hard Pullup
PB0: CMOS SCLK for SPI instruments
PF0: DIR+
PA0: STEP+
PA1: SD+
PA3: DAC /CLR
PA2: DAC /LD
PA4: TTLMux A1
PA5: TTLMux A0
PA6: 232Mux A1
PA7: 232Mux A0
#2 CD4504B Pin 10
#2 CD4504B Pin 15
TTL ADG509A Pin 11
TTL ADG509A Pin 6
#2 CD4504B Pin 9
#2 CD4504B Pin 14
#1 CD4504B Pin 3
#1 CD4504B Pin 5
#2 CD4504B Pin 11
#1 CD4504B Pin 11
#2 CD4504B Pin 5
#2 CD4504B Pin 3
#2 CD4504B Pin 7
#1 CD4504B Pin 7
#1 CD4504B Pin 9
TTL ADG509A Pin 16
TTL ADG509A Pin 1
RS232 ADG509A Pin 16
RS232 ADG509A Pin 1
Pluggable Terminal Block
Pluggable Terminal Block
+5V Aux Power
+12V Power
GND
-12V Power
PC1: RxD RS232 Serial
PC0: TxD RS232 Serial
PC3: RxC RS232 512CT dedicated Serial
PC2: TxC RS232 512 CT dedicated Serial
PD5: RxB TTL Serial
PD4: TxB TTL Serial
Both ADG509A Pin 3
MAX 231 Pin 9
MAX 231 Pin 8
MAX 231 Pin 6
MAX 231 Pin 7
TTL ADG509A Pin 9
#1 CD4504B Pin 14
Title
Main and Instrument Board Interconnects
Author
Daniel J. Breton
University of Maine
File
ktop\tinywork\MADGE_schematics\interconn.dsn
Document
MADGE
Revision
1.1
Date
14 Aug 2006
Sheets
1 of 1

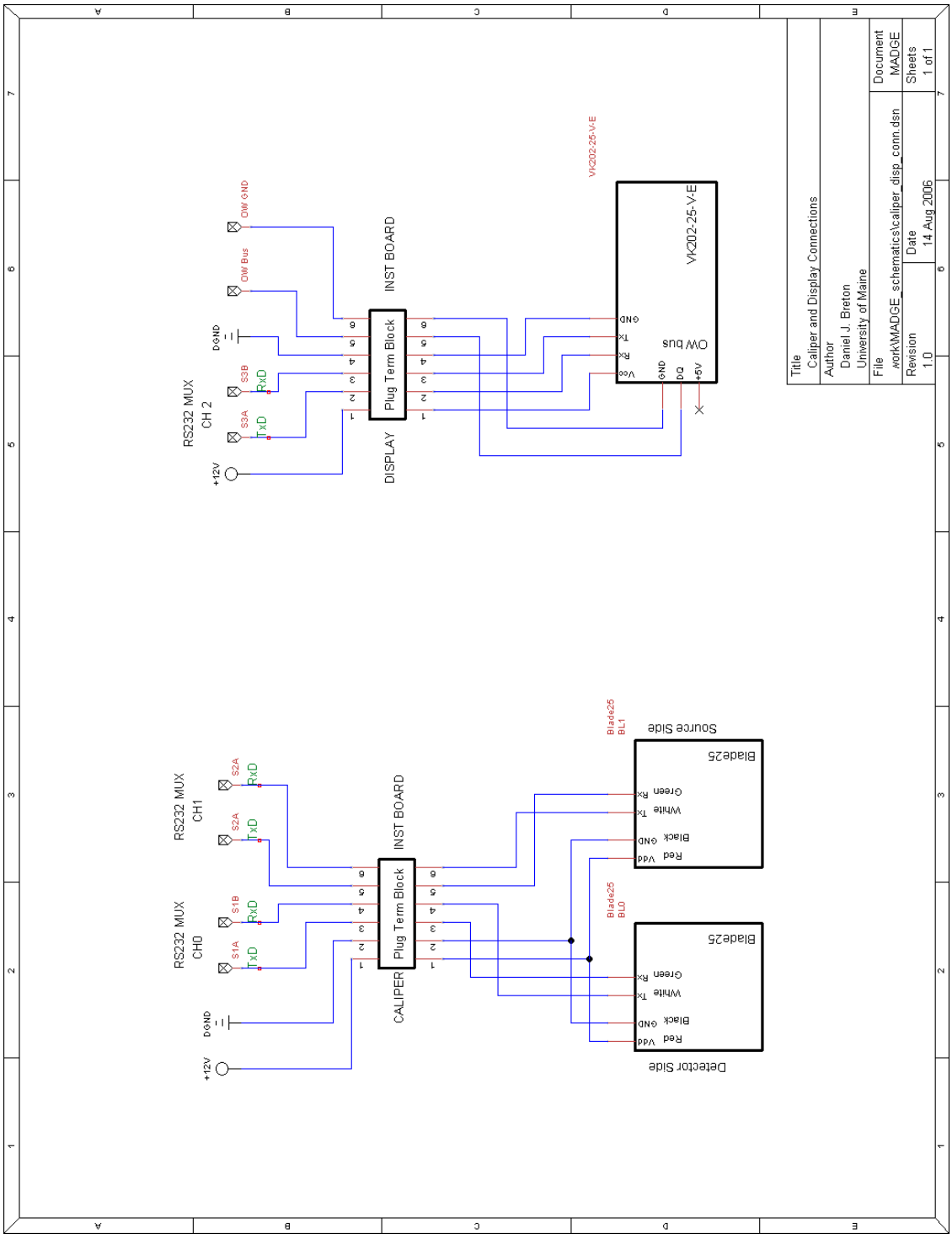
Title
Caliper and Display Connections
Author
Daniel J. Breton
University of Maine
File
work\MADGE_schematics\caliper_disp_conn.dsn
Document
MADGE
Revision
1.0
Date
14 Aug 2006
Sheets
1 of 1
VK202-25-V-E
OW GND
OW Bus
DGND
S3B
RxD
S3A
TxD
+12V
RS232 MUX
CH 2
INST BOARD
Plug Term Block
DISPLAY
GND
TX
RX
Vcc
DQ
+5V
S2A
S1B
S1A
CH1
CH0
CALIPER
Blade25
BL1
BL0
Source Side
Detector Side
Red
Black
White
Green
Vdd

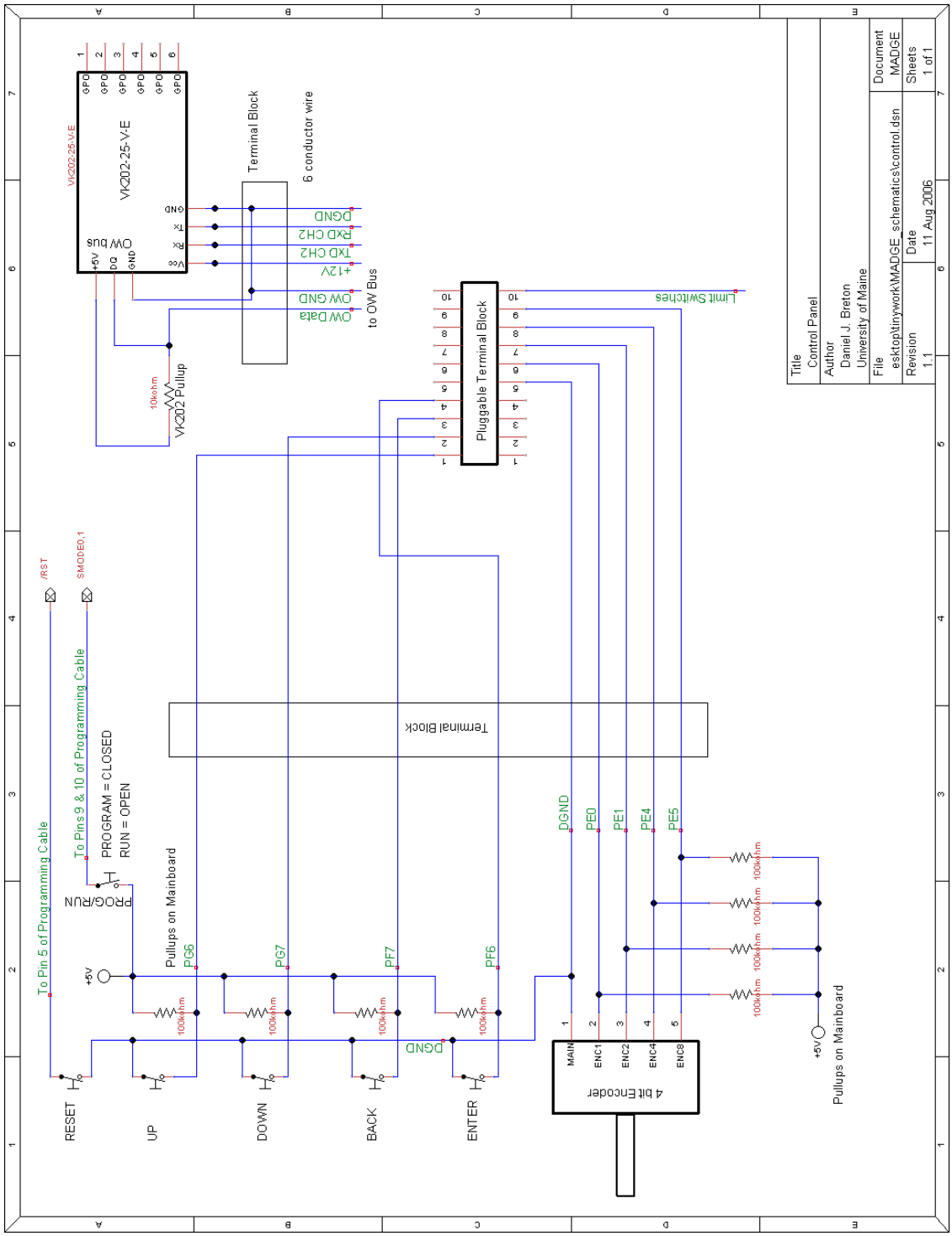
VK202-25-V-E
VK202-25-V-E
OW bus
+5V
DQ
GND
Vcc
Rx
Tx
GND
Terminal Block
6 conductor wire
DGND
RXD CH2
TXD CH2
+12V
OW GND
OW Data
to OW Bus
10kohm
VK202 Pullup
Pluggable Terminal Block
Limit Switches
Terminal Block
/RST
SMODE0,1
To Pin 5 of Programming Cable
To Pins 9 & 10 of Programming Cable
PROGRAM = CLOSED
RUN = OPEN
PROG/RUN
+5V
Pullups on Mainboard
PG6
PG7
PF7
PF6
100kohm
DGND
DGND
PE0
PE1
PE4
PE5
MAIN
ENC1
ENC2
ENC4
ENC8
4 bit Encoder
+5V
Pullups on Mainboard
RESET
UP
DOWN
BACK
ENTER
Title
Control Panel
Author
Daniel J. Breton
University of Maine
File
esktop\tinywork\MADGE_schematics\control.dsn
Document
MADGE
Revision
1.1
Date
11 Aug 2006
Sheets
1 of 1

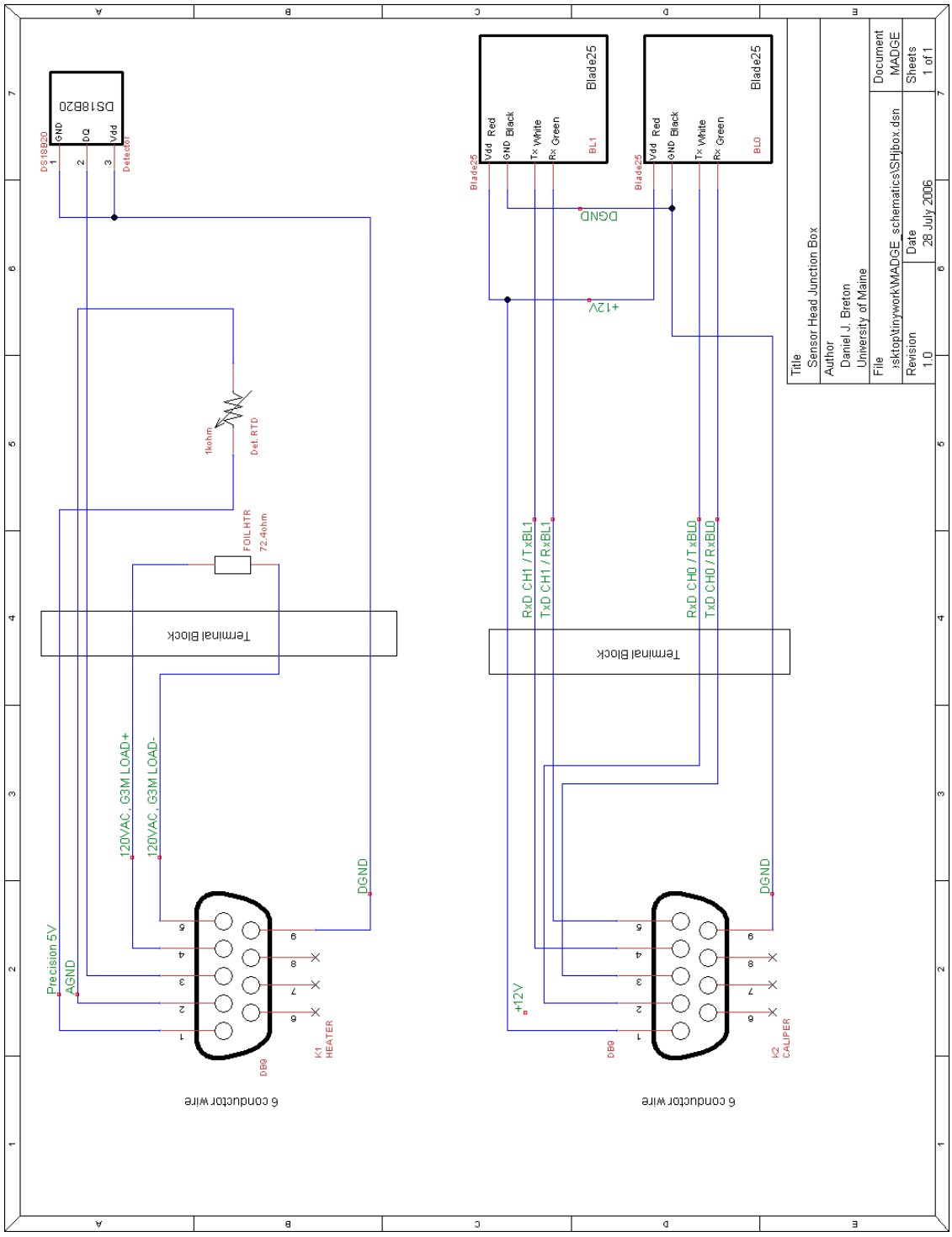
DS18B20
GND
DQ
Vdd
Detect
1kohm
Det.RTD
FOIL HTR
72.4ohm
Terminal Block
120VAC, G3M LOAD+
120VAC, G3M LOAD-
Precision 5V
AGND
DGND
DB9
K1
HEATER
6 conductor wire
Blade25
Vdd Red
GND Black
Tx White
Rx Green
BL1
BL0
+12V
RxD CH1 / TxBL1
TxD CH1 / RxBL1
RxD CH0 / TxBL0
TxD CH0 / RxBL0
K2
CALIPER
Title
Sensor Head Junction Box
Author
Daniel J. Breton
University of Maine
File
:sktop\tinywork\MADGE_schematics\SHjbox.dsn
Document
MADGE
Revision
1.0
Date
28 July 2006
Sheets
1 of 1

A.3.b Microcontroller and Instrumentation

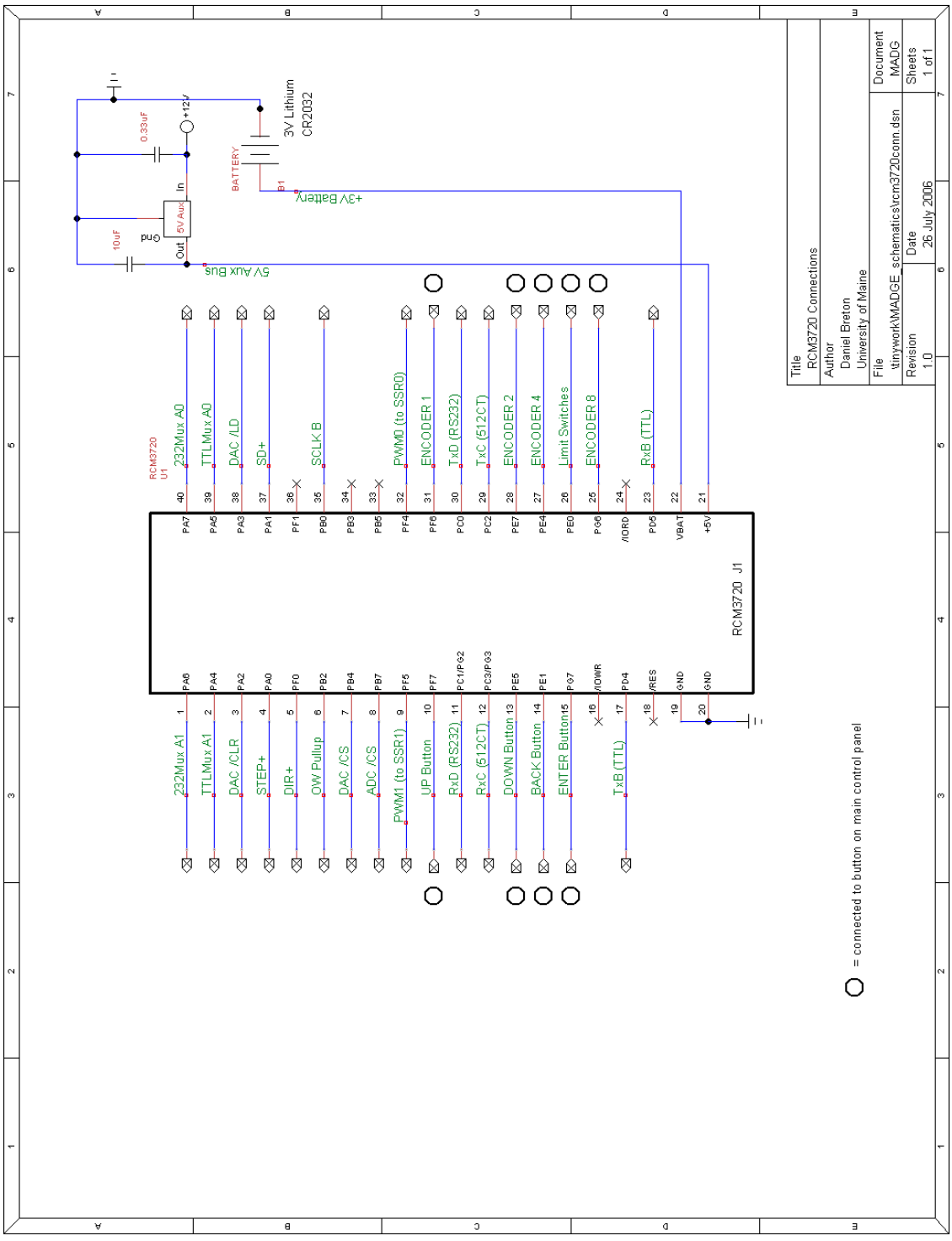

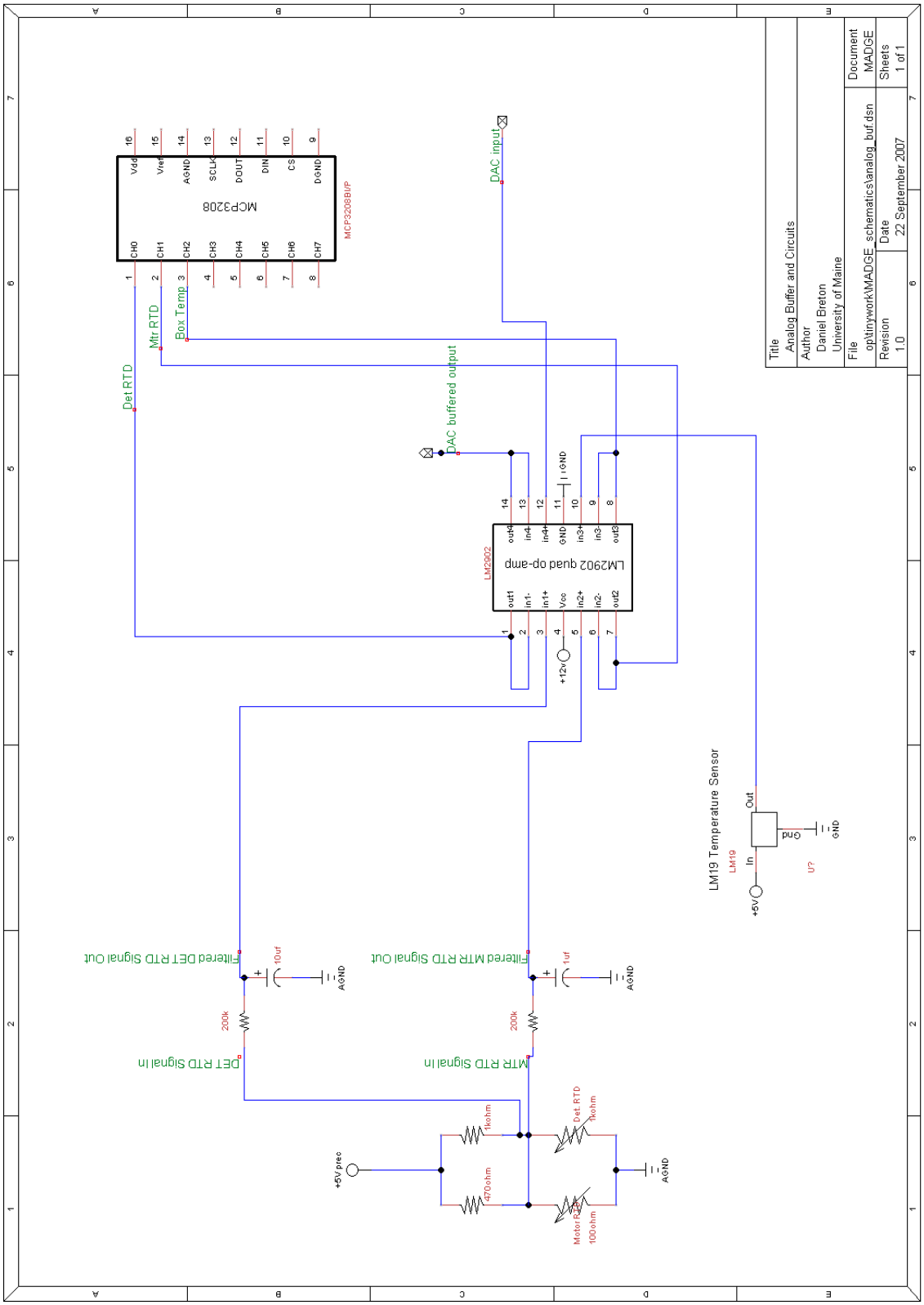
Title
Analog Buffer and Circuits
Author
Daniel Breton
University of Maine
File
opt\tinywork\MADGE_schematics\analog_buf.dsn
Document
MADGE
Revision
1.0
Date
22 September 2007
Sheets
1 of 1
MCP3208
MCP3208BUP
Vdd
Vref
AGND
SCLK
DOUT
DIN
CS
DGND
CH0
CH1
CH2
CH3
CH4
CH5
CH6
CH7
DAC input
DAC buffered output
Box Temp
Mtr RTD
Det RTD
LM2902 quad op-amp
LM2902
out4
in4-
in4+
GND
in3+
in3-
out3
out1
in1-
in1+
Vcc
in2+
in2-
out2
+12v
LM19 Temperature Sensor
LM19
Out
In
Gnd
+5v
GND
U?
Filtered DET RTD Signal Out
Filtered MTR RTD Signal Out
10uf
1uf
AGND
200k
DET RTD Signal In
MTR RTD Signal In
1kohm
Det RTD
1kohm
+5V prec
470ohm
Motor RTD
100ohm

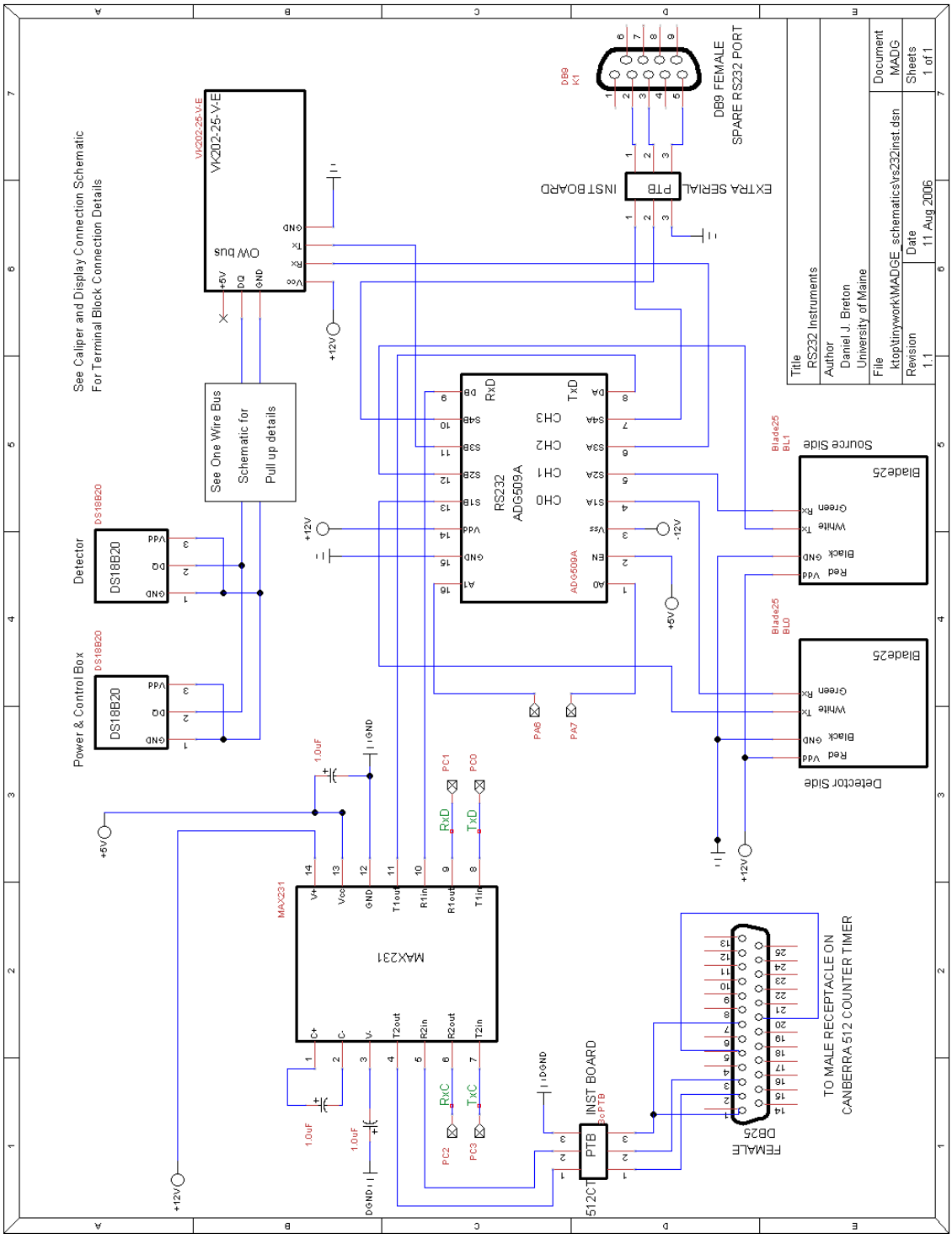
See Caliper and Display Connection Schematic
For Terminal Block Connection Details
VK202-25-V-E
OW bus
See One Wire Bus
Schematic for
Pull up details
Power & Control Box
Detector
DS18B20
RS232
ADG509A
CH0
CH1
CH2
CH3
RxD
TxD
MAX231
INST BOARD
PTB
512CT
FEMALE
DB25
TO MALE RECEPTACLE ON
CANBERRA 512 COUNTER TIMER
DB9 FEMALE
SPARE RS232 PORT
EXTRA SERIAL
INST BOARD
Source Side
Detector Side
Blade25
Title
RS232 Instruments
Author
Daniel J. Breton
University of Maine
File
ktop\tinywork\MADGE schematics\rs232inst.dsn
Date
11 Aug 2006
Revision
1.1
Document
MADG
Sheets
1 of 1

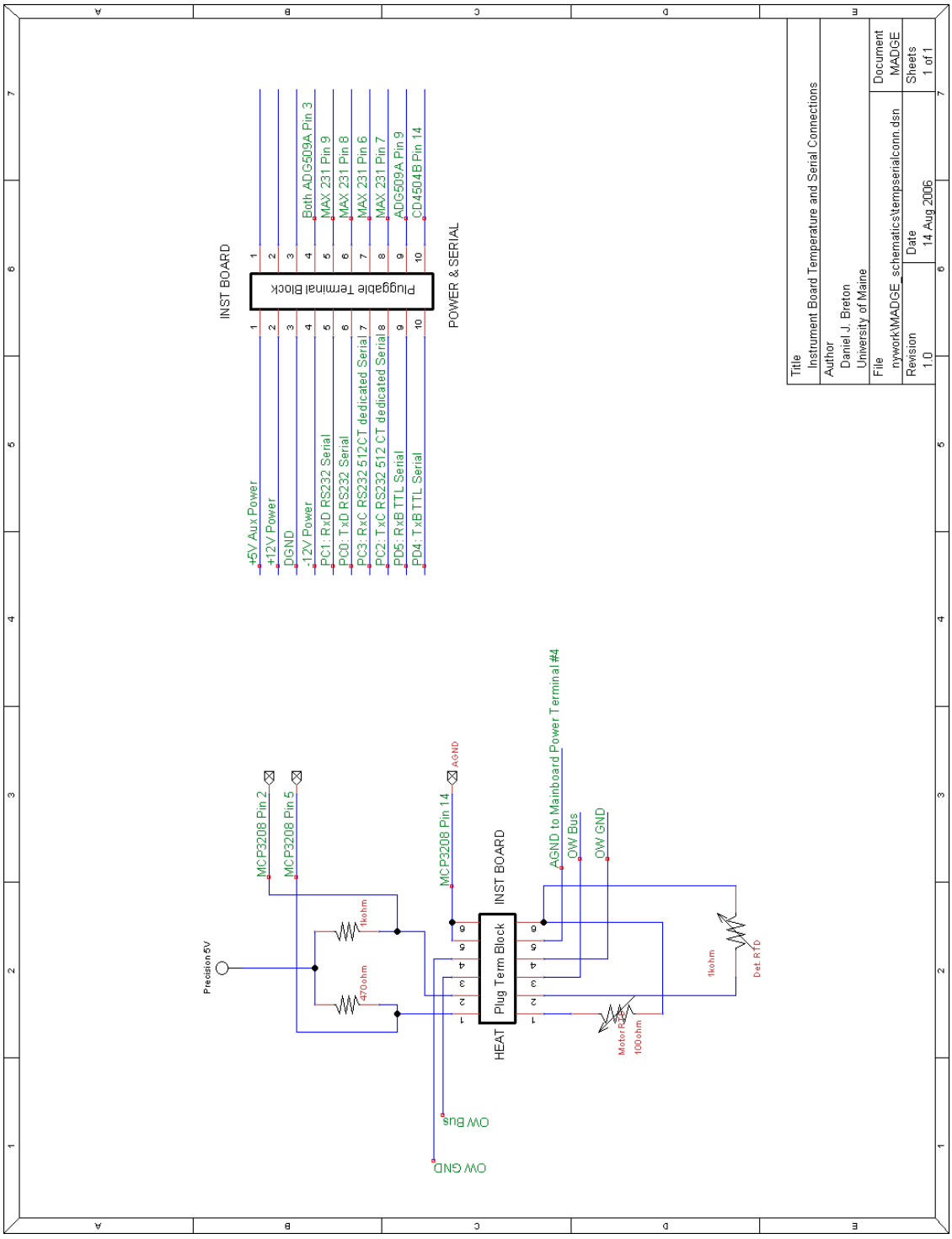
INST BOARD
Pluggable Terminal Block
POWER & SERIAL
+5V Aux Power
+12V Power
DGND
-12V Power
PC1: RxD RS232 Serial
PC0: TxD RS232 Serial
PC3: RxC RS232 512CT dedicated Serial
PC2: TxC RS232 512 CT dedicated Serial
PD5: RxB TTL Serial
PD4: TxB TTL Serial
Both ADG509A Pin 3
MAX 231 Pin 9
MAX 231 Pin 8
MAX 231 Pin 6
MAX 231 Pin 7
ADG509A Pin 9
CD4504B Pin 14
MCP3208 Pin 2
MCP3208 Pin 5
MCP3208 Pin 14
AGND
AGND to Mainboard Power Terminal #4
OW Bus
OW GND
Precision 5V
1kohm
470ohm
Plug Term Block
INST BOARD
HEAT
Motor RTD
100ohm
1kohm
Det. RTD
OW Bus
OW GND
Title
Instrument Board Temperature and Serial Connections
Author
Daniel J. Breton
University of Maine
File
nywork\MADGE_schematics\tempserialconn.dsn
Document
MADGE
Revision
1.0
Date
14 Aug 2006
Sheets
1 of 1

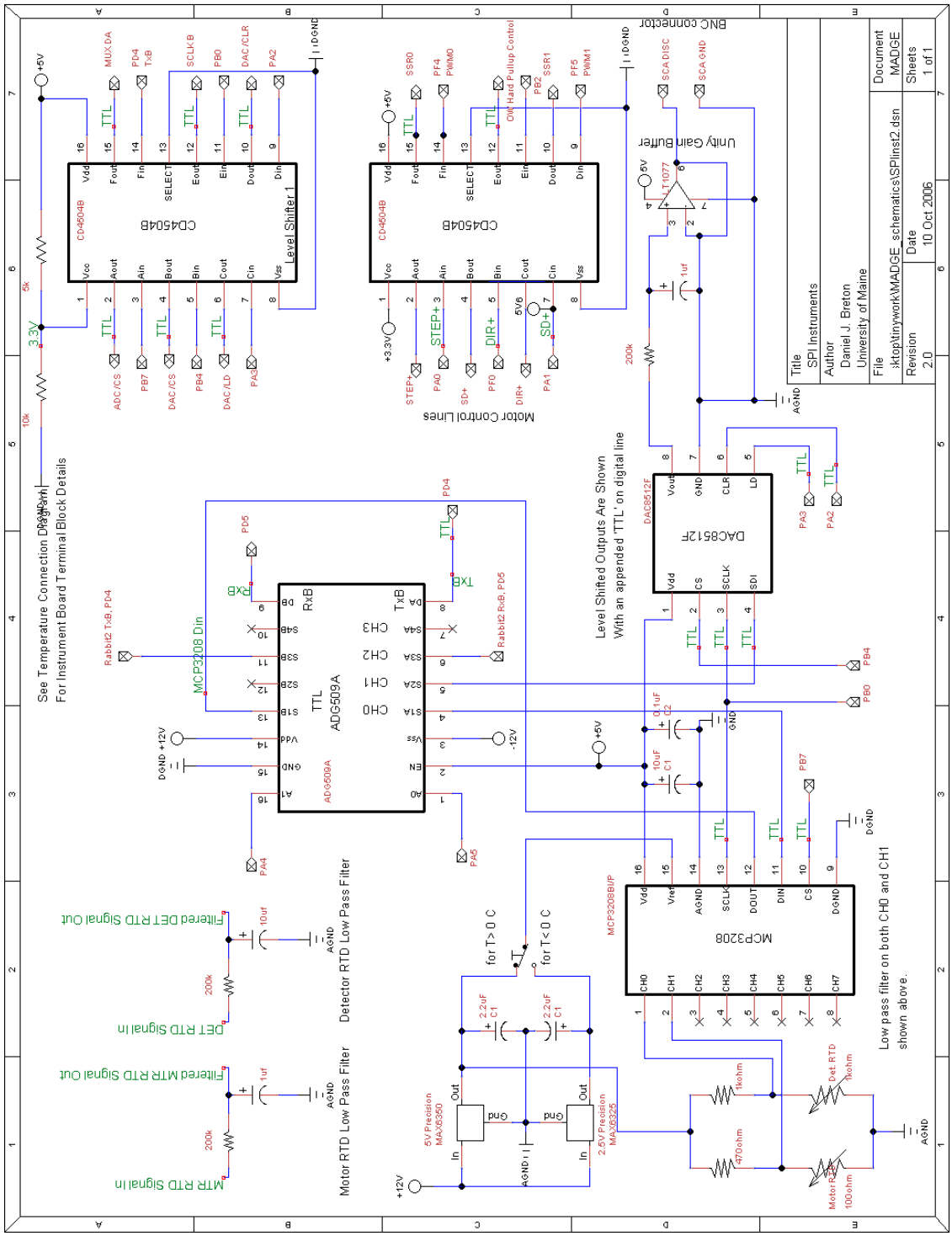
See Temperature Connection Diagram
For Instrument Board Terminal Block Details
Level Shifter 1
CD4504B
Motor Control Lines
Unity Gain Buffer
BNC connector
Level Shifted Outputs Are Shown
With an appended 'TTL' on digital line
ADG509A
MCP3208
DAC8512F
Rabbit2 TxB, PD4
Rabbit2 RxB, PD5
MCP3208 Din
Detector RTD Low Pass Filter
Motor RTD Low Pass Filter
Filtered DET RTD Signal Out
DET RTD Signal In
Filtered MTR RTD Signal Out
MTR RTD Signal In
for T> 0 C
for T< 0 C
Low pass filter on both CH0 and CH1
shown above.
Det. RTD
Motor RTD
Title
SPI Instruments
Author
Daniel J. Breton
University of Maine
File
Revision
2.0
Date
10 Oct 2006
Sheets
1 of 1

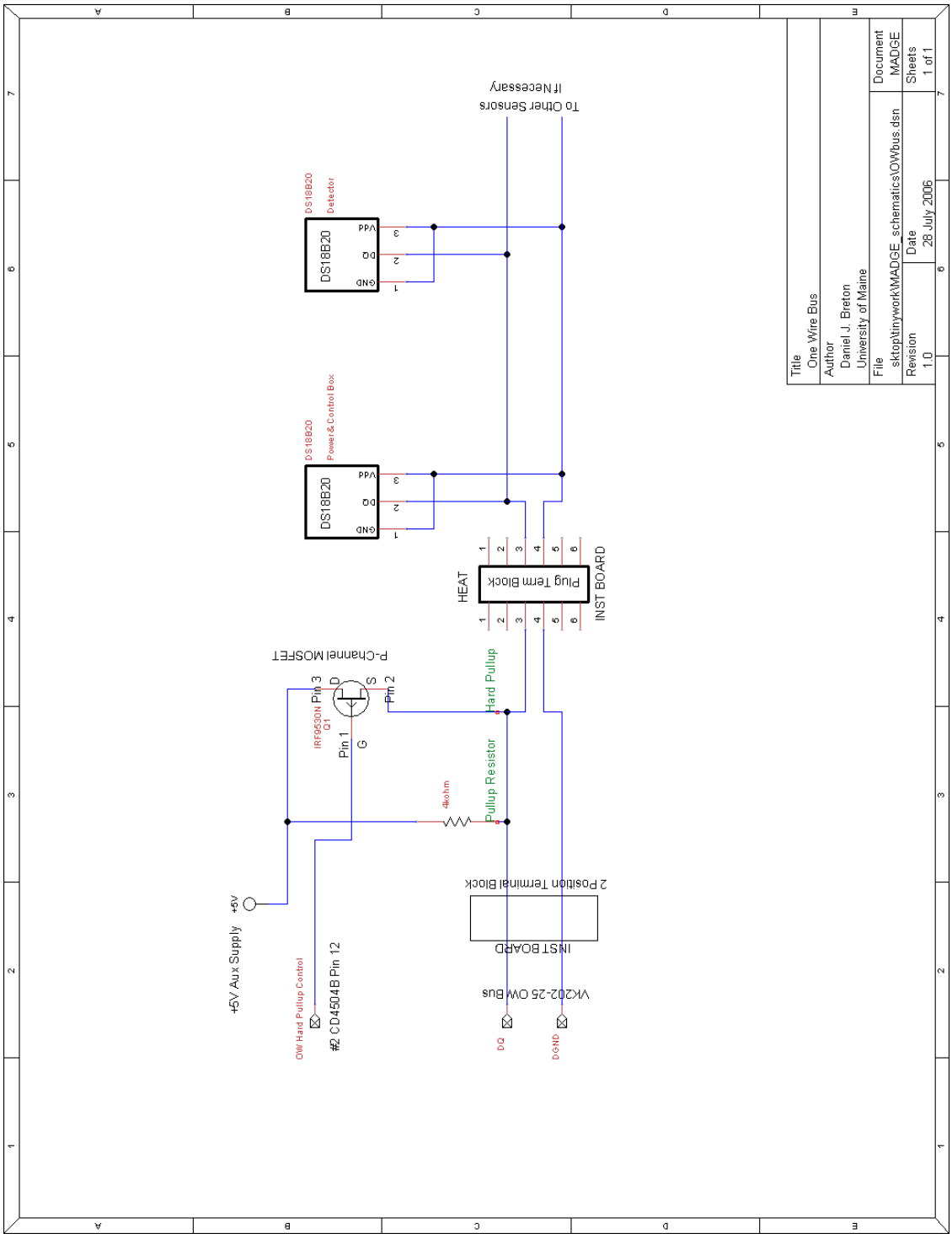
To Other Sensors
If Necessary
DS18B20
Detector
DS18B20
Power&Control Box
DS18B20
DS18B20
VDD
DQ
GND
HEAT
Plug Term Block
INST BOARD
P-Channel MOSFET
IRF9530N
Q1
Pin 3
Pin 2
Pin 1
D
S
G
Hard Pullup
Pullup Resistor
4kohm
2 Position Terminal Block
INST BOARD
VK202-25 OW Bus
DQ
DGND
+5V Aux Supply
+5v
OW Hard Pullup Control
#2 CD4504B Pin 12
Title
One Wire Bus
Author
Daniel J. Breton
University of Maine
File
sktop\tinywork\MADGE_schematics\OWbus.dsn
Date
28 July 2006
Document
MADGE
Revision
1.0
Sheets
1 of 1

A.3.c High Power Systems

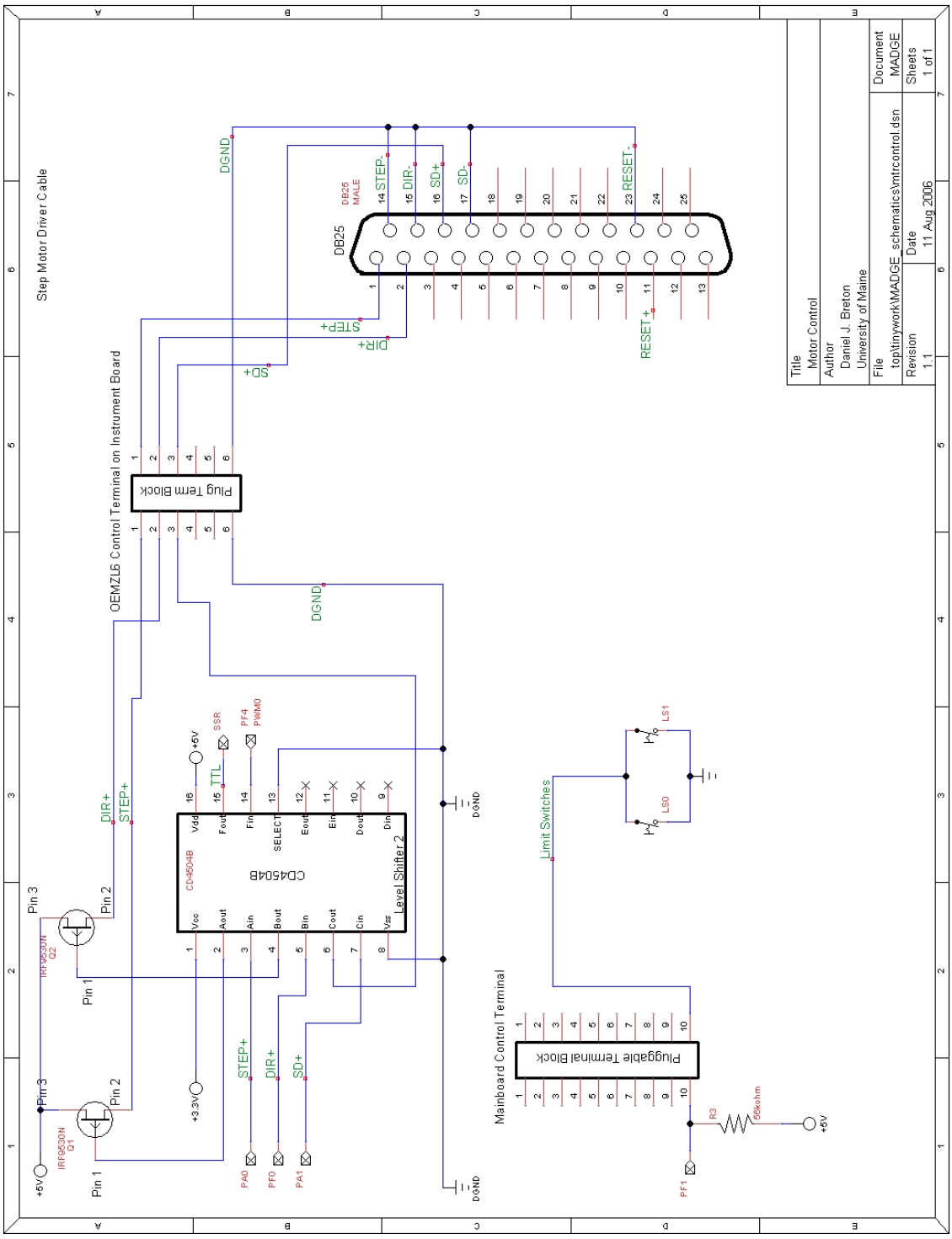

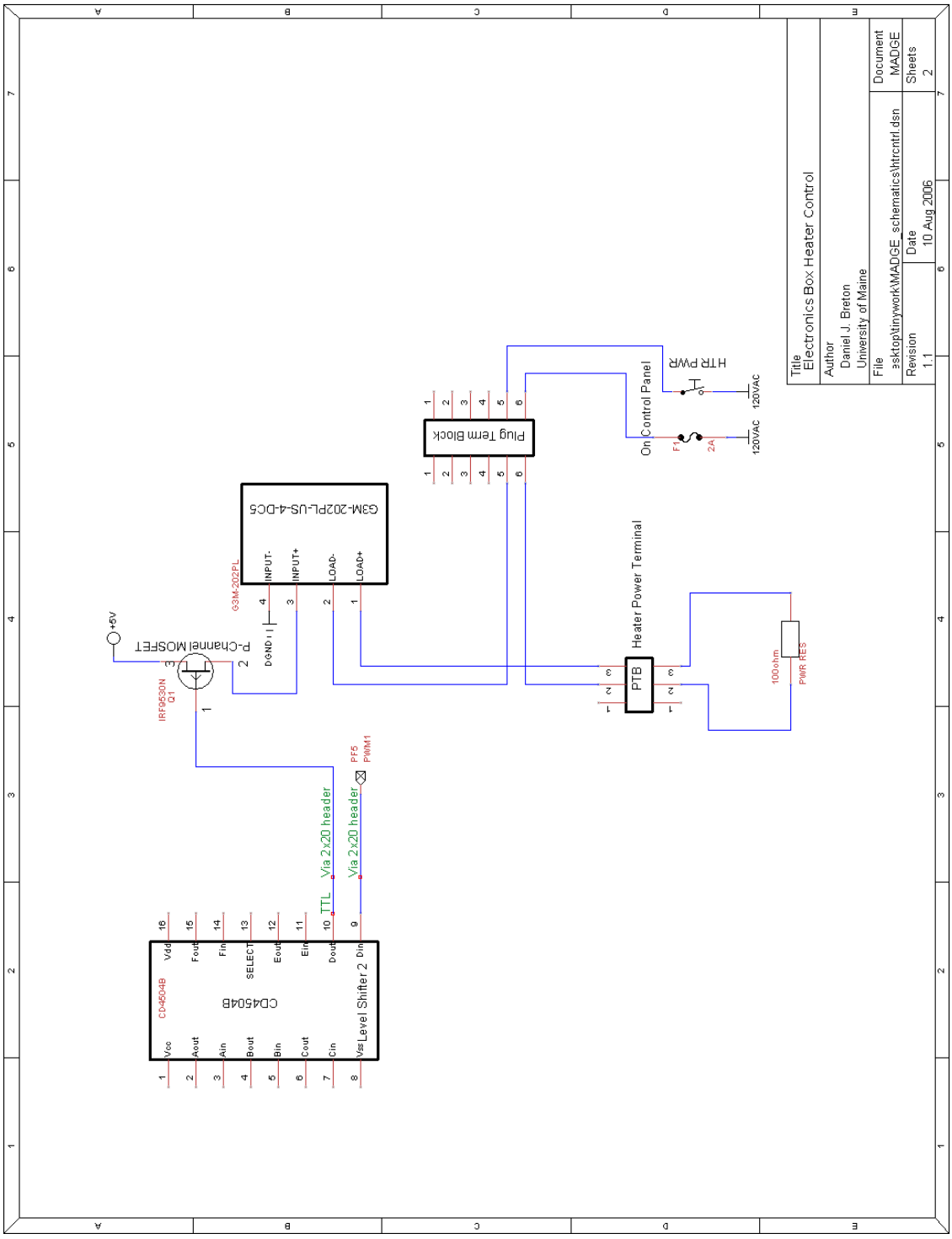
Title
Electronics Box Heater Control
Author
Daniel J. Breton
University of Maine
File
:sktop\tinywork\MADGE_schematics\htrcntrl.dsn
Document
MADGE
Revision
1.1
Date
10 Aug 2006
Sheets
2
HTR PWR
On Control Panel
F1
2A
120VAC
120VAC
Plug Term Block
G3M-202PL-US-4-DC5
G3M-202PL
INPUT-
INPUT+
LOAD-
LOAD+
+5V
P-Channel MOSFET
IRF9530N
Q1
Heater Power Terminal
PTB
100ohm
PWR RES
PF5
PWM1
Via 2x20 header
Via 2x20 header
TTL
CD4504B
Level Shifter 2
Vcc
Aout
Ain
Bout
Bin
Cout
Cin
Vss
Vdd
Fout
Fin
SELECT
Eout
Ein
Dout
Din

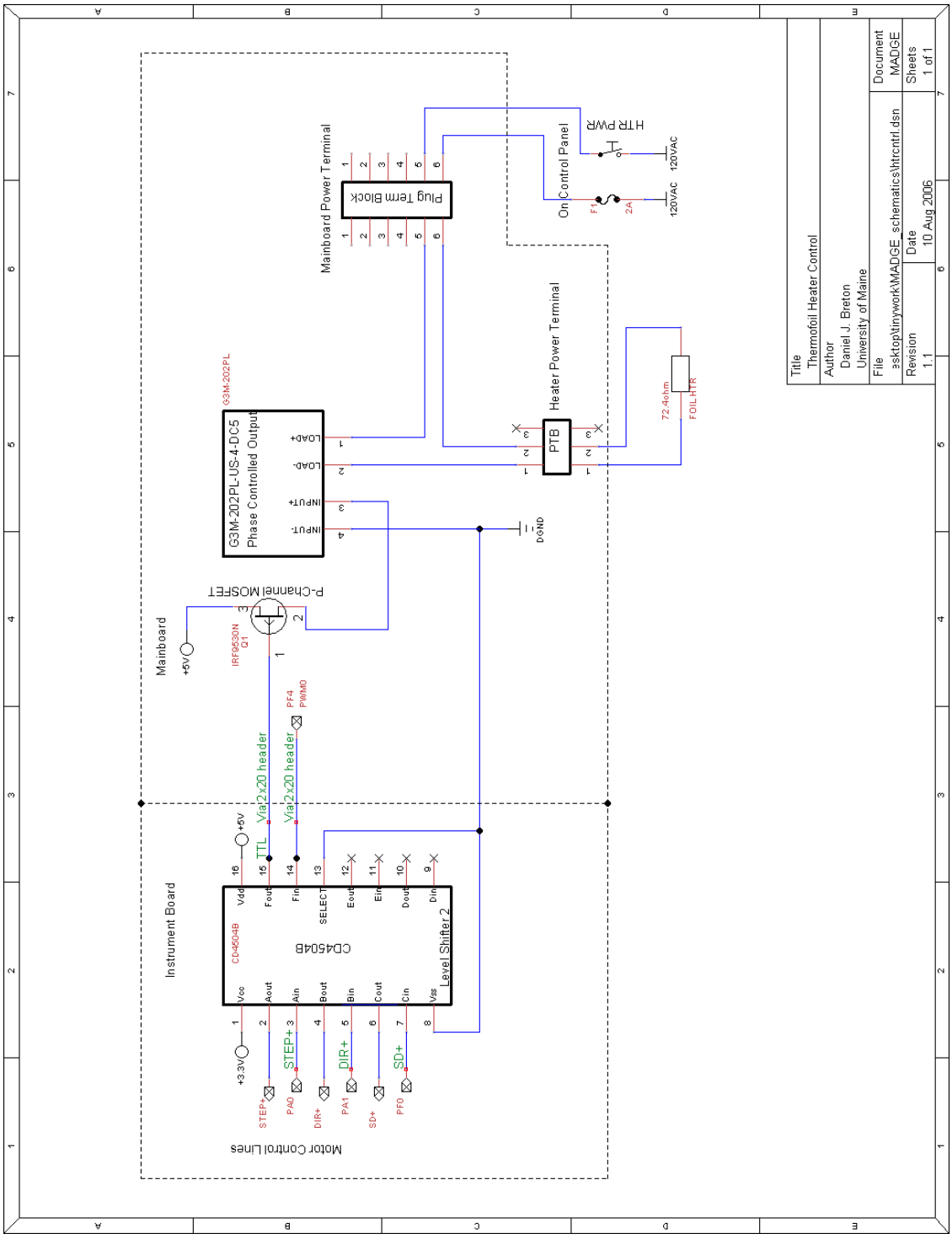
Title
Thermofoil Heater Control
Author
Daniel J. Breton
University of Maine
File
:sktop\tinywork\MADGE_schematics\htrcntrl.dsn
Date
10 Aug 2006
Revision
1.1
Document
MADGE
Sheets
1 of 1
Mainboard Power Terminal
Plug Term Block
On Control Panel
HTR PWR
F1
2A
120VAC
120VAC
Heater Power Terminal
PTB
72.4ohm
FOIL HTR
G3M-202PL
G3M-202PL-US-4-DC5
Phase Controlled Output
LOAD+
LOAD-
INPUT+
INPUT-
DGND
P-Channel MOSFET
IRF9530N
Q1
Mainboard
+5v
PF4
PWM0
Via2x20 header
Via2x20 header
TTL
+5v
Instrument Board
CD4504B
CD4504B
Level Shifter 2
Vcc
Aout
Ain
Bout
Bin
Cout
Cin
Vss
Vdd
Fout
Fin
SELECT
Eout
Ein
Dout
Din
+3.3v
STEP+
DIR+
SD+
PA0
PA1
PF0
Motor Control Lines

A.3.d Custom Made ±12V Power Supply for Canberra 512CT

Title 512 Counter Timer Power Supply		
Author Daniel Breton University of Maine Physics		Document
File \\desktop\tinywork\MADGE_schematics\512ps.dsn	Date 6 July 2006	Sheets 1 of 1
Revision 1.0		

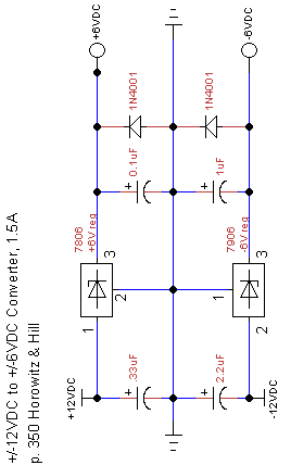

A.4 Mechanical Drawings

A.4.a Sensor Head Source Plate

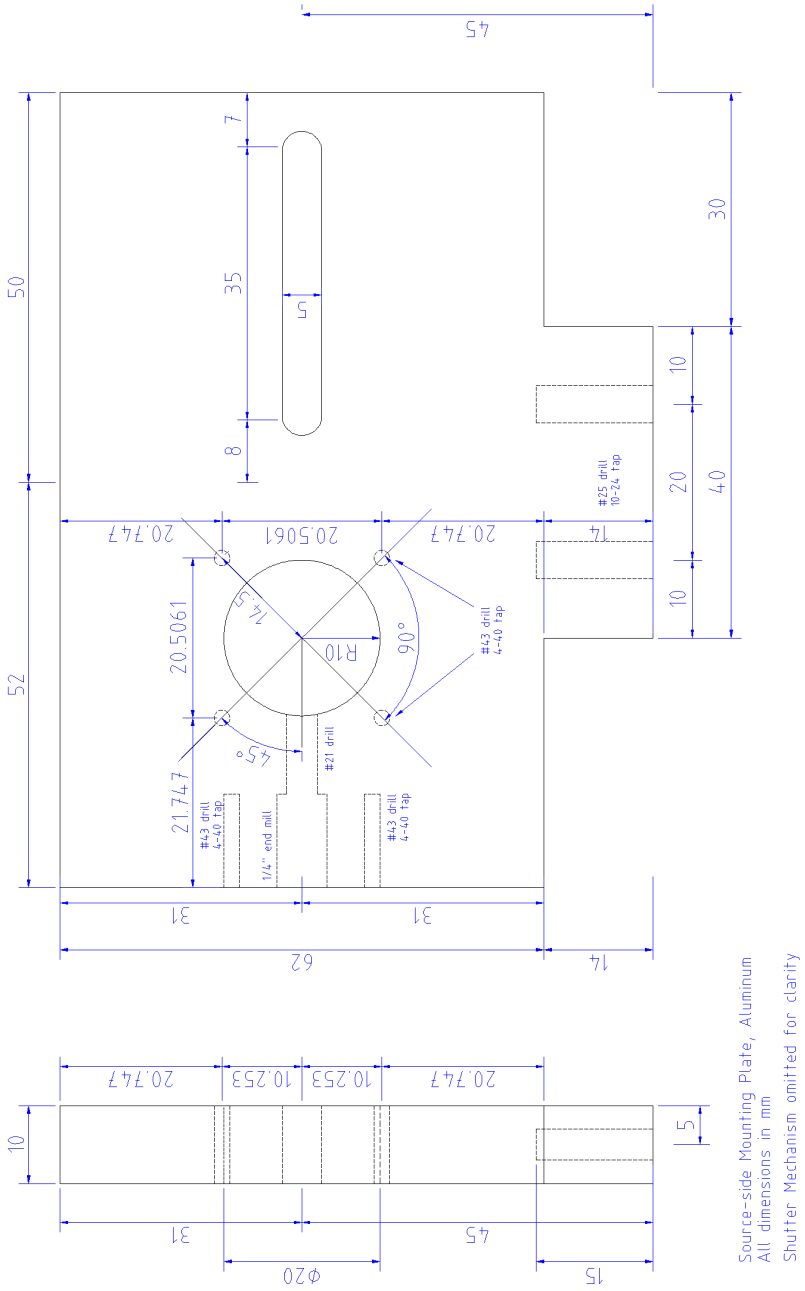

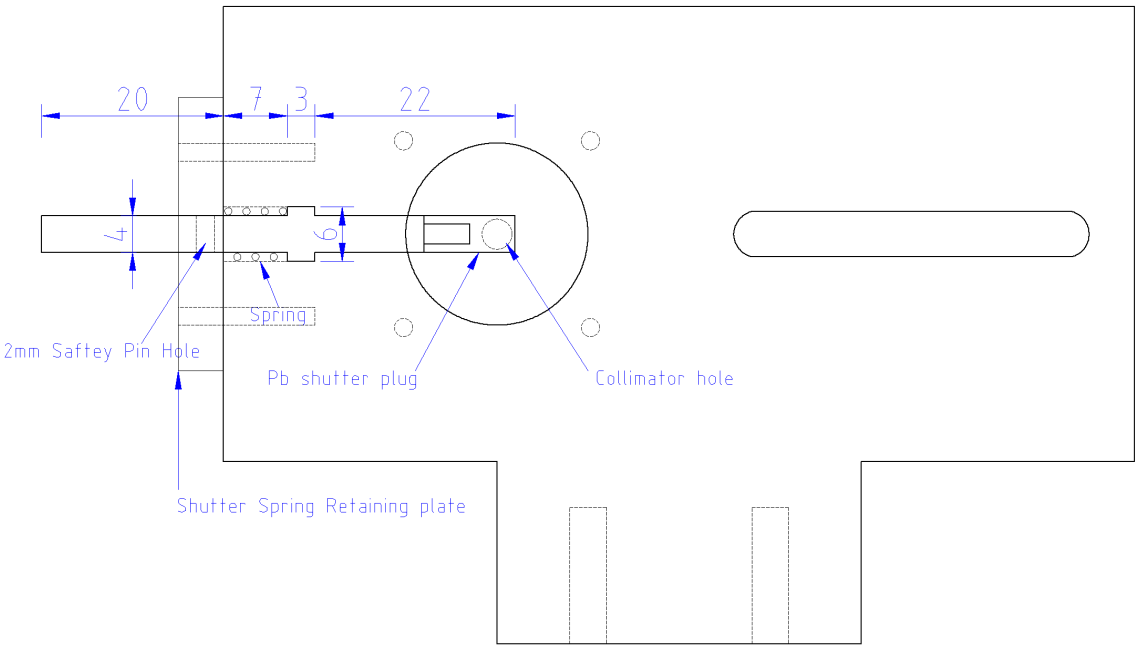

Side and top view of shutter in Source-side mounting plate. All dimensions in mm.

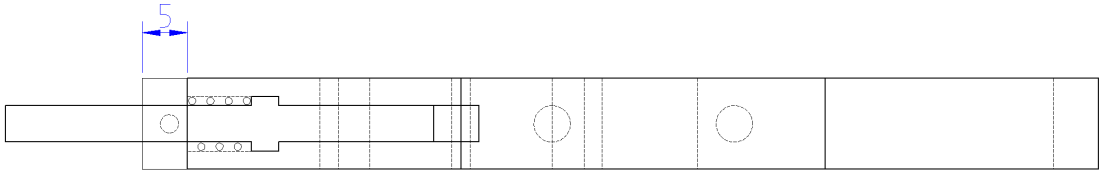

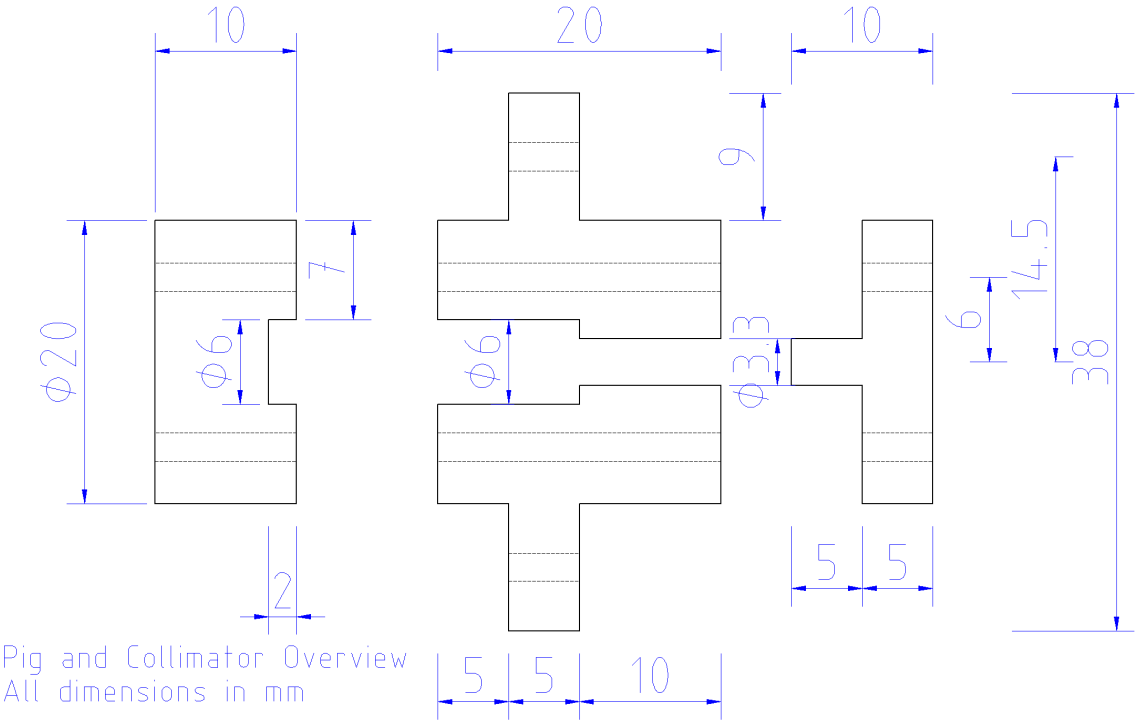

Pig and Collimator Overview
All dimensions in mm

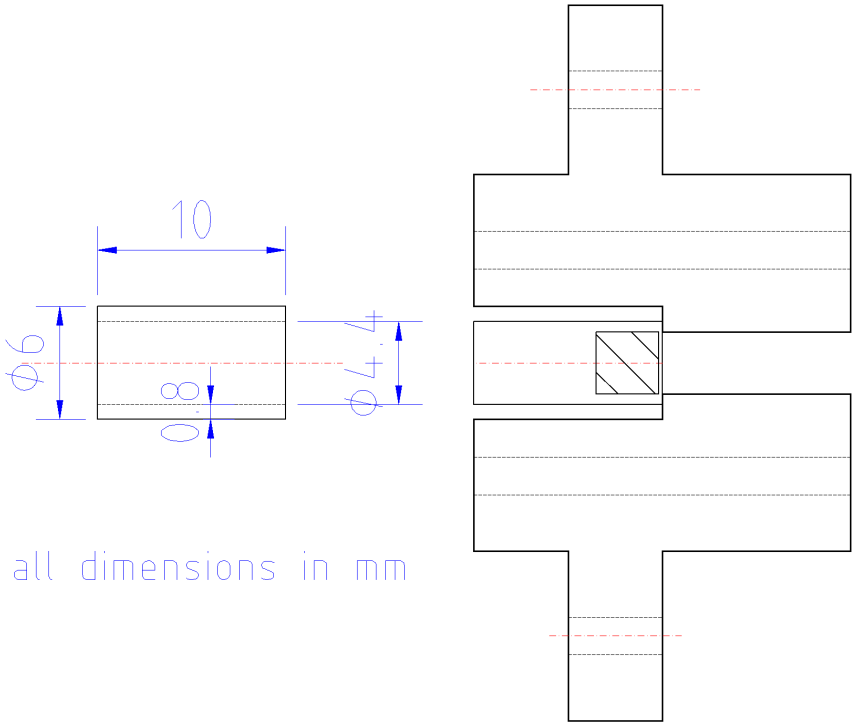

Source Collar, all dimensions in mm
Nylon

A.4.b Detector Head Plate

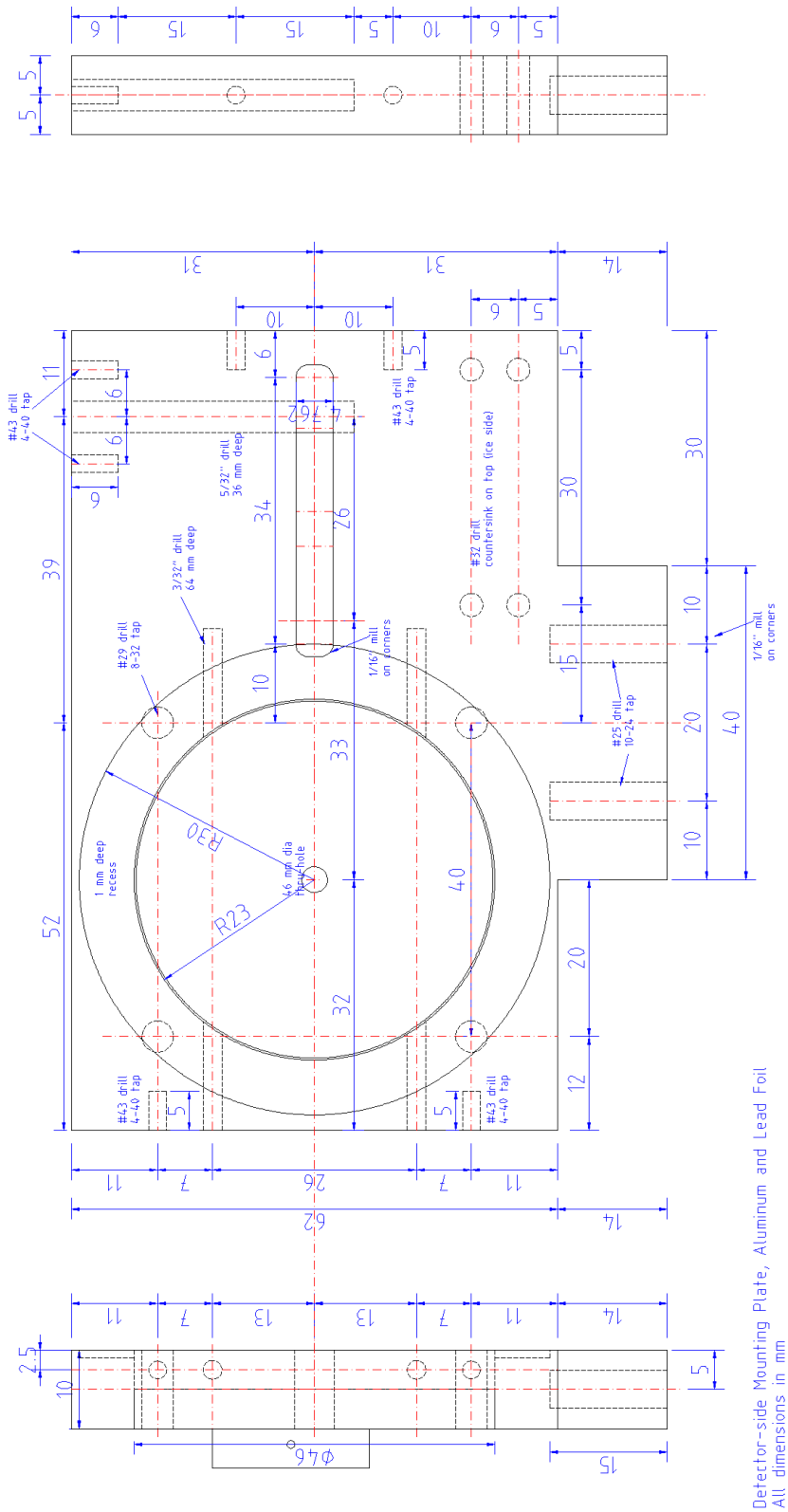

A.4.c Sensor Head Yokes

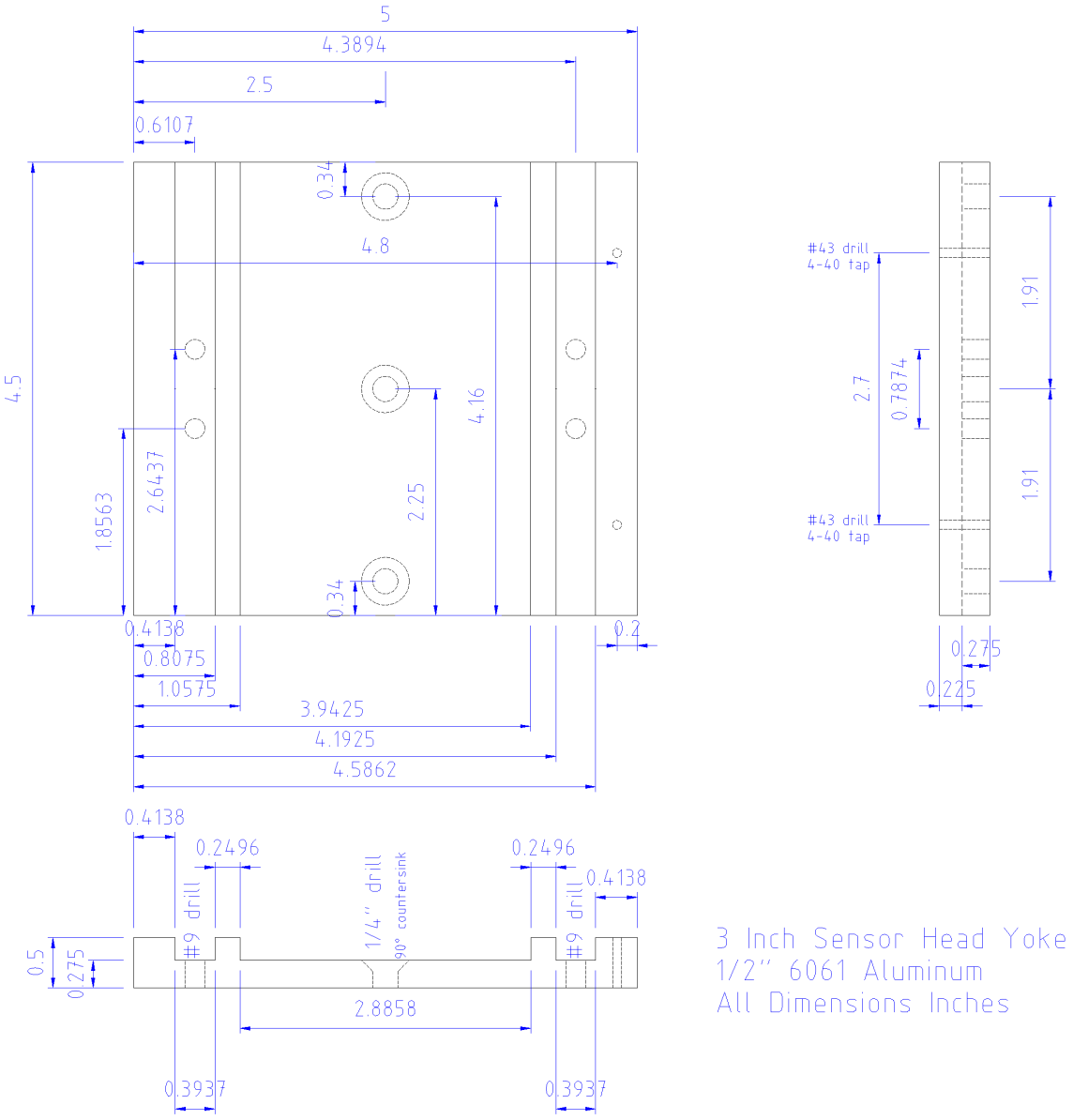

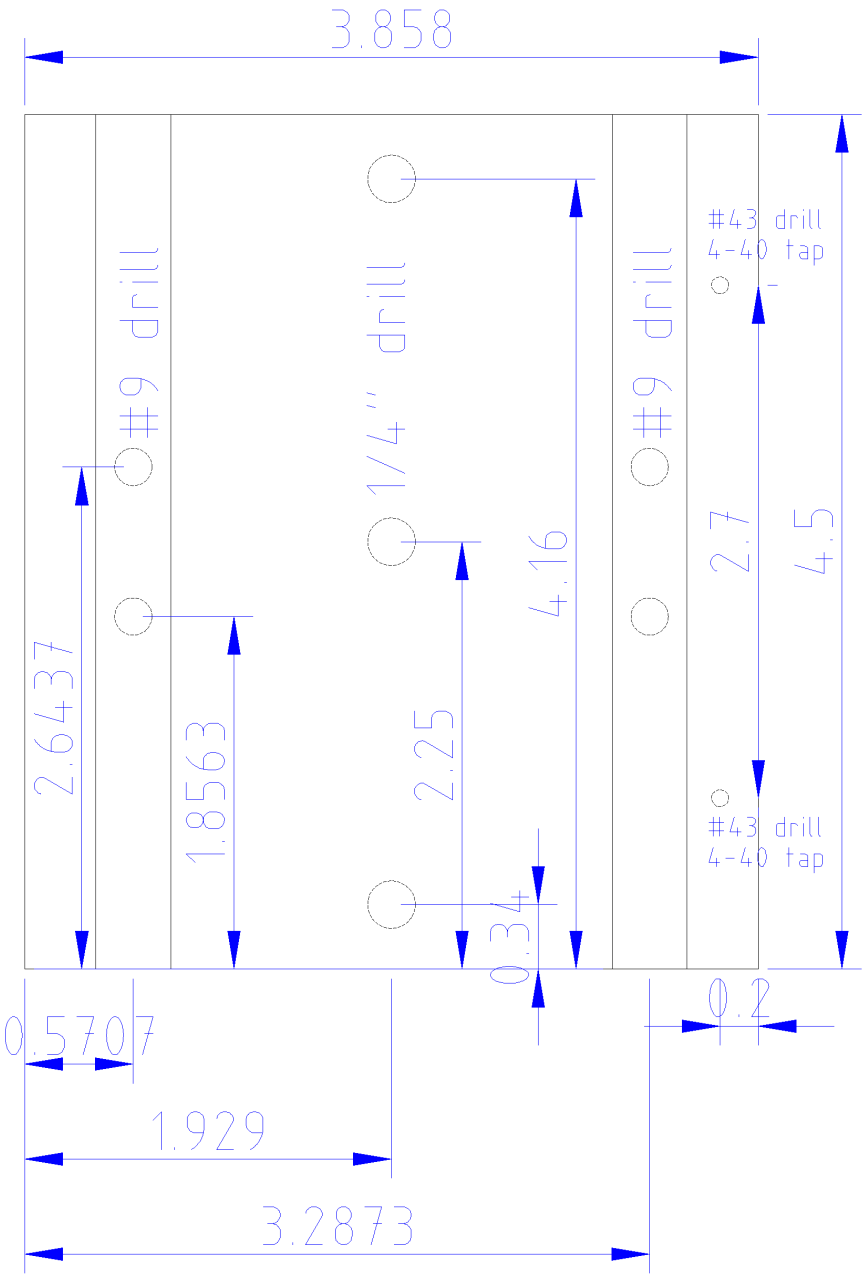

Two Inch Sensor Head Yoke
1/2'' 6061 Aluminum
All dimensions in inches

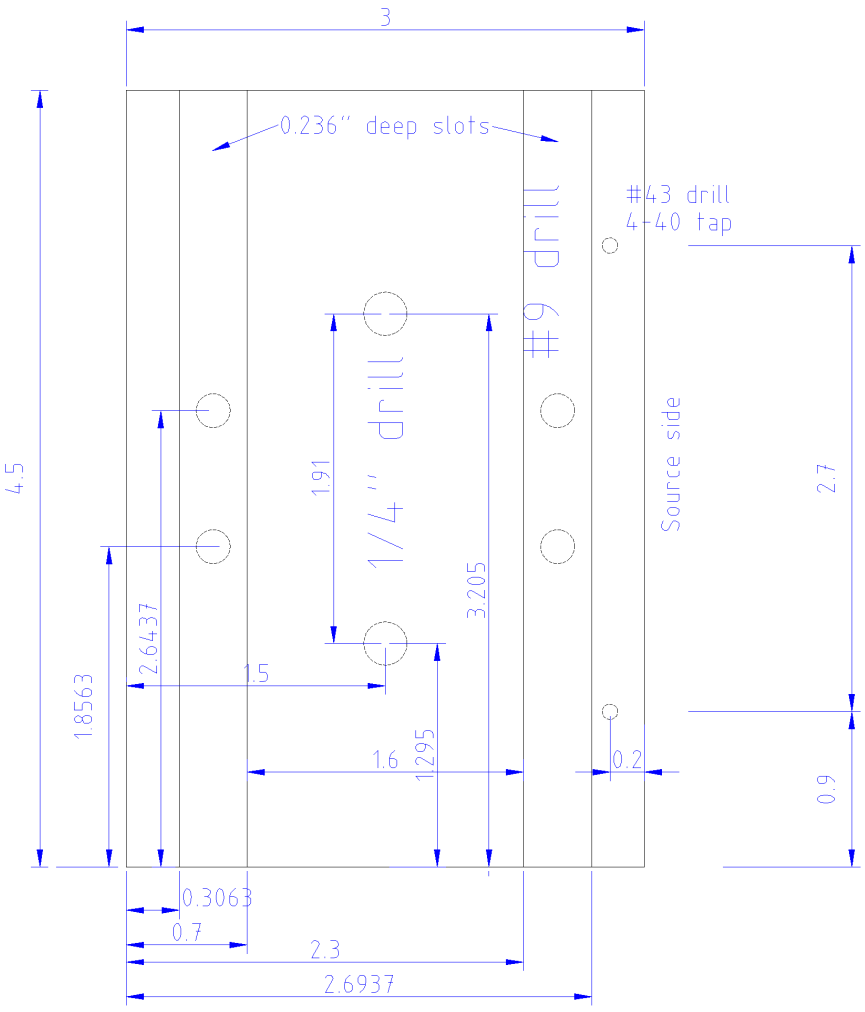

WAIS core yoke for MADGE
6061 Aluminum, 0.5" thick
All units in inches

A.4.d Core Calipers

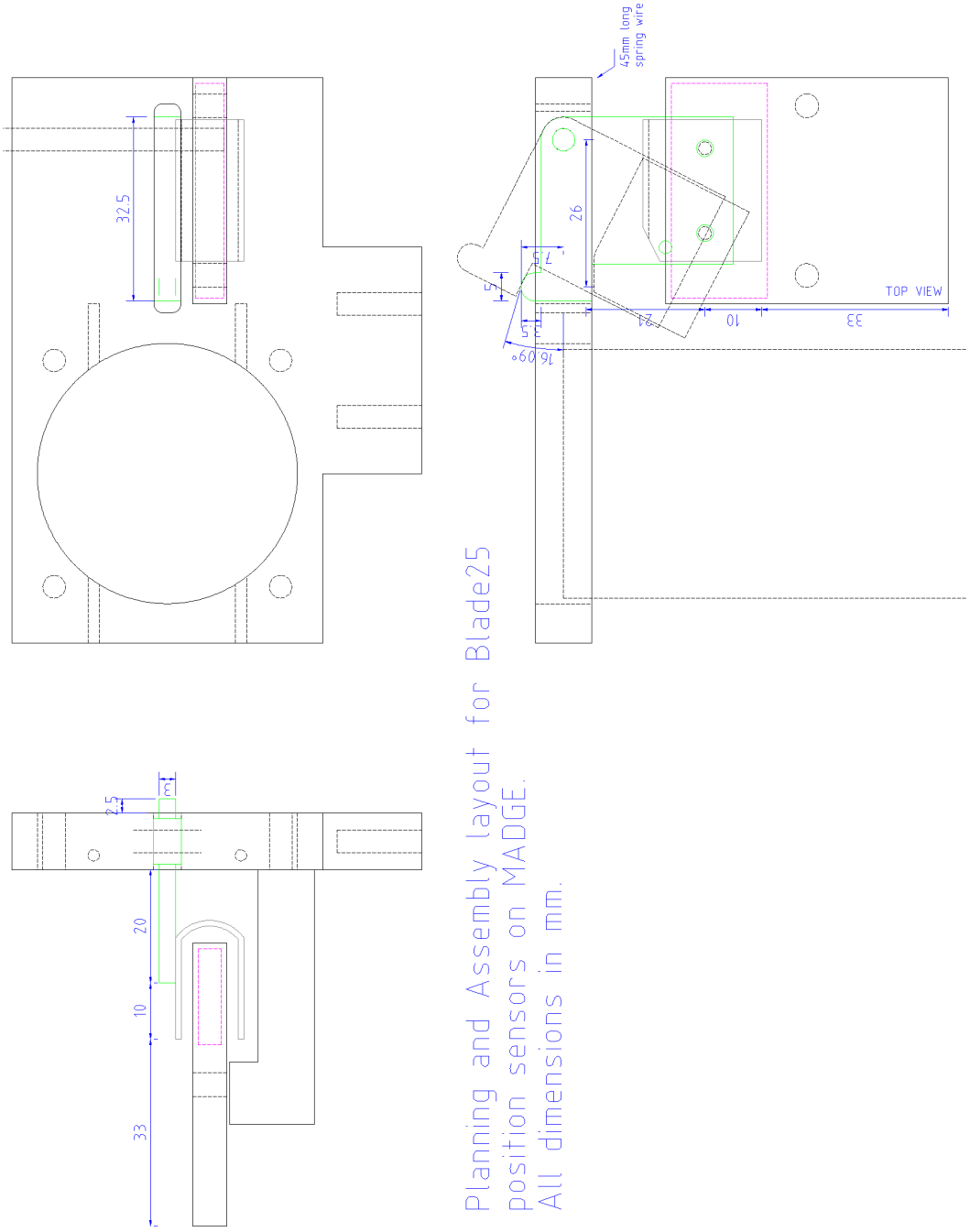

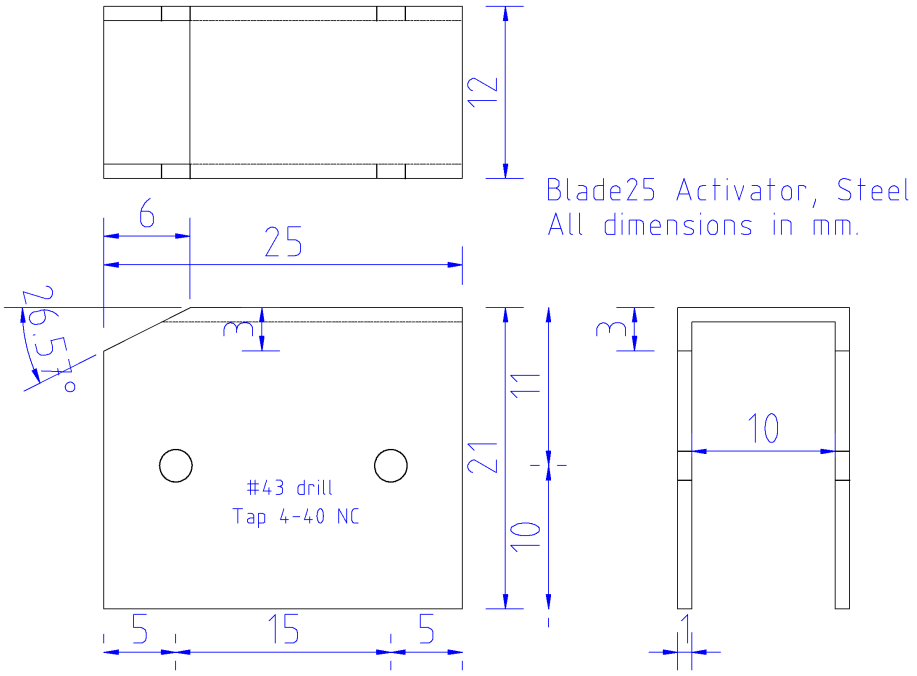
12
Blade25 Activator, Steel
All dimensions in mm.
6
25
26.57°
3
3
11
21
10
10
#43 drill
Tap 4-40 NC
5
15
5
1

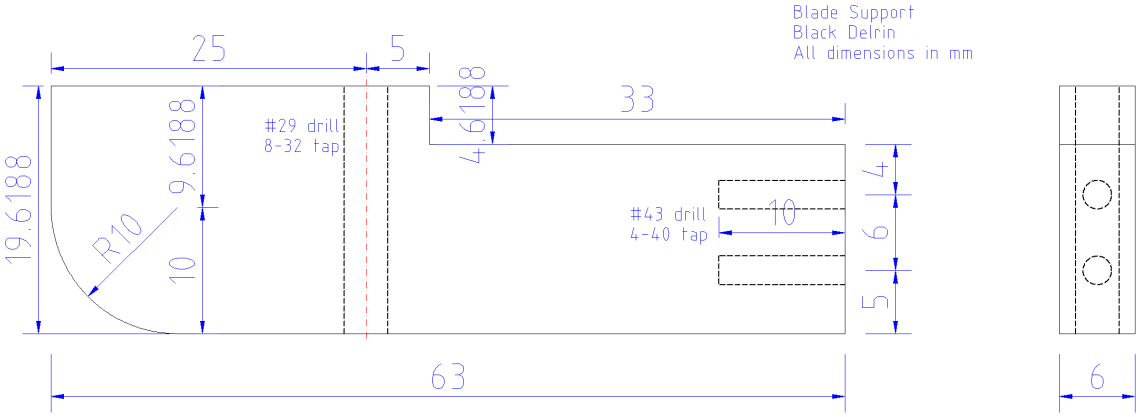
Blade Support
Black Delrin
All dimensions in mm
25
5
19.6188
9.6188
10
R10
#29 drill
8-32 tap
4.6188
33
#43 drill
4-40 tap
10
4
6
5
63
6

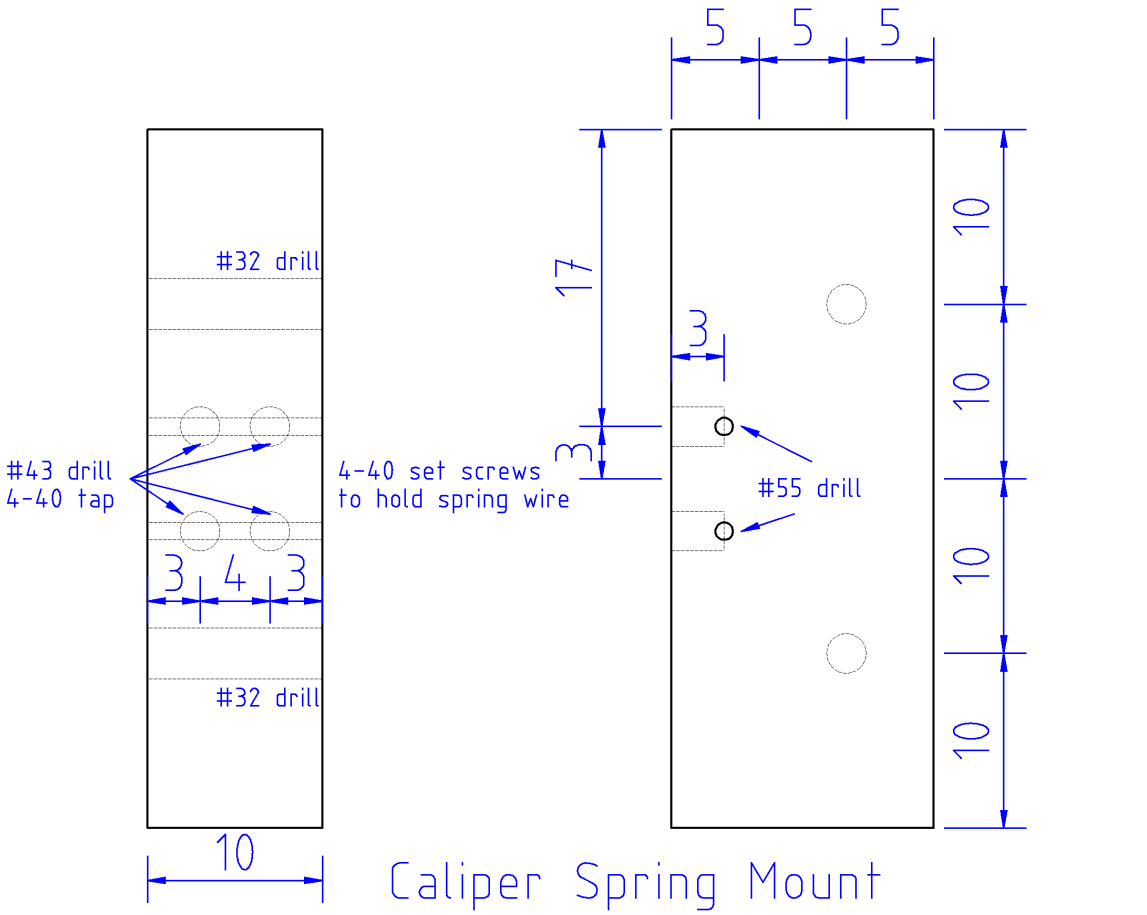
5
5
5
#32 drill
#43 drill
4-40 tap
4-40 set screws
to hold spring wire
17
3
3
#55 drill
10
10
10
10
3
4
3
#32 drill
10
Caliper Spring Mount
Aluminum, All dimensions in mm

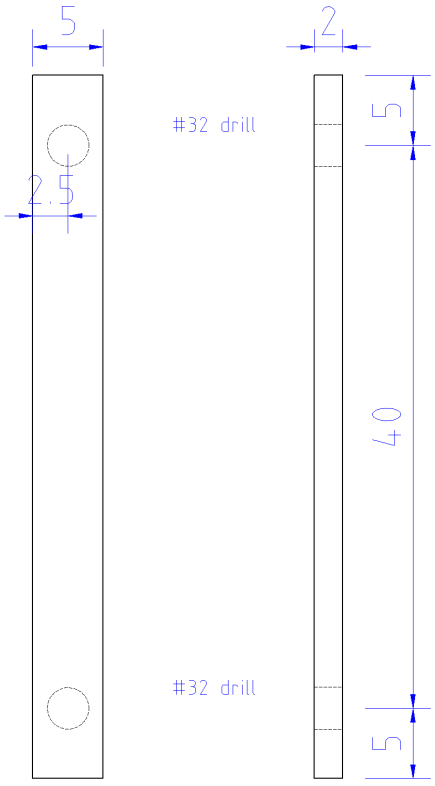

Detector Collimator Pin Keeper
Aluminum

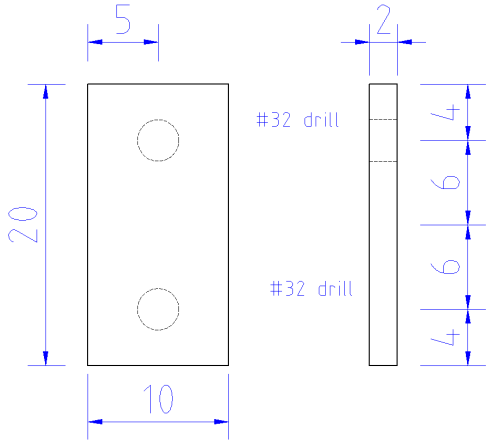

Caliper Axle Keeper
Aluminum
All dimensions in mm

A.5 MADGE Data Processing Service 1

```
#!/usr/bin/python
#version 0.2, including .tem file output
#Daniel J. Breton, UMaine Physics

#mdps1.py is the first part of the MADGE data processing service.
#it reads in raw data files from MADGE and splits them up into
#complete files to be processed by stage 2
#job #1 of mdps1.py: break raw MADGE output into files based on date-time-stamp
#job #2 of mdps1.py: create a user editable list of .d output files.  This
#file list will be used for the remainder of the processing to document:
#core tube order (using the t flag),
#local position of core breaks and damage (using cb and d flags respectively)
#and if a particular tube was scanned in the opposite direction of the rest
#of the project (using r flag)
#job #3 of mdps1.py: create temperature and C0 vs time .tem data file

#output .d files of this code look like:
#start ord day, start time, end ord day, end time, elapsed time
#preset C, dac_setting, start C0, start C0_time, end C0_time
#start Tbox, end Tbox, start Tdet, end Tdet

import sys
import os
from optparse import OptionParser
import re
from string import *
from datetime import *

#setup for parsing command line args
parser = OptionParser()

parser.add_option("-f", "--file", dest="fname",
                  help="read FILE", metavar="FILE")

parser.add_option("-s", "--start", dest="start_line", \
                  help="start processing at line LINE of input file", \
                  metavar="LINE", default=None)

parser.add_option("-e", "--end", dest="end_line", \
                  help="stop processing at line LINE of input file", \
                  metavar="LINE", default=None)

#old style (thru autoMADGE14.c) C preset values reported by MADGE
#report the value in thousands (i.e. 150.000000 represents 150E3)
#this option performs proper conversion
parser.add_option("-o", "--old", action="store_true", dest="oldCpreset",
        help="input uses old style C preset values",
        default=False)

parser.add_option("-y", "--year", dest='year',
        help="specify 4 digit year measurments begin", metavar="YEAR", \
                default=None)

parser.add_option("-l", "--label", dest='label',
        help="adds LABEL to start of output filenames", \
                  metavar="LABEL", default='')
```

```
parser.add_option("-p", "--project", dest='project', \
                  help="project and file list name.  Allows continuity if \
                  multiple input files are used, ", \
                  metavar="PROJECT", default='PROJ')

(options, args) = parser.parse_args()

#read in input file line by line, ignoring comments denoted
#by a leading # symbol

#setup regular expression for end of file tags
#finds either EOF or FILE tags
eof = re.compile('[E]')
filetag = re.compile('F')

#setup regular expression for comment line
comment = re.compile('#')  #looks for lines containing # followed by
                           #any number of alphanumeric characters

#setup re for time in hh:mm format, used to find subfile footer
time_data = re.compile('[0-9][0-9]:[0-9][0-9]')

#open input file
infile = open(options.fname, 'r')
data = infile.readlines()       #read in all lines of infile

listfile = open(options.project+'.ls1', 'a')    #opens list file for appending
listfile.write('#Source: '+options.fname+'\n')  #appends infile name to show
                                                #source of resulting .d files
temfile = open(options.project+'.tem', 'a')     #open temperature data file
temfile.write('#Source: '+options.fname+'\n')   #for appending, write source

logfile = open(options.project+'.log', 'a')
logfile.write('---mdps1-start-----------------------------------------------\n')
logfile.write('OPENED: '+options.fname+' on '+datetime.now().ctime()+'\n')
logfile.write('Project: '+options.project+ \
              '\tYear: '+options.year+'\tLabel: '+options.label+'\n')
logfile.write('Start Line:'+repr(options.start_line)+', End Line:'+ \
              repr(options.end_line)+', oldCpreset:'+repr(options.oldCpreset)\
              +'\n-------------------------------------------------------\n')

#initalize variables
sub_file_no = 0
ls1_list=[]

if(options.start_line == None):
    i = 0           #zero if no start line specified
else:
    i=int(options.start_line)-1 #applies proper start line

if(options.end_line == None):   #if no end line has been set
    max_lines = len(data)
else:               #else apply end line setting
    max_lines = int(options.end_line)-1

pyear = int(options.year)       #converts project year string to integer
```

```
m = None
subfile_start_found = False

print '\nProcessing ' + repr(max_lines-i) + ' lines from ' + options.fname
logfile.write('\nProcessing ' + repr(max_lines-i) + \
              ' lines from ' + options.fname+'\n')

while(i < max_lines):

    #start of search for start of first full data file
    while(not subfile_start_found and i < max_lines):

        if( comment.match(data[i]) ):   #if line is a comment
            # do not process line
            i = i + 1
            continue    #exits this iteration of for loop

        elif( data[i] == '\n' or data[i] == '\n\r'):
            i = i + 1
            continue

        elif( eof.search(data[i]) ):    #if line is EOF tag
            i = i + 1
            continue    #exits this iteration of for loop

        else:
            line = split( data[i] )
            #get ordinal day
            day_i=line[0]
            #get start time
            time_i=line[1]
            sub_file_no = sub_file_no + 1
            subfile_start_found = True
            print 'START SUBFILE ' + repr(sub_file_no) + ' @ ' \
                            +repr(i)+'\t'+day_i+' '+time_i
            logfile.write('START SUBFILE ' + repr(sub_file_no) + ' @ ' \
                            +repr(i)+' '+day_i+' '+time_i+'\n')
            i = i + 1
            break       #exits for loop entirely

    #exit big while loop if previous section runs to end of input file
    if(i >= max_lines):
        break

    #now open subfile output file with appropriate name
    if(options.year == None and options.label == None):
        subfilename = day_i + '-' + replace(time_i, ':', '') + '.d'
    elif(options.year == None):
        subfilename = options.label + '-' + day_i + '-' + \
                            replace(time_i, ':', '') + '.d'
    elif(options.label == ''):
        subfilename = repr(pyear) + '-' + day_i + '-' + \
                            replace(time_i, ':', '') + '.d'
    else:
        subfilename = options.label+ '-' + repr(pyear) + '-' + \
                            day_i + '-' + replace(time_i, ':', '') + '.d'
```

```
subfile = open(subfilename, 'w')
headerfile = open('header.tmp', 'w')

#process subfile header
line = split( data[i] )
#print line

C0 = line[0]
C0_time_i = line[1]

if(options.oldCpreset):
    C = float(line[2]) * 1000.0
else:
    C = float(line[2])

dac = line[3]
C=repr(C)   #re-convert to string for data writing

i=i+1   #process next header line
line = split( data[i] )
Tbox_i = line[0]    #box temperature at start of run, in C
Tdet_i = line[1]    #detector temp at start of run, in C

i=i+1   #process last header line
line = split( data[i] )
mode = line[0]  #0 for fixed time, 1 for fixed count modes
move = line[1]  #distance between measurements in cm
L_core = line[2]    #user entered length of core, mostly meaningless

i=i+1   #move to first subfile data line

#collect core data, running until getting to footer
#find footer by looking for line with time data (eg 23:12)
while( m == None):

    if( comment.match(data[i]) ):   #if line is a comment
        #do not process line
        i = i + 1
        continue    #exits this iteration of for loop

    elif( data[i] == '\n'):
        i = i + 1
        continue

    elif( eof.search(data[i]) ):    #if line is EOF tag
        i = i + 1
        continue    #exits this iteration of for loop

    else:           #if line is actual data
        line = split( data[i] )
        m = time_data.search(line[1])   #look for time data
        #if time data found, this means we are at the footer
        #next line which writes the line to the output file
        if(m==None):
            subfile.write( data[i] )
        else:
            #reset start of subfile flag since we are at
```

```
            #the end of the subfile
            subfile_start_found = False
            i=i-1   #do not advance line index if at footer

    i = i + 1   #look at the next line until footer is found

#gather footer information
day_f = line[0]
time_f = line[1]

#get actual Rabbit flash file number
if(filetag.search(data[i+3])):
        line=split( data[i+3] )
        flash_fn = line[1].rstrip(':')
        print 'FLASH FILE # '+flash_fn
        logfile.write('FLASH FILE # '+flash_fn+'\n')
    else:
        line=split( data[i+4] )
        flash_fn = line[1].rstrip(':')
        print 'FLASH FILE # '+flash_fn
        logfile.write('FLASH FILE # '+flash_fn+'\n')
print 'END SUBFILE ' + repr(sub_file_no) + ' @ ' + repr(i+2) + '\t' \
          + day_f+ ' '+ time_f
logfile.write('END SUBFILE ' + repr(sub_file_no) + ' @ ' + repr(i+2) \
                 + ' ' + day_f+ ' '+ time_f+' -> ')
i = i + 1

line=split( data[i] )
Tbox_f = line[0]
Tdet_f = line[1]
C0_time_f = line[2]

#calculate elapsed time for measurement, assigns options.year to year
start_d = date.fromordinal(int(day_i)).replace(year=pyear)

t = time_i.partition(':')   #split time_i into tuple
start_t = time(int(t[0]),int(t[2]))
start_dts = datetime.combine(start_d, start_t)

    if( int(day_f) < int(day_i) ):
            pyear = pyear+1    #increment the new year
    else:
            pass

    #otherwise, just use given value
    end_d=date.fromordinal(int(day_f)).replace(year=pyear)

t = time_f.partition(':')   #split time_i into tuple
end_t = time(int(t[0]),int(t[2]))
end_dts = datetime.combine(end_d, end_t)

elapsed=end_dts - start_dts #calculate elapsed time
logfile.write(repr(elapsed.seconds/60.0)+' min, ')

    #use the new start_dts and end_dts values to put data in .tem file
temfile.write(start_dts.strftime("%d-%b-%Y %H:%M")+'\t'+Tbox_i \
                 +'\t'+Tdet_i+'\t'+C0_time_i+'\n')
```

```
    temfile.write(end_dts.strftime("%d-%b-%Y %H:%M")+'\t'+Tbox_f \
                    +'\t'+Tdet_f+'\t'+C0_time_f+'\n')

    #build new header strings
    if(options.year == None):
        timestring = day_i+' '+time_i+' '+day_f+' '+time_f+' ' \
                            +repr(elapsed.seconds/60.0)+'\n'
    else:
        timestring = repr(pyear)+' '+day_i+' '+time_i+' '+day_f+' ' \
                            +time_f+' '+repr(elapsed.seconds/60.0)+'\n'

    nukestring = C+' '+dac+' '+C0+' '+C0_time_i+' '+C0_time_f+'\n'
    tempstring = Tbox_i+' '+Tbox_f+' '+Tdet_i+' '+Tdet_f+'\n'
    miscstring = flash_fn+' '+mode+' '+move+'\n###\n'

    #write header data to temporary header file
    headerfile.write('# Project: '+options.project+' Source: '+\
                         options.fname+' -> '+subfilename+'\n')
    headerfile.write('# '+timestring)
    headerfile.write('# '+nukestring)
    headerfile.write('# '+tempstring)
    headerfile.write('# '+miscstring)

    #close subfile & headerfile
    subfile.close()
    headerfile.close()

    if subfilename in ls1_list:
                logfile.write('Repeat '+subfilename+' skipped\n')
        else:
                listfile.write(subfilename+'\n')
                logfile.write(subfilename+'\n\n')
                ls1_list.append(subfilename)

    #join files together
    os.system('cat header.tmp '+ subfilename + ' > out.tmp')
    os.system('mv out.tmp ' + subfilename)
    os.system('rm header.tmp')

    m = None            #reset footer found flag
    i = i + 1           #look at next line

#finished with input file
print '\nClosing ' + options.fname
print 'Edit the .ls1 file to add core break,\n tube order and reversal flags.'
infile.close()
logfile.write('\nCLOSED: ' +options.fname+' on '+datetime.now().ctime()+'\n')
logfile.write('---mdps1-end-----------------------------------------------\n')
listfile.close()
temfile.close()
logfile.close()
```

A.6 MADGE Data Processing Service 2d

```
#!/usr/bin/python

#mdps2d.py is the second part of the MADGE data processing service.
#it takes the .d files output from mdps1.py OR reads the .lst file
#produced by mdps1 which lists all the .d files produced from the raw input file

#1. reads list file and processes the files in order.

#2. takes an input .d file and makes in into a .rho file by performing
#the density and uncertainty calculations, and applies caliper corrections,
#if necessary.
#a .rho file looks like:
#localpos(cm) rho(g/cm^3) d_rho corediam(cm) d_corediam refl* corebreak
#*reflectivity data to be added later

#3. flips the data upside down if core section was scanned in the -> direction
#(the preferred scan direction is the anti -> direction (from surface toward
#the bed)

#4. comments out densities below a certain threshold (to remove core breaks
#and air shots)

#changed 6 march 08 to include concatenation of .rho files in order
#and to add additional term (mu term) to error calculation

#changed to also include dead time corrections

import sys
import os
import fileinput
from optparse import OptionParser
import re
from string import *
from datetime import *
from fileinput import *
from math import *

#setup for parsing command line args
parser = OptionParser()

parser.add_option("-p", "--project", dest='project', \
                  help="project name.  Chooses PROJECT.ls1 as input", \
                  metavar="PROJECT", default='PROJ')

parser.add_option("-b", "--backward", dest='backwd', action="store_true",
        help="flips data for cores scanned in -> direction",
                default=False)

parser.add_option("-j", "--join", dest='join', action="store_true",
        help="joins .rho files into a final PROJECT.rho file",
                default=False)

parser.add_option("-r", "--remove", dest='r_rho', metavar="RHO", \
        help="remove records with density less than RHO g cm^-3", \
                default=0.1)

parser.add_option("-c", "--comment", dest='c_rho', metavar="RHO", \
```

```
        help="comment out records with density less than RHO g cm^-3",\
                default=0.2)

parser.add_option("-m", "--mu", dest='mu', metavar="MU_M", \
                  help="set mu_m value to MU_M, default 0.176 cm^2/g",\
                  default=0.1760)

parser.add_option("-t", "--tau", dest='tau', metavar="TAU", \
                  help="set DTC tau value to TAU (us), default 2.592 us",\
                  default=2.592)

parser.add_option("-n", "--nocum", dest='nocum', action="store_true", \
                  help="do not calculate pos as cumulative core depth",\
                  default=False)

(options, args) = parser.parse_args()

#maximum C0time before discarding value
maxC0time = 43.5

#mu_m setting
mu_m = float(options.mu)   #cm**2 / g

#dead time setting
tau = 1.0e-6 * float(options.tau) #seconds

#d_cd setting (coreD uncertainty)
d_cd = 0.01 #cm

#d_mu setting (mass attenuation coefficient uncertainty)
d_mu = 0.00034 #cm**2 / g

#d_tau setting (dead time uncertainty)
d_tau = 1.0e-6 * 0.0062 #sec

#reset depth counter
zold = 0.0

#initialize found_comment
found_comment = True

listfile = open(options.project+'.ls1', 'r')
logfile = open(options.project+'.log', 'a')
logfile.write('---mdps2d-start-----------------------------------------\n')
logfile.write('OPENED:'+options.project+'.ls1 at '+datetime.now().ctime()+'\n')
logfile.write('Project:'+options.project+'\tBackwd:'+repr(options.backwd)+'\n')
logfile.write('Remove records < '+repr(options.r_rho)+' g/cm^3\n')
logfile.write('Comment out records < '+repr(options.c_rho)+' g/cm^3\n')
logfile.write('Mu_m :'+repr(mu_m)+ ' cm^2/g\n')
logfile.write('Dead time tau:'+repr(tau)+ 'sec\n'
logfile.write('-------------------------------------------------------\n\n')

input_list = listfile.readlines()
df_list = []
join_list = []    #list of file names for final concatenation

#setup regular expression for comment line
```

```
comment = re.compile('#')
colon = re.compile(':')

#remove comment lines from list file
while(found_comment):
    for line in input_list:
        if( comment.search(line) ):
            input_list.remove(line)
            break   #leave for loop and start scanning list over from beginning
        else:
            continue #if not a comment, roll on to next line via for loop

    #when for loop has reached the end of input_list without finding comments,
    else:
        found_comment = False #exit while loop since comments have been removed

for line in input_list:
        df_list.append(line)

#big loop over all data files in list file
for item in df_list:
    #need
    coreD = [10,10,10,10,10,10,10,10,10,10]  #10 tens here for move=3.3mm
    print "coreD prepended by "+str(len(coreD))

    #prepend 10's to match coreD data with proper pos & ctime
    pos = []
    Ctime = []
    m=[]
    n=[]
    rho =  []
    d_rho= []
    i = 0

    dfile = open(item.rstrip(), mode='r')   #need the .rstrip() to remove \n
    rhofilename = replace(item, '.d\n', '.rho') #build output filename
    rhofile = open(rhofilename, 'w')
    join_list.append(rhofilename)   #add filename to joining list
    rhofile.write('#Project:'+options.project+' Source:'+ item.rstrip()+'\n')
    print 'Processing '+item.rstrip()+' -> '+rhofilename
    logfile.write('Processing '+item.rstrip()+' -> '+rhofilename+'\n')

    #extract header information
    h = dfile.readline()    #read first line
    h = dfile.readline()    #read second line
    h = split( dfile.readline() )
    #read third line, which finally has useful info

    C = float( h[1] )
    dac = float( h[2] )
    C0 = float( h[3] )
    C0timei = float( h[4] )
    C0timef = float( h[5] )

    logfile.write('initial C0 time = '+str(C0timei)+' sec\n')
    logfile.write('final C0 time   = '+str(C0timef)+' sec\n')
```

```
if(C0timei > maxC0time):
    print '**Abnormal start C0 in '+item.rstrip()
    logfile.write('WARNING: start C0 ='+str(C0timei)+' in '+item.rstrip()+ \
                  ': used end C0 only\n')
    C0time_avg = C0timef
elif(C0timef > maxC0time):
    print '**Abnormal start C0 in '+item.rstrip()
    logfile.write('WARNING: end C0 ='+str(C0timef)+' in '+item.rstrip()+ \
                  ': used start C0 only\n')
    C0time_avg = C0timei
else:
    C0time_avg = (C0timei + C0timef)/2.0

h = dfile.readline()  #read fourth line, temperatures only
h = split( dfile.readline() ) #read last header line

mode = h[1]     #counting mode: 0 fixed time, 1 fixed count
move = float(h[2])     #MOVE value in cm
if move != 0.33:
  print "Non-standard MOVE value, be sure you have correctly pre-pended coreD list"

for line in dfile:
    if( comment.match(line) ):
        continue        #skip comment lines, if any at this stage

    rawdata=split(line)        #split input data
    pos.append( float(rawdata[0]) ) #append index data to the list "pos"
    Ctime.append( float(rawdata[1]) ) #append Ctime data to the list "Ctime"
    coreD.append( float(rawdata[2]) ) #append core_D data to the list "coreD"

    ###calculate density for each record, append it to list 'rho'
#first, perform DTC
m0 = C0 / C0time_avg        #meas count rate for C0
n0 = m0 / (1.0 - m0*tau)    #DTC count rate for C0
m.append(  C / Ctime[i] )       #meas count rate for C
n.append( m[i] / (1.0 - m[i]*tau) ) #list of DTC count rates for C

    rho.append(-log( n[i]/n0 ) / (mu_m * coreD[i]))
#print n[i], n0, rho[i]

    #calculate uncertainty in density for each record
    #first, find n0 nuketerm squared (includes DTC)
n0_A = ( (1.0/(1-m0*tau)) + (m0*tau)/(1-m0*tau)**2 )**2 * (m0/C0time_avg)
n0_B = ( m0/(1-m0*tau) )**4 * d_tau**2
n0_nuketerm2 = (coreD[i]**2 * mu_m**2 * n0**2)**(-1) * (n0_A + n0_B)

#then find n nuketerm squared (includes DTC)
n_A = ( (1.0/(1-m[i]*tau)) + (m[i]*tau)/(1-m[i]*tau)**2 )**2 * (m[i]/Ctime[i])
n_B = ( m[i]/(1-m[i]*tau) )**4 * d_tau**2
n_nuketerm2 = (coreD[i]**2 * mu_m**2 * n[i]**2)**(-1) * (n_A + n_B)

    #then find core_d term squared
    cdterm2 = (d_cd**2 * log( (C*C0time_avg)/(C0*Ctime[i]) )**2) / (mu_m**2
            * coreD[i]**4)

    #then find mu_m term squared
    muterm2 = ( log( (C*C0time_avg)/(C0*Ctime[i]))/
```

```
                (coreD[i] *mu_m**2 ))**2 * (d_mu**2)

    #finally, find density uncertainty and append to list 'd_rho'
    d_rho.append( sqrt(n0_nuketerm2 + n_nuketerm2 + cdterm2 + muterm2) )
    #print repr(sqrt(nuketerm2 + cdterm2))

    i=i+1
#close data file
dfile.close()

#calculate ipcm (stepper motor index change per MOVE)
ipcm = abs(pos[0] - pos[1])/move
logfile.write('index per cm = '+str(ipcm)+'\n')

#reverse lists if requested
if(options.backwd):
    # pos.reverse() #don't reverse index positions
    coreD.reverse()
    rho.reverse()
    d_rho.reverse()
    #corebreak.reverse()   to be implemented laaaaater

i=0     #re-initialize i

#first off, find start of core and set reference position
while(rho[i] < float(options.c_rho) or coreD[i]==10):
    del pos[i]
    del coreD[i]
    del rho[i]
    del d_rho[i]

    #deletes all unacceptable records that move
    #into the top list position

start_ref = pos[i]    #sets starting reference position
print 'Found start of core at ' + str(start_ref)
logfile.write('Found start of core at '+str(start_ref)+'\n')

#now find end of core, and set end_ref position
i=-1    #set i to look at last record
while(rho[i] < float(options.c_rho) ):
    del pos[i]
    del coreD[i]
    del rho[i]
    del d_rho[i]    #delets unacceptable records that move into the
                    #last position in the list

end_ref = pos[i]    #sets starting reference position
print 'Found end of core at ' + str(end_ref)
logfile.write('Found end of core at '+str(end_ref)+'\n')

L = abs(end_ref - start_ref)/ipcm
if(L < 90.0):
    print 'Short core segment: '+str(L)+' cm in '+item.rstrip()
    logfile.write('WARNING: Short core seg length = '+str(L)+' cm\n')
else:
    print 'Core length = '+str(L)+' cm'+'\n'
```

```
        logfile.write('Core segment length = '+str(L)+' cm\n')

    #run through and calc proper positions, throw out bad values
    i=0     #reset i one more time
    while(i < len(rho) ):
        z = zold + (abs(pos[i]-start_ref))/ipcm

        if(rho[i] < options.r_rho ):
            logfile.write('REMOVE record at '+str(pos[i])+' -> '+str(z)+ \
                          'cm, rho='+str(rho[i])+'\n')
            i=i+1
            continue    #skip this line

        #comments values below threshold and above maximum ice density
        elif(rho[i] < options.c_rho or rho[i] > 0.92):
            out='#'+str(z)+'\t'+str(rho[i])+'\t'+str(d_rho[i]) \
                 +'\t'+str(coreD[i])+'\n'
            rhofile.write(out)
            logfile.write('COMMENT record at '+str(pos[i])+' -> '+str(z)+ \
                          'cm, rho='+str(rho[i])+'\n')
            i=i+1

        else:
            out=str(z)+'\t'+str(rho[i])+'\t'+str(d_rho[i]) \
                 +'\t'+str(coreD[i])+'\n'
            rhofile.write(out)
            i=i+1

    logfile.write('Wrote '+str(i)+' lines to '+rhofilename+'\n------------\n')
    zold = z + move
    if options.nocum:
      zold = 0
    logfile.write('Cumulative core length: '+str(z)+'cm\n------------\n')
    rhofile.close()

listfile.close()
logfile.write('\nCLOSED:' +options.project+'.ls1 on '+datetime.now().ctime()+\
              '\n')

if(options.join):
    ls2file = open(options.project+'.ls2', 'w')
    fstr='cat' #need to start with cat command
    #build command string
    for f in join_list:
        fstr = fstr + ' '+f
        ls2file.write(f+'\n')

    fstr = fstr + ' > '+ options.project+'.rho'
    ls2file.close()

    os.system(fstr)
    logfile.write('\nJoined all .rho files with this command:\n'+fstr)
    logfile.write('\nWrote .rho filenames to '+options.project+'.ls2\n')
logfile.write('\n---mdps2-end-----------------------------------------\n')
logfile.close()
```

APPENDIX B

RADIATIVE TRANSFER SIMULATION CODES

B.1 Radiative Transfer Code

```
/* Adapted from Small Monte Carlo by Scott Prahl (http://omlc.ogi.edu) */
/* Some modifications by T.J. Fudge and Ben Smith for glacial borehole work */
/* see "Light propagation in firn: application to borehole video", 2010
/*  J. Glaciology, Vol. 56, pp. 614.

/* Some modifications by Daniel J. Breton, University of Maine to support absorbing BC's
*/
/* and recording the cube face through which a photon packet exits */

#include <stdio.h>
#include <stdlib.h>
#include <math.h>
#include <time.h>
#include <unistd.h>

//Photon exit codes are as follows:
// -1 is emergence thru z=0
// -2 is reflectance back thru x=0
// -3 is transmittance through x=sample_thick
// -4 is leakage through y=-samplethick/2
// -5 is leakage through y=+samplethick/2
// -6 is leakage through z=samplethick

/* This code makes heavy use of global variables: */

double g = 0.89;        /* Default scattering Anisotropy -1<=g<=1 */
double g2=.7921;                /* square of default g */
long maxcount = 1e8;            /* maximum number of scatters before the photon is
discarded */
long endcount= 2e9;             /* flag indicating dead photon */
long   i, photons = 2e6;        /* number of photons to launch */
double launch_depth=2.0;       /* depth, in Lscat units, from slab top (z=0) for photon
launch */
double sample_thick=40.0;       /* thickness, in Lscat units from slab face (x=0) for
trans. tally*/
double x,y,z,u,v,w,weight, L;   /* book-keeping values */
long count;                     /* number of photons */
long emerged=0;                 // number of photons emerging from firn toward camera
long reflected=0;               // number of photons reflected from x=0 surface
long transmitted=0;               // number of photons transmitted out of x=sample_thick
surface
int j;                          /* current shell */
int N_rad;                      /* number of boreholes to check */
int flag;                       /* flag to indicate whether we've passed the half-plane:
for calculating the reflectance of a flat snow surface */

void launch() /* Start the photon */
{
    x = 0.0; y = 0.0; z = launch_depth;
    u = 1.0; v = 0.0; w = 0.0;
    L=0.0;
    count=0;
    flag=1;  //flag==1 implies photon is inside the sample geometry
    j=0;
}

void move() /* move to next scattering or absorption event */
```

```
{  /* or tally those that cross the absorbing boundaries and stop them */
  double a, b, c, x2, x_wall, y_wall, z_wall, L_wall,  dL;   /* variables for backing up
the photon to the wall */
  double z_plus_r_j2;
  double d = -log((rand()+1.0)/(RAND_MAX+1.0));  //choose movement distance
  x += d * u;
  y += d * v;
  z += d * w;
  L += d;
  x2=x*x;


  //TALLIES FOR ALBEDO, TRANSMISSION AND LEAKAGE
  if (flag) {    /* only report the first entry of the photon into the +z half-space */
    if (z<0) { //if we leave the top of sample,
      flag=0;
      dL=-z/w;   /* The intersection between the current ray and the z=0 plane is at
      distance z/w backwards */
      x_wall=x+dL*u;
      y_wall=y+dL*v;
      z_wall=z+dL*w;
      L_wall=L+dL;

      // if intersection was acutally with x=0 plane
      if(x_wall < 0) {
        dL=-x/u;   /* The intersection between the current ray and the x=0 plane is at
        distance x/u backwards */
        x_wall=x+dL*u;
        y_wall=y+dL*v;
        z_wall=z+dL*w;
        L_wall=L+dL;
        printf("%d %12.6f %12.6f %12.6f %12.6f %12.6f %12.6f %12.6f %10ld %10ld \n",
               -2, x_wall, y_wall, z_wall, u, v, w, L_wall, count, i);

      count = endcount;  //force launch of new photon, because the current one has left
      the firn
      reflected += 1;  //count total number of reflected photons
      } //if x_wall < 0
      // if intersection was acutally with x=sample_thick plane
      else if(x_wall > sample_thick) {
        dL=(sample_thick-x)/u;   /* The intersection between the current ray and the
        x=sample_thick plane */
        x_wall=x+dL*u;
        y_wall=y+dL*v;
        z_wall=z+dL*w;
        L_wall=L+dL;
        printf("%d %12.6f %12.6f %12.6f %12.6f %12.6f %12.6f %12.6f %10ld %10ld \n",
               -3, x_wall, y_wall, z_wall, u, v, w, L_wall, count, i);

      count = endcount;  //force launch of new photon, because the current one has left
      the firn
      transmitted += 1;  //count total number of transmitted photons
      } //if x_wall > sample_thick

      // if intersection was acutally with y = -sample_thick plane/2
      if(y_wall < -sample_thick/2.0) {
        dL=((-sample_thick/2.0)-y)/v;   /* The intersection */
```

```
        x_wall=x+dL*u;
        y_wall=y+dL*v;
        z_wall=z+dL*w;
        L_wall=L+dL;
        printf("%d %12.6f %12.6f %12.6f %12.6f %12.6f %12.6f %12.6f %10ld %10ld \n",
               -4, x_wall, y_wall, z_wall, u, v, w, L_wall, count, i);

      count = endcount;  //force launch of new photon, because the current one has left
      the firn
      emerged += 1;
      } //if
      // if intersection was acutally with y= +sample_thick plane/2
      else if(y_wall > sample_thick/2.0) {
        dL=(sample_thick/2.0-y)/v;   /* The intersection between the current ray and the
        x=sample_thick plane */
        x_wall=x+dL*u;
        y_wall=y+dL*v;
        z_wall=z+dL*w;
        L_wall=L+dL;
        printf("%d %12.6f %12.6f %12.6f %12.6f %12.6f %12.6f %12.6f %10ld %10ld \n",
               -5, x_wall, y_wall, z_wall, u, v, w, L_wall, count, i);

      count = endcount;  //force launch of new photon, because the current one has left
      the firn
      emerged += 1;  //count total number of transmitted photons
      } //if x_wall > sample_thick

      else {  //this is the case if the photon actually emerged from z=0 plane...
        printf("%d %12.6f %12.6f %12.6f %12.6f %12.6f %12.6f %12.6f %10ld %10ld \n",
               -1, x_wall, y_wall, z_wall, u, v, w, L_wall, count, i);

        count = endcount;  //force launch of new photon, because the current one has left
        the firn
        emerged += 1;  //count total number of emerged photons
        } //else
      } // if z < 0

      else if(z > sample_thick) {
        dL=(sample_thick-z)/w;   /* The intersection between the current ray and the z=0
        plane is at distance z/w backwards */
        x_wall=x+dL*u;
        y_wall=y+dL*v;
        z_wall=z+dL*w;
        L_wall=L+dL;

        printf("%d %12.6f %12.6f %12.6f %12.6f %12.6f %12.6f %12.6f %10ld %10ld \n", -6,
        x_wall, y_wall, z_wall, u, v, w, L_wall, count, i);

        count = endcount;  //force launch of new photon, because the current one has left
        the firn
        emerged += 1;  //count total number of emerged photons
      } //if z > samplethick

    } //flag

if((y < -sample_thick/2.0) && flag==1) {
        dL=((-sample_thick/2.0)-y)/v;
```

```
      x_wall=x+dL*u;
      y_wall=y+dL*v;
      z_wall=z+dL*w;
      L_wall=L+dL;
      printf("%d %12.6f %12.6f %12.6f %12.6f %12.6f %12.6f %12.6f %10ld %10ld \n",
             -4, x_wall, y_wall, z_wall, u, v, w, L_wall, count, i);

    count = endcount;  //force launch of new photon, because the current one has left
    the firn
    emerged += 1;
  }

  if((y > sample_thick/2.0) && flag==1) {
      dL=(sample_thick/2.0-y)/v;
      x_wall=x+dL*u;
      y_wall=y+dL*v;
      z_wall=z+dL*w;
      L_wall=L+dL;
      printf("%d %12.6f %12.6f %12.6f %12.6f %12.6f %12.6f %12.6f %10ld %10ld \n",
             -5, x_wall, y_wall, z_wall, u, v, w, L_wall, count, i);

    count = endcount;  //force launch of new photon, because the current one has left
    the firn
    emerged += 1;
    }


  //REFLECTION (BACKSCATTER) TALLY
  //only run this if photon HAS NOT YET CROSSED z=0 (i.e. flag still == 1)
  //otherwise double counting can occur
  if (x<0 && flag==1) {
    dL=-x/u;   /* The intersection between the current ray and the x=0 plane is at
    distance x/u backwards */
    x_wall=x+dL*u;
    y_wall=y+dL*v;
    z_wall=z+dL*w;
    L_wall=L+dL;
    printf("%d %12.6f %12.6f %12.6f %12.6f %12.6f %12.6f %12.6f %10ld %10ld \n",
           -2, x_wall, y_wall, z_wall, u, v, w, L_wall, count, i);

    count = endcount;  //force launch of new photon, because the current one has left
    the firn
    reflected += 1;  //count total number of reflected photons
  }

  //TRANSMISSION TALLY
  //only run this if photon HAS NOT YET CROSSED z=0 (i.e. flag still == 1)
  //otherwise double counting can occur
  if (x>sample_thick && flag==1) {
    dL=(sample_thick-x)/u;
    /* The intersection between the current ray and the x=sample_thick plane */
    x_wall=x+dL*u;
    y_wall=y+dL*v;
    z_wall=z+dL*w;
    L_wall=L+dL;

    printf("%d %12.6f %12.6f %12.6f %12.6f %12.6f %12.6f %12.6f %10ld %10ld \n",
```

```
            -3, x_wall, y_wall, z_wall, u, v, w, L_wall, count, i);

      count = endcount;  //force launch of new photon, because the current one has left
        the firn
      transmitted += 1;  //count total number of transmitted photons
    } // if x > sample_thick

  if ( count>=maxcount ) {  /* we've interacted too many times without hitting the center
    borehole */
    count=endcount;
  }

/* removed borehole stuff */
}

scatter() /* Scatter photon and establish new direction, mostly described in App. A1 of
Prahl (1988) */
{
  double x1, x2, x3, t, mu, mu2, fw, fv;
  double temp1;
    for(;;) {   /*new direction- pick two random values that work as direction cosines*/
        x1=2.0*rand()/RAND_MAX - 1.0;
        x2=2.0*rand()/RAND_MAX - 1.0;
        if ((x3=x1*x1+x2*x2)<1) break;
    }
    if (g==0) {  /* isotropic */
        u = 2.0 * x3 -1.0;
        v = x1 * sqrt((1-u*u)/x3);
        w = x2 * sqrt((1-u*u)/x3);
        return;
    }
    mu = (1.0-g2)/(1.0-g+2.0*g*rand()/RAND_MAX);
    mu = (1.0 + g2-mu*mu)/2.0/g;
    mu2 = mu*mu;
    if ( fabs(w) < 0.9 ) {  /* avoid round-off errors in w */
      temp1=sqrt((1-mu2)/(1-w*w)/x3);
      t = mu * u + temp1 * (x1*u*w-x2*v);
      v = mu * v + temp1 * (x1*v*w+x2*u);
      w = mu * w - sqrt((1-mu2)*(1-w*w)/x3) * x1;
    } else {
      temp1=sqrt((1-mu2)/(1-v*v)/x3);
      t = mu * u + temp1 * (x1*u*v + x2*w);
      w = mu * w + temp1 * (x1*v*w - x2*u);
      v = mu * v - sqrt((1-mu2)*(1-v*v)/x3) * x1;
    }
    u = t;
}

int main (int argc, char *argv[] )
{

  int index;
  char c;
  int  last_arg_processed=0;
  opterr = 0;

  if (argc==0) {
```

```
    fprintf (stderr, "mcsbc -g asymmetry_parameter -p n_Photons -m max_scattering -z
    launch_depth -t sample_thick \n");
  }
  while ((c = getopt (argc, argv, "hg:p:m:z:t:r:")) != -1) {
    last_arg_processed+=2;
    switch (c) {
    case 'g':
      g = (double) atof(optarg);
      break;
    case 'p':
      photons = (long) atol(optarg);
      break;
    case 'm':
      maxcount =(long) atol(optarg);
      break;
    case 'z':
      launch_depth = (double) atof(optarg);
      break;
    case 't':
      sample_thick = (double) atof(optarg);
      break;
    case 'r':
      N_rad = (int) atoi(optarg);
      break;
    case 'h':
      fprintf (stderr, "mc_borehole -g asymmetry_parameter -p n_Photons -m
      max_num_scatterings
                           -z launch depth -r Number_of_rad_values rad1 rad2 rad3 rad4....
                           \n");
      return 1;
    default:
      abort ();
    }
  }


  if (argc - last_arg_processed < N_rad+1) {
    printf("wrong number of arguments: have %d R vals, need %d R vals\n", argc-
    last_arg_processed -1, N_rad);
    return 0;
  }

  r=malloc(sizeof(double)*N_rad);
  r2=malloc(sizeof(double)*N_rad);

  for (index=0; index<N_rad; index++) {
    r[index]=(double) atof(argv[1+index+last_arg_processed]);
    r2[index]=r[index]*r[index];
  }

  srand (time (NULL));
  j=0;

  /* square the r variables */
  for (i = 0; i < N_rad; i++){
    r2[i] = r[i]*r[i];
  }
```

```
  /* square g->g2 */
  g2=g*g;

  /* start running photons */
  for (i = 1; i <= photons; i++){
    launch ();
    while (count < endcount ) {
      move ();
      count++;
      scatter ();
    }
  }
  printf("#Started: %ld\tReflected: %ld\tEmerged: %ld\tTransmitted: %ld\tLost: %ld\n", i,
  reflected, emerged, transmitted, i-(reflected+emerged+transmitted));
  return 0;
}
```

B.2 Setup Script for Batch Processing

```
## mcauto3bc.py - Daniel J. Breton, University of Maine Physics, 26 Oct 2010
## This code generates a batch que of MC RT runs with a range of
## grain/bubble sizes and bulk densities.
##
## N.B. Storage requirements for mcsbc output files are significant
## As root you'll need to start the at daemon:
## /usr/sbin/atd -l 1.5 -s
## designed for 2 cpu system, hence the " -l 1.5" bit

import os  #we need os module to send commands to operating system

#open output file
f = open("mcslogbc.txt", "w")

## fixed light source depth, m
lz = 0.020 # 2 cm below top of firn - center of 4x4x4 cube
## fixed firn sample thickness, m
lt = 0.040 # 4x4 cm thick and wide

Nphotons = 1000000  #one MILLION photons
maxscatter = 200000  #200k max scattering events...
labs = 8.3 # m per absorption event, for roughly 600nm light, from Warren
kabs = 1/labs

## list of grain sizes and GA densities to use in calculating Lscat
rgL = [0.1e-3, 0.2e-3, 0.3e-3, 0.4e-3, 0.5e-3, 1.0e-3]  #grain radii in m
rhogL = [300, 350, 400, 450, 500, 550, 600, 650, 700]  #firn density in kg/m^3

## list of bubble sizes and BI densities to use in calculating Lscat
rbL = [0.1e-3, 0.2e-3, 0.3e-3, 0.4e-3, 0.5e-3, 1.0e-3] #bubble radii in m
#firn/ice density in kg/m^3
rhobL = [600, 650, 700, 750, 800, 820, 840, 860, 880, 890, 900, 905, 910, 915, 917]

storage = 112*(len(rgL)+len(rbL))*(len(rhogL)+len(rhobL))
print "Expected storage requirement: %.1f MB" % (storage)
Qscat = 2.0  #scattering efficiency
gGA = 0.89  #grains in air value of asymmetry parameter
gBI = 0.89  #making this the same
D = [] #empty list of data

## SSA calculation for GA case
def ssag(x):
    return 3.0 / (919.0 * x)

## SSA calculation for BI case
def ssab(x,rho):
    return (3.0/x)*( (1.0/rho) - (1.0/919.0))

## process all GA cases
for rho in rhogL:
    for r in rgL:
        lscat = 4.0/ (Qscat * rho * ssag(r))  #scattering length, m
        #calculate single scattering albedo
        albedo = 1 - 0.85*kabs*r

        # need to make directory bc to contain all absorbing BC runs
        filename = "./bc/outbcG%d-%0.4f.txt" % (rho,r)
```

```
        # this data is written to the mcsbclog.txt file.
        # Post processing depends on this file being correct.
        string = "%s\t%f\t%f\t%d\t%f\t%f\t%f\t%f\n" % (filename,r,ssag(r),rho, lscat,
        lz/lscat, albedo, lt/lscat)
        f.write(string)

        # prepare command to the batch queing system
        cmd = "printf \"/home/dan/wais/mc_slab/mcsbc -g %0.3f -p %d -m %d -z %0.3f -t
        %0.03f > %s \" | batch"
              % (gGA, Nphotons, maxscatter, lz/lscat, lt/lscat, filename)
        os.system(cmd)  # submit to que

## process all BI cases
for rho in rhobL:
    for r in rbL:
        lscat = 4.0/ (Qscat * rho * ssab(r,rho))  #scattering length, m
        #calculate single scattering albedo (though not valid for BI case)
        albedo = 1 - 0.85*kabs*r

        filename = "./bc/outbcB%d-%0.4f.txt" % (rho,r)

        # this data is also written to the mcsbclog.txt file.
        # Post processing depends on this file being correct.
        string = "%s\t%f\t%f\t%d\t%f\t%f\t%f\t%f\n" %
                 (filename,r,ssab(r,rho),rho, lscat, lz/lscat, albedo, lt/lscat)
        f.write(string)

        # prepare command to the batch queing system
        cmd = "printf \"/home/dan/wais/mc_slab/mcsbc -g %0.3f -p %d -m %d -z %0.3f -t
        %0.03f > %s \" | batch" % (gBI, Nphotons, maxscatter, lz/lscat, lt/lscat,
        filename)
        os.system(cmd)   # submit to que

f.close()
```

B.3 Post Processing Script

```
## mcpost.py - Daniel J. Breton, University of Maine Physics
## 26 Oct 2010
## the purpose of this script is to automate running something like this:
## awk -f postGA.awk -v albedo=0.9998 out600-0.0006.txt
## OR
## awk -f postBI.awk -v K=-0.123 out850-0.0008.txt
## over and over again, with appropriate albedo/attenuation values.

## it requires the files postGA.awk and postBI.awk to exist in the current
## directory, and are reproduced here.  The awk codes can be modified to
## tally photons leaving the other cube faces if desired.

awkfileGA = """
# awk code for determining total emerging brightness
# this code is for the GRAINS IN AIR approximation
# will use --assign albedo=0.5 on command line to adjust

BEGIN {
  BR_cum = 0.0
  BE_cum = 0.0
  BT_cum = 0.0
}

{
    #if reflected at x = 0
    if($1==-2) { BR_cum = BR_cum + (albedo**$9) }

    #if emerging at z = 0
    if($1==-1) { BE_cum = BE_cum + (albedo**$9) }

    #if transmitted through x = sample_thick
    if($1==-3) { BT_cum = BT_cum + (albedo**$9) }
}

END { print BR_cum, BE_cum, BT_cum }
"""

awkfileBI = """
# postBI.awk - Daniel J. Breton, 27 Oct 2010
# awk code for determining total emerging brightness
# this code is for the BUBBLES IN ICE approximation
# assumes absorption length of 8.3 m => k_ice =0.12 1/m
# will use -v K=1234 to assign the appropriate absorption coefficient
# in mcpost.py

BEGIN {
  BR_cum = 0.0
  BE_cum = 0.0
  BT_cum = 0.0
}

{
    #if reflected at x = 0
    if($1==-2) { BR_cum = BR_cum + exp(K*$8) }

    #if emerging at z = 0
    if($1==-1) { BE_cum = BE_cum + exp(K*$8) }
```

```
    #if transmitted beyond x = sample_thick
    if($1==-3) { BT_cum = BT_cum + exp(K*$8) }
}

END { print BR_cum, BE_cum, BT_cum }
"""

import os

fin = open("mcslogbc.txt", "r")  # open log file of runs created by mcauto3bc.py

rhothreshold = 750  #threshold for changing from GA to BI approximation

for line in fin:
    q=line.split()
    name = q[0]
    rho = float(q[3])
    lscat = float(q[4]) # meters per scattering length
    albedo = float(q[6])

    # to generate correct BI attenuation coefficient, we must convert
    # 0.12 1/m into inverse scattering length units.
    # 0.12 is 1/8.3m absorption length for 600 nm light in ice
    K = -0.12*lscat*rho/919.0

    if rho < rhothreshold:
        awkcmd = "awk -f postGA.awk -v albedo=%f %s" % (albedo, name)
        a = os.popen(awkcmd, 'r')
        print line.rstrip('\n') + "  " + a.readline().rstrip('\n')

    if rho >= rhothreshold:
        awkcmd = "awk -f postBI.awk -v K=%f %s" % (K, name)
        a = os.popen(awkcmd, 'r')
        print line.rstrip('\n') + "  " + a.readline().rstrip('\n')
```

BIOGRAPHY OF THE AUTHOR

Daniel James Breton was born in Portland, Maine and subsequently raised in Bangor, Maine. He was a 1993 graduate from Cheverus High School in Portland, Maine. Upon completing a B.S. in Nuclear Engineering at Rensselaer Polytechnic Institute in 1997, he volunteered for the U.S. Navy Submarine Force. Commissioned in 1998, he served two years in training and four years on board the USS Parche (SSN 683) based out of Bangor, Washington. At the end of his service, he returned to Maine to pursue more scholarly endeavors, including a M.Eng in Engineering Physics at the University of Maine.

Daniel James Breton is a candidate for the Doctor of Philosophy degree in Physics from The University of Maine in May 2011.